ABOUT THE RELEVANCE OF SNOW MICROSTRUCTURE STUDY IN CRYOSPHERIC SCIENCES

EDITED BY: Maurine Montagnat, Guillaume Chambon, Johan Gaume, Melody Sandells and Pascal Hagenmuller

PUBLISHED IN: Frontiers in Earth Science

frontiers Research Topics

ISSN 1664-8714
ISBN 978-2-88966-359-0
DOI 10.3389/978-2-88966-359-0

About Frontiers

Frontiers is more than just an open-access publisher of scholarly articles: it is a pioneering approach to the world of academia, radically improving the way scholarly research is managed. The grand vision of Frontiers is a world where all people have an equal opportunity to seek, share and generate knowledge. Frontiers provides immediate and permanent online open access to all its publications, but this alone is not enough to realize our grand goals.

Frontiers Journal Series

The Frontiers Journal Series is a multi-tier and interdisciplinary set of open-access, online journals, promising a paradigm shift from the current review, selection and dissemination processes in academic publishing. All Frontiers journals are driven by researchers for researchers; therefore, they constitute a service to the scholarly community. At the same time, the Frontiers Journal Series operates on a revolutionary invention, the tiered publishing system, initially addressing specific communities of scholars, and gradually climbing up to broader public understanding, thus serving the interests of the lay society, too.

Dedication to Quality

Each Frontiers article is a landmark of the highest quality, thanks to genuinely collaborative interactions between authors and review editors, who include some of the world's best academicians. Research must be certified by peers before entering a stream of knowledge that may eventually reach the public - and shape society; therefore, Frontiers only applies the most rigorous and unbiased reviews.
Frontiers revolutionizes research publishing by freely delivering the most outstanding research, evaluated with no bias from both the academic and social point of view. By applying the most advanced information technologies, Frontiers is catapulting scholarly publishing into a new generation.

What are Frontiers Research Topics?

Frontiers Research Topics are very popular trademarks of the Frontiers Journals Series: they are collections of at least ten articles, all centered on a particular subject. With their unique mix of varied contributions from Original Research to Review Articles, Frontiers Research Topics unify the most influential researchers, the latest key findings and historical advances in a hot research area! Find out more on how to host your own Frontiers Research Topic or contribute to one as an author by contacting the Frontiers Editorial Office: researchtopics@frontiersin.org

ABOUT THE RELEVANCE OF SNOW MICROSTRUCTURE STUDY IN CRYOSPHERIC SCIENCES

Topic Editors:
Maurine Montagnat, Centre National de la Recherche Scientifique (CNRS), France
Guillaume Chambon, National Research Institute of Science and Technology for Environment and Agriculture (IRSTEA), France
Johan Gaume, École Polytechnique Fédérale de Lausanne, Switzerland
Melody Sandells, Northumbria University, United Kingdom
Pascal Hagenmuller, UMR3589 Centre national de recherches météorologiques (CNRM), France

Citation: Montagnat, M., Chambon, G., Gaume, J., Sandells, M., Hagenmuller, P., eds. (2021). About the Relevance of Snow Microstructure Study in Cryospheric Sciences. Lausanne: Frontiers Media SA. doi: 10.3389/978-2-88966-359-0

Table of Contents

frontiers in Earth Science

EDITORIAL
published: 20 November 2020
doi: 10.3389/feart.2020.619509

Editorial: About the Relevance of Snow Microstructure Study in Cryospheric Sciences

Maurine Montagnat[1,2]*, *Guillaume Chambon*[3], *Johan Gaume*[4,5], *Pascal Hagenmuller*[2] and *Melody Sandells*[6]

[1]Univ. Grenoble Alpes, CNRS, IGE, Grenoble, France, [2]Université Grenoble Alpes, Université de Toulouse, Météo-France, CNRS, CNRM, Centre d'Études de la Neige, Grenoble, France, [3]Université Grenoble Alpes, INRAE, UR ETNA, St-Martin-d'Hères, France, [4]Ecole Polytechnique Fédérale de Lausanne (EPFL), Lausanne, Switzerland, [5]WSL Institute for Snow and Avalanche Research SLF, Davos Dorf, Switzerland, [6]Northumbria University, Newcastle upon Tyne, United Kingdom

Keywords: snow, microstructure, mechanical properties, optical properties, microCT

Editorial on the Research Topic

About the Relevance of Snow Microstructure Study in Cryospheric Sciences

Snow is an ubiquitous material in the Earth cryosphere and knowledge of its physical, electromagnetical and mechanical properties is critical for many applications such as estimating the Earth energy balance in a changing climate, forecasting avalanches or predicting water run-off.

Snow on Earth exists close to its melting point and presents a high porosity. Active metamorphism leads to the existence of a wide range of snow forms, usually described under the term "microstructure". This Research Topic emphasizes the link between snow microstructure and snow properties but also illustrates that the exact definition of snow microstructure highly depends on the considered application, scale, and the available instruments in the field or in the cold-room. Microstructural proxies range from a complete description of the 3D arrangement of ice and pore space obtained by X-ray microtomography (microCT), to density measurements recovered by remote sensing techniques.

Historically, snow microstructure was classified visually by grain size and shape with a crystal card and magnifying glass (Fierz et al., 2009). Langlois et al. revisit this classical technique by means of micro-photographs taken under angular directional LED lighting. Numerical processing of the micro-photographs enables the automatic retrieval of the size distribution and specific surface area of thousands of snow grains. Moreover, different light angles help reduce the bias caused by a 2D representation of 3D grains. The directional LED technique appears as a cheap, efficient and field adapted tool to characterise snow microstructure and give input for Radiative Transfer Models. The main limitation remains the necessity to individualise grains in the material, which questions (again) the definition of a snow grain.

Microstructural properties govern mechanical properties of snow. Conversely, the mechanical response of the material can be analyzed as a proxy of the microstructure. Cone penetration tests as the Snow Micro Penetrometer (Schneebeli and Johnson, 1998), are well adapted to take up the challenge of providing microstructural proxies from simple mechanical field tests. However, a rigorous inversion of the penetration signals requires a detailed investigation of the interaction between the cone tip and snow microstructure. Peinke et al. combine cone penetration tests laboratory experiments and *in-situ* microCT characterisation to quantify 3D grain displacements in the sample. They observe both compaction and local dilation around the cone tip, and evaluate the extent of the compaction zone. Comparisons with currently existing models point out their limitations.

OPEN ACCESS

Edited and reviewed by:
Regine Hock,
University of Alaska Fairbanks,
United States

***Correspondence:**
Maurine Montagnat
maurine.montagnat@univ-grenoble-alpes.fr

Specialty section:
This article was submitted to Cryospheric Sciences, a section of the journal Frontiers in Earth Science

Received: *20 October 2020*
Accepted: *30 October 2020*
Published: *20 November 2020*

Citation:
Montagnat M, Chambon G, Gaume J, Hagenmuller P and Sandells M (2020) Editorial: About the Relevance of Snow Microstructure Study in Cryospheric Sciences. Front. Earth Sci. 8:619509. doi: 10.3389/feart.2020.619509

The mechanical response of snow is often modeled based on microCT measurements by Discrete Element approaches that consider snow grains as (e.g., spherical) individual elements interacting through contact forces (Hagenmuller et al., 2015). Willibald et al. tackle the problem of evaluating these micro-mechanical approaches using analogous snow samples with simplified geometry. They present mechanical experiments performed on synthetic samples made of sintered ice beads. They focus on the role of grain arrangement and sintering on the evolution of some mechanical properties (Young's modulus and compressive strength), and show that ice beads assembly response is consistent with near-natural snow.

To avoid manipulating extremely fragile snow samples, Lieblappen et al. show that ultrasonic waves can be used to retrieve snow porosity and tortuosity. They consider ultrasonic reflections instead of classical transmissions suitable for stronger samples (Umnova et al., 2005). Porosity is measured with only 8% difference with microCT measurements, while tortuosity shows larger discrepancies, depending on the snow type. This technique is sensitive enough to detect changes over a single day in fresh snow. With the technical aspects well detailed, transfer of the technique to field conditions appear highly feasible and opens new opportunities.

Understanding the process of snow to firn and ice densification is key for retrieving the accurate delta-age between ice and air trapped along ice cores, and thus the interpretation of climate records. Most densification models stand on 1D geometry and simplified mechanical schemes (Lundin et al., 2017). Fourteau et al. report here on an attempt to take a proper account of the real firn microstructure (obtained from microCT) together with a physically-based treatment of surface diffusion in the pores and viscoplastic deformation of the ice matrix. By doing so, based on the Level-Set formalism to track the ice/pore interface, they decipher the precise mechanisms at play during pore closure.

Montagnat et al. present the first continuous, high-resolution profiles of both snow microstructure (by microCT) and crystallographic fabric in Greenland surface snow. A clear seasonal signal from alternating temperature gradients is recovered from the anisotropy parameters. It is also shown that in the warmest conditions, load over the deepest snow layers might imprint the crystallographic fabric. Interestingly, Moser et al. analyze a 3 m Antarctic snow core and similarly find a seasonal pattern in snow anisotropy. On top of that, they combine isotope and trace element analysis with microCT to reconstruct the deposition history from the core. Both studies offer new insights in snow densification processes.

While a useful tool for dating, chemical composition of snow can also affect its mechanical and electromagnetic properties. Courville et al. complement the existing research on dust deposition impact on snow by focusing on the location of dust within the microstructure and its microbiological content. MicroCT observations locate dust particles mostly in the snow grains, at the snow/pore interface, leaving contact with the air and biological elements. Clues are given that dust could also interact with metamorphism processes. These data could help tracing the origin of dust and its evolution with time. Measurements of microbial communities suggest links between dust and microbial impact on snowpack characteristics.

Finally, Adachi et al. offer new perspectives on the characterisation of liquid water content in snow by using Magnetic Resonance Imaging (MRI). In contrast to classical calorimetry and dielectric measurements, MRI is non-destructive and gives access to distribution of water in the sample at a millimetric resolution. Besides providing a validation of the method, they illustrate its potential through measurements of the hysteresis of the snow-water retention curve during wetting-drying cycles.

The state-of-the-art review gathered in this Research Topic illustrates how available techniques for snow microstructure characterisation have come a long way since hand lens measurements. Advent of microCT constituted a step change to decipher the variety of geometrical arrangements in different snow types, and bridge the gap between microstructure and macroscopic properties. Future works will go further in complementing microCT measurements with MRI, crystallographic, chemical and biological analyses, in order to provide ever deeper insights into fundamental processes such as melt drainage, avalanche formation, dust origins, and formation of climatic records.

AUTHOR CONTRIBUTIONS

MM wrote the first draft of the Editorial based on the content of the articles from the Research Topic. The other authors all equally participated in correcting, modifying and improving the first version toward the final one.

REFERENCES

Fierz, C., Armstrong, R. L., Durand, Y., Etchevers, P., Greene, E., McClung, D. M., et al. (2009). "The international classification for seasonal snow on the ground." in *IHP technical documents in hydrology 83*. Paris, France: UNESCO–International Hydrological Programme.

Hagenmuller, P., Chambon, G., and Naaim, M. (2015). Microstructure-based modeling of snow mechanics: a discrete element approach. *Cryosphere* 9 (5), 1969–1982. doi:10.5194/tc-9-1969-2015

Lundin, J. M. D., Stevens, C. M., Arthern, R., Buizert, C., Orsi, A., Ligtenberg, S. R. M., et al. (2017). Firn model intercomparison experiment (firnmice). *J. Glaciol.* 63, 401–422. doi:10.1017/jog.2016.114

Schneebeli, M., and Johnson, J. B. (1998). A constant-speed penetrometer for high-resolution snow stratigraphy. *Ann. Glaciol.* 26, 107–111. doi:10.3189/1998AoG26-1-107-111

Umnova, O., Attenborough, K., Shin, H.-C., and Cummings, A. (2005). Deduction of tortuosity and porosity from acoustic reflection and transmission measurements on thick samples of rigid-porous materials. *Appl. Acoust.* 66, 607–624. doi:10.1016/j.apacoust.2004.02.005

Conflict of Interest: The authors declare that the research was conducted in the absence of any commercial or financial relationships that could be construed as a potential conflict of interest.

frontiers in Earth Science

ORIGINAL RESEARCH
published: 06 September 2019
doi: 10.3389/feart.2019.00229

Ice Spheres as Model Snow: Tumbling, Sintering, and Mechanical Tests

Carolin Willibald[1], Sophia Scheuber[2], Henning Löwe[1], Jürg Dual[2] and Martin Schneebeli[1]*

[1] WSL Institute for Snow and Avalanche Research SLF, Davos, Switzerland, [2] Institute of Mechanical Systems, ETH Zürich, Zurich, Switzerland

The snow microstructure is crucial for the mechanical behavior of snow, but is usually simplified in numerical models. In Discrete Element Models (DEM), often used in snow mechanics, the microstructure is typically represented by sphere assemblies. This renders a model validation difficult, as the real snow crystal shapes affect the actual contacts and consequently the macromechanical behavior. To approach this problem from the experimental side, we created simplified microstructures comprising spherical ice particles and examined this model snow under structural and mechanical aspects. We developed a new method to create uniform ice spheres and performed a detailed particle characterization using 3D computed tomography (CT). We examined sintered sphere assemblies to relate microstructural and macromechanical properties in a geometrically well-defined system. Microstructural variation was created by varying the sample density and sintering time, to study the role of the number and size of contacts. 3D CT scans were taken of sintered sphere samples, which were then tested in unconfined compression experiments together with a nature identical snow type as a reference. The scans were evaluated regarding the number of particles and contacts, and were used to compute the elastic modulus, as additional mechanical property. The results of the particle characterization showed the spherical shape and sharp size-distribution of the particles, which are the main prerequisites for model validation. The CT image analysis showed the reproducibility of the sphere assemblies and can be applied for efficient reconstruction of the experimental samples as initial condition for simulations. The mechanical properties conform with the reference snow and the expectations from literature, however, the CT scans revealed a complex geometry of the sintered contacts with measurable impact on the mechanical properties.

Keywords: snow mechanics, microstructure, sintering, ice spheres, CT image analysis, compression experiments, discrete element modeling

OPEN ACCESS

Edited by:
Guillaume Chambon, National Research Institute of Science and Technology for Environment and Agriculture (IRSTEA), France

Reviewed by:
Ian Baker, Dartmouth College, United States
Sandra Piazolo, University of Leeds, United Kingdom
Antoine Wautier, National Research Institute of Science and Technology for Environment and Agriculture (IRSTEA), France

****Correspondence:***
Carolin Willibald
carolin.willibald@slf.ch

Specialty section:
This article was submitted to Cryospheric Sciences, a section of the journal Frontiers in Earth Science

Received: *29 March 2019*
Accepted: *20 August 2019*
Published: *06 September 2019*

Citation:
Willibald C, Scheuber S, Löwe H, Dual J and Schneebeli M (2019) Ice Spheres as Model Snow: Tumbling, Sintering, and Mechanical Tests. Front. Earth Sci. 7:229. doi: 10.3389/feart.2019.00229

1. INTRODUCTION

Snow mechanics is still an active field of research, despite its considerable history over the past 90 years (Mellor, 1975; Shapiro et al., 1997). Avalanche risk forecasting, snow mobility, snow sports or snow and firn compaction, in general, are just a few of the applications that require quantitative characterization of the dominant mechanical processes. The main challenge thereby comes from the versatile and changeable nature of snow microstructure. Snow is a porous material that consists

of an ice skeleton and air. The skeleton forms from single ice crystals that grow at mutual contacts via (early stage) sintering and later evolve in time via (late stage) sintering which are commonly subsumed in the term snow metamorphism. The geometry of the microstructure manifests itself in diverse snow types and physical properties. A reliable mechanical model would only need to combine a geometrical description (snow microstructure) with mechanical properties of ice to fully predict the mechanical behavior of snow (Schneebeli, 2004; Chandel et al., 2014; Hagenmuller et al., 2014).

The geometrical characterization of snow microstructure has considerably advanced in recent years, mainly due to micro-computed tomography (CT). CT imaging allows us to constrain the microstructure in simulations for comparison with experiments. Combining microstructural and mechanical properties of snow has considerably enhanced the comprehension of snow mechanics (Wang and Baker, 2013; Hagenmuller et al., 2014; Kochle and Schneebeli, 2014; Srivastava et al., 2016). For example, it has been shown that the sintered contacts between the grains are the mechanically weakest parts where the structure fractures (Hagenmuller et al., 2014); or that the elastic moduli can be fully predicted from the microstructure measured by CT and the elastic properties of ice (Gerling et al., 2017). However, the incorporation of the microstructure comes along with high methodological and computational effort. A detailed reconstruction (Hagenmuller et al., 2015) is restricted to small volumes, whereas in a simplified representation (Theile and Schneebeli, 2011) the precision is limited by the complexity of the snow crystal shape that renders an unambiguous identification of grains and contacts impossible. Quite generally, if a model utilizes a microstructure model comprising grains, the mapping onto the real bicontinuous geometry obtained from CT images remains the main difficulty.

The difficulty of incorporating the microstructure is an inherent problem of discrete element modeling (DEM) of snow. DEM has become a powerful tool to model snow mechanics (Johnson and Hopkins, 2005; Gaume et al., 2015; Hagenmuller et al., 2015; Michael et al., 2015; Kabore and Peters, 2018) and has also been employed in snow optics (Kaempfer et al., 2007). DEM is widely used to simulate granular materials by calculating particle dynamics and interactions. For snow, DEM is appropriate because the granular particles can also be bonded and thereby represent the sintered, solid-like structure of snow, and yet fracture can be described, as under fast deformation. Then the two key ingredients that need to be specified in DEM modeling are particles and contacts between them. In the simplest and computationally most efficient case, the particles are spherical. The remaining difficulty is then to map the experimental microstructures onto a sphere assembly that captures properties of real snow. The existing approaches include e.g., generic (ballistic) deposition models (Mulak and Gaume, 2019) or configurations drawn from Baxter's sticky hard spheres (Gaume et al., 2017). While these approaches capture some aspects of the microstructure, they do not overcome the complex shape of the snow crystals that affects the particle interactions, and thus the mechanical response is strongly simplified. The effects of the snow particle shape and the actual micro-mechanical contacts cannot be resolved. This was pointed out by Hagenmuller et al. (2015) who studied diverse snow microstructures and their mechanical properties through DEM compression tests. They underlined the necessity of mechanical experiments in combination with CT scans to reduce the uncertainties of the microscopic contact parameters and to validate models. This problem, namely the comparability of experiments and simulations, can be tackled in two ways. First, on the modeling side, the representation of microstructure in DEM could be made more sophisticated (Mede et al., 2018) to represent the true microstructure by only using spheres. Second, it is possible to explore the problem also from the experimental side, and experimentally create synthetic microstructures that closely resemble ideal sphere assemblies.

Snow made of spherical ice particles has been prepared and used in several studies on sintering, the formation of solid necks at the contact points (Kingery, 1960; Kuroiwa, 1961; Hobbs and Mason, 1964; Chen and Baker, 2010). The spheres were commonly produced by spraying water into liquid nitrogen or oxygen to obtain particles in a diameter range of 20 µm up to 4 mm. Ideally grown necks were observed in conformance with the theoretical prediction (Hobbs and Mason, 1964). This renders systems of sintered ice spheres as ideal candidates for DEM models since the key entities of particles and contacts are well-defined. The contact size can even be modified by varying the sintering time. These are ideal preconditions to examine microstructural and mechanical properties of an artificial microstructure comprising spheres. However, the size-dependent sintering process is faster on smaller particles, and the deviations from the ideal spherical shape, due to mass transporation from bulk to neck growth, are more pronounced on smaller particles. Therefore, rather large spheres seem practical to examine contact properties of a sphere assembly while preserving the spherical particle shape for a longer time.

In the present paper, we examine the potential of spherical model snow as a mean to close the gap between experiments and simulations of snow mechanics, that remains despite detailed CT imaging of the microstructure. The ice spheres with clearly defined shapes and contacts, seem to be an ideal intermediate step, to examine contact properties and facilitate a close model validation. We present a new method to create spherical model snow and idealized microstructures, together with a careful characterization of geometrical (spheres, contacts) and mechanical (elasticity and strength) properties. We seek to provide experimental data that can be used for actual DEM simulations. To this end, we developed a novel method for ice bead production and performed a detailed characterization of the particles in terms of particle size and sphericity, using CT images. For the mechanical characterization, unconfined compression experiments of sintered ice bead samples were performed in combination with 3D CT scans. The scans were used to analyze the microstructure and relate it to the mechanical response, and to compute the elastic modulus through FEM simulations as an additional macro-mechanical parameter. Two important contact parameters relevant for DEM (number of contacts, mechanical properties of contacts) were experimentally

manipulated: some of the ice bead samples were densified to increase the number of contacts, and different sintering times were investigated to influence the size of the contacts between the particles. As a reference we performed experiments also with nature identical snow.

The results of the particle characterization, namely high sphericity, and narrow size distribution, are ideal prerequisites for an experimental DEM analogon. The CT image analysis showed the reproducibility of the sphere assemblies, and can be applied for efficient reconstruction of the experimental sphere assemblies, as initial condition for simulations. However, the CT images revealed a complex geometry of the bonds after the manipulation by sintering with measurable impact on the mechanical properties.

The paper is organized as follows: The next section starts with the description of the production of the ice beads and snow samples, followed by the specification of the compression experiment. The CT-based methods for particle and structure analysis, as well as the simulation of the elastic modulus are explained together with a qualitative analysis of the ice bead crystallography. The order of particle and structure characterization, simulations of elastic modulus, and compression tests is given in the result section as well as in the subsequent discussion.

2. MATERIALS AND METHODS

2.1. Ice Bead Production

To meet the requirements of very round ice particles with a narrow size distribution, we constructed a tumbling machine to round off frozen water droplets, similar as in industrial methods like tumbling or barrel finishing (Gillespie, 2007). The droplets were obtained by dropping deionized, purified water with a syringe on a Teflon sheet at −20°C. Using the syringe, the particles had approximately the same initial size. For the tumbling machine we mounted an aluminum can with a diameter of 15.5 cm on a rotary motor, sketched in **Figure 1A**. The can is coated with sand paper (ISO grit P100) on the inside and closed with a cap during tumbling. The rotational velocity ($\approx 3\,s^{-1}$) was chosen such that the granular flow kept in the rolling regime and no particles stick to the wall due to the centrifugal force. During tumbling the particles become smaller and round off by abrasion to a spherical shape. Tumbling velocity and time determine the size of the particles. For our analysis we produced ice beads in the size range of 2−2.2 mm and we stopped the tumbling process once the particles passed a 2.2 mm sieve. Dust and smaller particles were sieved out with a 2 mm sieve. The frozen water droplets need to be tumbled for ∼24 h at −20°C to turn into ice beads in this size range. A microscopy image of one exemplary particle is shown in **Figure 2B**.

Within the scope of the present application, ice beads can be reused as they were not destroyed in the experiments. We did neither observe fractured particles after the experiment nor any changes of the regarded particle characteristics, like size, or shape. However, before using them in a next experiment, they were tumbled again for about half an hour to smooth the surface which became rough during sintering.

2.2. Nature Identical Snow

As reference for the analysis and the mechanical tests, we included a prevalent and widely investigated snow type in the analysis with isothermally metamorphed rounded grains. The snow was produced in the lab using fresh, dendritic snow from a snowmaker (Schleef et al., 2014) as base material. It was sieved into a Styrofoam box and stored at −5°C over 3 month. Rounded grains developed in a sub-millimeter size range (**Figure 2A**). According to Schleef et al. (2014), who performed a comprehensive comparison of lab-produced and natural snow, we refer to this snow as "nature identical snow" and classify it as large rounded grains RG according to Fierz et al. (2009).

For the compression tests, the snow was sieved with two sieves with mesh sizes of 1.4 and 0.7 mm, to obtain separated particles in a restricted size range. A 2D cross-section of a 3D binary CT image is presented in **Figure 3D**. CT images were used to characterize the snow structure in terms of density and specific surface area (SSA).

2.3. Sample Preparation

With the freshly tumbled ice beads we prepared cylindrical samples (**Figure 2C**) for the compression experiments. The sample holders consisted of a round base with a diameter of 33.6 mm and a cylindrical wall around. The wall could be fixed on the base to fill in and sinter the particles, and slid down to perform the unconfined compression test (**Figures 1B,C**). The

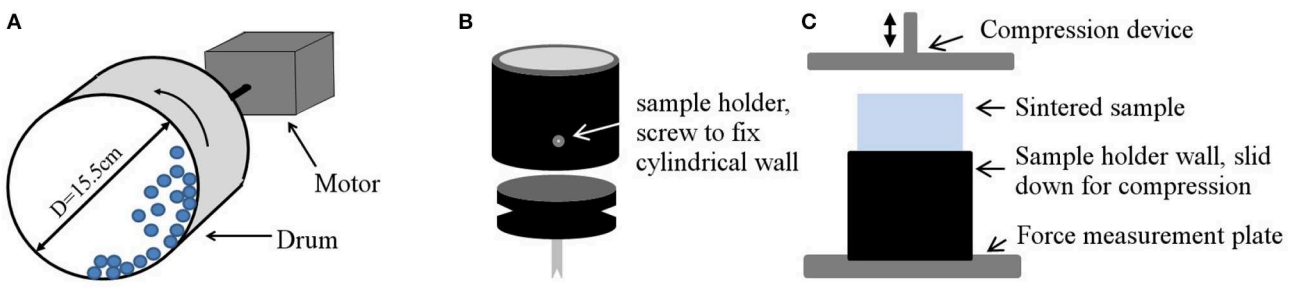

FIGURE 1 | (A) Sketch of the tumbling machine consisting of a cylindrical drum and a rotary motor. **(B)** Sketch of the sample holder and **(C)** the experimental set-up for the compression tests.

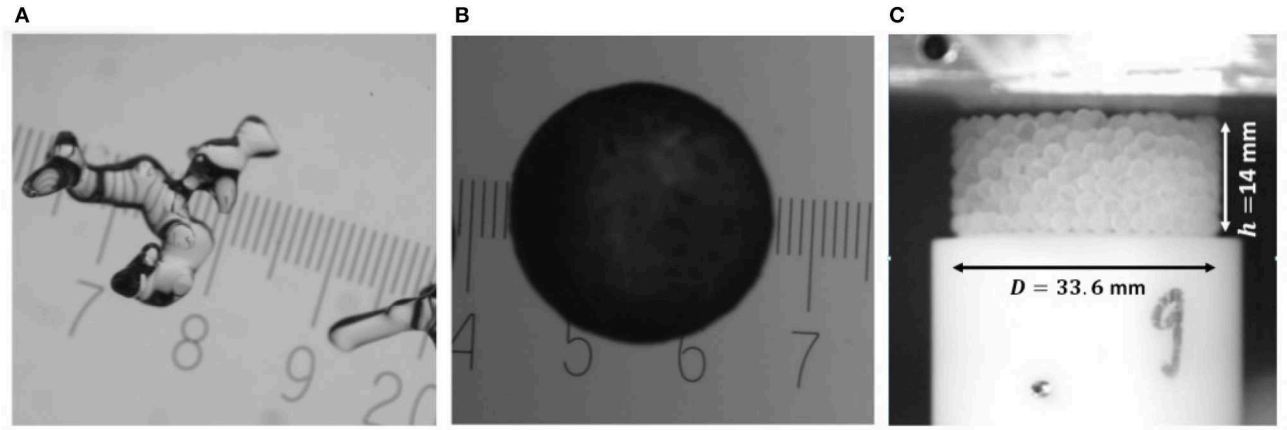

FIGURE 2 | Microscopy images of exemplary particles of nature identical snow **(A)** and ice beads **(B)**, same scale (mm) in both images. **(C)** Sample of unconfined sintered ice beads, after removal of sample holder wall, before compression test.

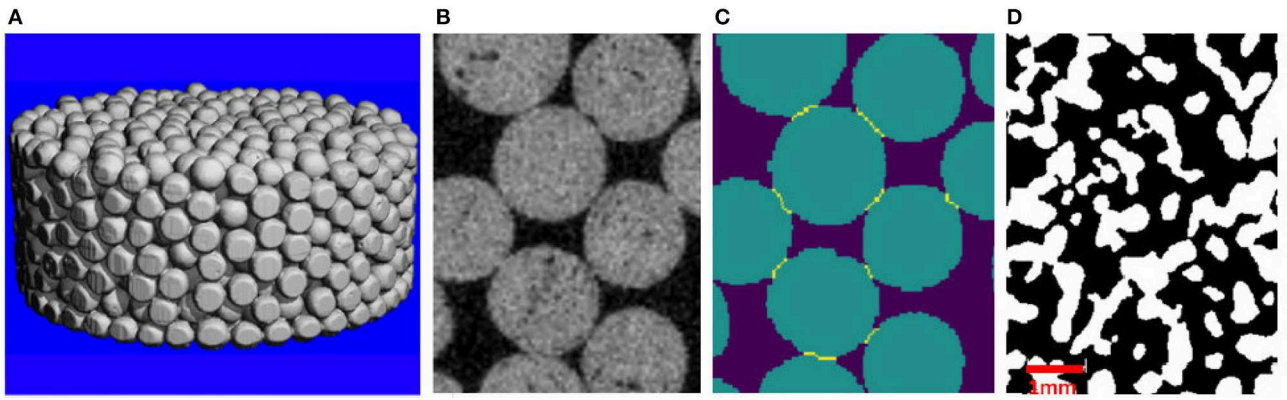

FIGURE 3 | CT images of the samples: **(A)** binary 3D image of experimental cylindrical ice bead sample (the particles at the rim appear flat, due to the chosen section, to cut out the sample holder wall). **(B)** 2D slice of ice bead sample, gray image with 18 μm resolution; **(C)** downscaled and segmented binary image, ice beads were identified using a watershed algorithm and the watersheds as contacts between the particles are depicted as yellow lines. **(D)** Binary microstructure of nature identical snow (white ice phase), identification of particles and contacts is ambiguous.

fixed cylinder wall determined the sample height of 14 mm. With the ice beads, we created two sample classes, namely compacted and uncompacted samples. For the uncompacted samples (referred to as poured beads), the wall was fixed and the particles were poured in. Before they were sealed with a lid to avoid evaporation, particles that stick out were carefully removed to flatten the surface, without pushing them into the sample. For the compacted samples (referred to as tapped beads) the cylindrical wall was held higher than 14 mm for filling in the particles and tapping them 30 times on the table, to densify the structure. After the tapping the wall was slid down and fixed to the same height of 14 mm, to flatten the surface and close the sample with a lid. The samples of the nature identical RG snow were prepared in the same way as the poured ice bead samples: the snow was sieved into the sample holder with the fixed wall and the surface was flattened by removing additional particles.

For sintering, the samples were then placed in a Styrofoam box in a −10°C cold room. The temperature during the entire sintering process was measured for the tapped samples. The fluctuation in the box was ±0.5°C. For all sample classes we investigated different sintering times t_s. We chose two main sintering times with a higher number of samples and some sintering times in between, with less samples, to cover a wider time-range. The numbers of samples per sintering time are listed in **Table 1**. The number of samples with CT scans is written in the parentheses and also counted in the total number of samples. We have chosen different main sintering times for ice beads and RG snow. This reflects the differences in sintering behavior of different snow types (van Herwijnen and Miller, 2013). In the experiments we aimed to cover the time ranges with highest sintering rates, which are different for ice beads and nature identical snow.

2.4. Unconfined Uniaxial Compression Experiments

Unconfined compression experiments were performed to derive with the compressive strength a macro-mechanical property of the samples. The experiments were conducted at −10°C with a

TABLE 1 | Overview of the tested samples per sintering time t_s.

Sample class	5 min	2 h	4 h	8 h	1 day	2 days	3 days	5 days	10 days
Poured ice beads	–	–	–	–	4	6	13 (2)	12 (2)	5 (2)
Tapped ice beads	–	–	–	–	–	–	–	7 (7)	7 (6)
RG snow	11	6	20 (3)	6	16 (3)	7	–	5	–

Number in parentheses is the number of samples with CT scan.

friction and compression testing machine described by Theile et al. (2009). To compress a sample it was fixed on a force measurement plate, where the outer wall of the sample holder was removed by sliding it down, as sketched in **Figures 1B,C**. The unconfined specimen was then compressed to a depth of 8 mm with a constant velocity of 10 mm/s. A force—displacement curve was recorded with a sampling rate of 10 kHz. For the stress—strain conversion, the force was normalized by the circular sample area. Taking the sample area as contact area included the simplification of a constant area. The change of the actual contact area, due to falling out particles during compression, could not be recorded.

2.5. Micro-Computed Tomography

For some samples, 3D CT scans were taken before the compression tests by using a Scanco Medical CT 40 scanner, that is operated in a cold room. The X-ray scanner was held constant at -10 ± 1°C. The trade-off between scanning time and resolution led to a scanning duration of 3 h and a voxel size of 18 µm, resulting in a sample dimension of about (2,000 × 2,000× 800) voxel. With that, the entire cylindrical sample was scanned to allow for a complete reconstruction of all particles in the experimental samples, as input for DEM simulations, (**Figure 3A**). The scans were timed as close as possible to the compression tests ($t_s - 3$ h) to capture the final sintering state in the images, but some variations were unavoidable.

2.6. 3D Image Analysis

First, the gray images (**Figure 3B**) need to be segmented to define ice and air phase. For each image, the appropriate threshold was determined by fitting the sum of three Gaussian distributions to the grayscale histogram, as described by Hagenmuller et al. (2013). A sub-volume of the binary image was then used to compute the elastic modulus, as described below, and to determine the specific surface area SSA via interface triangulation. The triangulation based method is a standard evaluation of the CT images that is provided by the vendor software from Scanco Medical (Hildebrand et al., 1999), for which a deviation of 5% was determined for a reference object with known surface area (Hagenmuller et al., 2016). For the structural analysis of the samples, the image resolution was decreased by a factor two, for numerical reasons. The downscaling was performed on the gray images and therefore acted like a filter. The preservation of the mean gray value before and after downscaling implies the invariance of the air-ice ratio, thus the scaling should not affect the derived parameters (number and size of particles and number of bonds). For the scaling eight voxels were integrated into one before the threshold was determined and the images segmented, as described above. A 2D slice of the downscaled binary image is shown in **Figure 3C**, where the ice phase is green (1) and the air is blue (0).

The subsequent image analysis was done in Python. The particles needed to be identified to determine the size distribution of the beads and to characterize the structure in terms of the number of particles n_p and the number of contacts n_b. In a first step, air bubbles in the ice phase had to be removed as they disturbed the segmentation process. This is achieved by identifying the largest connected air component and assigning all other voxels the ice value 1. On the bubble-free image a watershed algorithm was applied to identify the particles. This common algorithm is contained in the Python Scipy library. It is often used for similar problems and works well on clear defined shapes (Spettl et al., 2016), as the ones of the ice beads. With a distance transform on the ice phase, local maxima are found around the center of the particles. From these points the watershed algorithm starts to "flood" the ice phase, until a constriction – a watershed – is reached. Such a watershed should be located at the contact, the narrow part between two particles. When the contacts were found the particles were identified. The watersheds themselves were counted as the contacts and are depicted as yellow lines in **Figure 3C**.

To determine the size r_p of the ice beads, the voxels belonging to each particle were counted. Knowing the voxel size, we calculated the particle volume and translated this to the radius of an ideal sphere with equivalent volume. This method works well, given the spherical particle shape. For the sample density ρ the ice volume fraction ϕ was determined and multiplied by the density of ice, $\rho = \phi\rho_{ice}$.

2.7. FEM Simulation of the Elastic Modulus

A voxel-based Finite Element (FE) code (Garboczi, 1998) was used to compute the elastic moduli E of the samples. This was done to obtain a second macro-mechanical property, independent from the compression experiments. It has been shown by Gerling et al. (2017) that this microstructure-based method can be considered as a reliable estimate of the true elastic modulus of snow. In the FEM code, effective elastic moduli are computed from volume-averaged stresses when the sample is subjected to a prescribed volume-averaged strain. We used the same parameterization as Gerling et al. (2017) by assuming a microstructure made of isotropic, polycrystalline ice, with the ice bulk and shear moduli $K = 8.9$ GPa and $G = 3.5$ GPa. The simulations were performed on a cubic sub-volume of the binary images with the original resolution of 18 µm. For obtaining

equivalent cutouts, we analyzed the vertical density profiles of the samples and cut the uppermost slices off at a comparable density value. The x- and y-dimensions were the same for all images and chosen such that a maximum cube was cut out of the cylindrical sample volume. The sample dimension was then (1,200 × 1,200 ×650) voxel, corresponding to (21.6 × 21.6 × 11.7) mm, with slight variations in the z-dimension.

2.8. Qualitative Ice Bead Crystallography

As the internal crystalline structure of the ice beads is of potential relevance for model validation, we provide a fabric analysis, as part of the particle characterization. The analysis is based on polarized light microscopy (Riche et al., 2012). This method for visualizing the internal crystalline structure exploits the crystal-axis-orientation dependent optical properties of ice. Thin sections of ice were illuminated under different angles and from the refraction of the translucent light the crystal orientation was deduced. Due to the absence of a calibration of the microscope, only a qualitative picture can be provided. This is, however, sufficient to visualize differences in intensity and to identify differently oriented grains. We examined 31 particles, a random selection of which is shown in **Figure 4**. The ice bead slices we analyzed in this way consisted of 1 – 10 crystals. While we observed several mono-crystalline beads, we could not find an ice bead consisting of more than 10 crystals. The expectation value and standard deviation was (2.3 ± 1.5) crystals per bead.

3. RESULTS

3.1. Characterization of Ice Beads and RG Snow

The key requirements for the particles are a spherical shape and a narrow size distribution. To assess these properties, we analyzed the particle radius r_p and the specific surface area SSA. The particle radii r_p of the beads were calculated from all CT samples, with the average and standard deviation:

$$\bar{r}_p = (1.12 \pm 0.1)\,\text{mm}.$$

For the specific surface area SSA we obtained from all CT samples the average and standard deviation:

$$\overline{\text{SSA}} = (3.1 \pm 0.1)\,\text{m}^2\text{kg}^{-1}.$$

With a deviation of 6% this is very close to the SSA of an ideal sphere with the mean radius $\bar{r}_p$ of the ice beads, with 2.9 m^2kg^{-1}. Since the SSA, the surface to volume ratio, for a given volume is minimal for a sphere, this result implies that the ice beads are close to an ideal spherical shape. From these results, a measure of sphericity can be derived, by the ratio of the surface of a volume-equivalent sphere and the surface of an object (Wadell, 1935). For an ideal sphere, the sphericity is one, for the ice beads the computed sphericity is 0.92.

The nature identical snow was characterized in terms of density and SSA, both derived from the CT images. The respective mean values of the six samples are given by: $\overline{\rho} = (399 \pm 50)\,\text{kg/m}^3$ and $\overline{\text{SSA}} = (10.7 \pm 1.2)\,\text{m}^2\text{kg}^{-1}$.

The SSA of all CT samples, from RG snow and ice beads, is presented in **Figure 5B** together with the respective sintering time. The dotted lines indicate the averages and shows that the SSA is rather constant and no trend with sintering time can be seen.

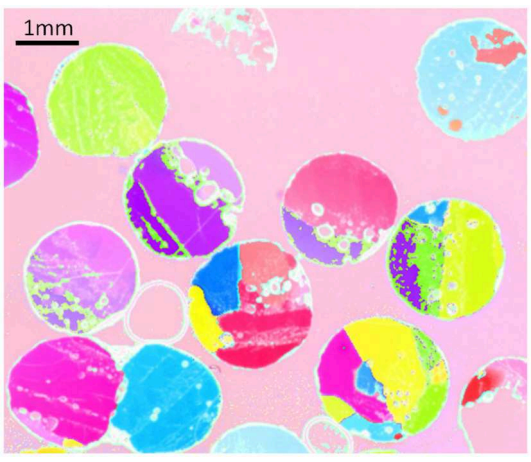

FIGURE 4 | Visualization of crystalline structure of several ice beads, ground to 50 μm thick slices. A mono-crystal is represented by one color.

3.2. Characterization of the Ice Bead Structures

To demonstrate the reproducibility of the ice bead structures, we determined the number of particles n_p, the number of bonds n_b and the ice volume fraction ϕ as structural parameters from the CT images, **Table 2**. From these values we calculated the contact density $\nu_c = \phi Z_c$, as used by Gaume et al. (2017), with the coordination number $Z_c = 2n_b/n_p$. For all samples these values, normalized by the mean of the respective sample class, are shown in **Figure 5A**, for the poured (left) and tapped beads (middle). The standard deviation of <10% as indicated in the dotted lines underlines the reproducibility of the structures. The sintering time of the samples can be read on the abscissa. To relate these parameters to the elastic moduli, all values were determined from the cubic sub-volumes of the images which were used for the computation of the elastic moduli.

To show the differences between the two sample classes, the contact density ν_c is plotted against the ice volume fraction ϕ in **Figure 6**. Although there is no sharp transition, it reveals the trend that the tapped samples have a higher density and more bonds per particle than the poured.

For the nature identical snow only density and elastic modulus are shown in **Figure 5A** (right), since no contact density could be determined. For both parameters the scatter is higher than for the ice bead samples and E exceeds the ±10% range.

3.3. FEM Simulations of the Elastic Modulus

The results for the elastic modulus are shown in **Figure 7A** against the sintering time t_s of the respective sample and in

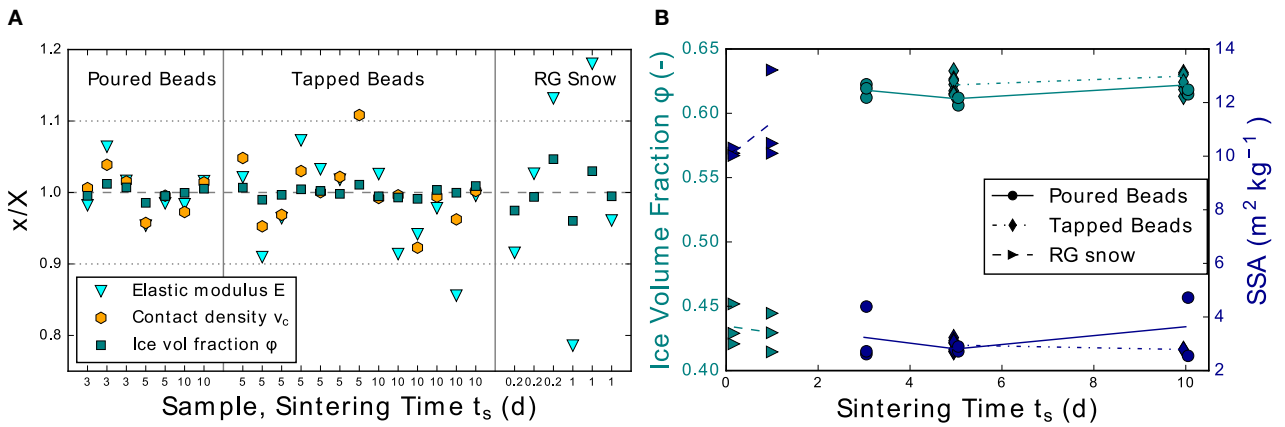

FIGURE 5 | (A) Structural parameters, $x = \nu_C$, ρ, and E normalized by the mean X of all images of one sample class are shown for all samples of the poured (left) and the tapped beads (middle) and for RG snow (right). The dotted lines indicate ±10%; the sintering time is denoted on the abscissa. **(B)** Ice volume fraction and SSA of all samples against the sintering time.

TABLE 2 | Mean and standard deviation of the ice volume fraction ϕ, contact density ν_C and elastic modulus E.

	Poured beads	Tapped beads	RG snow
ϕ	0.62 ± 0.01	0.63 ± 0.01	0.43 ± 0.05
ν_C	3.47 ± 0.1	3.6 ± 0.13	–
E (GPa)	1.03 ± 0.04	1.0 ± 0.11	0.44 ± 0.01

Figure 7B against the ice volume fraction ϕ. The contact density ν_c of the ice bead samples is color-coded and magnified in the inset. For the ice beads and the RG snow the values of E are clearly separated and each in a narrow range, between 0.34 and 0.52 GPa for RG snow and 1.2 and 1.5 GPa for the ice beads. **Figure 7A** distinguishes the two ice bead classes in symbols and colors and reveals a rather large scatter of elastic moduli for the tapped samples, compared to the poured. A relation with the sintering time cannot be extracted which indicates that the effect of sintering is not resolved in the images. **Figure 7B** shows the increase of E with the ice volume fraction, as expected from the literature (Kochle and Schneebeli, 2014; Gerling et al., 2017). The inset shows the elastic moduli for the ice beads as a function of the two investigated parameters with a potential influence on E: on the abscissa is the ice volume fraction and the contact density in the colors. The general picture looks as expected: an increase of E with ϕ and ν_c. However, a closer look and an intercomparison of the points reveals that examples can be found with similar ice volume fractions, and contact densities but different elastic moduli.

3.4. Compression Experiments

For a visual inspection of the compression curves we show an example of a poured ice bead sample in **Figure 8A**. The sample has been sintered for 5 days and shows the typical behavior observed in all samples: strongly pronounced peaks occur when clusters of particles fall out (**Figure 8B**), the stress drops until a new contact is formed and the sample further compressed. The sampling rate of 10 kHz proved to be high enough to resolve the fracture, as is depicted in magnification of the highest peak in the inset of **Figure 8A**.

In order to derive an objective characteristic of the rather irregularly shaped curves, the maximum within the first 10% strain (red star) was extracted from all curves. To examine its significance, it was compared to the maximum of the respective smoothed curve, which was calculated with a moving average over 1,000 data points (black curve and star in **Figure 8A**). The correlation of the two maxima is presented in the inset for all ice bead samples. Despite the scatter, both definitions of strength are reasonably correlated and led to the same overall-picture (**Figure 9**), indicating the usability of the first definition. Therefore, the raw data maximum within the first 10% strain is considered as characteristic for the sample. It is presented in **Figure 9** as compressive strength σ against the sintering time t_s, for all samples.

The log-log plot in **Figure 9** summarizes all experiments of ice beads and RG snow. It shows the relation of compressive strength and sintering time and allows to intercompare the sample types. The RG snow sinters much faster and stronger than the ice beads, thus shorter sintering times were examined. A monotonic increase of the strength with sintering time was observed for the RG snow. In analogy to van Herwijnen and Miller (2013) we fitted the power-law $\sigma = a \cdot t_s^b$ to the data. For RG snow, a good fit (RMSE = 2.96 kPa) was achieved with an exponent $b = 0.3$. For the ice beads no fit was possible. The strength increases monotonously only up to 5 days (poured) and decreases toward 10 days again. The strength of the tapped samples exceeds the one of the poured after 5 days sintering, but it decreases after 10 days to about the same value.

A high-speed video of an ice bead compression experiment is available in the **Video S1**.

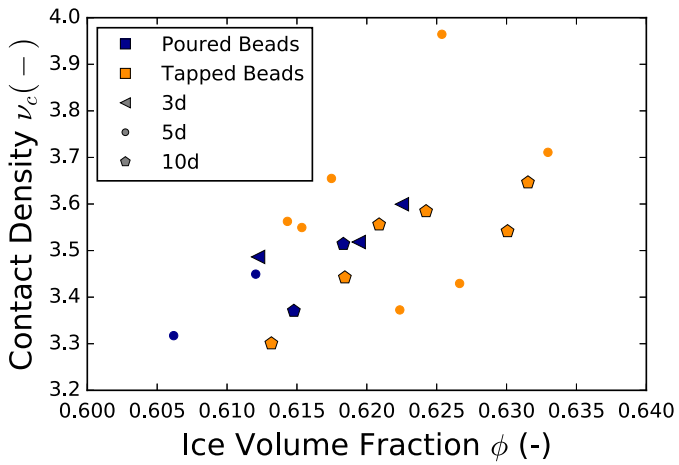

FIGURE 6 | The distinctiveness of poured and tapped samples in the contact density against the ice volume fraction: the tapped samples have by tendency higher densities and more contacts, but also more variability. The sintering time is indicated in the symbols.

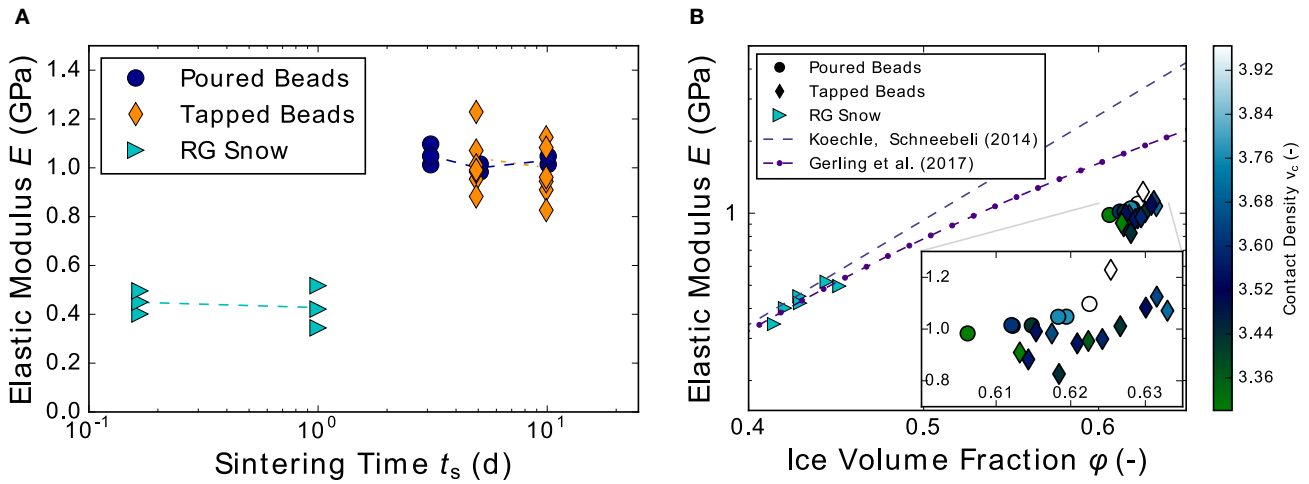

FIGURE 7 | Elastic moduli computed on the CT images: **(A)** against the logarithmic sintering time, the lines indicate the averages; **(B)** against the ice volume fraction, with the color-coded contact density for the ice beads. The inset shows a magnification of the ice bead results.

4. DISCUSSION

4.1. Methods and Ice Bead Characterization

In mechanical tests and CT-based investigations of ice bead packings, we examined the potential of spherical model snow. In the tumbling of frozen water droplets, we found a method to produce suitable, uniform ice spheres: the standard deviation of the size distribution is <10 % and the SSA is close to the one of a volume-equivalent ideal sphere, which implies high sphericity. Spherical shape and monodiseperse size are the main requirements for the experimental discrete element counterparts and critical for model validation. The sphericity, derived from the SSA, was constant for samples of different sintering times, implying the preservation of the spherical shape throughout the experiments (**Figure 5B**). The particle size can be modified by the tumbling time, and smaller particles with an optical diameter of natural snow crystals can be produced as well. The qualitative evaluation of the crystallography indicates that the ice beads consist of one to 10 crystals. The growth of monocrystals would probably be favored under warmer conditions when the water freezes slower. This could be of interest for further sintering and optical experiments, or mechanical tests with the incorporation of the crystal orientation. So far, most "spherical ice particles" presented in the literature (Kuroiwa, 1961; Chen and Baker, 2010; Molaro et al., 2019) were produced by spraying water into liquid nitrogen and were not characterized in a similar way, which allows only qualitative comparison. A multicrystalline ice structure of particles with a 4 mm diameter was shown in SEM images (Chen et al., 2013), and on microscopy images these particles look less spherical than the ones presented here. Hobbs and Mason (1964) report about mono- and poly-crystalline,

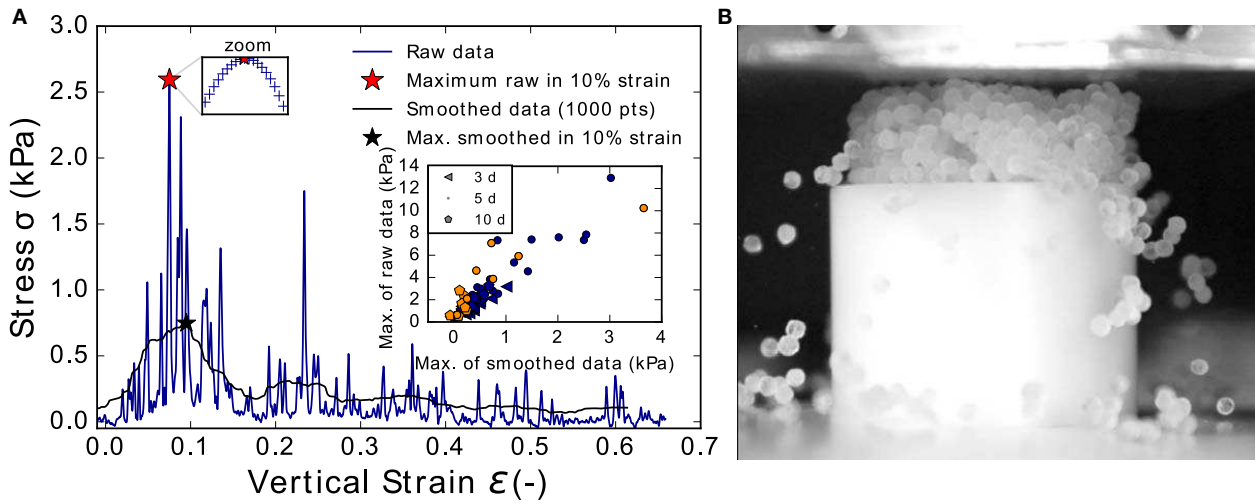

FIGURE 8 | Compression experiment of a poured ice bead sample after 5 days sintering. **(A)** Example of stress-strain curve as experimental result: the blue curve shows the raw data, the black curve its smoothed version, which was calculated with a moving average over 1,000 data points. The magnification of the blue maximum shows that the sampling rate of 10 kHz resolved the fracture. The maxima within the first 10% of strain were extracted from each curve, as marked by the stars. The inset shows the relation between the maxima of raw and smoothed data. **(B)** Photography of sample during compression: single particles and clusters of particles break out and lead to the pronounced peaks shown in **(A)** and a changing contact area during compression.

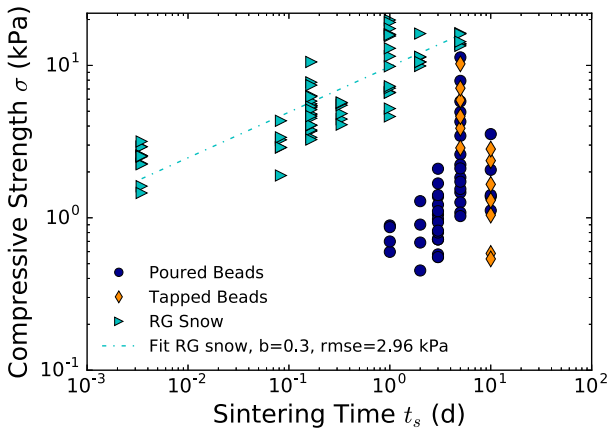

FIGURE 9 | The compressive strength of nature identical snow increases monotonously with sintering time, a power-law fit could be performed. For the ice beads, an increasing strength can only be observed up to 5 days. The 10-days-samples are weaker for both sample types.

mono-disperse spheres with a diameter within one percent in the range of 20–300 μm. No measure for the sphericity was given. Therefore, we believe that the mechanical tumbling method presented here is an interesting alternative to produce idealized model snow comprising spheres.

Besides the particle characterization, a well-working image processing with particle identification is the basis for our analysis of microstructure and contacts, as well as the reconstruction toward mapping onto models. To this end, a watershed algorithm could successfully be applied to the 3D CT images to identify the particles and characterize the samples in terms of the number of particles and contacts. The contact size, as second relevant contact parameter besides the number of contacts, is expected to change with sintering time. This was observed in the experiments through increasing compressive strength, but could not be derived from the images, which were analyzed regarding the watershed sizes (number of voxels of the watersheds, which were counted as contacts). The constant watershed sizes must be due to the image resolution of 18 μm and the fact that these narrow parts in the microstructure are most sensitive to binary segmentation, which comes along with a loss of information. However, the image processing can be applied for a complete reconstruction of the samples. Besides the contacts and number of particles, the position of all particles and contacts could be determined. Together with the high sphericity and quasi-monodispersity, this renders the system an ideal candidate for model validation: experimental samples can be reconstructed as input for (DEM) models for a close comparison.

4.2. Relation Between Microstructure and Mechanics

The structural analysis of the CT images showed the reproducibility of the ice bead samples, with a standard deviation of the structural parameters of <10 %. The variation of density and elastic modulus of the RG snow samples was higher than for the ice bead samples. The densities of the ice bead samples lie in the range of a close random packing, which allows little structural variation. Yet, the effect of the sample compaction by tapping can be seen in higher densities and more contacts. The differences between the tapped and poured structures are small and without a sharp transition. But they are also mirrored in the mechanical properties, the simulated elastic modulus, and the experimentally measured compressive

strength. While in the present paper the tapping was only employed as a proof of concept, a more systematic tapping method (using e.g., vibrations with a given frequency) may open the door for targeted manipulation of the packings.

Two main contact parameters were manipulated in the ice bead samples—the number of contacts by tapping and the size of the contacts through variation of the sintering time—and can be related to the mechanical response. The effect of sintering was not resolved in the CT images and consequently in the elastic modulus, for which a relationship with the contact density and ice volume fraction was observed. The compressive strength is related to both parameters, even though only indirectly. Since the sintering time did not change the other structural parameter (SSA, density, contact density) that potentially affect the compressive strength, the increasing strength can be ascribed to the increase of the contact size. As the contact size matters but could not be quantified, no relation with contact density and compressive strength could be derived.

The Elastic moduli E were determined by voxel-based FEM simulations of 3D CT images. With a voxel size of 18 µm the image resolution was too low to resolve details of the sintering effect, as particularly the bond area is sensitive to the image resolution. Thus, no relation of E with sintering time was observed (**Figure 7A**). E is dominated by the particle geometry and structural arrangement of the sample. While in snow science E is usually related to the ice volume fraction ϕ (Mellor, 1975; Kochle and Schneebeli, 2014; Wautier et al., 2015; Srivastava et al., 2016), for the ice beads, we could additionally relate it to the contact density ν_c, which is shown in the colors of **Figure 7B**. Regarding the relation with the ice volume fraction ϕ, the results of the RG snow samples are in very good agreement with the fits of Kochle and Schneebeli (2014) and Gerling et al. (2017) who utilized the same method. Their empirical power-law [$E = 2 \cdot 10^{-8} \cdot \rho^{3.98}$ (MPa)] fits with RMSE = 0.021 GPa our results for the RG snow samples. However, it overestimates E of the ice beads, as does the fit of Kochle and Schneebeli (2014). In both studies, the fits are restricted to a certain density range. Kochle and Schneebeli (2014) even specify two fits for two ranges, which underlines the restricted validity. As their ranges do not cover the ice volume fractions of the ice bead samples, the fits are not expected to describe the elastic moduli of the beads. Yet, lower E are presumed toward higher ϕ, as E must saturate at some point to the value of solid ice. The ranges of both, ice volume fraction and elastic moduli, are clearly separated for RG snow and ice beads, but the ranges of these parameters within the respective systems are small. The RG snow samples line up on the fit, i.e., clearly increasing E with ϕ. The ice bead samples, in contrast, are rather clustered. Partially this can be explained by looking at the contact density ν_c, as resolved in the magnification (**Figure 7B**), for which an increasing relation with E is expected (Gaume et al., 2017) and seen in the results of the poured samples. For tapped samples, the relation is rather vague, due the uncertainty intervals of all parameters and their small ranges. The higher variability of the tapped samples compared to the poured, is already observed in the relation of ϕ and ν_c (**Figure 6**) as well as in the relation of E and t_s (**Figure 7A**). This might be due to the sensitivity of the applied tapping method to small variations, whereas the pouring of the particles is better constraint.

The compressive strengths σ were extracted from the experimental stress-strain curves which are difficult to interpret on the first sight (**Figure 8**). The focus in this study was on a mechanical characteristic that allows for comparison of different sintering times and sample types, rather than on the fracture mechanism itself. Such a characteristic was found in the highest peak within the first 10% of strain and referred to as compressive strength, after an alternative evaluation of the smoothed curves and the deformational energy confirmed the results. The relation of compressive strength and sintering time (**Figure 9**) shows the reproducibility of the experiments, despite the large scatter, which however is typical for snow. The requirements for the representative elementary volume (REV) are met for the ice beads with 32 r_p and $n_p \in (1,000, 1,200)$ at the lower limit, which was found in 30 r_p (Wiacek and Molenda, 2016) or $n_p \geq 1,000$ particles (Gaume et al., 2017). In contrast, the requirements are clearly fulfilled for the RG snow samples. Yet, the experimental results have a similarly high scatter, which is considered to be the (reproducible) variability of the compressive strength. On the contrary, the scatter of the structural parameters is comparably small, within ±10%. This indicates the relevance of the exact arrangement of the particles and the formation and mechanical importance of force bearing chains in snow structures (Kry, 1975).

Taking the highest peak of the stress-strain curves as compressive strength, as a characteristic of the sample, renders the comparison of different samples and sintering times possible (**Figure 9**). The compressive strengths of the ice bead samples reflect the variation of both contact parameters: tapped samples with higher contact densities exceed the poured samples; and for the poured samples an increasing strength with sintering times between 1 and 5 days was observed, assigned to the change of the contact size. A quantitative relation of strength, contact density, and contact size cannot be discussed, lacking information about the evolution of the sintered contacts. The relation of compressive strength and sintering time was examined in confined compression experiments and also related to the particle size (Jellinek, 1959). A similar relation with time was found as we observed in the RG snow, but the increase of compressive strength with particle size is in contrast to our results. Reasons for this are discussed in the next paragraph.

4.3. Effect of Sintering on Compressive Strength and Sintering Anomaly of Ice Beads

In the relation of compressive strength and sintering time, large differences of RG snow and ice beads were observed. This relation has been investigated for snow in confined compression experiments (Jellinek, 1959), where an exponential fit was applied ($\sigma \propto e^{kt_s}$) that represented well the monotonic increase of the compressive strength with the age of snow. To the similarly progressing curve of the RG snow, however, we fitted a power-law $\sigma = a \cdot {t_s}^b$ in analogy to van Herwijnen and Miller (2013). The exponent b is related to the standard sintering theory and

links the locally and globally increasing strength. The obtained exponent $b = 0.3$ for the RG snow compares well to their ones for comparable snow (natural and nature identical rounded grains), considering the different densities. According to the standard sintering theory, the bond-to-grain ratio develops in time following the power-law:

$$\left(\frac{r_b}{r_p}\right)^n = \frac{B(T)}{{r_p}^m} \cdot t_s, \tag{1}$$

with the temperature dependent B that captures geometrical and material properties. Assuming vapor transport as the dominant sintering mechanism for the regarded time scales (Hobbs and Mason, 1964; Blackford, 2007; Chen and Baker, 2010), the exponents are $n = 5$ and $m = 3$ and the bond-to-grain ratio should grow in time with ${t_s}^{1/5}$. Hence, the relation of compressive strength and sintering time is due to the locally growing bonds and for the RG snow in good agreement with the literature.

Compared to the RG snow, the ice beads sinter much slower and weaker. First compression tests were initially performed after 1 day, but most of the ice bead samples fragmented when the outer wall of the sample holder was removed and could not be used for compression tests. In contrast, the RG snow could be tested after only 5 min. This difference can only partially be explained by the particle size. The size dependence of the sintering rate is prescribed by Equation (1) that predicts decreasing sintering rates for increasing grain sizes, as do the simulation results of van Herwijnen and Miller (2013).

The ice bead samples evolve similarly as RG snow but only for sintering times up to 5 days, with weaker but still increasing strength. Unexpectedly, the 10 days samples were weaker than the 5 days samples, for both sample classes. This result presently lacks a sound theoretical explanation. However, the CT images and observations reported in the literature indicate that due to the porous nature of the bonds the growth is not monotonic. The results of the structural analysis and the elastic moduli—that show no variation with sintering time—do not indicate any remarkable differences in the structures of the 10 days-samples, as they are not conspicuous, e.g., in the relation between E and ν_c. Moreover, different temperatures or large fluctuations of the temperature during the sintering process can be excluded from the temperature measurement of the 5 and 10 days tapped sintering process. In both cases the temperature fluctuations were restricted to $\pm 0.5^{\circ}$C. The sintering theory behind Equation (1) describes the growth of a solid neck between two particles in contact, as it developed for the RG snow. In additional CT images with higher resolution (6 μm), we observe porous bonds, several column-like structures form the contact between two particles (**Figure 10**). A very similar observation is described by Chen and Baker (2010), for polycrystalline ice spheres of a 4 mm diameter under temperature-gradient and quasi-isothermal (–10°C) conditions, and by Adams et al. (2008) for natural snow crystals (sieved with a 0.99 mm sieve). Chen and Baker (2010) reported the growth of several "protrusions" from one particle to the other, forming a porous bond. Interestingly, they report a retreat of the protrusions after growth of 6 days, but only if the protrusions could not get in contact with the opposite sphere (if the spheres were initially not in contact but separated by a small gap). The described images of the bonds were taken after 6 (maximum extension of the protrusions) and 12 days (retreated protrusions), which matches the time frame of our observation, the weakening of the compressive strength. Their observation is an optical one and no mechanical tests were performed. The retreat is reported only for initially separated particles. Our results show their mechanical relevance, i.e., weaker sintering of large ice particles and indicate that the reversal of bonding also takes place when the particles were in contact, i.e., that the porosity of an existing bond can increase in time. These results may help to explain the empirical observations of weakly sintered spring snow on ski slopes or roads, consisting of large and round grains, the weak layer potential of hail and graupel or even spherical ice particles in the food industry.

The porously growing bonds seem to be related to the particle size, as it has only been observed in 4 mm particles so far (Chen and Baker, 2010). In other studies of sintering of ice spheres with diameters between 20 and 300 μm the growth of a solid neck was observed, as predicted by the theory (Kuroiwa, 1961; Hobbs and Mason, 1964). The size of our particles with 2–2.2 mm

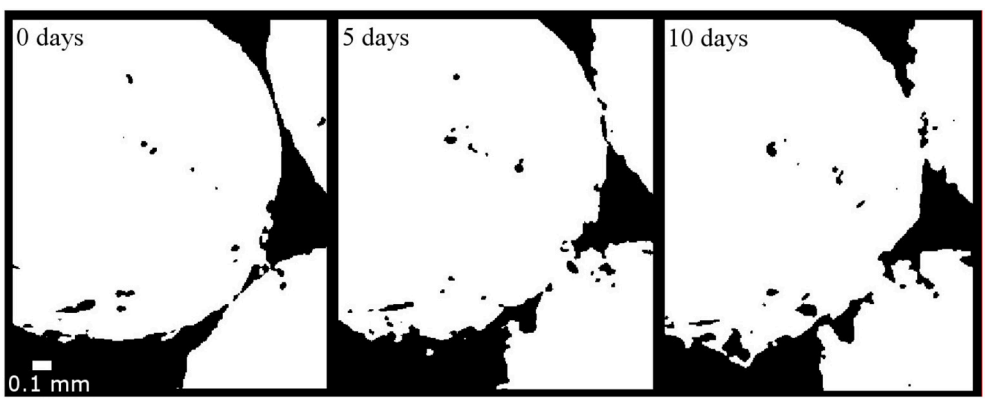

FIGURE 10 | High resolution (6 μm) CT scans of ice beads, after 0, 5, and 10 days sintering. The 2D cross-sections of the binary images show porous bonds between the particles and their evolution.

is in between. Though unexpected, our results fit the former observations, which indicate some effects for the sintering of large spheres that are not captured by sintering theory. The onset of these effects lies supposedly between particle sizes of 0.3 and 2 mm. Further investigation of this seems worthwhile to explore the size dependence and the mechanisms for these protrusions.

5. CONCLUSION

In this paper we presented a novel tumbling method for producing model snow that comprises highly spherical ice beads. We characterized the spheres and analyzed the structures and mechanics of sintered sphere assemblies. This showed that the investigated ice beads are well suited for snow model comparison, due to their clearly defined size, high sphericity and the well-working structural analysis by means of CT-imaging. The tumbling method presented here enables the production of uniform ice beads in different size ranges. Smaller and larger spherical ice particles than the ones presented here can be generated as well. The microstructures of the samples were characterized and related to the mechanical properties, by examining CT images of the samples that were used in the compression experiments. Microstructural variation was generated by densification of some samples and by variation of the sintering time. The sintered bonds of the ice beads developed with a complex geometry, contrasting the predictions from the standard sintering theory. This was observed by optical inspection of the CT images, as well as in the evolution of compressive strength with sintering time. In the compression tests, the ice bead samples exhibited after 10 days sintering lower strength than after 5, in contrast to the monotonic increase of the reference snow and the expectation from theory. The sintering artifacts, revealed in the CT images, impede the quantification of the contact size. Although unexpected in our experiments, similar observations are documented in the literature and indicate that the artifacts could be circumvent by utilizing smaller particles to allow for a complete quantification of the contact parameters (number and size of bonds). Despite these complications, the ice beads qualified also in the mechanical tests for model snow: until 5 days the ice beads developed a similar relation of strength and sintering time as the reference snow and the sintering-independent results of the elastic moduli, conform very well with the expectations from literature. Overall we believe that model snow comprising spheres with low variability in size and shape may be well exploited for applications such as DEM to address open questions regarding the calibration of contact parameters and the mapping of snow microstructure onto simplified geometries.

DATA AVAILABILITY

The datasets for this study can be found at https://doi.org/10.16904/envidat.83.

AUTHOR CONTRIBUTIONS

This work was led by CW. The laboratory experiments, including CT scans, were conducted by CW and SS. FEM simulations were done by HL. Construction and testing of the tumbling machine for ice bead production, 3D CT image analysis and the writing of the manuscript was done by CW. The data was analyzed and interpreted by all authors.

FUNDING

This work has been funded by the Swiss National Science Foundation (Project SnowDEM).

ACKNOWLEDGMENTS

The authors would like to acknowledge Matthias Jaggi for laboratory support on the compression experiments and on the crystal analysis of the ice beads.

SUPPLEMENTARY MATERIAL

The Supplementary Material for this article can be found online at: https://www.frontiersin.org/articles/10.3389/feart.2019.00229/full#supplementary-material

Video S1 | Unconfined compression experiment of an ice bead poured sample after 10 days sintering.

REFERENCES

Adams, E., M. Jepsen, S., and Close, B. (2008). A bonding process between grains in mechanically disaggregated snow. *Ann. Glaciol.* 48, 6–12. doi: 10.3189/172756408784700770

Blackford, J. R. (2007). Sintering and microstructure of ice: a review. *J. Phys. D Appl. Phys.* 40, R355–R385. doi: 10.1088/0022-3727/40/21/R02

Chandel, C., Srivastava, P. K., and Mahajan, P. (2014). Micromechanical analysis of deformation of snow using x-ray tomography. *Cold Reg. Sci. Tech.* 101, 14–23. doi: 10.1016/j.coldregions.2014.01.005

Chen, S., and Baker, I. (2010). Structural evolution during ice-sphere sintering. *Hydrol. Process.* 24, 2034–2040. doi: 10.1002/hyp.7787

Chen, S., Baker, I., and Frost, H. (2013). Surface instability and mass transfer during the bonding of ice spheres. *Philos. Magaz.* 93, 3177–3193. doi: 10.1080/14786435.2013.805274

Fierz, C., Armstrong, R. L., Durand, Y., Etchevers, P., Greene, E., Mcclung, D., et al. (2009). "The international classification for seasonal snow on the ground," in *IHP-VI Technical Documents in Hydrology* (UNESCO/IHP).

Garboczi, E. (1998). "Finite element and finite diierence programs for com- puting the linear electric and elastic properties of dig- ital images of random materials." *Report NISTIR*.

Gaume, J., Löwe, H., Tan, S., and Tsang, L. (2017). Scaling laws for the mechanics of loose and cohesive granular materials based on baxter's sticky hard spheres. *Phys. Rev. E* 96:032914. doi: 10.1103/PhysRevE.96.032914

Gaume, J., van Herwijnen, A., Chambon, G., Birkeland, K. W., and Schweizer, J. (2015). Modeling of crack propagation in weak snowpack layers using the discrete element method. *Cryosphere* 9, 1915–1932. doi: 10.5194/tc-9-1915-2015

Gerling, B., Löwe, H., and van Herwijnen, A. (2017). Measuring the elastic modulus of snow. *Geophys. Res. Lett.* 44, 11,088–11,096. doi: 10.1002/2017GL075110

Gillespie, L. K. (2007). *Mass Finishing Handbook*. New York, NY: Industrial Press.

Hagenmuller, P., Chambon, G., Lesaffre, B., Flin, F., and Naaim, M. (2013). Energy-based binary segmentation of snow microtomographic images. *J. Glaciol.* 59, 859–873. doi: 10.3189/2013JoG13J035

Hagenmuller, P., Chambon, G., and Naaim, M. (2015). Microstructure-based modeling of snow mechanics: a discrete element approach. *Cryosphere* 9, 1969–1982. doi: 10.5194/tc-9-1969-2015

Hagenmuller, P., Matzl, M., Chambon, G., and Schneebeli, M. (2016). Sensitivity of snow density and specific surface area measured by microtomography to different image processing algorithms. *Cryosphere* 10, 1039–1054. doi: 10.5194/tc-10-1039-2016

Hagenmuller, P., Theile, T. C., and Schneebeli, M. (2014). Numerical simulation of microstructural damage and tensile strength of snow. *Geophys. Res. Lett.* 41, 86–89. doi: 10.1002/2013GL058078

Hildebrand, T., Laib, A., Müller, R., Dequeker, J., and Rüegsegger, P. (1999). Direct three-dimensional morphometric analysis of human cancellous bone: Microstructural data from spine, femur, iliac crest, and calcaneus. *J. Bone Min. Res.* 14, 1167–1174.

Hobbs, P. V., and Mason, B. J. (1964). The sintering and adhesion of ice. *Philos. Magaz.* 9, 181–197.

Jellinek, H. H. G. (1959). Compressive strength properties of snow. *J. Glaciol.* 3, 345-354.

Johnson, J. B., and Hopkins, M. A. (2005). Identifying microstructural deformation mechanisms in snow using discrete-element modeling. *J. Glaciol.* 51, 432–442. doi: 10.3189/172756505781829188

Kabore, B. W., and Peters, B. (2018). Micromechanical model for sintering and damage in viscoelastic porous ice and snow. Part I: theory. *arXiv: 1808.04394*.

Kaempfer, T. U., Hopkins, M. A., and Perovich, D. K. (2007). A three-dimensional microstructure-based photon-tracking model of radiative transfer in snow. *J. Geophys. Res. Atmos.* 112, 1–14. doi: 10.1029/2006JD008239

Kingery, D. W. (1960). Regelation, surface diffusion, and ice sintering. *J. Appl. Phys.* 31, 833–838.

Kochle, B., and Schneebeli, M. (2014). Three-dimensional microstructure and numerical calculation of elastic properties of alpine snow with a focus on weak layers. *J. Glaciol.* 60, 705–713. doi: 10.3189/2014JoG13J220

Kry, P. R. (1975). The relationship between the visco-elastic and structural properties of fine-grained snow. *J. Glaciol.* 14, 479-500.

Kuroiwa, D. (1961). A study of ice sintering. *Tellus* 13, 252–259.

Mede, T., Chambon, G., Hagenmuller, P., and Nicot, F. (2018). A medial axis based method for irregular grain shape representation in dem simulations. *Granular Matter* 20. doi: 10.1007/s10035-017-0785-7

Mellor, M. (1975). A review of basic snow mechanics. *IASH Pub* 114, 251–291.

Michael, M., Nicot, F., and Peters, B. (2015). Advanced micromechanical description of snow behaviour — PART I — mechanical and numerical modelling. *Int. J. Sol. Struct.*

Molaro, J. L., Choukroun, M., Phillips, C. B., Phelps, E. S., Hodyss, R., Mitchell, K. L., et al. (2019). The microstructural evolution of water ice in the solar system through sintering. *J. Geophys. Res. Plan.* 124, 243–277. doi: 10.1029/2018JE005773

Mulak, D., and Gaume, J. (2019). Numerical investigation of the mixed-mode failure of snow. *Comput. Mech.* 6, 439–447. doi: 10.1007/s40571-019-00224-5

Riche, F., Schneebeli, M., and Tschanz, S. (2012). Design-based stereology to quantify structural properties of artificial and natural snow using thin sections. *Cold Reg. Sci. Technl.* 79–80, 67–74. doi: 10.1016/j.coldregions.2012.03.008

Schleef, S., Jaggi, M., Löwe, H., and Schneebeli, M. (2014). Instruments and methods: An improved machine to produce nature-identical snow in the laboratory. *J. Glaciol.* 60, 94–102. doi: 10.3189/2014JoG13J118

Schneebeli, M. (2004). Numerical simulation of elastic stress in the microstructure of snow. *Ann. Glaciol.* 38, 339–342. doi: 10.3189/172756404781815284

Shapiro, H. L., Johnson, J., Sturm, M., and Blaisdell, G. (1997). *Snow Mechanics: Review of the State of Knowledge and Applications*, 40.

Spettl, A., Bachstein, S., Dosta, M., Goslinska, M., Heinrich, S., and Schmidt, V. (2016). Bonded-particle extraction and stochastic modeling of internal agglomerate structures. *Adv. Powder Technl.* 27, 1761–1774. doi: 10.1016/j.apt.2016.06.007

Srivastava, P. K., Chandel, C., Mahajan, P., and Pankaj, P. (2016). Prediction of anisotropic elastic properties of snow from its microstructure. *Cold Reg. Sci. Technl.* 125, 85–100. doi: 10.1016/j.coldregions.2016.02.002

Theile, T., and Schneebeli, M. (2011). Algorithm to decompose three-dimensional complex structures at the necks: tested on snow structures. *Image Process. IET* 5, 132–140. doi: 10.1049/iet-ipr.2009.0410

Theile, T., Szabo, D., Luthi, A., Rhyner, H., and Schneebeli, M. (2009). Mechanics of the ski–snow contact. *Tribol. Lett.* 36, 223–231. doi: 10.1007/s11249-009-9476-9

van Herwijnen, A., and Miller, D. A. (2013). Experimental and numerical investigation of the sintering rate of snow. *J. Glaciol.* 59, 269-274. doi: 10.3189/2013JoG12J094

Wadell, H. (1935). Volume, shape, and roundness of quartz particles. *J. Geol.* 43, 250–280. doi: 10.1086/624298

Wang, X., and Baker, I. (2013). Observation of the microstructural evolution of snow under uniaxial compression using x-ray computed microtomography. *J. Geophys. Res. Atmos.* 118, 12,371–12,382. doi: 10.1002/2013JD020352

Wautier, A., Geindreau, C., and Flin, F. (2015). Linking snow microstructure to its macroscopic elastic stiffness tensor: a numerical homogenization method and its application to 3-d images from x-ray tomography. *Geophys. Res. Lett.* 42, 8031–8041. doi: 10.1002/2015GL065227

Wiacek, J., and Molenda, M. (2016). Representative elementary volume analysis of polydisperse granular packings using discrete element method. *Particuology* 27, 88–94. doi: 10.1016/j.partic.2015.08.004

Conflict of Interest Statement: The authors declare that the research was conducted in the absence of any commercial or financial relationships that could be construed as a potential conflict of interest.

frontiers in Earth Science

ORIGINAL RESEARCH
published: 22 January 2020
doi: 10.3389/feart.2019.00347

Presenting Snow Grain Size and Shape Distributions in Northern Canada Using a New Photographic Device Allowing 2D and 3D Representation of Snow Grains

Alexandre Langlois[1,2], Alain Royer[1,2], Benoit Montpetit[3], Alexandre Roy[2,4] and Martin Durocher[5]*

[1] Centre d'Applications et de Recherches en Télédétection, Université de Sherbrooke, Sherbrooke, QC, Canada, [2] Centre d'Études Nordiques, Kuujjuarapik, QC, Canada, [3] Canadian Wildlife Service, Ottawa, ON, Canada, [4] Département des Sciences de l'Environnement, Université du Québec à Trois-Rivières, Trois-Rivières, QC, Canada, [5] Department of Civil and Environmental Engineering, University of Waterloo, Waterloo, ON, Canada

OPEN ACCESS

Edited by:
Melody Sandells, CORES Science and Engineering Limited, United Kingdom

Reviewed by:
Veijo Pohjola, Uppsala University, Sweden
Pascal Hagenmuller, UMR 3589 Centre National de Recherches Météorologiques (CNRM), France
Jinmei Pan, Institute of Remote Sensing and Digital Earth (CAS), China

***Correspondence:**
Alexandre Langlois
a.langlois2@usherbrooke.ca

Specialty section:
This article was submitted to Cryospheric Sciences, a section of the journal Frontiers in Earth Science

Received: *24 July 2019*
Accepted: *16 December 2019*
Published: *22 January 2020*

Citation:
Langlois A, Royer A, Montpetit B, Roy A and Durocher M (2020) Presenting Snow Grain Size and Shape Distributions in Northern Canada Using a New Photographic Device Allowing 2D and 3D Representation of Snow Grains. Front. Earth Sci. 7:347. doi: 10.3389/feart.2019.00347

Geophysical properties of snow are known to be sensitive to climate variability and are of primary importance for hydrological and climatological process simulations. Numerous studies using passive microwaves have attempted to quantify snow from space, but the methods suffer from poor spatial resolution retrievals, combined with a great sensitivity to snow grain morphology. Those issues motivated work using active microwaves that are now core to space mission concept proposals currently under development. However, a clear limitation remains with regards to snow microstructure contribution to backscattering, especially in large depth hoar (DH) layers typical of polar snowpacks. This leads to difficulties retrieving snow water equivalent (SWE) from space or developing radiative transfer models used in assimilation approaches owing to a lack of field observations of snow microstructure. As such, this paper presents an innovative technique to measure various snow grain metrics in the field where micro-photographs of snow grains are taken under angular directional LED lighting. The projected shadows are digitized so that a 3D reconstruction of the snow grains is possible and distribution functions can be proposed for various snow grain metrics and grain types. This device, dLED, has been used in several field campaigns and a very large dataset was collected and is presented in this paper. Distribution histograms from >160,000 digitized grains were produced for each metric for all grains considered as a whole dataset (unclassified), and also for each grain type: (1) defragmented/broken (DF), (2) DH, (3) facets (F), (4) rounds (R), and (5) precipitation particles (PP). We selected distribution functions for each metric per grain time by analyzing L-moment diagrams that summarize the shape of a probability distribution. Our results show that the logarithmic Kappa (LKAP) distribution is well suited to explain the snow grain metric distribution for each grain type. Location, scale and shape parameter values for each distribution are presented and a

comparison with values derived from our shortwave infrared laser device, the InfraRed Integrating Sphere (IRIS), is provided. A discussion is presented on the pros and cons of the dLED and the use of the distributions presented in this paper for microwave radiative transfer modeling work.

Keywords: snow grain, distribution, radiative transfer modeling, microstructure, snow

INTRODUCTION

In the context of global climate change observed over the past four decades in northern regions, numerous studies have focused on the retrieval of surface state variables to monitor the rate and amplitude of observed changes (Takala et al., 2011; Brown and Derksen, 2013; Estilow et al., 2015). Globally, the rate of temperature increase has vary in the last decade (Kosaka and Xie, 2013), but Arctic air temperatures have continued to increase (+1.3°C warmer in 2015 when compared to the 1981–2010 mean) (National Oceanic and Atmospheric Administration [NOAA], 2017). Currently, the Arctic is warming at more than twice the rate of lower latitudes, leading to a decrease in sea ice cover (Serreze and Stroeve, 2015), glacier mass balance (Papasodoro et al., 2015), permafrost extent (Schuur et al., 2015) and snow cover (Derksen and Brown, 2012). This is of particular relevance in a context where snow covers up to 40 million km^2 during winter in North America and supports freshwater supplies for consumption, agriculture and hydroelectricity. Snow also supports a multi-billion dollar tourism and recreation industry while controlling the surface energy budget of northern ecosystems playing a crucial role on how the Earth reacts to climate change.

Numerous studies have thus focused on the retrieval of this crucial state variable over the past four decades. Pioneering work in the 1970s and 1980s (Chang et al., 1987) proposed new approaches to retrieve snow depth and water equivalent from space using passive microwave brightness temperatures. Over the years, considerable research (Foster et al., 1997; Kelly and Chang, 2003; Derksen et al., 2012; Langlois et al., 2012; King et al., 2015) has found that microwave approaches depend strongly on snow grain morphology (size and shape), which was poorly parameterized in models. This led to strong biases in the retrieval calculations (Domine et al., 2006; Langlois et al., 2010; Montpetit et al., 2012). Related uncertainties from space retrievals and the development of complex thermodynamic multilayer snow and microwave emission models motivated several studies on the development of new approaches to quantify snow grain (e.g., Domine et al., 2006; Matzl and Schneebeli, 2006; Langlois et al., 2010; Montpetit et al., 2012) given the lack of field measurements.

Until recently, grain size was poorly defined and measured, mainly due to the unstable nature of snow grain size and shape under metamorphic processes (Gallet et al., 2009). In dry conditions, snow grains can change size and shape under a temperature gradient where grain growth is observed owing to the mass transfer from warmer to colder grains, typically forming faceted and depth hoar grains (Colbeck, 1983; Gubler, 1985). In the absence of a sufficient temperature gradient (0.1 to 0.3°C/cm, Sturm et al., 2002), equilibrium metamorphism will occur where the bottom grains are at equilibrium with water vapor at a higher density than the upper grains. The high Specific Surface Area of snow (SSA), i.e., the ratio of the grain volume to its surface, then provides a lot of energy to induce microscale heat and mass transfer (e.g., Bader et al., 1939; Colbeck, 1982), changing the structure of the snow grain through a decrease in SSA (Cabanes et al., 2002). In wet conditions, the metamorphic process will change given saturated or unsaturated snow where saturated conditions will promote large grain growth from adhesion of water to the ice crystals while undersaturated conditions will lead to the formations of clusters (Denoth, 1980; Langlois and Barber, 2007).

The complexity of the thermodynamic processes involved, combined with measurement constraints, led to the development of SSA and optical diameter retrievals from optical methods. The optical diameter of snow grains can be quantified using near infrared and shortwave infrared reflectance (Kokhanovsky and Zege, 2004; Domine et al., 2006; Matzl and Schneebeli, 2006; Langlois et al., 2010; Montpetit et al., 2012) and now, measurement devices are available commercially and used by several groups. However, since such devices are expensive, traditional micro-photographs of snow grains remain widely used to "quantify" various snow grain metrics for different applications (e.g., Lesaffre et al., 1998; Langlois et al., 2007; Bartlett et al., 2008). Such photographs, if digitized, can provide interesting information and fair estimation on metamorphism processes in place but yield no information on the volume and SSA, which are key variables for microwave radiative transfer models (RTMs) (Royer et al., 2017) and retrieval approaches from space. For instance, several studies coupling RTMs with measured snow SSA for simulations of brightness temperatures have all found that a scaling factor is needed in order to optimize the difference between simulated and measured brightness temperatures (Langlois et al., 2012; Roy et al., 2013). Roy et al. (2013) hypothesized that the scaling factor is related to the grain size distribution of snow and the stickiness between grains. Even more relevant to this study is the fact that RTMs such as the Dense Media Radiative Transfer – Multi Layers (DMRT-ML) model assumes a Rayleigh snow grain size distribution (Picard et al., 2013).

Recent work has proposed innovative techniques in the measurement of SSA and correlation length. *In situ* techniques using near-infrared and short-wave infrared photography or shortwave infrared lasers have been rather successful, but are often cost prohibitive and very few datasets exist to date for polar snowpacks. Other well-known methods using methane absorption techniques and microCT measurements are arguably

still considered as the reference methods for precise SSA measurement but are cost-prohibitive, and sample extraction for casting very large depth hoar remains extremely difficult contributing to the fact that very few research groups can build snow microstructure datasets for arctic regions. Hence, our group developed a new approach to the "traditional" measurements of snow grain metrics where micro-photographs of snow grains are taken under angular directional LED lighting. The projected shadows are digitized so that a 3D reconstruction of the snow grains is possible and distribution functions can be found for various snow grain metrics and grain types. This device, dLED (see section " Data and Methods"), has been used in several field campaigns and a very large dataset was collected and is presented in this paper. Hence, objectives of this paper are to: (1) present the low-cost dLED approach used to measure snow grain metrics, (2) provide various snow grain metric distribution functions for different grain types from over 160,000 digitized snow grains, (3) evaluate the effect of snow grain types on different snow grain metric distributions and (4) compare metrics retrieved from dLED, including the surface specific area (SSA), with well-established SSA measurements using our InfraRed Integrated Sphere (IRIS) laser-based device.

DATA AND METHODS

Study Site

The fieldwork occurred in winter 2009–2010 for the European Space Agency "Cold Regions Hydrology high-resolution Observatory" mission concept proposal. Although the mission concept was not funded, the fieldwork allowed the collection of a very unique snow, lake ice and permafrost dataset (Derksen et al., 2012). More precisely, our field campaign was conducted in Churchill, Manitoba, Canada with logistical support from the Churchill Northern Studies Centre. The area includes forests, open areas, dry and wet fens as well as numerous lakes. The main objective of the field campaign was to acquire coincident passive and active microwave measurements over snow and lake ice, under a range of soil and vegetation conditions.

Although the field campaign included a total of six intensive observing periods from November 2009 to May 2010, this paper focuses on data collected during the four following periods: (1) January 4th–17th; (2) February 7th–20th; (3) March 14th–27th, and (4) April 18th–30th of 2010. During those short campaigns, a total of 127 snowpits were dug across wet and dry fens and forested and open areas. Of the 127 snowpits, 78 included IRIS measurements [see section "InfraRed Integrating Sphere (IRIS)"]; 107 included dLED (see section "dLED") for a total 588 photos spanning across the four measurement periods.

Snow Measurements

dLED

The dLED was developed by our group in 2009 and consists of an enclosed box equipped of about 30 cm × 30 cm × 45 cm (first described in Royer et al., 2017), with four LEDs mounted inside on the side of the box (separated by 90°) at a height of 20 cm from the snow grain plate. They are angled at 45° in relation to the snow sample s extracted from a given layer. A Nikon D1X is mounted on top of the box and the LEDs, to take successive pictures of the illuminated grains. The Nikon D1X has a 5.0MP APS-C (23.7 cm × 15.5 mm) sized CCD sensor which provides a resolution of 3008 × 1960 pixels. A total of five pictures are taken: (1) full sample with white lighting from top (**Figures 1A,B**); (2) with the LED placed at azimuth 0° (**Figure 1C**); (3) LED at azimuth 90° (**Figure 1D**); (4) LED at azimuth 180° (**Figure 1E**), and (5) LED at azimuth 270° (**Figure 1F**).

In **Figure 1**, the grains are first digitized individually, then the projected shadows in each azimuth direction are also digitized. Once digitized, for each photo, a calibration is conducted where the 2 mm grid is digitized as scale so that the length of each pixel is known, to allow for any variability in the focus. Using the scale, the program calculates the length of each "lines" of the projected shadow in the four azimuthal directions so that the height of the snow grain's edge creating this shadow can be calculated. As such, each 2D pixel from the initial grain digitized can be associated to a height, and a 3D representation of the snow grains is then possible. The 2D polygons are used to extract eccentricity, minor axis, major axis, projected surface and perimeter that are used in section "Snow Grains Analyzed," of this paper. The 3D reconstruction data are used to derive SSA and compared with IRIS data in section "dLED vs. IRIS Comparison." In both 2D and 3D cases, calculations can be done for both individual grain data, and photo averages, which in fact corresponds to a layer average. In order to avoid a user selection bias, all the snow grains from each plate (i.e., samples from a given layer) were digitized so that for the 581 photos (i.e., 581 layers), a total of 162,516 grains were digitized (averaging 263 grains digitized/photo), from which a sub-sample was manually selected for the 3D reconstruction. All metric calculations were conducted using the digitized photos. Seven snow grain metrics in total were computed:

Eccentricity

Eccentricity corresponds to the eccentricity of the ellipse that has the same second-moments as the snow grain. It considers ratio of the distance between the foci of the snow grain and its major axis length. An ellipse whose eccentricity is 0 is actually a circle, while an ellipse whose eccentricity is 1 is a line segment.

Area (mm^2)

Area (mm^2) computes the projected surface of the snow grain (i.e., polygon), with respect to the photograph scale. It considers the actual number of pixels in the snow grain polygon.

Minor axis (mm)

Minor axis (mm) corresponds to the length of the minor axis of the ellipse that has the same normalized second central moments as the snow grain polygon.

Major axis (mm)

Major axis (mm) corresponds to the length of the major axis of the ellipse that has the same normalized second central moments as the snow grain polygon.

Ratio

Ratio computed from the ratio between minor and major axes.

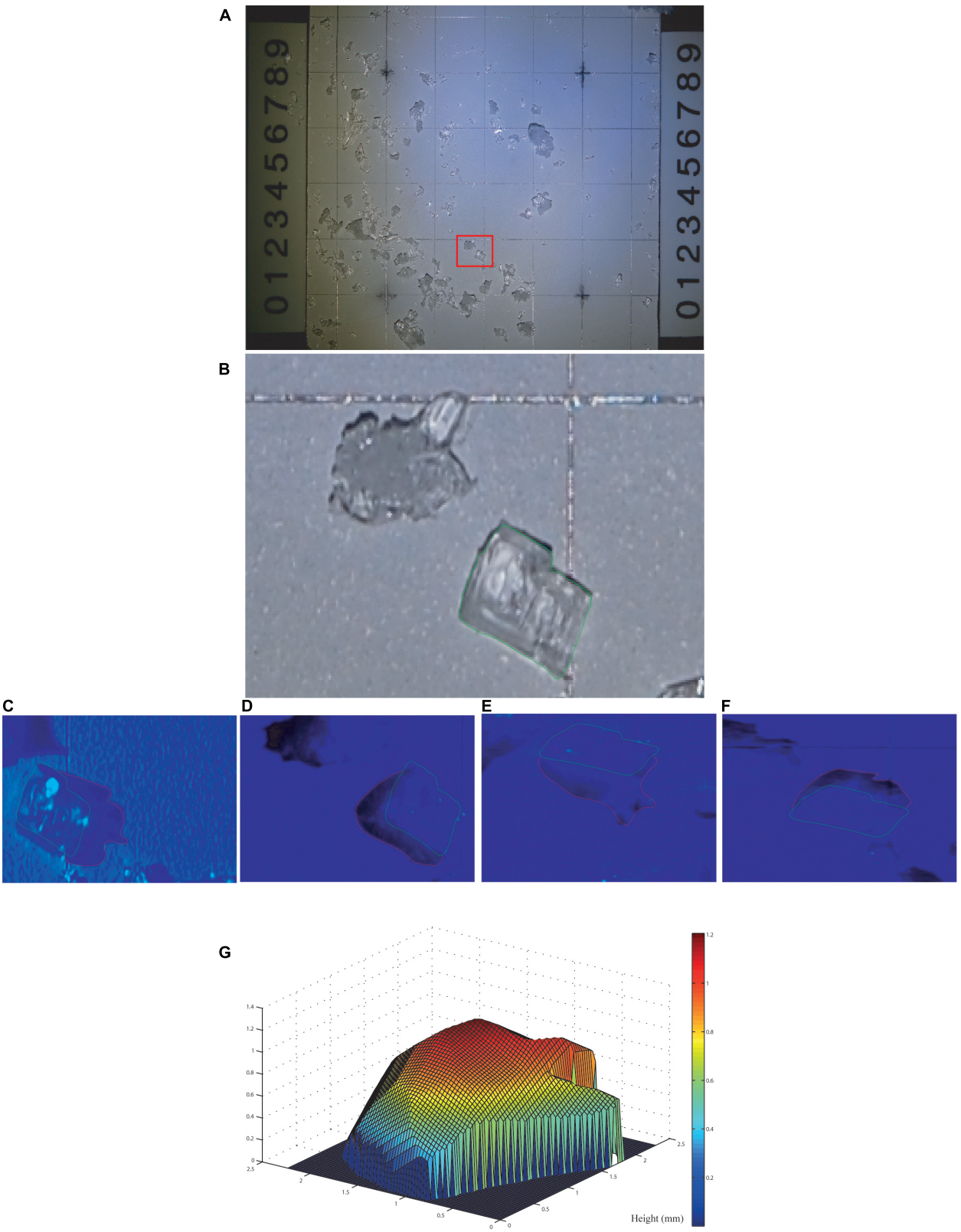

FIGURE 1 | Illustration of the different steps to compute snow grain metrics from the dLED. The two photographs at the top **(A,B)** represent the process of selecting a single grain, and the bottom four photographs highlight the projected shadow digitization **(C–F)** for a 3D reconstruction **(G)** of each individual grain.

Perimeter (mm)
Perimeter (mm) computes the contour length of the snow grain polygon.

Equivalent sphere (mm)
Equivalent sphere (mm) diameter of a circle with the same area as the region.

With regards to the SSA retrieval precision, calibration tests using metallic bearings/balls were conducted in a laboratory, and mathematically, it can be demonstrated that the SSA derived from the projected shadows is identical to the theoretical SSA for which the rationale is presented here:

The total volume of a snow grain measured by the dLED is in fact a half-sphere, mounted on a cylinder since the projected shadows make abstraction of the curvature below the grain. In our case, the height of the cylinder is equal to the radius (r = h) with a total surface of the cylinder expressed as: $2\pi r^2 + 2\pi rh = 4\pi r^2$ if r = h. In our case, we must subtract 1 x πr^2 which corresponds to the cylinder surface, located under the sphere so that we now have $3\pi r^2$, and to add half the sphere surface = $4\pi r^2/2$, giving a total surface = $5\pi r^2$ with an overestimation of πr^2.

For the volume, we simply add the cylinder volume to that of half the sphere such that: cylinder volume = $\pi r^2 h = \pi r^3$ if r = h and a half sphere volume = $(4/3\pi r^3)/2 = 2/3\ \pi r^3$, giving a total volume of $5/3\ \pi r^3$ with an overestimation of $1/3\pi r^3$. In the context of SSA, the theoretical perfect sphere SSA can be expressed by S/V = $4\pi r^2/4/3\ \pi r^3 = 3/r$; which is identical to the SSA derived from the dLED expressed by S/V = $5\pi r^2/5/3\ \pi r^3 = 3/r$. Calibration tests using metallic sphere (steel balls from 0.8 to 4.8 mm) showed that the retrieval error (bias) on Dmax was estimated of the order of 0.03 mm.

InfraRed Integrating Sphere (IRIS)

The InfraRed Integrating Sphere (IRIS) is a laser-based device mounted on an integrating sphere collecting snow reflectance data. Based on original work from Gallet et al. (2009) (after Domine et al., 2006), who developed the first integrating sphere system for snow grain studies, our group adapted the original version for which details can be found in Montpetit et al. (2012). IRIS measures reflectance (R) at 1300 nm, which can physically be linked to SSA following the (Kokhanovsky and Zege, 2004) such that:

$$R_{a,\lambda} = \exp\left(-K_0 b\sqrt{\gamma_\lambda\left(\frac{6}{SSA}\right)}\right) \quad (1)$$

Where K_0 represents the escape function set at 1.26 given the geometry of the integrating sphere, which creates a mix of directional/diffuse hemispherical albedo, b a shape factor set at 4.53 that corresponds to spheres that are best described in the shortwave infrared spectrum (Picard et al., 2009) and γ_λ the absorption coefficient of ice. IRIS outputs voltages measured by a photodiode, and reflectance can be retrieved from reflectance targets measurements at 5%, 20%, 50%, 75% and 99%. This calibration is conducted for each snowpit (refer to Montpetit et al. (2012) for further details on IRIS).

Distribution Analysis

The histograms for each metric were produced for all grains considered as a whole dataset (unclassified), and separately for each grain type: (1) DF, (2) Depth Hoar (DH), (3) Facets (F), (4) Rounds (R), and (5) precipitation particles (PP). DF precipitation particles (DF) are usually found near the surface where fresh snow is broken by saltation from wind redistribution. This type of snow grain is associated with a decrease in surface area (i.e., rounding), which can lead to sintering and increase in density (Fierz et al., 2009). Depth hoar (DH) grains can be present in various forms such as striated crystals or hollows, and are typical of bottom snowpack layers formed by kinematic metamorphism under a sustained temperature gradient. Facetted snow grains (F) consist of hexagonal prisms that can be found near the surface if they develop from PP or deeper in the snowpack at early stages of DH development. Rounded grains (R) can also be found

TABLE 1 | Definition of frequency distribution used.

Frequency distribution	Acronym	Parameters	Remarks	Derived parameters
Kappa	KAP	ξ, α, k, h	Eqs 2 and 3	
Generalized logistic distribution	GLO	ξ, α, k, $h = -1$	$k \neq 0$	For a fixed value of h, skewness and kurtosis are function of ξ, α, k, and the gamma function Γ
Generalized pareto distribution	GPA	ξ, α, k, $h = 1$	$k \neq 0$	
Generalized extreme value distribution	GEV	ξ, α, k, $h- > 0$	$k \neq 0$	
Generalized normal distribution	GN	μ *(mean)*; σ *(scale)*; β *(shape)*		The thickness of probability distribution tails is measured by kurtosis. For a normal distribution, β = 2 and kurtosis = 3
Pearson type III	PE3	*a (scale)*, *d*, *p*	$a > 0$, $d > 0$ and $p > 0$	PE3 is a generalized gamma distribution

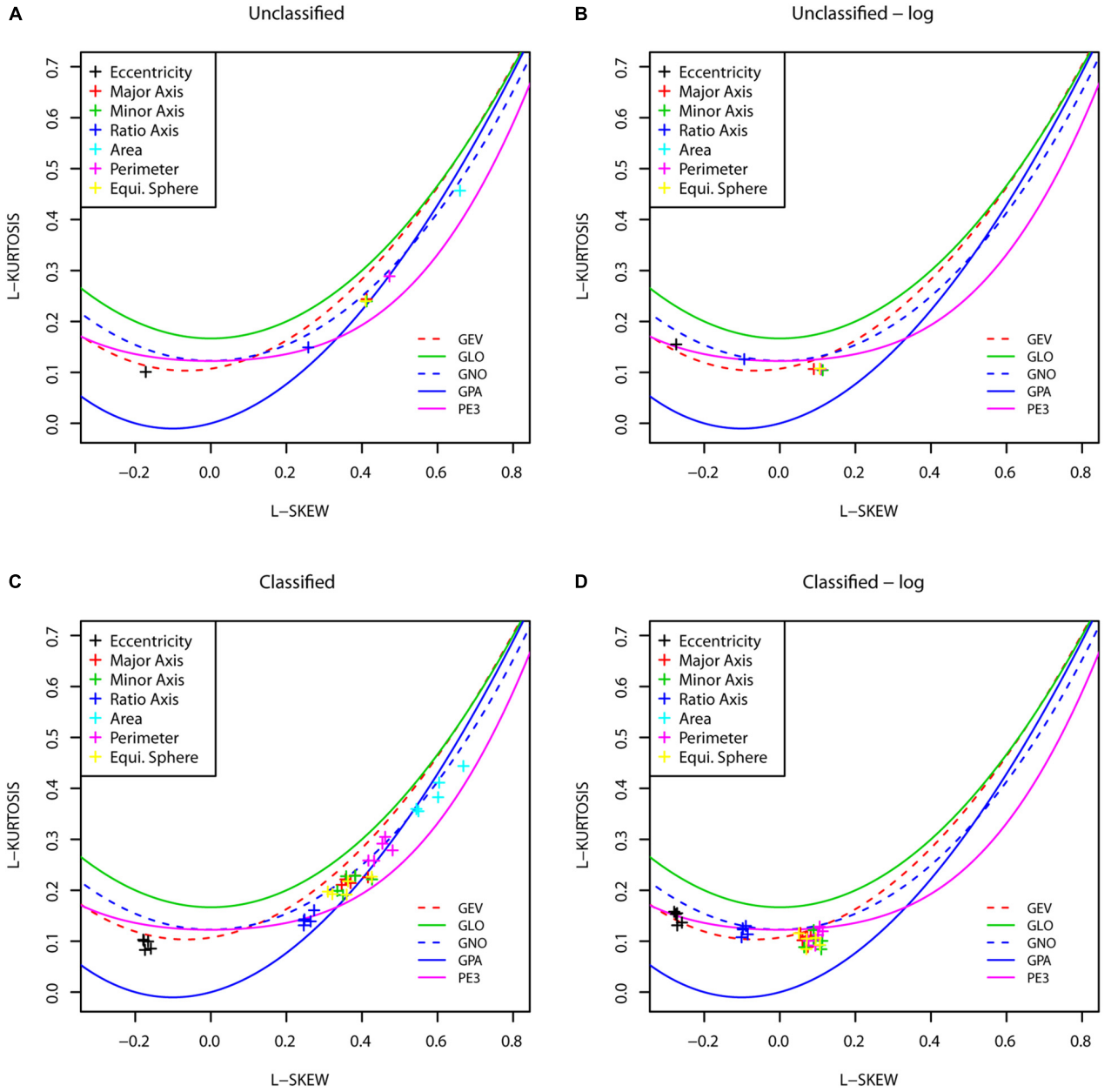

FIGURE 2 | L-moment ratio diagrams for the unclassified snow grain dataset **(A,B)** (only one point for each metric) and for classified snow grains **(C,D)**. Classified snow grains include one point for each category: Facets, Depth Hoar and Precipitation Particles. The lines represent theoretical relationship between the L-skewness and L-kurtosis of known family of distributions.

within the snow cover or near the surface and are formed from equilibrium metamorphism (within the snowpack) and by wind redistribution (near the surface). In all cases, they correspond to dense layers with an increase in strength. PP are found in numerous forms, depending on the formation process in the atmosphere driven by temperature and supersaturation levels. Their forms include dendrites, needles, plates and columns for which the rate of rounding will vary. For complete details on snow grain types, please refer to the International classification for seasonal snow on the ground (Fierz et al., 2009).

In order to select an appropriate distribution, visual diagnostics were employed to assess the quality of the fitting. We used among others, the four-parameter Kappa (KAP) distribution that has been encountered for modeling extreme hydrological values. It includes as a special case the common three-parameter distributions: generalized extremes values distribution (GEV), generalized logistic distribution (GLO), and generalized pareto distribution (GPA). The other three-parameter distributions considered are the generalized normal distribution (GNO) and Pearson type III (PE3)

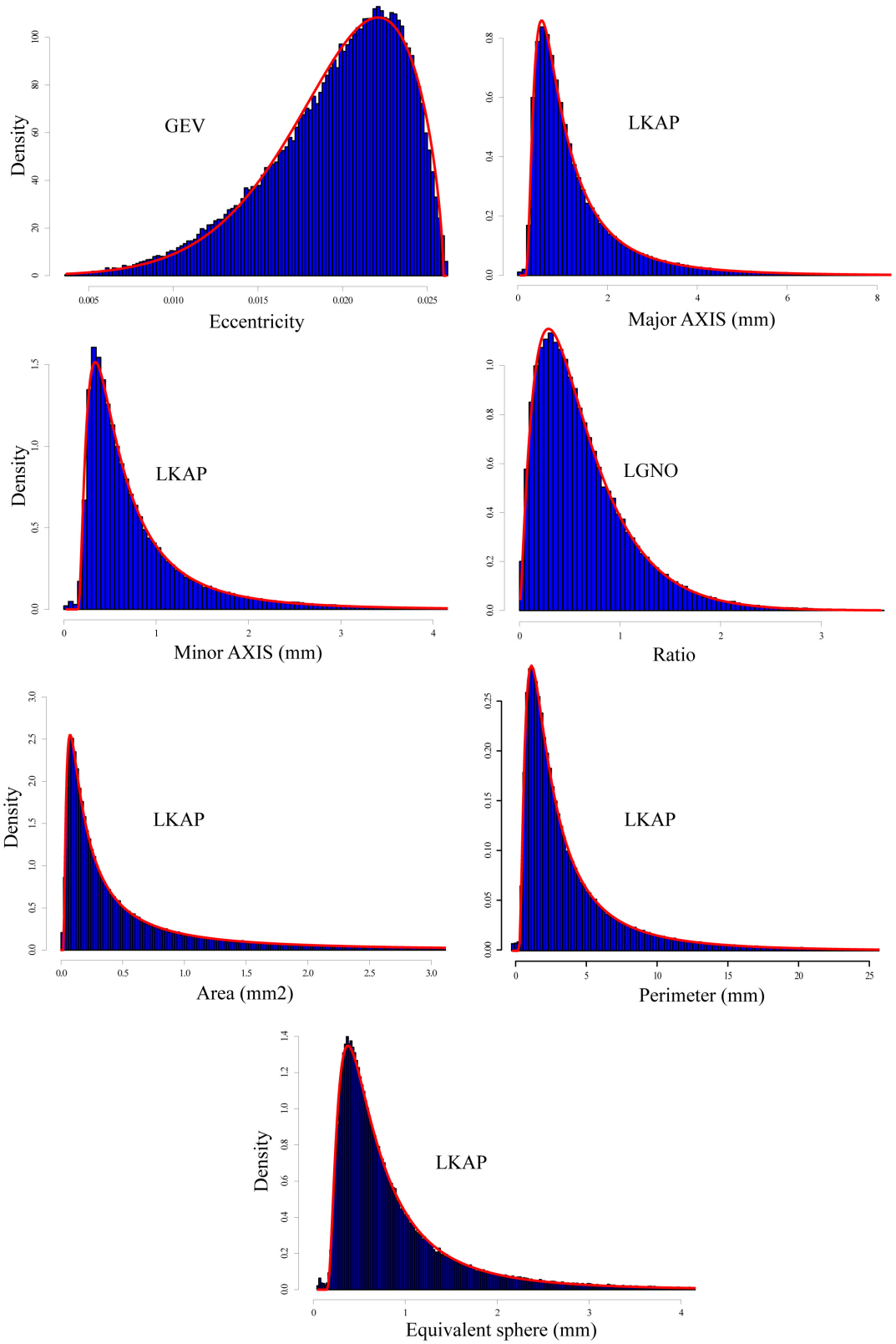

FIGURE 3 | Snow grain metric distribution fits for all snow grains, unclassified with a total of 162,515 grains. The generalized extreme values distribution (GEV) is best for Eccentricity. The distribution of the log transformed data generalized normal distribution (LGNO) is best for Ratio while the log transformed four-parameter Kappa (LKAP) function fits Major/minor axis (mm), Area (mm^2), and equivalent sphere (mm).

distribution, which, respectively, extend the common log-normal and gamma distributions with two parameters. For all these candidate distributions, the parameterization proposed by Hosking and Wallis (1997) is used, which includes a location and scale parameter, as well as 1 or 2 shape parameters, depending on the choice of the distributions. These distributions are used directly to model the snow grain metrics at the original scale, but also at the logarithm scale. The distribution of the log transformed data can be converted back to the original scale, which will be denoted, respectively, LKAP, LGEV, LGLO, LGNO, LGPA, and LPE3. Estimation is performed using L-moments (Greenwood et al., 1979; Hosking, 1992) and by removing 1% of the data (0.5% at the beginning of the distribution and 0.5% at the end) that behaves differently from the center of the distribution and has an undesirable effect on the quality of the estimation. Considering x to be the grain size, the cumulative distribution function (cdf) of the Kappa distribution can be defined as:

$$F(x) = \left\{1 - h\left[1 - \frac{k(x-\xi)}{\alpha}\right]^{1/k}\right\}^{1/h} \quad (2)$$

where ξ (location, that control the center of the distribution; central tendency), α (scale), k (shape 1), and h (shape 2) are parameters. The associated quantile function is given as:

$$x(F) = \xi + \frac{\alpha}{k}\left\{1 - \left(\frac{1-F^h}{h}\right)^k\right\} \quad (3)$$

The Kappa distribution is a generalization of some of the more commonly used three-parameter distributions: for $k \neq 0$, the GPA, GEV, and GLO distributions are all special cases for $h = 1$, $h = 0$ and $h = -1$, respectively. The cdf, quantile function and L-moment parameter estimators for the GLO and GEV distributions can be found in Hosking and Wallis (1997) (**Table 1**).

RESULTS AND DISCUSSION

L-Moments Analysis

Figure 2 shows the L-moment ratio diagrams that compare the sample L-skewness and L-kurtosis to their theoretical values, which is useful to summarize their shapes. L-skewness, like classical skewness, measures asymmetry, where a positive value indicates a relatively heavier right tail compared to the left tail. Similarly, L-kurtosis is a flattening measurement where higher values correspond to relatively lower density in the center of the distribution and heavier tails. In **Figure 2**, sample L-moments are represented as dots. For all considered distributions except Kappa, a relationship between the L-skewness and L-kurtosis exist and takes the shape of a theoretical line as shown in **Figure 2**. Dots close to this theoretical line suggest good agreement between sample and theoretical L-moments. For example, in the top-left panel the black cross representing the Eccentricity metric is closer to the GEV line, which suggests this distribution as a good fit. Also, the metrics like the Major or Minor axis in the top-right panel are further from the lines, which suggests that a log-kappa that is more general maybe needed. From **Figure 2**, it is clear that (1) there is an appropriate distribution for each classified snow grain and (2) the distribution of each grain metric is similar for each classified snow grain.

Snow Grains Analyzed

The 581 photographs were classified individually by dominant "grain type" (Fierz et al., 2009) and a total of five main classes were identified as: (1) Defragmented/broken (DF) (12,338 grains), (2) Depth Hoar (48,387 grains), (3) Facets (50,190 grains), (4) Rounds (50,633 grains), and (5) PP (967 grains). The DF grains were not used in the distribution analysis since the grains had too much visual damage to be classified. This mainly occurred in crusted layers where the insertion of the plate for the photographs was difficult. In this paper, the "unclassified" snow grain distributions correspond to the distribution analysis of the whole dataset (i.e., 162,515 snow grains), while the "classified" snow grain distributions correspond to the distribution analysis based on grain type. Also, there are many types of PP (columns, plates, dendrites and plates, hollow columns, etc.), but the distributions presented in this paper only include dendrites and plates and one should be careful when applying the distribution functions to other types of PP.

Unclassified Snow Grain Distributions

A first analysis was conducted including all digitized snow grains (i.e., 162,515 grains) so that no distinctions were made according to grain type. Distribution histograms were produced for each metric such as: eccentricity, area (projected surface 2D, mm^2); minor axis (mm); major axis (mm); axis ratio (major/minor); perimeter (mm) and equivalent optical diameter (mm) and the best distribution fits were chosen from **Figures 2A,B**, highlighted in **Figure 3** and summarized in **Table 2**.

TABLE 2 | Statistical fits summary for unclassified snow grains for the distribution of the log transformed data.

Metric	Distribution	Location ξ	Scale α	Shape1 k	Shape2 h
Eccentricity	GEV	0.0189	0.0044	0.6208	–
AxisMAJ	LKAP	−0.3468	0.7465	0.2024	0.1887
AxisMIN	LKAP	−0.8501	0.7275	0.1996	0.2874
Ratio	LGNO	−0.6073	0.7836	0.1931	–
Area	LKAP	−1.7171	1.4170	0.1895	0.2283
Perimeter	LKAP	0.6775	0.8655	0.1941	0.2519
Eq. sphere	LKAP	−0.7378	0.7085	0.1895	0.2283

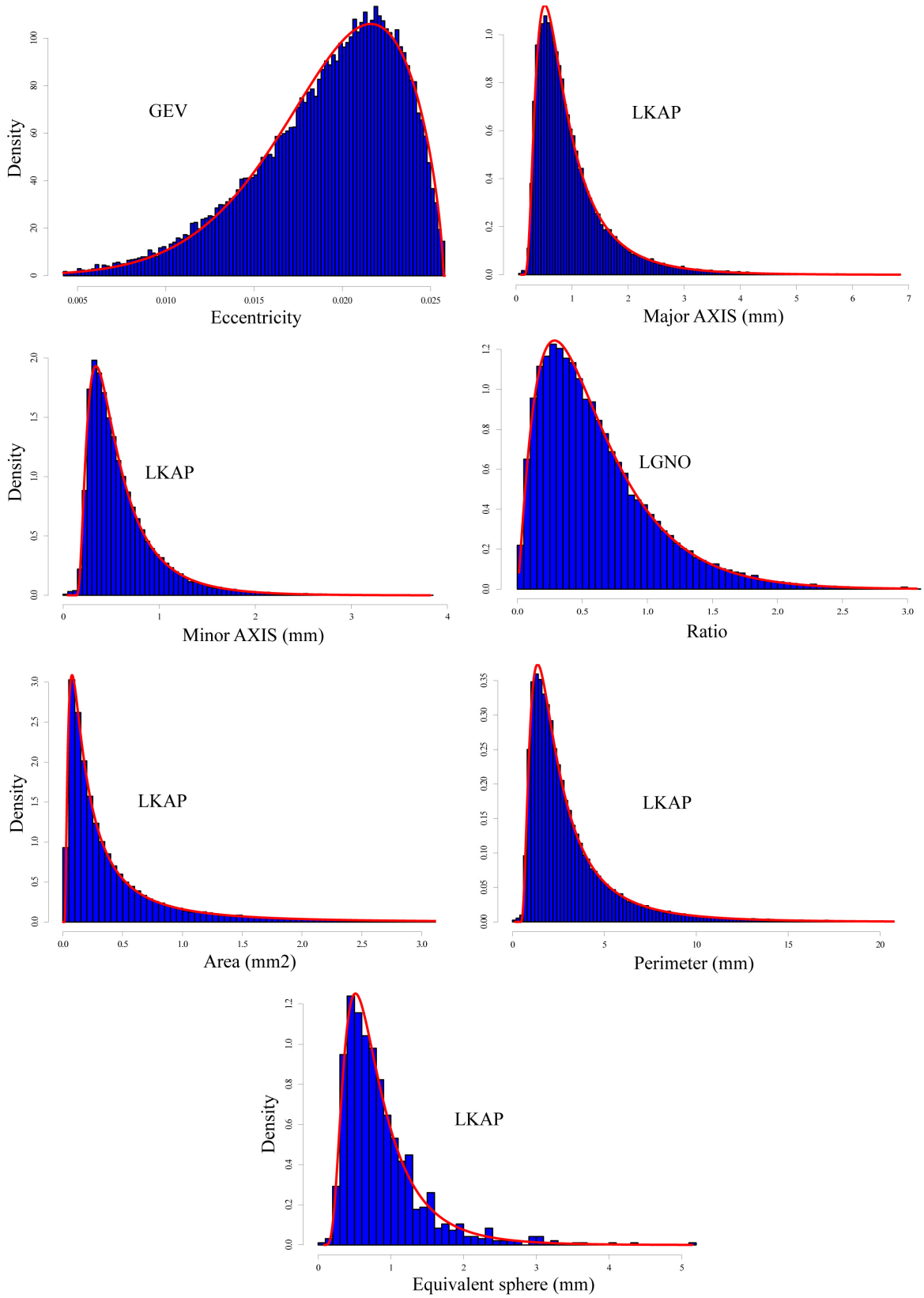

FIGURE 4 | Same as **Figure 3** but for all snow grains classified as "rounded" with a total of 50,633 grains.

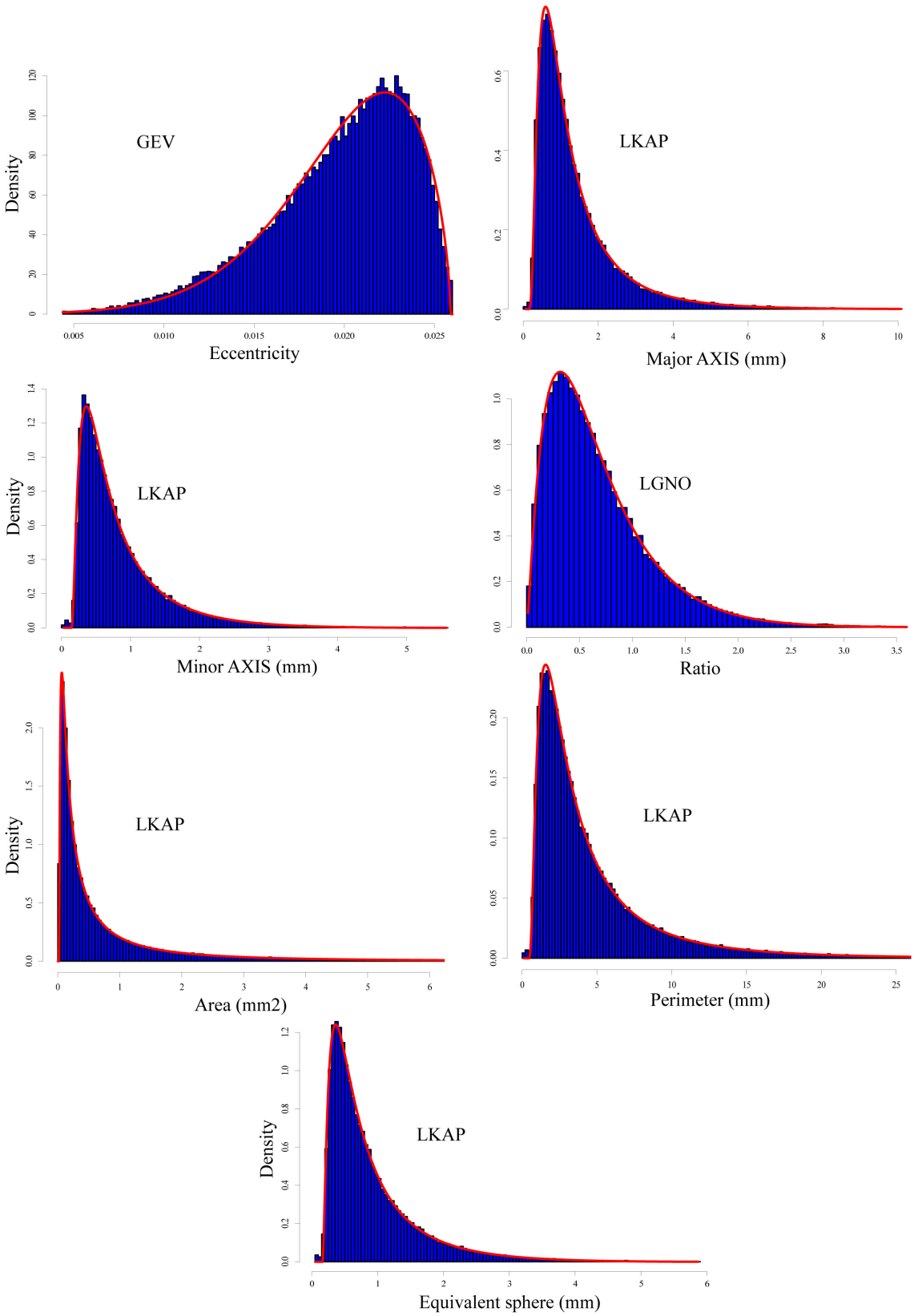

FIGURE 5 | Same as **Figure 3** but for all snow grains classified as "facetted" with a total of 50,190 grains.

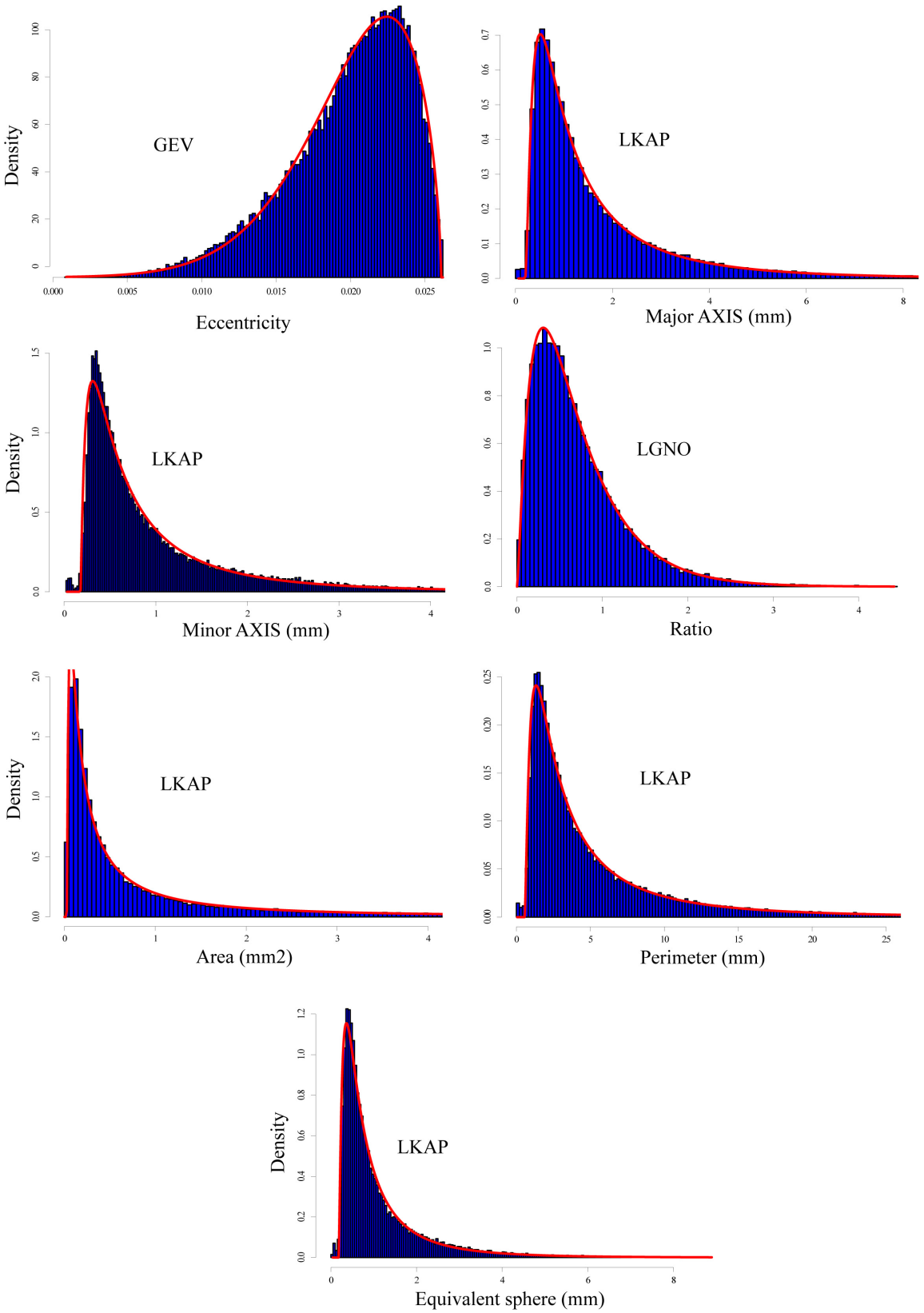

FIGURE 6 | Same as **Figure 3** but for all snow grains classified as "depth hoar" with a total of 48,387 grains.

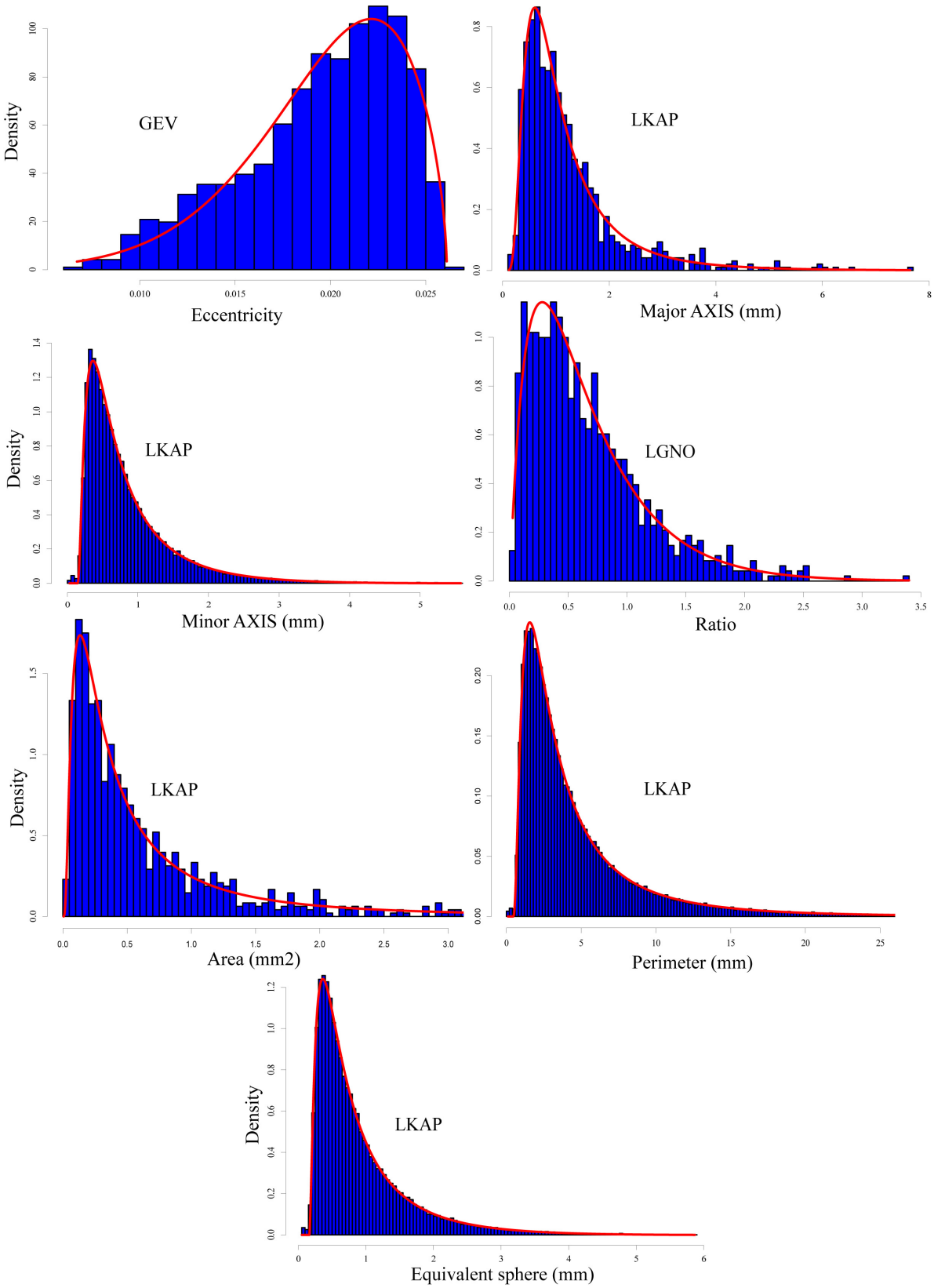

FIGURE 7 | Same as **Figure 3** but for all snow grains classified as "precipitation particles" with a total of 967 grains.

TABLE 3 | Statistical fits summary for classified snow grains for the distribution of the log transformed data.

Grain type	Metric	Distribution	Location ξ	Scale α	Shape1 k	Shape2 h
Rounded	Eccentricity	GEV	0.0185	0.0044	0.6077	–
Rounded	AxisMAJ	LKAP	−0.4736	0.5963	0.2047	0.1166
Rounded	AxisMIN	LKAP	−0.9284	0.5645	0.2118	0.2066
Rounded	Ratio	LGNO	−0.6840	0.7718	0.2003	–
Rounded	Area	LKAP	−1.8674	1.1353	0.2232	0.1557
Rounded	Perimeter	LKAP	0.5586	0.6769	0.1711	0.1622
Rounded	Eq. sphere	LKAP	−0.8128	0.5676	0.2231	0.1553
Facets	Eccentricity	GEV	0.0191	0.0043	0.6311	–
Facets	AxisMAJ	LKAP	−0.2408	0.7356	0.2454	0.1573
Facets	AxisMIN	LKAP	−0.7789	0.7908	0.3061	0.3029
Facets	Ratio	LGNO	−0.5776	0.7716	0.2015	–
Facets	Area	LKAP	−1.7715	1.6936	0.3189	0.3519
Facets	Perimeter	LKAP	0.8100	0.8627	0.2377	0.2088
Facets	Eq. sphere	LKAP	−0.7648	0.8466	0.3187	0.3515
Depth hoar	Eccentricity	GEV	0.0192	0.0044	0.6347	–
Depth hoar	AxisMAJ	LKAP	−0.3035	0.9776	0.2958	0.3225
Depth hoar	AxisMIN	LKAP	−0.8918	1.0103	0.2965	0.4800
Depth hoar	Ratio	LGNO	−0.5531	0.7998	0.1849	–
Depth hoar	Area	LKAP	−1.6937	1.8484	0.2590	0.3893
Depth hoar	Perimeter	LKAP	0.7171	1.0939	0.2687	0.3530
Depth hoar	Eq. sphere	LKAP	−0.7235	0.9213	0.2577	0.3844
Precip. Part	Eccentricity	GEV	0.0188	0.0046	0.6248	–
Precip. Part	AxisMAJ	LKAP	−0.2644	0.6048	0.1873	−0.0029
Precip. Part	AxisMIN	LKAP	−0.7224	0.5067	0.1387	0.0268
Precip. Part	Ratio	LGNO	−0.6236	0.8136	0.2073	–
Precip. Part	Area	LKAP	−1.2569	1.0246	0.1933	−0.0048
Precip. Part	Perimeter	LKAP	0.7543	0.6384	0.1019	−0.0026
Precip. Part	Eq. sphere	LKAP	−0.5076	0.5123	0.1933	−0.0049

Classified Snow Grain Distributions

As mentioned earlier, the 581 photos were classified into grain "types." Four classes are highlighted here where a distribution fit was identified for each class (**Figures 4–7** and **Table 3**).

From **Figures 4–7**, we compiled the average metric statistics for the classified snow grains. The results are depicted in **Table 4**:

From the table above, the metamorphic processes behind the formation of depth hoar are such that large snow grain are found due to the upward migration of vapor following a temperature gradient (Colbeck, 1989). Consequently, snow grain eccentricity is expected to increase as snow grains get longer. Furthermore, the area, perimeter and both minor and major axes are expected to be larger, which is the case in **Table 4**. Interestingly, the difference between facets and depth hoar is more marked in the "size" metrics (i.e., area, perimeter, axes and equivalent sphere) than in the shape metrics (i.e., ratio and eccentricity). When we look at rounded grains (rounds), again the changes in eccentricity and axis ratio are not as significant as changes in the "size" metrics. The rounded grains are the consequence of equilibrium metamorphism (or melt, although not the case in this study) where the large grains are eroded by a mass redistribution from the snow grain's convex areas to its concave areas with lower saturation vapor pressure values. This process, along with significant sublimation in the absence of a temperature gradient, will lead to small and rounder grains, in agreement with the numbers presented in **Table 4**. Finally, PP have shape metrics similar to those of depth hoar and facets. As mentioned above, in our study, only 967 snow grains from two photographs were identified as PP. Looking at the pictures, the PP mainly consisted of flakes and a couple of needles that increased the values of eccentricity and axis ratio, but of smaller size (about 50% of area, and 25% in equivalent diameter, minor and major axes). Given what is presented, it is suggested that the size metrics present more important changes than the shape metrics from

TABLE 4 | Snow metric averages for depth hoar, facets, rounds, and precipitation particles.

Metric	Units	Depth hoar	Facets	Rounds	Precip. part
Eccentricity	–	0.0198	0.0197	0.0192	0.0195
Area	mm^2	2.2	1.24	0.62	1.05
Axis minor	mm	1.05	0.87	0.63	0.75
Axis major	mm	1.78	1.46	1.02	1.27
Perimeter	mm	6.24	5.13	3.4	4.34
Axis ratio	–	1.73	1.7	1.62	1.67
Eq. sphere	mm	1.15	0.94	0.7	0.89

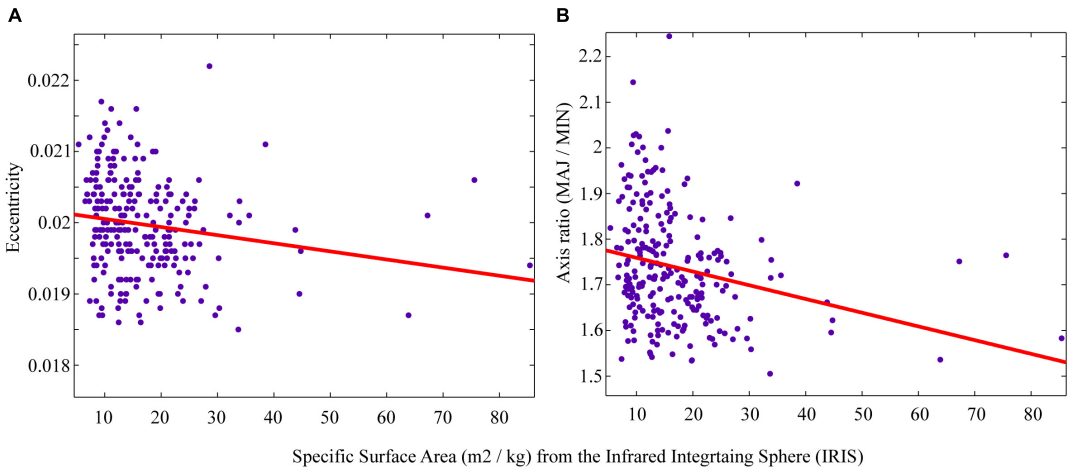

FIGURE 8 | Measured SSA values compared with **(A)** eccentricity and **(B)** axis ratio computed from the dLED.

one grain type to another. However, one should note that more precipitation particle types should be considered. Fresh particles can consist of snowflakes, needles or columns, depending on the atmospheric conditions in which they formed (temperature, vapor pressure) (St-Pierre and Thériault, 2015), and considering their shape metrics individually would greatly affect the numbers presented in **Table 4**.

dLED vs. IRIS Comparison

Snow grain metrics from the dLED are compared to SSA measurements from the IRIS system in order to evaluate if the latter can provide information on snow grain shape. First, SSA measurements were compared to the two "shape" metrics, namely eccentricity and computed axis ratio (**Figure 8**).

The comparison between IRIS SSA measurements and computed grain shape metrics did not show any statistically significant correlation. The highest correlations (although not significant) were obtained using a linear regression, with an important scatter centered around SSA values of 10 to 15 m^2/kg. However, the decrease in either eccentricity and/or axis ratio with increasing SSA makes sense since an eccentricity of 0 corresponds to a perfect sphere. Therefore, for large grains such as depth hoar, the expected eccentricity would increase, whereas SSA values are usually very low for such grains. In our case, small eroded grains (rounded) would also correspond to low SSA, but would have low eccentricity. Therefore, since our dataset is mostly comprised of both grain types, it is not surprising to see that no statistical relationship can be found when comparing both. One should note, however, that the high SSA values in **Figure 8** correspond to PP, which were primarily digitized as circles since the camera resolution did not produce the level of detail needed to properly draw the complicated contours of such grains. As a consequence, they are associated with low eccentricity values. The statistical fitting results are depicted in **Figure 9**.

The comparison between measured SSA from the IRIS and size metrics computed from the dLED highlights stronger correlations when compared to the shape metrics analysis from **Figure 9**. The strongest correlations are found with an exponent function, with best results obtained with minor and major axes, where the major axis can be considered, and the geometrical diameter (Langlois et al., 2010; maximum snow grain extent).

The 3D reconstruction allowed the retrieval of volume and surface for the grains so that SSA could be computed. We thus compared the computed SSA from the dLED to the IRIS in order to see if proper SSA values could be retrieved considering that the IRIS remains the best approach for SSA measurements on the field. The comparison is depicted in **Figure 10** for the whole dataset, and for a measured (from IRIS) range of SSA values between 0 and 30 m^2/kg.

Results from **Figure 10** suggest an underestimation of SSA values derived from the dLED. Although statistically significant, the relationship seems to saturate for measured SSA above 30 m^2/kg. The resolution of the camera and the digitization approach are such that high SSA snow grains (i.e., fresh snowflakes) are thin and complex to digitize. The projected shadows are very small so that large uncertainties can be found with such types of grains. In **Figure 10A**, this can be seen for SSA values above 30 m^2/kg where no statistical relationship can be found. When considering values in the range of measured SSA from 0 to 30 m^2/kg in **Figure 10B**, the correlation improves with an R^2 of 0.52. The underestimation remains, but results suggest that for lower SSA snow grains (i.e., easier to digitize with clear shadows), the dLED could retrieve SSA with reasonable accuracy.

DISCUSSION

Past studies have investigated the use of snow micro-photographs to quantify various metrics (Lesaffre et al., 1998; Langlois et al., 2007, Langlois et al., 2008; Royer et al., 2017). The purpose of our study was not to overcome 2D techniques, but rather to use a new technique that allows digitizing a sufficient amount of grain to produce statistical distributions on various metrics of interests for radiative transfer models. Past works were mainly

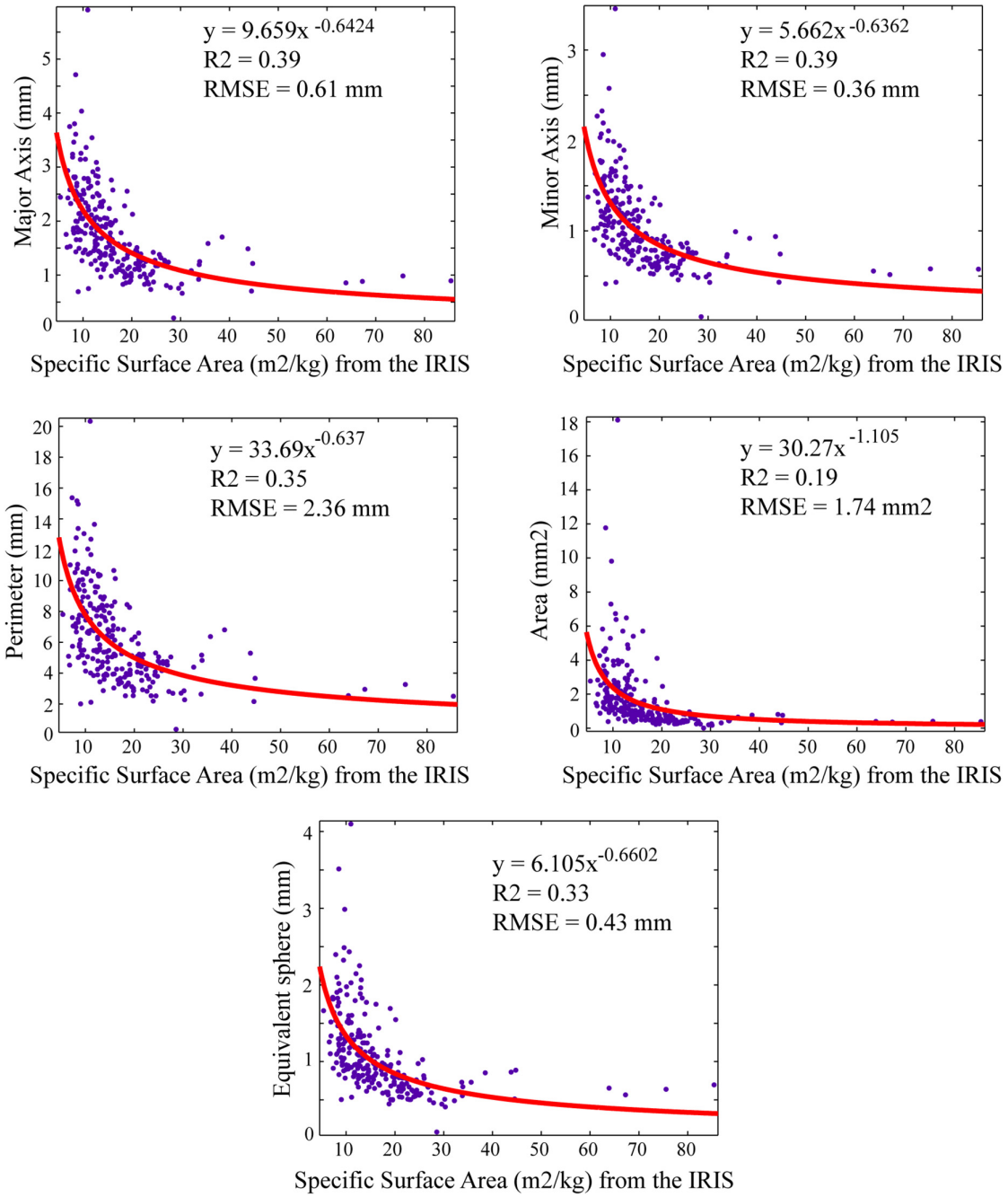

FIGURE 9 | Measured SSA values compared with: Major axis, Minor axis, Perimeter, Area, and Equivalent sphere computed from the dLED.

limited by the number of grains (sample size) digitized. Digitizing few snow grains per sample will lead to a user selection bias, which is avoided in our context where all shapes present in the photos are considered, and likely located in the tails of the distribution fits presented.

One limitation for this study resides in the definition of what constitutes a snow grain, which is a matter of ongoing debate in the snow community. From snow grain photographs, we must digitize snow grains as polygons, but one should note that bonded grains were not separated manually. This would have been necessary in refrozen crusts, or depth hoar chains, which were not observed in our dataset from the nature of the snow and the climate. Likely some depth hoar chains might have been broken if present by extracting the sample, but that brings us back to the definition of what constitutes a "grain." This is an ongoing debate, especially in the metamorphism and energy exchange formulations in future snow models. This said, from a RTM perspective, we must quantify a "scatterer", so that the proposed

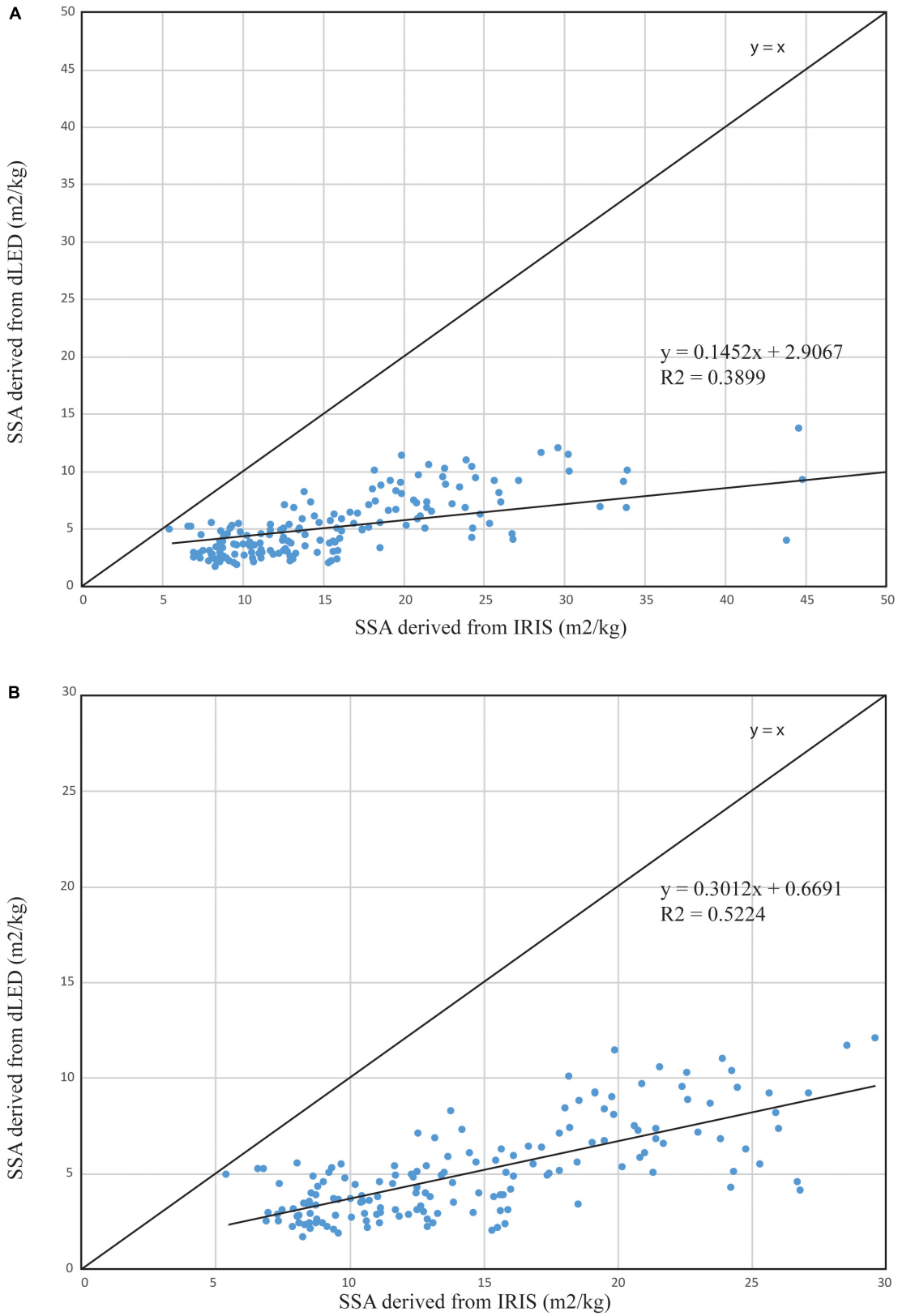

FIGURE 10 | Comparison between specific surface area (SSA) measured with both IRIS and dLED for **(A)** the whole dataset and **(B)** measured over the value range of 0–30 m^2/kg from IRIS (considered here as the reference).

method in this paper remains relevant. As far as identifying the snow grains, they were manually digitized by four trained users that were asked to digitize every polygon visible on each photograph to avoid a "selection bias." This represents several months, full time for four trained people, but we believed this was necessary to overcome limitations of past studies identified earlier. However, the authors acknowledge that this will lead to the digitization of broken grains but again, we are confident that by digitizing several hundred snow grains the contribution of broken grains will not affect the averaged metric values. Such grains would be located in the tails of the statistical distributions, thus not affecting the distribution types.

CONCLUSION

The work presented a very large dataset of >160,000 digitized snow grains including depth hoar, facets, rounded, and PP. The dataset was collected over a period of 6 months using a new device allowing the digitization of projected snow grain shadows under LED illumination. The use of the dLED allows the analysis and retrieval of both shape (eccentricity, axis ratio) and metric (area, perimeter, diameter, axis length) information. We analyzed various distribution functions of the classified snow grains (i.e., depth hoar, rounded, facets, and PP) and showed that the Kappa distribution function provided the best fit to the derived distributions from the dLED. More specifically, when considering all the snow grains independently from the type, the snow grain metric distributions can be explained using GEV (eccentricity), LGNO (ratio), and LKAP (minor/major axes, area, perimeter and equivalent sphere). When the snow grains are classified by type, the same distribution functions are found for each metric, but with different location, scale and shape values provided in the Tables in section "Results and Discussion." This suggests that the distribution function with a snow cover is not only grain type dependent but depends also on the shape/metric analyzed.

The derived morphology parameters from the dLED were compared to SSA measured by the IRIS, which was considered as a reference in this paper. Results showed that a statistically significant relationship can be found between IRIS SSA and "metric" parameters, with strongest correlation with the axis lengths. This suggests that the dLED can be used to derive snow grain metrics but does not provide any significant information on grain shape (other that the ability to visually identify grain types). Furthermore, we investigated the potential in using the dLED to derive SSA from the computed volume and surface of the digitized 3D grains. Results showed that the dLED SSA are underestimated compared to the IRIS values, which can be linked to an overestimation of snow grain volume by the dLED. Although the comparison between dLED and IRIS SSA is statistically significant, the correlation improves when considering a shorter range of SSA between 0 and 30 m^2/kg. In that range, the linear correlation has an R^2 value of 0.52. The dLED SSA remain underestimated, but in that range it can be suggested that the dLED allows SSA (mostly rounds, and depth hoar) to be derived.

This paper thus suggests distribution functions that are reproducible, and therefore useful in RTMs. The distributions found in this paper can be implemented in RTMs such as the Snow Microwave Radiative Transfer model (Picard et al., 2018) and to evaluate the improvement in simulations of brightness temperatures and the sensitivity of scaling factors to different snow grain metrics that could help assess the stickiness effect on the simulation biases. Improvements to RTMs will help improve the monitoring of snow state variables in space and time with the coupling of such models to snow thermodynamic models such as SNOWPACK (Langlois et al., 2012) or Crocus (Larue et al., 2018). For instance, SWE retrievals are critical in understanding changes in hydrological patterns at various scales. Other potential approaches using assimilation schemes to derive snow density with more accuracy will contribute largely in quantifying trends in ungulates foraging conditions that are currently endangered from snow densification (Langlois et al., 2017; Dolant et al., 2018). This is of particular relevance with the new MEaSUREs Calibrated Enhanced-Resolution Passive Microwave dataset recently available at 3.125 and 6.5 km spatial resolution (Brodzik et al., 2018), which will help produce improved maps of snow state variables at the watershed scale.

DATA AVAILABILITY STATEMENT

The datasets generated for this study are available on request to the corresponding author.

AUTHOR CONTRIBUTIONS

AL and AAR conducted the snow grain analysis, and supervised the dataset digitization, classification/distribution, and fieldwork. AL wrote the manuscript and led the manuscript analysis. AAR designed the data collection, distribution analysis, and dLED. BM performed the dataset analysis and digitization of snow grains, and contributed to the IRIS analysis. AER contributed to the microwave context, fieldwork, and data collection as well as distribution analysis on the manuscript. MD contributed to the statistical and distribution analysis. All authors reviewed the manuscript.

FUNDING

This work was funded by the Natural Sciences and Engineering Research Council of Canada (NSERC), the International Polar Year, and the Cold Regions H2O mission, Environment and Climate Change Canada.

ACKNOWLEDGMENTS

The authors would like to thank the Churchill Northern Studies Centre for tremendous logistical support during fieldwork. Special thanks to Miroslav Chum for designing the dLED and to Roxanne Lanoix for great support in digitizing the snow grain photos.

REFERENCES

Bader, H. P., Haefeli, R., Bucher, E., Neher, J., Eckel, O., Tharms, C., et al. (1939). Snow and its metamorphism. *U. S. Army Corps Eng. Snow Ice Permafr. Res. Establishment Transl.* 14:313.

Bartlett, S. J., Rüedi, J.-D., Craig, A., and Fierz, C. (2008). Assessment of techniques for analyzing snow crystals in two dimensions. *Anns. Glaciol.* 48, 103–112.

Brodzik, M. J., Long, D. G., Hardman, M. A., Paget, A., and Armstrong, R. L. (2018). *MEaSUREs Calibrated Enhanced-Resolution Passive Microwave Daily EASE-Grid 2.0 Brightness Temperature ESDR, Version 1*. Boulder, CO: National Snow and Ice Data Center. Digital Media, doi: 10.5067/MEASURES/CRYOSPHERE/NSIDC-0630.001

Brown, R., and Derksen, C. (2013). Is Eurasian October snow cover increasing? *Environ. Res. Lett.* 8:024006. doi: 10.1088/1748-9326/8/2/024006

Cabanes, A., Legagneux, L., and Domine, F. (2002). Evolution of the specific surface area and of crystal morphology of Arctic fresh snow during the ALERT 2000 campaign. *Atmos. Environ.* 36, 2767–2777.

Chang, A. T. C., Foster, J. L., and Hall, D. K. (1987). Nimbus 7 derived global snow cover parameters. *Ann. Glaciol.* 9, 39–44.

Colbeck, S. C. (1982). An overview of seasonal snow metamorphism. *Rev. Geophys.* 20, 45–61.

Colbeck, S. C. (1983). Theory of metamorphism of dry snow. *J. Geophys. Res.* 88, 5475–5482.

Colbeck, S. C. (1989). On the micrometeorology of surface hoar growth on snow in mountainous area. *Boundary Layer Meteorol.* 44, 1–12.

Denoth, A. (1980). The pendular-funicular liquid transition in snow. *J. Glac.* 25, 93–97.

Derksen, C., and Brown, R. (2012). Spring snow cover extent reductions in the 2008-2012 period exceeding climate model projections. *Geophys. Res. Lett.* 39:L19504.

Derksen, C., Smith, S. L., Sharp, M., Brown, L., Howell, S., Copland, L., et al. (2012). Variability and change in the canadian cryosphere. *Clim. Change* 115, 59–88. doi: 10.1007/s10584-012-0470-0

Dolant, C., Montpetit, B., Langlois, A., Brucker, L., Zolina, O., Johnson, C.-A., et al. (2018). Assessment of the Barren Ground caribou die-off during winter 2015-2016 using passive microwave observations. *Geophy. Res. Lett.* 45, 4908–4916. doi: 10.1029/2017GL076752

Domine, F., Salvatori, R., Legagneux, L., Salzano, R., Fily, M., and Casacchia, R. (2006). Correlation between the specific surface area and the short wave infrared (SWIR) reflectance of snow. *Cold Reg. Sci. Technol.* 46, 60–68.

Estilow, T. W., Young, A. H., and Robinson, D. A. (2015). A long-term Northern Hemisphere snow cover extent data record for climate studies and monitoring. *Earth Syst. Sci. Data.* 7, 137–142.

Fierz, C., Armstrong, R. L., Durand, Y., Etchevers, P., Greene, E., McClung, D. M., et al. (2009). *The International Classification for Seasonal Snow on the Ground. International Association of Cryospheric Sciences-IACS, SC.2009/WS/15*. Paris: UNESCO-IHP,

Foster, J. L., Chang, A. T. C., and Hall, D. K. (1997). Comparison of snow mass estimates from a prototype passive microwave snow algorithm, a revised algorithm and a snow depth climatology. *Remote Sens. Environ.* 62, 132–142.

Gallet, J.-C., Domine, F., Zender, C. S., and Picard, G. (2009). Rapid and accurate measurement of the specific surface area of snow using infrared reflectance at 1310 and 1550 nm. *Cryosphere* 3, 167–189.

Greenwood, J. A., Lanwehr, J. M., Matalas, N. C., and Wallis, J. R. (1979). Probability weighted moments: definition and relation to parameters of several distributions expressable in inverse form. *Water Resour. Res.* 15, 1049–1054.

Gubler, H. (1985). Model for dry snow metamorphism by interparticle vapor flux. *J. Geophys. Res.* 90, 8081–8092.

Hosking, J. R. M. (1992). Moments or L moments? An example comparing two measures of distributional shape. *Am. Stat.* 46, 186–189.

Hosking, J. R. M., and Wallis, J. R. (1997). *Regional Frequency Analysis: An Approach Based on L-moments*. Cambridge: Cambridge University Press.

Kelly, R. E. J., and Chang, A. T. C. (2003). Development of a passive microwave global snow depth retrieval algorithm for SSM/I and AMSR-E data. *Radio Sci.* 38:8076. doi: 10.1029/2002RS002648

King, J., Kelly, R., Kasurak, A., Duguay, C., Gunn, G., Rutter, N., et al. (2015). Spatio-temporal influence of tundra snow properties on Ku-band (17.2GHz) backscatter. *J. Glac.* 61, 267–279.

Kokhanovsky, A. A., and Zege, E. P. (2004). Scattering optics of snow. *Appl. Opt.* 43, 1589–1602.

Kosaka, Y., and Xie, S.-P. (2013). Recent global-warming hiatus tied to equatorial Pacific surface cooling. *Nature* 501, 403–407. doi: 10.1038/nature12534

Langlois, A., and Barber, D. G. (2007). Passive microwave remote sensing of seasonal snow covered sea ice. *Prog. Phys. Geogr.* 31, 539–573.

Langlois, A., Fisico, T., Barber, D. G., and Papakyriakou, T. N. (2008). Response of snow thermophysical processes to the passage of a polar low-pressure system and its impact on *in situ* passive microwave radiometry: a case study. *J. Geophys. Res.* 113:C03S04. doi: 10.1029/2007JC004197

Langlois, A., Johnson, C.-A., Montpetit, B., Royer, A., Blukacz-Richards, E. A., Neave, E., et al. (2017). Detection of rain-on-snow (ROS) events and ice layer formation using passive microwave radiometry: a context for the Peary caribou habitat in the Canadian arctic. *Rem. Sens. Environ.* 189, 84–95.

Langlois, A., Mundy, C. J., and Barber, D. G. (2007). Overwintering evolution of geophysical and electrical properties of snow cover over first-year sea ice. *Hydrol. Proc.* 21, 705–716. doi: 10.1002/hyp.6407

Langlois, A., Royer, A., Derksen, C., Montpetit, B., Dupont, F., and Goita, K. (2012). Coupling of the snow thermodynamic model SNOWPACK with the Microwave Emission Model for Layered Snowpacks (MEMLS) for subarctic and arctic Snow Water Equivalent retrievals. *Water Resour. Res.* 48:W12524.

Langlois, A., Royer, A., Montpetit, B., Picard, G., Brucker, L., Arnaud, L., et al. (2010). On the relationship between measured and modeled snow grain morphology using infrared reflectance. *Cold Reg. Sci. Technol.* 61, 34–42.

Larue, F., Royer, A., De Séve, D., Roy, A., Picard, G., and Vionnet, V. (2018). Simulation and assimilation of passive microwave data using a snowpack model coupled to a calibrated radiative transfer model over Northeastern Canada. *Water Resour. Res.* 54, 4823-4848. doi: 10.1029/2017WR022132

Lesaffre, B., Pougatch, E., and Martin, E. (1998). Objective determination of snow-grain characteristics from images. *Anns. Glaciol.* 26, 112–118.

Matzl, M., and Schneebeli, M. (2006). Areal measurement of specific surface area in snow profiles by near infrared reflectivity. *J. Glac.* 52, 558–564.

Montpetit, B., Royer, A., Langlois, A., Cliche, P., Roy, A., Champollion, N., et al. (2012). New short wave infrared albedo measurements for snow specific surface area retrieval. *J. Glac.* 58, 941–952. doi: 10.3189/2012JoG11j248

National Oceanic and Atmospheric Administration [NOAA], (2017). *Global Climate Report - Annual, 2017*. Silver Spring, MD: NOAA.

Papasodoro, C., Berthier, E., Royer, A., Zdanowic, C., and Langlois, A. (2015). Area, elevation and mass changes of the two southernmost ice caps of the Canadian Arctic Archipelago between 1952 and 2014. *Cryosphere* 9, 1535–1550.

Picard, G., Arnaud, L., Domine, F., and Fily, M. (2009). Determining snow specific surface area from near-infrared reflectance measurements: numerical study of the influence of grain shape. *Cold Reg. Sci. Technol.* 56, 10–17.

Picard, G., Brucker, L., Roy, A., Dupont, F., Fily, M., Royer, A., and Harlow, C. (2013). Simulation of the microwave emission of multi-layered snowpacks using the Dense Media Radiative transfer theory: the DMRT-ML model. *Geosci. Model Dev.* 6, 1061–1078. doi: 10.5194/gmd-6-1061-2013

Picard, G., Sandells, M., and Löwe, H. (2018). SMRT: an active–passive microwave radiative transfer model for snow with multiple microstructure and scattering formulations (v1.0). *Geosci Model Dev.* 11, 2763–2788.

Prowse, T. D., Furgal, C., Melling, H., and Smith, S. L. (2012). Variability and change in the Canadian cryosphere. *Clim. Change* 115, 59–88. doi: 10.1007/s10584-012-0470-0

Roy, A., Picard, G., Royer, A., Montpetit, B., Dupont, F., Langlois, A., et al. (2013). Snow brightness temperature simulations driven by measurements of

the specific surface area of snow grains. *IEEE TGRS* 51, 4692–4704. doi: 10.1109/TGRS.2013.2250509

Royer, A., Roy, A., Montpetit, B., Saint-Jean-Rondeau, O., Picard, G., Brucker, L., et al. (2017). Comparison of commonly-used microwave radiative transfer models for snow remote sensing. *Rem. Sens. Environ.* 190, 247–259.

Schuur, E. A. G., McGuire, A. D., Schädel, C., Grosse, G., Harden, J. W., Hayes, D. J., et al. (2015). Climate change and the permafrost carbon feedback. *Nature* 520, 171–179. doi: 10.1038/nature14338

Serreze, M. C., and Stroeve, J. (2015). Arctic sea ice trends, variability and implications for seasonal ice forecasting. *Philos. Trans. R. Soc. London Ser. A.* 373, 20140159–20140159. doi: 10.1098/rsta.2014.0159

St-Pierre, M., and Thériault, J. M. (2015). Clarification of the water saturation represented on ice crystal growth diagrams. *J. Atmos. Sci.* 72, 2608–2611. doi: 10.1175/JAS-D-14-0357.1

Sturm, M., Perovich, D. K., and Holmgren, J. (2002). Thermal conductivity and heat transfer through the snow on the ice of the Beaufort Sea. *J. Geophys. Res.* 107:8043. doi: 10.1029/2000JC000409

Takala, M., Luojus, K., Pulliainen, J., Derksen, C., Lemmetyinen, J., Kärnä, J.-P., et al. (2011). Estimating northern hemisphere snow water equivalent for climate research through assimilation of space-borne radiometer data and ground-based measurements. *Remote Sens. Environ.* 115, 3517–3529.

Conflict of Interest: The authors declare that the research was conducted in the absence of any commercial or financial relationships that could be construed as a potential conflict of interest.

frontiers in Earth Science

ORIGINAL RESEARCH
published: 12 February 2020
doi: 10.3389/feart.2020.00023

Microstructure of Snow and Its Link to Trace Elements and Isotopic Composition at Kohnen Station, Dronning Maud Land, Antarctica

Dorothea Elisabeth Moser[1,2], Maria Hörhold[1], Sepp Kipfstuhl[1] and Johannes Freitag[1]**

[1] *Alfred-Wegener-Institut, Helmholtz-Zentrum für Polar- und Meeresforschung (AWI), Bremerhaven, Germany,* [2] *Institut für Geologie und Paläontologie, University of Münster, Münster, Germany*

Understanding the deposition history and signal formation in ice cores from polar ice sheets is fundamental for the interpretation of paleoclimate reconstruction based on climate proxies. Polar surface snow responds to environmental changes on a seasonal time scale by snow metamorphism, displayed in the snow microstructure and archived in the snowpack. However, the seasonality of snow metamorphism and accumulation rate is poorly constrained for low-accumulation regions, such as the East Antarctic Plateau. Here, we apply core-scale microfocus X-ray computer tomography to continuously measure snow microstructure of a 3-m deep snow core from Kohnen Station, Antarctica. We compare the derived microstructural properties to discretely measured trace components and stable water isotopes, commonly used as climate proxies. Temperature and snow height data from an automatic weather station are used for further constraints. Dating of the snow profile by combining non-sea-salt sulfate and density crusts reveals a seasonal pattern in the geometrical anisotropy. Considering seasonally varying temperature-gradient metamorphism in the surface snow and the timing of the anisotropy pattern observed in the snow profile, we propose the anisotropy to display the deposition history of the site. An annually varying fraction of deposition during summer months, ranging from no or negative deposition to large deposition events, leads to the observed microstructure and affects trace components as well as stable water isotopes.

Keywords: snow microstructure, anisotropy, snow metamorphism, deposition seasonality, microfocus X-ray computer tomography, Kohnen Station, Antarctica

OPEN ACCESS

Edited by:
Maurine Montagnat, Centre National de la Recherche Scientifique (CNRS), France

Reviewed by:
Jesper Sjolte, Lund University, Sweden
Neige Calonne, UMR 3589 Centre National de Recherches Météorologiques (CNRM), France

****Correspondence:***
Dorothea Elisabeth Moser
dorothea.moser@wwu.de
Johannes Freitag
Johannes.Freitag@awi.de

Specialty section:
This article was submitted to Cryospheric Sciences, a section of the journal Frontiers in Earth Science

Received: *28 July 2019*
Accepted: *24 January 2020*
Published: *12 February 2020*

Citation:
Moser DE, Hörhold M, Kipfstuhl S and Freitag J (2020) Microstructure of Snow and Its Link to Trace Elements and Isotopic Composition at Kohnen Station, Dronning Maud Land, Antarctica. Front. Earth Sci. 8:23. doi: 10.3389/feart.2020.00023

INTRODUCTION

Ice cores from polar ice sheets serve as climate archives and deep ice cores retrieved from Antarctica reveal a wealth of information on past climatic conditions (e.g. EPICA Community Members, 2006; Jouzel et al., 2007; Lüthi et al., 2008; Steig et al., 2013). Snow layers deposited on the ice-sheet's surface carry chemical and physical proxy information for atmospheric and environmental conditions of the time of their formation. Retrieving these climate proxies from ice cores allows to reconstruct past changes in earth's climate history from annual to glacial-interglacial time scales (e.g. Brook and Buizert, 2018; Münch and Laepple, 2018). More specifically, stable water isotopes

are a well-established proxy for past air temperature variations in Greenland (e.g. White et al., 1997; Vinther et al., 2010; Furukawa et al., 2017; Zheng et al., 2018) and Antarctica (e.g. Masson-Delmotte et al., 2008; Stenni et al., 2017). Composition and concentration of trace elements give insight into aerosol source areas, atmospheric circulation, and deposition processes (e.g. Legrand and Mayewski, 1997; Hoshina et al., 2016; Iizuka et al., 2016). Sodium has proven to be a reliable tracer of sea spray in a variety of studies from Dronning Maud Land, Antarctica (e.g. Sommer et al., 2000; Weller and Wagenbach, 2007), or Dome C, Antarctica (e.g. Wolff et al., 2010; Udisti et al., 2012). Sulfate concentrations in central Antarctica vary seasonally mainly due to varying aerosol fluxes from biogenic, volcanic and sea-salt emissions (e.g. Göktas et al., 2002; Iizuka et al., 2004; Kaufmann et al., 2010). The non-sea-salt fraction of sulfate is assumed to originate from marine, biogenic dimethylsulfide production (e.g. Legrand, 1995; Göktas et al., 2002).

Unbiased annually and seasonally resolved ice-core records rely on regular snow deposition, evenly distributed throughout the year (e.g. Jouzel et al., 1997). However, a reconstruction of seasonal cycles of ice-core proxies in low-accumulation regions such as the East Antarctic Plateau is impeded by precipitation intermittency (e.g. Helsen et al., 2005; Persson et al., 2011; Laepple et al., 2018), wind-driven redistribution of snow (e.g. Laepple et al., 2016; Münch et al., 2016), and interannual changes in the accumulation rate (e.g. Hoshina et al., 2014). Redistribution of the snow deposits, for example, causes mechanical mixing of trace elements in the snow (e.g. Jonsell et al., 2007; Hoshina et al., 2014). While the above processes hamper a continuous recording of all proxies over time, post-depositional firn diffusion (e.g. Johnsen, 1977), vapor exchange (e.g. Town et al., 2008; Ritter et al., 2016; Touzeau et al., 2016; Casado et al., 2018) or sublimation of surface snow (e.g. Ekaykin et al., 2002; Pang et al., 2019) can additionally alter original climate signals of stable water isotopes in the snow. Altogether, profiles of stable water isotopes and trace elements retrieved from the East Antarctic Plateau may display discontinuous records and do not necessarily represent the mean conditions during snowfall (e.g. Noone et al., 1999; Wolff et al., 2005; Kameda et al., 2008). A site-specific assessment of processes forming the proxy record is vital (e.g. Fujita et al., 2011; Hoshina et al., 2014).

The snow layers deposited on the ice sheet do not only record chemical constitutions of the atmosphere but also contain information on deposition and post-depositional processes in their microstructures (e.g. Palais et al., 1982; Alley, 1988; Groot Zwaaftink et al., 2013). Due to seasonally varying snowfall conditions, snow density can exhibit a seasonal pattern, when spatial variability is considered (e.g. Laepple et al., 2016; Schaller et al., 2016). Strong wind events can lead to high-density layers as tracers of dune formations (e.g. Birnbaum et al., 2010; Proksch et al., 2015). When snow surfaces are exposed to the atmosphere including wind polishing and insolation, thin crusts and glazed surfaces of high density form (e.g. Koerner, 1971; Fegyveresi et al., 2018).

In addition to density, the snow microstructure displays signatures from temperature-gradient metamorphism imprinted in different parameters such as grain size (e.g. Picard et al., 2012), specific surface area (e.g. Carlsen et al., 2017), or crystal fabric orientation (e.g. Calonne et al., 2017). Since air temperatures at the surface vary daily (seasonally), whereas snowpack temperatures change much slower at several centimeters (meters) depth, respectively, an alternating vertical temperature gradient is induced in the snow (e.g. Brun et al., 2011). This gradient leads to preferred vertical transport of water vapor within the snow, which imposes vertical anisotropy in the ice matrix and connected physical properties (e.g. Schneebeli and Sokratov, 2004; Calonne et al., 2014, 2017). Especially in the low-accumulation areas of the East Antarctic Plateau, the prolonged exposure times of surface snow to temperature gradients foster the formation of anisotropic structures like depth hoar (e.g. Mosley-Thompson et al., 1985; Courville et al., 2007; Hörhold et al., 2009).

To understand the formation of climate records based on the deposition history of snow layers containing proxies and to interpret ice-core-proxy records from East Antarctic sites, combined analyses of physical and chemical surface-snow parameters are essential (e.g. Palais et al., 1982; Hoshina et al., 2014). Here, we aim to reveal a detailed deposition history of a snowpack profile from Kohnen Station, Dronning Maud Land, Antarctica.

Kohnen Station is located in the Atlantic sector of the East Antarctic Plateau at 75°00′S 00°04′E (**Figure 1**). It lies 500 km off the coast at an elevation of 2892 m above sea level. The station was built as a summer station in 1998/99 during the European Project for Ice Coring in Antarctica (EPICA) and used as the logistic platform for the drilling of the deep ice core EDML (Drücker et al., 2002). Since it is situated about 10 km SW of an ice divide, the ice flows with low surface velocities of up to ∼1 m per year (Wesche et al., 2007).

An automatic weather station (AWS 9) provides detailed information about the weather conditions at Kohnen since the late 90s, including 2-m air temperature, wind speed, and snow

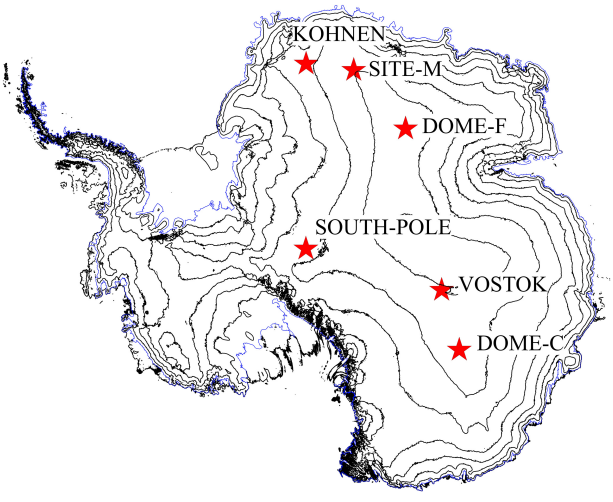

FIGURE 1 | Map of Antarctica including our study area and other ice-core drilling sites for comparison; elevation model according to Howat et al. (2019).

height (Reijmer and Van Den Broeke, 2003; Helsen et al., 2005). The summer 2-m air temperature varies between −16 and −36°C with pronounced diurnal cycles of −10 to −15°C, whereas winter temperature drops down to −70°C. However, warm low-pressure air masses interrupt the cold winter period and give reason for air temperatures up to −30°C. Generally, the region is characterized by light katabatic winds downslope the ice divide. These stable weather conditions are superimposed by near-coastal, synoptic developments that occasionally lead to strong wind events at Kohnen Station (Reijmer and Van Den Broeke, 2003). Wind speeds >10 m s^{-1} are associated with snowdrift and occasionally followed by dune formation (Birnbaum et al., 2010).

The accumulation rate, derived from firn core records, averages to 62 kg $m^{-2}a^{-1}$ over the last two centuries (Oerter et al., 2000). Medley et al. (2018) have documented a continuous increase to ∼75 kg $m^{-2}a^{-1}$ over the last 50 years. Compared to other sites on the East Antarctic plateau (**Figure 1**), this is relatively high accumulation. For example, it is two to three times higher than at Site M (36–53 kg $m^{-2}a^{-1}$, Karlöf et al., 2005), Dome C (∼25 kg $m^{-2}a^{-1}$, Stenni et al., 2016), Dome Fuji (27.3 ± 1.5 kg $m^{-2}a^{-1}$, Kameda et al., 2008), or Vostok (20–24 kg $m^{-2}a^{-1}$, Ekaykin et al., 2002; Touzeau et al., 2016). On the other hand, the accumulation rate at Kohnen Station is below ∼100 kg $m^{-2}a^{-1}$, which Hoshina et al. (2016) have proposed as lower resolution limit of seasonal cycles in major-ion and $\delta^{18}O$ profiles.

While the estimated accumulation rate is in the upper range found on the East Antarctic Plateau, the following studies indicate that processes related to low accumulation are highly relevant at Kohnen. Neighboring profiles of density and stable water isotopes are poorly correlated in the low-accumulation Kohnen area (Laepple et al., 2016; Münch et al., 2016). Surface roughness ranges in the same order of magnitude as accumulation rate (Laepple et al., 2016), and intermittent (re-) deposition (Helsen et al., 2005) as well as sporadic formation of barchan dunes have been reported (Birnbaum et al., 2010; Proksch et al., 2015). Further, Münch et al. (2017) showed in a trench study that the stable water isotopic record at Kohnen is decoupled from the local temperature, even after spatially averaging over several profiles.

In this study, we present a multi-parameter analysis of a top-3-m snow profile retrieved from Kohnen Station. We compare sub-millimeter-resolved microstructure records of density, crusts, and structural anisotropy with discrete measurements of sulfate, sodium, and $\delta^{18}O$ of the same profile as well as AWS 9 data. Our findings highlight the interplay of the (post-)deposition history of the snow and proxy signal formation at this low-accumulation site on the East Antarctic Plateau.

MATERIALS AND METHODS

Snow Sampling

In January 2015 during the Austral summer season, a 50-m long and 3.4-m deep trench (T15-1) was excavated and sampled for temporal and spatial analysis of stable water isotopes (Münch et al., 2017). The trench T15-1 was located about 500 m southeast of the EDML deep-drilling site. Snow sampling for the present study was performed in the undisturbed snowpack at the first sampling position (0 m) of T15-1, a few centimeters next to the sampling of Münch et al. (2017). To retrieve a 3-m profile of snowpack, three carbon-fiber tubes (liners) of 1 m length, 10 cm diameter, and 0.1 cm wall thickness were carefully pushed into the snow. After each push, we checked that snow surfaces inside and surrounding the liner were consistent to guarantee sampling without compression. The second and third meters were sampled on freshly prepared surfaces 10 cm laterally displaced to the former liner positions without vertical overlaps. Then, the snow-filled liners were cut out sideward from the trench wall. We sealed their top and bottom faces with plastic bags and stored them in isolated transport boxes. At the end of the summer field season, the frozen samples were shipped home, stored at −28°C and analyzed in the cold lab at AWI, Bremerhaven, in April–May 2016.

Core-Scale Microfocus X-Ray Computer Tomography

First, the snow filled liners are non-destructively analyzed by the means of a core-scale microfocus X-ray computer tomograph (ice-μCT). The device is specially designed for ice core applications and methodologically based on microfocus X-ray computer tomography (Freitag et al., 2013). It is placed in a radiation-protected walk-in cold lab at −14°C so that no additional construction is needed to keep the sample frozen during the measurements. Main components of the ice-μCT are a 140 kV X-ray source, a rotation desk with a sample holder and a 20 × 40 cm detector unit operating in fourfold-binned mode with 1000 × 2000 pixels in this specific application. All components are mounted on movable axes placed on air bearings. Spindle positioning allows the control of lateral and vertical movements of source and detector with displacements of up to 1.1 m traverse path. To avoid damage and to hold the snow core vertically aligned on the sample stage, the snow is kept inside the liners.

Density

The 2D density profile is generated with the ice-μCT operating in fly-by-mode. Thereby, radioscopic images are continuously captured during a synchronous upward movement of X-ray source and detector from bottom to top along the vertical axis of the snow-liner. The recorded stack of ∼2000 images provides information on integrated X-ray attenuation over beam paths with different off-axis angles through the snow sample. We use only the centerlines and the two adjacent pixel lines from each image to generate an image composite. It compiles the X-ray attenuation in horizontal layers with a vertical resolution of 110 μm. Aiming to transfer X-ray attenuation to density information, we measure the attenuation of pure ice blocks with defined dimensions at the start of every snow-scan (Freitag et al., 2013). The replicate calibration takes into account instability plus aging of the X-ray source and improves the accuracy of the density estimates. In fact, the averaged densities of the ice-μCT profiles differ only ± 5 kg m^{-3} from bulk densities based on weight and volume with the same uncertainty band. Since the first

0.1 m of the upper liner filled with drifting snow during trench sampling, this section is not representative for the microstructure record.

Structural Parameters

All structural parameters are derived from 3D-volume reconstructions of the snow liners. For this, we perform ice-μCT measurements in a helical scan mode especially developed for vertically aligned objects like snow or ice cores. Starting at the top of the sample, X-ray source and detector move downward in a stop-and-go mode while the sample rotates stepwise. During conventional CT measurements, the sample rotates 360° before source and detector positions change. Comparing these 3D measurement set-ups, the helical mode avoids cone-beam artifacts leading to depth-dependent segmentation errors. For a full 3D reconstruction of one snow liner, a series of ∼35,000 images is taken. Its spatial resolution is 57 μm in lateral and vertical direction. The reconstructed volume image is segmented in ice and air fraction using an Otsu-threshold after smoothing with a 3 × 3 × 3 median filter (Otsu, 1979). A comparison of the 3D and 1D density shows only slight deviations <10 kg m^{-3} for all available depth intervals and confirms the accuracy of image segmentation. Subsequently, 3D structural parameters are derived from a running volume window of 1000 × 1000 × 77 voxels, corresponding to 5.7 × 5.7 × 0.44 cm in size. After the measurement campaign, we realized that the oversized tube holder in the beamline had reduced image quality in the lower 0.2 m of each snow core. Thus, we excluded these depth intervals from the analysis.

Detection of Crusts

Crusts are thin layers of heavily sintered grains. They are one-tenth of a millimeter thick, which is of the order of the diameter of one grain. In principle, they are visible as density peaks in a density profile with 110 μm vertical resolution. However, not all crusts lie perpendicular to the vertical axis and therefore are hard to detect as sharp spikes in the density profile. To account for their irregular shape, we additionally inspect the segmented 3D volume reconstructions. We visually check each layer for localized, dense ice clusters embedded in a regular pattern of the porous ice matrix. If such an anomaly extends in adjacent layers over the entire horizontal area, the feature is defined as a crust.

Mean Chord Length and Geometrical Anisotropy

The mean chord length (MCL) of the ice matrix is defined as the mean over all intersections of an object within a volume along a certain direction. Here, we calculate the MCLs of the ice phase in two horizontal directions (MCL_X, MCL_Y) and in vertical direction (MCL_Z) within a running volume window of 5.7 × 5.7 × 0.44 cm along the snow profile. The upper limits for $MCL_{X,Y,Z}$ are the window dimensions with the lowest bound of 0.44 cm in z-direction. All truncated chord lengths with direct contact to the border faces of the running window are not considered. Horizontal directions are arbitrary directions. The calculated values are assigned to the mean depth of the running volume window. Note that CT reconstructions are not able to resolve grain boundaries, and chord lengths are not strictly synonymous with grain or crystallite size dimensions (Freitag et al., 2008).

In this study, we define geometrical anisotropy a as a ratio between the horizontal and the vertical MCL. Thereby, we use the mean of MCL_X and MCL_Y as the best estimate for the horizontal chord length. Then, geometric anisotropy a can be calculated using

$$a = \frac{MCL_x + MCL_y}{2 \times MCL_z}$$

A value of $a = 1$ means that the ice matrix of the snow is geometrical isotropic in horizontal and vertical direction. A value of $a > 1$ refers to a horizontally elongated ice matrix, a value of $a < 1$ points to a vertically elongated ice matrix. Vertically elongated structures are expected in snow affected by vertically oriented temperature-gradient metamorphism. We note that this calculation of anisotropy differs from previous studies (e.g. Löwe et al., 2013; Calonne et al., 2014), in which a is the vertical component over the horizontal one.

Discrete Measurements of Stable Water Isotopes and Trace Components

In order to measure impurities and isotopic composition, the core is cut into discrete samples at an interval of 1.1 cm. We stabilize the core segments in a stainless-steel trough and sequentially cut samples with a ceramic knife. While the knife transects the snow, we extract inner sample material by screwing in a bottle of 6.3 cm diameter. Due to the brevity of contact with ambient air, this inner part is considered uncontaminated. A range of ion concentrations is measured by means of ion chromatography (Thermo Fisher Scientific Co., ICS2100).

Here, we specifically focus on sodium and sulfate. Based on their concentrations, we compute the non-sea-salt sulfate (nss-SO_4^{2-}) fraction by subtracting the sea salt contribution from bulk sulfate concentration (Göktas et al., 2002).

$$[\text{nss-}SO_4^{2-}] = [SO_4^{2-}] - 0.252 \times [Na^+]$$

The outer part of the snow samples is analyzed regarding stable water isotopic composition by means of cavity ring-down spectroscopy (Gupta et al., 2009), using commercially available Picarro instruments. The data are calibrated against in-house standards and corrected for memory effects as well as drift during measurements (Van Geldern and Barth, 2012). The measurements are reported against the international standard of Vienna Standard Mean Ocean Water (V-SMOW). The precision is in the range of 0.1‰ for $\delta^{18}O$.

Temperature and Snow Height Data From AWS 9

We use the 2-m air temperature record of the weather station AWS 9, 500 m northwest of our sampling site, to derive daily temperatures and temperature gradients, i.e. the difference between daily temperature minimum and maximum. The snow height sensor record is analyzed for relative changes in the surface height. Thereby, a decreasing distance between the

sensor and the snow surface implies deposition. The annual change in height is fitted linearly and counted as cumulative deposition at the surface. In this study, we specifically assess the fraction of deposition over the summer season. In this regard, we define a narrow 4-month summer window from November to February and a broader 6-month summer period from September equinox to March equinox, respectively. Snow height changes within these intervals are hereafter referred to as summer deposition. In order to determine the expected summer deposition, we assume equally distributed deposition throughout the year, calculate the portion of total annual deposition for each month, and subsequently compute the four-fold and sixfold portion, respectively. Afterward, we compare observed changes in snow height during summer months to the expected summer deposition. If the observed fraction of deposition matches the expected deposition, the ratio equals 1. If less (more) deposition is observed than expected, the ratio is smaller (larger) than 1.

RESULTS

Physical Properties and Features of the Profile

Density

The density profile of the uppermost 3-m snowpack at Kohnen Station is characterized by strong variations (**Figure 2A**). Single values range between 250 and 450 kg m^{-3}. The snowpack is composed of cm-thick layers, each displaying a specific density value. The differences in density between adjacent layers range between 50 and 100 kg m^{-3}. The liner average density values rise from 366 kg m^{-3} (liner 1) to 394 kg m^{-3} (liner 3). This overall increase of 30 kg m^{-3} is smaller than the observed changes among adjacent layers, indicating that the compaction within the first 3 m is negligible in comparison to the inter-layer variations on a cm scale.

Crusts

Crusts are evident as sharp high-density peaks on a sub-millimeter scale (**Figure 2A**). In total, we counted 75 crusts in both the 1D and 3D reconstruction and indicate them as vertical lines in **Figure 2**. Extent and tilt of such crusts are visible in the 3D volume reconstruction (**Figure 3**). They often appear in close conjunction with thin layers of very low density. Approximately 40% of the detected crusts cluster in multi-crust sections, which appear localized in 10–12 horizons throughout the profile.

Layer Thickness

We find the cm-thick layers in the density record to be typically separated by crusts (**Figure 2A**). Therefore, we use crusts to separate single (density) layers and derive the thickness of the deposits. Our layer separation technique by the means of crusts is independent of absolute density values and avoids the arbitrary definition of thresholds as separation markers. The resulting frequency distribution of layer thickness, given as the distance between two adjacent crusts, is displayed on a logarithmic scale (**Figure 4**). The layer thickness distribution follows roughly a bimodal distribution, separating sections with multiple thin crusts on the left-hand side from a thickness distribution of layers without intersecting crusts on the right-hand side (**Figure 4**). Both distributions are fitted by Gaussian functions. A small contribution of extraordinary large layer thickness at the upper tail of the latter distribution is excluded from the Gaussian fits. We interpret these few sections as layers not confined by crusts but differing levels of density. The layer thickness distributions for the multi-crust layers center at 0.8 cm and 68% of the layers range between 0.2 and 3 cm. For deposited layers with defined single crusts as borders, the median lies at 4 cm with 68% ranging between 2 and 9 cm. Since the local accumulation rate of 70–80 kg $m^{-2}a^{-1}$ equals ∼20 cm of snow per year, the derived mean layer thickness of 4 cm snow implies that the snow at Kohnen Station is deposited during five to six events per year, i.e. the snow profile consists of event-based deposits like at 0.24–0.54 m depth (**Figure 2A**). However, we note that deposition is not equal to precipitation.

Mean Chord Lengths

The MCLs MCL_X, MCL_Y, and MCL_Z increase from ∼300 to ∼600 μm in the uppermost meter (**Figure 2B**) and then remain approximately constant until 3 m depth. The record shows a recurring pattern of sharp increases in MCL followed by a steady decline, for example, at 0.24–0.54 m depth. In the following, we refer to this pattern as saw-tooth pattern. It is more pronounced in the vertical MCL_Z than in the other two directions, with a mean offset of 75 μm and the largest difference just after each sharp increase. In the uppermost meter, for example at 0.24–0.54 m depth, this MCL pattern is by no means visible in the density data. In the third meter, however, one can observe a gradual increase in density in parallel with a decrease in MCL, e.g. at 2.28–2.50 m depth.

Anisotropy

The geometric anisotropy record of the ice matrix starts with values around 1, indicating isotropic snow at the surface (**Figure 2C**). Below, we find the saw-tooth pattern introduced by a varying difference between vertical and horizontal MCL values. The first saw tooth begins 0.1 m below the surface with an abrupt drop to 0.85, a moderate vertical anisotropy. This jump is followed by a smooth increase with depth, until it reaches values of $\geq$1 in a thin layer. The saw-tooth pattern is repeated three times within the first meter of the profile and recurs at 1.4–1.6 and 2.3–2.5 m depth (**Figure 2C**). Thereby, the vertical extent of the saw tooth ranges from 0.10 to 0.25 m, and minor substructures exist, for example, at 0.52–0.7 and 2.37–2.52 m depth. At 1.1–1.4 and 1.6–1.8 m depth, the anisotropy stays at almost constant values. Apart from a thin layer at 0.23 m depth, the anisotropy values are <1 throughout the profile and result from vertically elongated structures of the ice matrix.

Chemical Properties of the Profile

Sulfate concentration varies periodically between a base level of nearly 40 ppb and peaks up to 115 ppb throughout the profile (**Figure 2D**). Between 14 and 17 peaks can be counted. Most of them have a broad base, but some rise sharply or display double peaks. We find sulfate peaks linked with the sharp

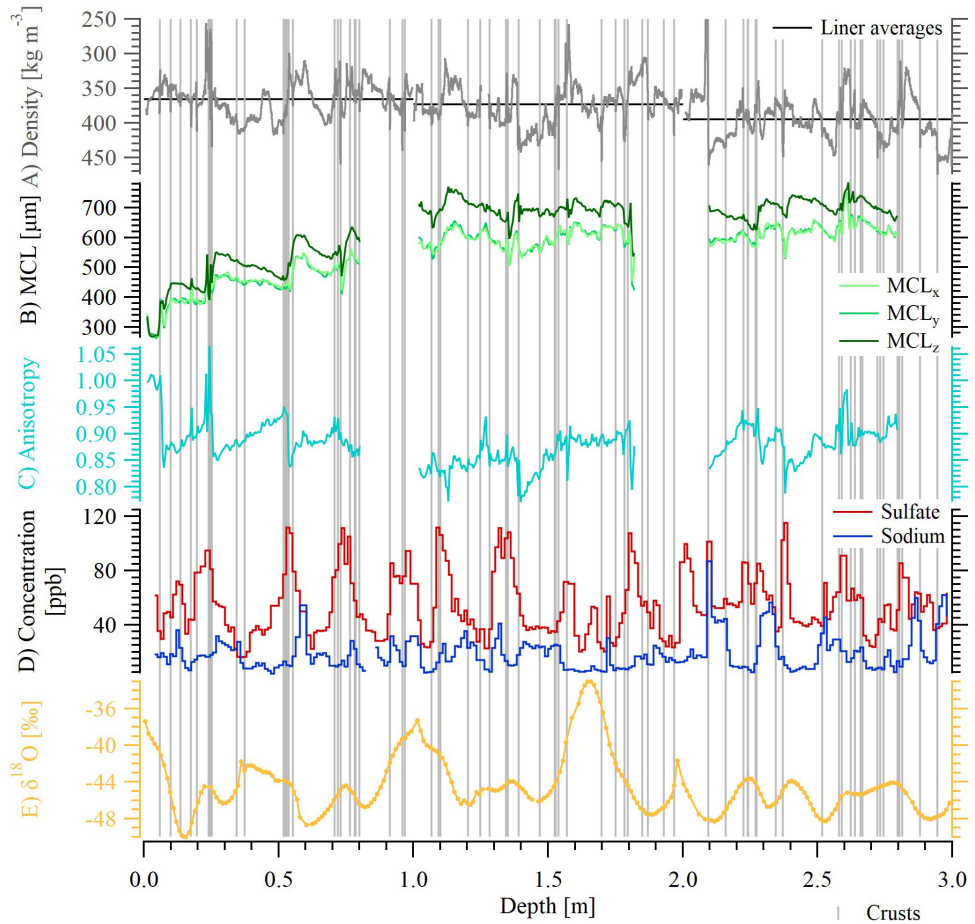

FIGURE 2 | Microstructure, trace elements, and isotopic composition displayed against depth from the single snow profile near Kohnen Station. **(A)** Density retrieved from a 2D radioscopic scan composite, and liner averages, note the reversed axis. **(B)** Mean chord lengths along *x*-, *y*-, and *z*-axis (MCL$_X$, MCL$_Y$, MCL$_Z$) of the ice phase based on a 3D volume scan, color code according to the legend. **(C)** Geometric anisotropy based on a 3D volume scan and derived from MCL. **(D)** Total sulfate (red) and sodium (dark blue) concentrations from discrete measurements. **(E)** Stable water isotopic δ^{18}O measured discretely; surface crust positions are indicated by light gray markers.

jumps in anisotropy and crust positions, for example, at 0.53 m depth. The nss-SO_4^{2-} record closely resembles the behavior of bulk sulfate.

Sodium concentrations range between minimum 4 and 40 ppb. The mean concentration is 20 ppb (**Figure 2D**). Intervals of minor and higher sodium concentration alternate continuously. Some sodium intervals like at 2.2 m depth are bounded by distinct concentration changes. The vertical extent of specific sodium concentration values tends to correlate with (density) layers as defined from the crust profile (**Figures 2A,D**). For example, homogeneously elevated sodium concentrations at 1.4–1.54 m depth are abruptly taken over by a depleted sodium plateau at 1.54–1.71 m depth. These sodium signals correspond two intervals of increasing and decreasing density at the according depth.

The values of δ^{18}O range between −50 and −33‰ with a mean of −44‰ (**Figure 2E**). We identify 12 ± 1 cycles in the snow profile. As displayed at 1.2–1.4 and 2.6–2.8 m depth, some of them are of small amplitude and occur as double peaks. Prominent high and broad peaks exist around 1.0 and 1.7 m depth.

Air Temperatures and Summer Deposition

Based on mean daily temperatures measured over the period from the year 2000 to 2015, the average annual cycle ranges from −24°C in summer to −50°C in winter (**Figure 5**). Even temperatures down to −70°C are common during winter. Temperature differences between day and night in the range of 10–15°C occur in spring and autumn, when the sun warms the air during daytime, but the low angle of the sun causes cold nights.

The annual snow height change averages 22.5 cm over the entire observation period 2000–2015. Thus, 7.5 cm snow and 11.25 cm snow are expected during the 4-month and 6-month summer season, respectively. However, the fraction of deposition derived from the snow height sensor reveals inhomogeneous deposition of snow during the summer months (**Figures 6**, **7D**).

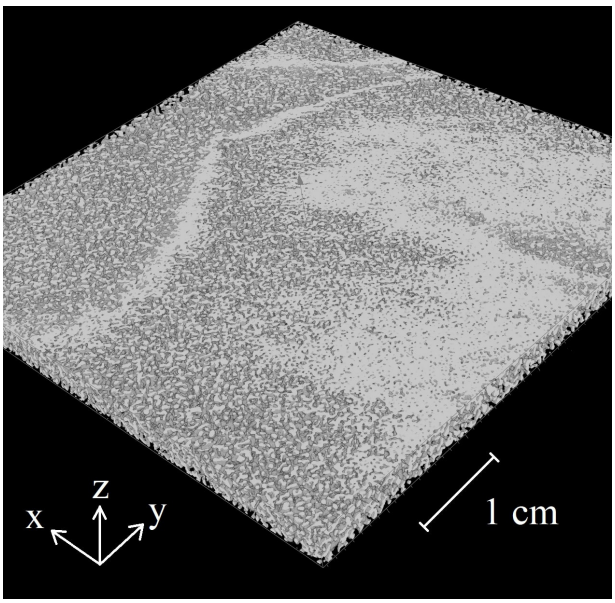

FIGURE 3 | 3D section of a crust at ~0.26 m depth; color code: white = ice, black = air.

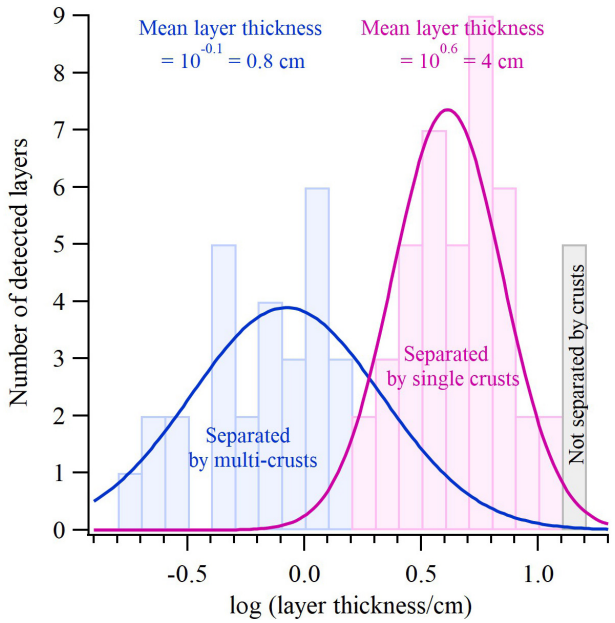

FIGURE 4 | Bimodal Gaussian distribution of logarithmic layer thickness for the deposited layers of the snow profile near Kohnen Station; the mean layer thickness in multi-crust-clusters centers at 0.8 cm; layers confined by single crusts have an average thickness of 4 cm; sections separated by changes in density but without internal crusts lie at the top tail of the Gaussian distribution.

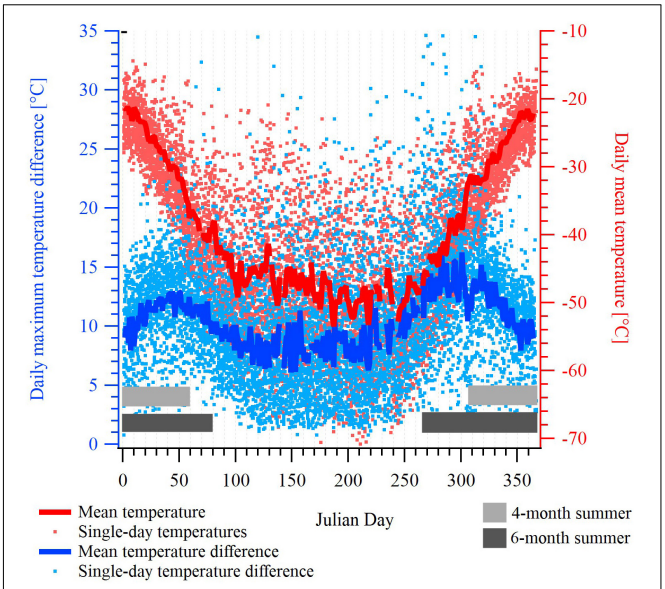

FIGURE 5 | Daily air temperature measurements of the years 2000–2015 (red dots) derived from AWS 9 and averaged to obtain an average annual cycle (red thick line); the difference between daily minimum and maximum temperature was calculated accordingly (blue); gray bars indicate a narrow, 4-month and a broader, 6-month summer period for summer deposition evaluation below (see text), color code according to the legend.

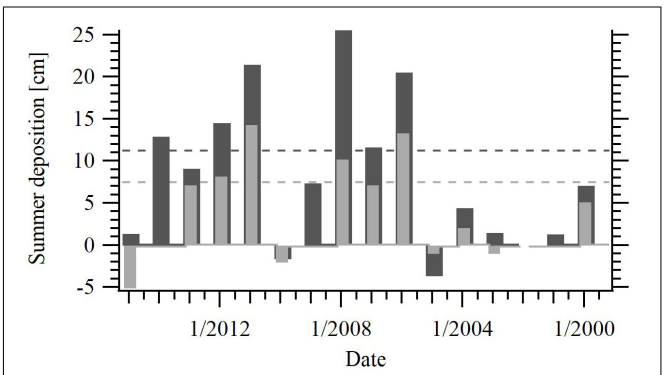

FIGURE 6 | Summer deposition of the years 2000–2015 derived from the AWS 9 snow height sensor displayed against time; dashed lines indicate the expected summer deposition, bars show the observed summer deposition; color code: light gray = 4-month summer period November–February, dark gray = 6-month summer period from September equinox to March equinox.

In the Austral summers 2005–2006, 2007–2008, and 2010–2011, more deposition than expected was recorded at the AWS 9. In other years, like 2002–2005, 2009–2010, or 2013–2015, the site experienced much less deposition or even erosion during the summer months. Assuming uniform deposition throughout the year, the 4-month summer period receives on average 52% and the 6-month summer half-year 74% of the deposition expected. Though we note that the AWS snow height sensor is only a point measurement and lacks information about the spatial variability of deposition, it gives evidence for a trend of weaker summer deposition.

Dating

In order to date the snow profile, we combine nss-SO_4^{2-} concentration and surface crust positions (**Figure 7**). We

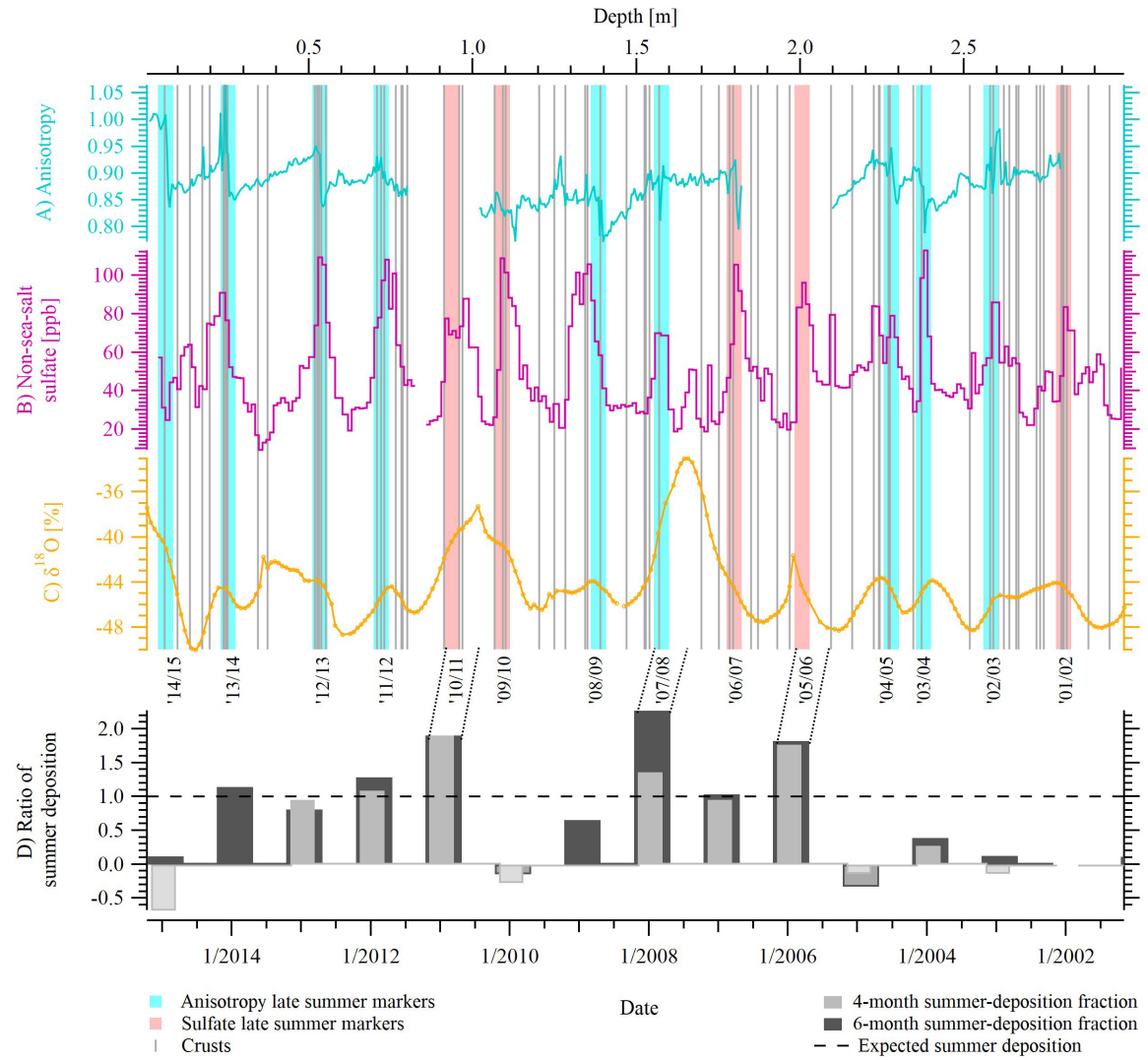

FIGURE 7 | Comparison of **(A)** geometric anisotropy, **(B)** non-sea-salt sulfate, and **(C)** stable water isotoe $\delta^{18}O$; summer markers are based on seasonality in geometric anisotropy and completed using sulfate peaks; **(D)** ratio between expected and observed snow accumulation during the 4-month and 6-month summer period derived from AWS 9; color code according to legend.

interpret nss-SO_4^{2-} peaks as a late summer-to-fall signal because atmospheric nss-SO_4^{2-} concentration at Kohnen Station peaks in summer, January–February (Piel et al., 2006; Weller and Wagenbach, 2007), whereas elevated nss-SO_4^{2-} concentration in ice cores are markers of fall (Göktas et al., 2002). Following previous studies on the East Antarctic Plateau (Koerner, 1971; Ren et al., 2004; Hoshina et al., 2014), density crusts were applied as summer markers, because strong solar insolation during this season fosters their formation. Based on the agreement of these two parameters, we identify 14–15 summer layers in our snow profile, and the snow profile covers the period from 2002 until 2015 (**Figure 7**). Comparing our dating approach with the anisotropy record, we find the jumps in anisotropy to coincide with summer-to-fall markers of crusts and nss-SO_4^{2-} peaks throughout the profile (**Figure 7**).

DISCUSSION

Seasonal Anisotropy and Deposition

The observed co-variation of microstructural anisotropy with the peaks of nss-SO_4^{2-} and crusts implies a seasonal pattern in the snow microstructure. Here, we discuss possible reasons and mechanisms for the repeated formation of microstructural anisotropy and its saw-tooth shape.

Previous studies have shown that vertical anisotropy in the snowpack results from temperature-gradient metamorphism (Srivastava et al., 2010; Calonne et al., 2017). The effective heat conductivity of snow results from several aspects such as structure, density, history of the snow pack, and applied temperature (Satyawali et al., 2008; Calonne et al., 2019). The latter varies on a daily and seasonal time scale as recorded by

the AWS (**Figure 5**). Accordingly, a macroscopic temperature gradient persists in the snow column (Picard et al., 2012; Pinzer et al., 2012; Calonne et al., 2014), which can be as high as 25–50°Cm^{-1} on a daily time scale. Such conditions are similar to gradients applied in laboratory experiments (Pfeffer and Mrugala, 2002; Riche et al., 2013), leading to a gradual formation of chain-like structures in vertical direction and depth hoar.

In order to explain the observed saw-tooth-shaped anisotropy profile, a snow layer must be exposed to a persistent temperature gradient over a certain period. Then, the impact of the gradient and the formation of anisotropy is strongest at the surface and penetrates deeper into the snowpack with decreasing strength (e.g. Colbeck, 1989; Picard et al., 2012; Calonne et al., 2014), leading to the observed gradual decrease with depth. Since we find surface crusts, formed by sun radiation and wind polishing in times of non-deposition (e.g. Gow, 1965; Koerner, 1971), clustered in depth intervals of strongest anisotropy, we suggest that, while the gradient is applied to the snowpack, no new deposition is added on top. The sharp drop in anisotropy, indicating an interruption of the previous temperature-gradient regime, could be a combination of decreased water vapor pressure, i.e. a temperature decrease toward the end of summer, and new snow on top.

With respect to the timing of the repeated anisotropy formation, we note that the intensity of metamorphism depends on both the ambient temperature and the diurnal gradient (Colbeck, 1989; Fukuzawa and Akitaya, 1991; Kamata et al., 1999). While absolute temperatures at Kohnen Station are highest during summer and enable larger water-vapor-pressure gradients in the snowpack, gradients are strongest during spring and autumn (**Figure 5**). Thus, anisotropic growth could occur from spring to autumn, depending on when the snow is exposed at the surface over a longer period. At the South Pole, anisotropic depth hoar has been designated as stratigraphic marker of late summer to autumn (Gow, 1965; Koerner, 1971). Considering the overall warmer mean air temperatures during summer and the observed large gradients in the spring and autumn, the conditions favoring enhanced temperature-gradient metamorphism at Kohnen appear in the summer months.

The repetitive saw-tooth pattern in anisotropy indicates not only periodic conditions favoring metamorphism but points to the daily gradient as reason for anisotropy formation. A saw tooth with the observed, vertical extent of 0.1–0.25 m can result from the limited penetration depth of the daily gradient and solar radiation (Colbeck, 1989). Furthermore, the saw-tooth pattern imprinted at the surface would probably experience modification, if enhanced temperature-gradient metamorphism took place at greater depth due to a seasonal-induced gradient. However, we also find the pattern at depths of 1.4–1.6 and 2.3–2.5 m.

We hypothesize that the formation of the observed anisotropy pattern is related to inhomogeneous deposition in summer, i.e. precipitation intermittency. Arguments are (a) the dating, where we find peak anisotropy to coincide with summer-to-fall peaks in nss-SO_4^{2-} and clusters of crusts, (b) the combination of highest mean air temperatures and strong gradients favoring grain growth in summer to fall, and (c) the irregular summer deposition derived from AWS 9: We find sometimes very reduced or even negative amount of deposition, i.e. erosion. On the other hand, we find years with higher-than-expected values of summer deposition, such as in the summers 2007/2008 and 2010/2011 (**Figures 6**, **7D**). In the snow profile, these years can be linked to depth intervals with homogenous anisotropy lacking a saw tooth, comparably high $\delta^{18}O$ values, and lower nss-SO_4^{2-} concentrations with multiple peaks (**Figure 7D**).

From AWS 9 data, we know that no or negative deposition over the entire summer is only an extreme case of the trend to weaker summer deposition. Considering the case of occasional summer deposition, the initial anisotropy of the surface snow is low but develops faster than the anisotropy of the overburden snow. Thus, summer snow can reach the same anisotropy values after a certain time of exposure. We note that, in order to generate a steady saw-tooth pattern over all summer snow layers, exposure time and strength of temperature-gradient metamorphism must be balanced. Otherwise, the anisotropy profile shows a more step-like, sub-structured behavior. Since our anisotropy profile exhibits minor substructures in the saw-tooth pattern at 0.52–0.72 and 2.37–2.52 m depth, it permits such an interpretation. Altogether, we propose that the development of a saw tooth points to phases of non-deposition, as the combined observation of microstructure, impurities, crusts, and AWS allows of such hypothesis.

Besides a formation during discontinuities in precipitation, the saw-tooth pattern in anisotropy can also develop in consequence of surface undulations. Wind-induced dune layers are exposed at the surface even after new snowfall fills up the intermediate troughs. Consequently, surface snow exposure to temperature gradients is prolonged and may generate a saw tooth in anisotropy. This additional formation factor cannot be neglected because dune formation is evident at Kohnen Station, and the spatial variability of accumulation on the East Antarctic plateau is large (Frezzotti et al., 2005; Fujita et al., 2011).

Implications for Chemical Proxies

Considering the discontinuous character of snow deposition at our site and the observed tendency for decreased summer deposition, we can evaluate not only the derived microstructure but also the impurity concentration profiles in the snowpack. We here do not intend to discuss fluxes of aerosols to the snow but discuss the deposition history of trace component concentrations and what we can learn about deposition mechanisms.

As sulfate peaks go along with surface crusts and jumps of anisotropy in this profile (**Figures 2**, **7**), sulfate and nss-SO_4^{2-} concentrations could be related to the deposition conditions at the end of summer. The peak found in the summer-to-fall transition is then related to the deposition of new snow after a deposition-free period, i.e. it cumulates in the new snow. This could either indicate increased atmospheric concentrations during summer, which are just collected within the snow of the late summer-to-fall deposition, or it indicates a seasonal peak of sulfate in the fall rather than summer, which is directly displayed in the snow profile. At Dome Fuji, Iizuka et al. (2004) demonstrated non-sea-salt sulfate minima during summer and proposed a diurnal sublimation-condensation

mechanism as explanation. However, this mechanism has not been observed at Kohnen Station so far. To disclose the enrichment process of sulfate in the surface snow at Kohnen Station, a timely resolved analysis of the exact timing of the sulfate with respect to the microstructure is necessary. However, its cannot be retrieved at this point due to the discrete, vertical sampling resolution of 1.1 cm, the ± 1 cm uncertainty in depth assignments, and the sub-millimeter dimensions of crusts.

Since plateaus with homogeneous sodium concentration record are frequently linked to the extent of (density) layers (**Figure 2**), we propose that specific (density) layers carry a specific chemical load. This load depends on their deposition in consequence of precipitation or wind-driven redistribution (Groot Zwaaftink et al., 2013; Hoshina et al., 2014). Combined analyses of density and sodium concentration could therefore help to distinguish whether a snow record displays a deposition history based on few-events-only or a continuous deposition throughout the year.

The stable water isotope record seems to be affected by the proposed precipitation intermittency (this snow profile, and Münch et al., 2017). For example, in the years 2003–2005, 2008–2009, or 2009–2010 with little-to-no summer deposition, we find depleted $\delta^{18}O$ signatures during summer. Complementary, we observe less depleted $\delta^{18}O$ values in the years 2007–2008 and 2010–2011 with larger summer deposition, supporting the AWS-derived finding of more, warmer summer snow deposition in these years. Indeed, warm temperature periods during synoptic events are associated with increased amounts of precipitation (Helsen et al., 2005). This indicates that the retrieved stable water isotope record and the related annual mean values from Kohnen Station could be dominated by few deposition events.

Among other processes affecting the isotope records in East Antarctica (Neumann et al., 2005; Town et al., 2008; Hoshina et al., 2014; Ritter et al., 2016; Casado et al., 2018; Laepple et al., 2018), the here derived precipitation intermittency could partly explain the previously observed decoupling of $\delta^{18}O$ from the annual mean air temperature record (Münch et al., 2017).

Comparison of Accumulation Rate and Precipitation Intermittency to Previous Studies

Comparing our findings to previous meteorological studies at Kohnen Station, our dating approach leads to 4–5 years per meter and confirms recent accumulation-rate estimates of 0.2–0.25 m of snow per year (Medley et al., 2018). In greater detail, Reijmer and Van Den Broeke (2003) stated that both small snowfall events of 1–2 cm thickness and synoptic precipitation >5 cm contribute to the annual accumulation at the site. Our bimodal distribution of layer thickness, centering at 0.8 and 4 cm, also suggests two modes of accumulation (**Figure 4**). With approximately five (density) layers per year, our microstructure profile resembles previous estimates of three to five synoptic snowfall events per year (Noone et al., 1999; Birnbaum et al., 2006; Schlosser et al., 2010). However, the number of layers could also originate from post-depositional redistribution. Synoptic snowfall conditions in conjunction with wind can lead to dune formation, and Birnbaum et al. (2010) suggest an annual frequency of three to eight dune formation events of 4 ± 2 cm each. For now, a discrimination between deposition of layers resulting from precipitation and layers resulting from wind-redistribution remains unclear in our density profile.

On the other hand, the expression of a precipitation or deposition intermittency in the Kohnen area, appearing in snow microstructure and proxy concentration variations measured in the snow, has not been documented yet. Previous studies of Reijmer and Van Den Broeke (2003) and Helsen et al. (2005) have discussed both against and for a seasonality of precipitation around the Kohnen Station, respectively. Thus, our seasonal interpretation of the repeated anisotropy saw-tooth remains controversial, even though it agrees with AWS data and field observations of S. Kipfstuhl throughout the last 15 years.

Comparison to Other Sites

In this study, we applied the combination of non-sea-salt sulfate, typically used at high-accumulation sites (Minikin et al., 1998), and surface crusts, previously used at low-accumulation sites like the South Pole (Gow, 1965; Koerner, 1971), to date the snow profile. In contrast to findings of Hoshina et al. (2014) at Dome Fuji, the crust record at Kohnen Station alone is not unambiguous, but multi-crust layers are concentrated in depth intervals of large non-sea-salt sulfate and anisotropy (**Figure 7**). This illustrates that Kohnen Station is not typical for the East Antarctic Plateau, but that its annual accumulation rate at the upper end of the low-accumulation range allows for distinct snow characteristics (Hoshina et al., 2016). Transferring our interpretation of anisotropy to other sites on the East Antarctic Plateau is challenging because most of them receive even less accumulation than Kohnen Station, and the temporal and spatial variability of precipitation is large (Ekaykin et al., 2002; Kameda et al., 2008; Stenni et al., 2016). Longer exposure times at the surface could amplify the impact of temperature-gradient metamorphism at other sites. However, anisotropic structures may be readily destroyed, if snow deposits persistently undergo wind redistribution. Whether microstructural anisotropy develops and is preserved under various environmental conditions on the East Antarctic Plateau needs site-specific investigation.

CONCLUSION

With this study, we aim to give insight into the deposition history of the East Antarctic snowpack near Kohnen Station and to better understand the processes shaping climate proxy records in ice cores from sites with low to moderate accumulation rates. Therefore, we have performed combined measurements of microstructure, trace elements, and stable water isotopes on a 3-m snow core retrieved at Kohnen Station and

used meteorological data from AWS 9. A very prominent feature of the microstructure profile is the recurring saw-tooth pattern in geometric anisotropy formed by (daily) temperature-gradient metamorphism. Combining the microstructural record with chemical and meteorological information, we draw the following conclusions: (1) the anisotropy saw-tooth develops seasonally and confirms a summer-to-fall dating approach based on nss-SO_4^{2-} concentration and clusters of surface crusts at Kohnen Station; (2) snow microstructure indicates deposition intermittency with an underrepresentation of summer snow, which is supported by snow height measurements of the automatic weather station; and (3) summer deposition intermittency strongly affects the interpretation of climate proxy parameters: it determines the recording of sulfate and sodium in the snow deposits in various ways, and stable water isotopes show a systematic bias toward the winter season or interannual variations decoupled from climatic changes. After all, this multi-parameter study discloses a yearly resolved record instead of a solely layered snowpack. To elaborate the site-specific potential of snow-microstructure information for the interpretation of climate proxy records at other East Antarctic sites, further investigations in low-accumulation areas will be necessary. The quantification of deposition hiatus based on microstructure would be of particular interest because years of missing snow are difficult to judge so far.

DATA AVAILABILITY STATEMENT

$\delta^{18}O$, trace element profiles and the derived microstructure data will be made available in the PANGAEA data library. Raw CT data of this article will be made available by the authors to any qualified researcher. Requests to access the datasets should be directed to JF.

AUTHOR CONTRIBUTIONS

SK, JF, MH, and DM conceptualized the study. DM and JF conducted the ice-μCT measurements. DM, JF, and MH contributed to the interpretation of the results and wrote the first draft of the manuscript. All authors contributed to the manuscript revision and read and approved the submitted version.

ACKNOWLEDGMENTS

We thank the reviewers for their constructive comments, which have improved our manuscript substantially. We also thank C. Reijmer for providing daily data from AWS 9, which is operated by the University of Utrecht. Furthermore, we want to thank B. Twarloh, T. Bluszcz, and Y. Schlomann for conducting the measurements on stable water isotopes and ion concentrations.

REFERENCES

Alley, R. B. (1988). Concerning the deposition and diagenesis of strata in polar firn. *J. Glaciol.* 34, 283–290. doi: 10.3189/S0022143000007024

Birnbaum, G., Brauner, R., and Ries, H. (2006). Synoptic situations causing high precipitation rates on the antarctic plateau: observations from Kohnen Station, Dronning Maud Land. *Antarct. Sci.* 18, 279–288. doi: 10.1017/S0954102006000320

Birnbaum, G., Freitag, J., Brauner, R., König-Langlo, G., Schulz, E., Kipfstuhl, S., et al. (2010). Strong-wind events and their influence on the formation of snow dunes: observations from Kohnen station, Dronning Maud Land, Antarctica. *J. Glaciol.* 56, 891–902. doi: 10.3189/002214310794457272

Brook, E. J., and Buizert, C. (2018). Antarctic and global climate history viewed from ice cores. *Nature* 558, 200–208. doi: 10.1038/s41586-018-0172-175

Brun, E., Six, D., Picard, G., Vionnet, V., Arnaud, L., Bazile, E., et al. (2011). Snow/atmosphere coupled simulation at Dome C, Antarctica. *J. Glaciol.* 57, 721–736. doi: 10.3189/002214311797409794

Calonne, N., Flin, F., Geindreau, C., Lesaffre, B., and Rolland Du Roscoat, S. (2014). Study of a temperature gradient metamorphism of snow from 3-D images: time evolution of microstructures, physical properties and their associated anisotropy. *Cryosphere* 8, 2255–2274. doi: 10.5194/tc-8-2255-2014

Calonne, N., Milliancourt, L., Burr, A., Philip, A., Martin, C. L., Flin, F., et al. (2019). Thermal conductivity of snow, firn, and porous ice from 3-D image-based computations. *Geophys. Res. Lett.* 46, 13079–13089. doi: 10.1029/2019GL085228

Calonne, N., Montagnat, M., Matzl, M., and Schneebeli, M. (2017). The layered evolution of fabric and microstructure of snow at point Barnola, Central East Antarctica. *Earth Planet. Sci. Lett.* 460, 293–301. doi: 10.1016/j.epsl.2016.11.041

Carlsen, T., Birnbaum, G., Ehrlich, A., Freitag, J., Heygster, G., Istomina, L., et al. (2017). Comparison of different methods to retrieve optical-equivalent snow grain size in central Antarctica. *Cryosphere* 11, 2727–2741. doi: 10.5194/tc-11-2727-2017

Casado, M., Landais, A., Picard, G., Münch, T., Laepple, T., Stenni, B., et al. (2018). Archival processes of the water stable isotope signal in East Antarctic ice cores. *Cryosphere* 12, 1745–1766. doi: 10.5194/tc-12-1745-2018

Colbeck, S. C. (1989). Snow-crystal growth with varying surface temperatures and radiation penetration. *J. Glaciol.* 35, 23–29. doi: 10.3189/002214389793701536

Courville, Z. R., Albert, M. R., Fahnestock, M. A., Cathles, I. M., and Shuman, C. A. (2007). Impacts of an accumulation hiatus on the physical properties of firn at a low-accumulation polar site. *J. Geophys. Res. Earth Surf.* 112, 1–11. doi: 10.1029/2005JF000429

Drücker, C., Wilhelms, F., Oerter, H., Frenzel, A., Gernandt, H., and Miller, H. (2002). "Design, transport, construction, and operation of the summer base Kohnen for ice-core drilling in Dronning Maud Land, Antarctica," in *Proceedings of the Fifth International Workshop on Ice Drilling Technology* (Nagaoka: Nagaoka University of Technology), 302–312.

Ekaykin, A. A., Lipenkov, V. Y., Barkov, N. I., Petit, J. R., and Masson-Delmotte, V. (2002). Spatial and temporal variability in isotope composition of recent snow in the vicinity of Vostok station, Antarctica: implications for ice-core record interpretation. *Ann. Glaciol.* 35, 181–186. doi: 10.3189/172756402781816726

EPICA Community Members (2006). One-to-one coupling of glacial climate variability in greenland and Antarctica. *Nature* 444, 195–198. doi: 10.1038/nature05301

Fegyveresi, J. M., Alley, R. B., Muto, A., Orsi, A. J., and Spencer, M. K. (2018). Surface formation, preservation, and history of low-porosity crusts at the WAIS Divide site, West Antarctica. *Cryosphere* 12, 325–341. doi: 10.5194/tc-12-325-2018

Freitag, J., Kipfstuhl, S., and Faria, S. H. (2008). The connectivity of crystallite agglomerates in low-density firn at Kohnen station, Dronning Maud Land, Antarctica. *Ann. Glaciol.* 49, 114–119. doi: 10.3189/172756408787814852

Freitag, J., Kipfstuhl, S., and Laepple, T. (2013). Core-scale radioscopic imaging: a new method reveals density-calcium link in Antarctic firn. *J. Glaciol.* 59, 1009–1014. doi: 10.3189/2013JoG13J028

Frezzotti, M., Pourchet, M., Flora, O., Gandolfi, S., Gay, M., Urbini, S., et al. (2005). Spatial and temporal variability of snow accumulation in East Antarctica from traverse data. *J. Glaciol.* 51, 113–124. doi: 10.3189/172756505781829502

Fujita, S., Holmlund, P., Andersson, I., Brown, I., Enomoto, H., Fujii, Y., et al. (2011). Spatial and temporal variability of snow accumulation rate on the East Antarctic ice divide between Dome Fuji and EPICA DML. *Cryosphere* 5, 1057–1081. doi: 10.5194/tc-5-1057-2011

Fukuzawa, T., and Akitaya, E. (1991). An experimental study on the growth rates of depth hoar crystals at high temperature gradients (I). *Low Temp. Sci. Ser. A* 50, 9–14.

Furukawa, R., Uemura, R., Fujita, K., Sjolte, J., Yoshimura, K., Matoba, S., et al. (2017). Seasonal-scale dating of a shallow ice core from greenland using oxygen isotope matching between data and simulation. *J. Geophys. Res. Atmos.* 122, 10873–10887. doi: 10.1002/2017JD026716

Göktas, F., Fischer, H., Oerter, H., Weller, R., Sommer, S., Miller, H., et al. (2002). A glaciochemical characterization of the new EPICA deep-drilling site on Amundsen-isen, dronning Maud Land, Antarctica. *Ann. Glaciol.* 35, 347–354. doi: 10.3189/172756402781816474

Gow, A. J. (1965). On the accumulation and seasonal stratification of snow at the South Pole. *J. Glaciol.* 5, 467–477. doi: 10.1017/S002214300001844X

Groot Zwaaftink, C. D., Cagnati, A., Crepaz, A., Fierz, C., MacElloni, G., Valt, M., et al. (2013). Event-driven deposition of snow on the Antarctic Plateau: analyzing field measurements with snowpack. *Cryosphere* 7, 333–347. doi: 10.5194/tc-7-333-2013

Gupta, P., Noone, D., Galewsky, J., Sweeney, C., and Vaughn, B. H. (2009). Demonstration of high-precision continuous measurements of water vapor isotopologues in laboratory and remote field deployments using wavelength-scanned cavity ring-down spectroscopy (WS-CRDS) technology. *Rapid Commun. Mass Spectrom.* 23, 2534–2542. doi: 10.1002/rcm.4100

Helsen, M. M., Van de Wal, R. S. W., Van Den Broeke, M. R., As, D., Va1eijer, H. A. J., and Reijmer, C. H. (2005). Oxygen isotope variability in snow from western dronning Maud Land, Antarctica and its relation to temperature. *Tellus B Chem. Phys. Meteorol.* 57, 423–435. doi: 10.3402/tellusb.v57i5.16563

Hörhold, M. W., Albert, M. R., and Freitag, J. (2009). The impact of accumulation rate on anisotropy and air permeability of polar firn at a high-accumulation site. *J. Glaciol.* 55, 625–630. doi: 10.3189/002214309789471021

Hoshina, Y., Fujita, K., Iizuka, Y., and Motoyama, H. (2016). Inconsistent relationships between major ions and water stable isotopes in Antarctic snow under different accumulation environments. *Polar Sci.* 10, 1–10. doi: 10.1016/j.polar.2015.12.003

Hoshina, Y., Fujita, K., Nakazawa, F., Iizuka, Y., Miyake, T., Hirabayashi, M., et al. (2014). Effect of accumulation rate on water stable isotopes of near-surface snow in inland Antarctica. *J. Geophys. Res.* 119, 274–283. doi: 10.1002/2013JD020771

Howat, I. M., Porter, C., Smith, B. E., Noh, M.-J., and Morin, P. (2019). The reference elevation model of Antarctica. *Cryosphere* 13, 665–674. doi: 10.5194/tc-13-665-2019

Iizuka, Y., Fujii, Y., Hirasawa, N., Suzuki, T., Motoyama, H., Furukawa, T., et al. (2004). SO2-4 minimum in summer snow layer at Dome Fuji, Antarctica, and the probable mechanism. *J. Geophys. Res. Atmos.* 109:4138. doi: 10.1029/2003jd004138

Iizuka, Y., Ohno, H., Uemura, R., Suzuki, T., Oyabu, I., Hoshina, Y., et al. (2016). Spatial distributions of soluble salts in surface snow of East Antarctica. *Tellus Ser. B Chem. Phys. Meteorol.* 68:29285. doi: 10.3402/tellusb.v68.29285

Johnsen, S. J. (1977). "Stable isotope homogenization of polar firn and ice," in *Proceedings of Symposium on Isotopes and Impurities in Snow and Ice, International Association of Hydrological Sciences, Commission of Snow and Ice, I.U.G.G. XVI*, Wallingford.

Jonsell, U., Hansson, M. E., and Mörth, C. M. (2007). Correlations between concentrations of acids and oxygen isotope ratios in polar surface snow. *Tellus Ser. B Chem. Phys. Meteorol.* 59, 326–335. doi: 10.1111/j.1600-0889.2007.00272.x

Jouzel, J., Alley, R. B., Cuffey, K. M., Dansgaard, W., Grootes, P., Hoffmann, G., et al. (1997). Validity of the temperature reconstruction from water isotopes in ice cores. *J. Geophys. Res. Ocean.* 102, 26471–26487. doi: 10.1029/97JC01283

Jouzel, J., Masson-Delmotte, V., Cattani, O., Dreyfus, G., Falourd, S., Hoffmann, G., et al. (2007). Orbital and millennial antarctic climate variability over the past 800,000 years. *Science* 317, 793–796. doi: 10.1126/science.1141038

Kamata, Y., Sokratov, S. A., and Sato, A. (1999). "Temperature and temperature gradient dependence of snow recrystallization in depth hoar snow," in *Advances in Cold-Region Thermal Engineering and Sciences*, eds K. Hutter, Y. Wang, and H. Beer ((Heidelberg: Springer), 395–402. doi: 10.1007/bfb0104197

Kameda, T., Motoyama, H., Fujita, S., and Takahashi, S. (2008). Temporal and spatial variability of surface mass balance at Dome Fuji, East Antarctica, by the stake method from 1995 to 2006. *J. Glaciol.* 54, 107–115. doi: 10.3189/002214308784409062

Karlöf, L., Isaksson, E., Winther, J.-G., Gundestrup, N., Meijer, H. A. J., Mulvaney, R., et al. (2005). Accumulation variability over a small area in east Dronning Maud Land, Antarctica, as determined from shallow firn cores and snow pits: some implications for ice-core records. *J. Glaciol.* 51, 343–352. doi: 10.3189/172756505781829232

Kaufmann, P., Fundel, F., Fischer, H., Bigler, M., Ruth, U., Udisti, R., et al. (2010). Ammonium and non-sea salt sulfate in the EPICA ice cores as indicator of biological activity in the Southern Ocean. *Quat. Sci. Rev.* 29, 313–323. doi: 10.1016/j.quascirev.2009.11.009

Koerner, R. M. (1971). A stratigraphic method of determining the snow accumulation rate at plateau station, Antarctica, and application to south pole-queen maud land traverse 2, 1965-1966. *Antarct. Ice Stud.* 2, 225–238. doi: 10.1029/AR016p0225

Laepple, T., Hörhold, M., Münch, T., Freitag, J., Wegner, A., and Kipfstuhl, S. (2016). Layering of surface snow and firn at Kohnen Station, Antarctica: noise or seasonal signal? *J. Geophys. Res. Earth Surf.* 121, 1849–1860. doi: 10.1002/2016JF003919

Laepple, T., Münch, T., Casado, M., Hoerhold, M., Landais, A., and Kipfstuhl, S. (2018). On the similarity and apparent cycles of isotopic variations in East Antarctic snow pits. *Cryosphere* 12, 169–187. doi: 10.5194/tc-12-169-2018

Legrand, M. (1995). Sulphur-derived species in polar ice: a review. *Ice Core Stud. Glob. Biogeochem. Cycles* 30, 91–119. doi: 10.1007/978-3-642-51172-1-5

Legrand, M., and Mayewski, P. (1997). Glaciochemistry of polar ice cores: a review. *Rev. Geophys.* 35, 219–243. doi: 10.1029/96RG03527

Löwe, H., Riche, F., and Schneebeli, M. (2013). A general treatment of snow microstructure exemplified by an improved relation for thermal conductivity. *Cryosphere* 7, 1473–1480. doi: 10.5194/tc-7-1473-2013

Lüthi, D., Le Floch, M., Bereiter, B., Blunier, T., Barnola, J. M., Siegenthaler, U., et al. (2008). High-resolution carbon dioxide concentration record 650,000-800,000 years before present. *Nature* 453, 379–382. doi: 10.1038/nature06949

Masson-Delmotte, V., Hou, S., Ekaykin, A., Jouzel, J., Aristarain, A., Bernardo, R. T., et al. (2008). A review of antarctic surface snow isotopic composition: observations, atmospheric circulation, and isotopic modeling. *J. Clim.* 21, 3359–3387. doi: 10.1175/2007JCLI2139.1

Medley, B., McConnell, J. R., Neumann, T. A., Reijmer, C. H., Chellman, N., Sigl, M., et al. (2018). Temperature and snowfall in western queen maud land increasing faster than climate model projections. *Geophys. Res. Lett.* 45, 1472–1480. doi: 10.1002/2017GL075992

Minikin, A., Legrand, M., Hall, J., Wagenbach, D., Kleefeld, C., Wolff, E., et al. (1998). Sulfur-containing species (sulfate and methanesulfonate) in coastal Antarctic aerosol and precipitation. *J. Geophys. Res. Atmos.* 103, 10975–10990. doi: 10.1029/98JD00249

Mosley-Thompson, E., Kruss, P. D., Thompson, L. G., Pourchet, M., and Grootes, P. (1985). Snow stratigraphic record at South pole: potential for paleoclimatic reconstruction. *Ann. Glaciol.* 7, 26–33. doi: 10.3189/S0260305500005863

Münch, T., Kipfstuhl, S., Freitag, J., Meyer, H., and Laepple, T. (2016). Regional climate signal vs. local noise: a two-dimensional view of water isotopes in Antarctic firn at Kohnen Station, Dronning Maud Land. *Clim. Past* 12, 1565–1581. doi: 10.5194/cp-12-1565-2016

Münch, T., Kipfstuhl, S., Freitag, J., Meyer, H., and Laepple, T. (2017). Constraints on post-depositional isotope modifications in East Antarctic firn from analysing temporal changes of isotope profiles. *Cryosphere* 11, 2175–2188. doi: 10.5194/tc-11-2175-2017

Münch, T., and Laepple, T. (2018). What climate signal is contained in decadal-to centennial-scale isotope variations from Antarctic ice cores? *Clim. Past* 14, 2053–2070. doi: 10.5194/cp-14-2053-2018

Neumann, T. A., Waddington, E. D., Steig, E. J., and Grootes, P. M. (2005). Non-climate influences on stable isotopes at Taylor Mouth, Antarctica. *J. Glaciol.* 51, 248–258. doi: 10.3189/172756505781829331

Noone, D., Turner, J., and Mulvaney, R. (1999). Atmospheric signals and characteristics of accumulation in dronning Maud Land, Antarctica. *J. Geophys. Res. Atmos.* 104, 19191–19211. doi: 10.1029/1999JD900376

Oerter, H., Wilhelms, F., Jung-Rothenhausler, F., Goktas, F., Miller, H., Graf, W., et al. (2000). Accumulation rates in Dronning Maud Land, Antarctica, as revealed by dielectric-profiling measurements of shallow firn cores. *Ann. Glaciol.* 30, 27–34. doi: 10.3189/172756400781820705

Otsu, N. (1979). A threshold selection method from gray-level histograms. *IEEE Trans. Syst. Man. Cybern.* 9, 62–66. doi: 10.1109/TSMC.1979.4310076

Palais, J. M., Whillans, I. M., and Bull, C. (1982). Snow stratigraphic studies at dome C, East Antarctica: an investigation of depositional and diagenetic processes. *Ann. Glaciol.* 3, 239–242. doi: 10.3189/S0260305500002846

Pang, H., Hou, S., Landais, A., Masson-Delmotte, V., Jouzel, J., Steen-Larsen, H. C., et al. (2019). Influence of summer sublimation on δD, δ18O, and δ17O in precipitation, East Antarctica, and implications for climate reconstruction from ice cores. *J. Geophys. Res. Atmos.* 124, 7339–7358. doi: 10.1029/2018JD030218

Persson, A., Langen, P. L., Ditlevsen, P., and Vinther, B. M. (2011). The influence of precipitation weighting on interannual variability of stable water isotopes in Greenland. *J. Geophys. Res. Atmos.* 116, 1–13. doi: 10.1029/2010JD015517

Pfeffer, W. T., and Mrugala, R. (2002). Temperature gradient and initial snow density as controlling factors in the formation and structure of hard depth hoar. *J. Glaciol.* 48, 485–494. doi: 10.3189/172756502781831098

Picard, G., Domine, F., Krinner, G., Arnaud, L., and Lefebvre, E. (2012). Inhibition of the positive snow-albedo feedback by precipitation in interior Antarctica. *Nat. Clim. Chang.* 2, 795–798. doi: 10.1038/nclimate1590

Piel, C., Weller, R., Huke, M., and Wagenbach, D. (2006). Atmospheric methane sulfonate and non-sea-salt sulfate records at the European project for ice coring in Antarctica (EPICA) deep-drilling site in dronning Maud Land, Antarctica. *J. Geophys. Res. Atmos.* 111, 1–13. doi: 10.1029/2005JD006213

Pinzer, B. R., Schneebeli, M., and Kaempfer, T. U. (2012). Vapor flux and recrystallization during dry snow metamorphism under a steady temperature gradient as observed by time-lapse micro-tomography. *Cryosphere* 6, 1141–1155. doi: 10.5194/tc-6-1141-2012

Proksch, M., Löwe, H., and Schneebeli, M. (2015). Density, specific surface area, and correlation length of snow measured by high-resolution penetrometry. *J. Geophys. Res. Earth Surf.* 120, 346–362. doi: 10.1002/2014JF003266

Reijmer, C. H., and Van Den Broeke, M. R. (2003). Temporal and spatial variability of the surface mass balance in dronning Maud Land, Antarctica, as derived from automatic weather stations. *J. Glaciol.* 49, 512–520. doi: 10.3189/172756503781830494

Ren, J., Sun, J., and Qin, D. (2004). Preliminary results of ionic concentrations in snow pits along the zhongshan-dome a traverse route, Antarctica. *Ann. Glaciol.* 39, 155–160. doi: 10.3189/172756404781814366

Riche, F., Montagnat, M., and Schneebeli, M. (2013). Evolution of crystal orientation in snow during temperature gradient metamorphism. *J. Glaciol.* 59, 47–55. doi: 10.3189/2013JoG12J116

Ritter, F., Steen-Larsen, H. C., Werner, M., Masson-Delmotte, V., Orsi, A., Behrens, M., et al. (2016). Isotopic exchange on the diurnal scale between near-surface snow and lower atmospheric water vapor at Kohnen station, East Antarctica. *Cryosphere* 10, 1647–1663. doi: 10.5194/tc-10-1647-2016

Satyawali, P. K., Singh, A. K., Dewali, S. K., Kumar, P., and Kumar, V. (2008). Time dependence of snow microstructure and associated effective thermal conductivity. *Ann. Glaciol.* 49, 43–50. doi: 10.3189/172756408787814753

Schaller, C. F., Freitag, J., Kipfstuhl, S., Laepple, T., Christian Steen-Larsen, H., and Eisen, O. (2016). A representative density profile of the North Greenland snowpack. *Cryosphere* 10, 1991–2002. doi: 10.5194/tc-10-1991-2016

Schlosser, E., Manning, K. W., Powers, J. G., Duda, M. G., Birnbaum, G., and Fujita, K. (2010). Characteristics of high-precipitation events in dronning Maud Land, Antarctica. *J. Geophys. Res. Atmos.* 115, 1–14. doi: 10.1029/2009JD013410

Schneebeli, M., and Sokratov, S. A. (2004). Tomography of temperature gradient metamorphism of snow and associated changes in heat conductivity. *Hydrol. Process.* 18, 3655–3665. doi: 10.1002/hyp.5800

Sommer, S., Wagenbach, D., Mulvaney, R., and Fischer, H. (2000). Glacio-chemical study spanning the past 2 kyr on three ice cores from dronning Maud Land, Antarctica 2. Seasonally resolved chemical records. *J. Geophys. Res. Atmos.* 105, 29423–29433. doi: 10.1029/2000JD900450

Srivastava, P. K., Mahajan, P., Satyawali, P. K., and Kumar, V. (2010). Observation of temperature gradient metamorphism in snow by X-ray computed microtomography: measurement of microstructure parameters and simulation of linear elastic properties. *Ann. Glaciol.* 51, 73–82. doi: 10.3189/172756410791386571

Steig, E. J., Ding, Q., White, J. W. C., Küttel, M., Rupper, S. B., Neumann, T. A., et al. (2013). Recent climate and ice-sheet changes in West Antarctica compared with the past 2,000 years. *Nat. Geosci.* 6, 372–375. doi: 10.1038/ngeo1778

Stenni, B., Curran, M. A. J., Abram, N. J., Orsi, A., Goursaud, S., Masson-Delmotte, V., et al. (2017). Antarctic climate variability on regional and continental scales over the last 2000 years. *Clim. Past* 13, 1609–1634. doi: 10.5194/cp-13-1609-2017

Stenni, B., Scarchilli, C., Masson-Delmotte, V., Schlosser, E., Ciardini, V., Dreossi, G., et al. (2016). Three-year monitoring of stable isotopes of precipitation at Concordia Station, East Antarctica. *Cryosphere* 10, 2415–2428. doi: 10.5194/tc-10-2415-2016

Touzeau, A., Landais, A., Stenni, B., Uemura, R., Fukui, K., Fujita, S., et al. (2016). Acquisition of isotopic composition for surface snow in East Antarctica and the links to climatic parameters. *Cryosphere* 10, 837–852. doi: 10.5194/tc-10-837-2016

Town, M. S., Warren, S. G., Walden, V. P., and Waddington, E. D. (2008). Effect of atmospheric water vapor on modification of stable isotopes in near-surface snow on ice sheets. *J. Geophys. Res. Atmos.* 113, 1–16. doi: 10.1029/2008JD009852

Udisti, R., Dayan, U., Becagli, S., Busetto, M., Frosini, D., Legrand, M., et al. (2012). Sea spray aerosol in central Antarctica. Present atmospheric behaviour and implications for paleoclimatic reconstructions. *Atmos. Environ.* 52, 109–120. doi: 10.1016/j.atmosenv.2011.10.018

Van Geldern, R., and Barth, J. A. C. (2012). Optimization of instrument setup and post-run corrections for oxygen and hydrogen stable isotope measurements of water by isotope ratio infrared spectroscopy (IRIS). *Limnol. Oceanogr. Methods* 10, 1024–1036. doi: 10.4319/lom.2012.10.1024

Vinther, B. M., Jones, P. D., Briffa, K. R., Clausen, H. B., Andersen, K. K., Dahl-Jensen, D., et al. (2010). Climatic signals in multiple highly resolved stable isotope records from Greenland. *Quat. Sci. Rev.* 29, 522–538. doi: 10.1016/j.quascirev.2009.11.002

Weller, R., and Wagenbach, D. (2007). Year-round chemical aerosol records in continental Antarctica obtained by automatic samplings. *Tellus, Ser. B Chem. Phys. Meteorol.* 59, 755–765. doi: 10.1111/j.1600-0889.2007.00293.x

Wesche, C., Eisen, O., Oerter, H., Schulte, D., and Steinhage, D. (2007). Surface topography and ice flow in the vicinity of the EDML deep-drilling site, Antarctica. *J. Glaciol.* 53, 442–448. doi: 10.1594/PANGAEA.611331

White, J. W. C., Barlow, L. K., Fisher, D., Grootes, P., Jouzel, J., Johnsen, S. J., et al. (1997). The climate signal in the stable isotopes of snow from Summit, Greenland: results of comparisons with modern climate observations. *J. Geophys. Res. Ocean.* 102, 26425–26439. doi: 10.1029/97JC00162

Wolff, E. W., Barbante, C., Becagli, S., Bigler, M., Boutron, C. F., Castellano, E., et al. (2010). Changes in environment over the last 800,000 years from chemical analysis of the EPICA Dome C ice core. *Quat. Sci. Rev.* 29, 285–295. doi: 10.1016/j.quascirev.2009.06.013

Wolff, E. W., Cook, E., Barnes, P. R. F., and Mulvaney, R. (2005). Signal variability in replicate ice cores. *J. Glaciol.* 51, 462–468. doi: 10.3189/172756505781829197

Zheng, M., Sjolte, J., Adolphi, F., Vinther, B. M., Steen-Larsen, H. C., Popp, T. J., et al. (2018). Climate information preserved in seasonal water isotope at NEEM: relationships with temperature, circulation and sea ice. *Clim. Past* 14, 1067–1078. doi: 10.5194/cp-14-1067-2018

Conflict of Interest: The authors declare that the research was conducted in the absence of any commercial or financial relationships that could be construed as a potential conflict of interest.

frontiers in Earth Science

ORIGINAL RESEARCH
published: 19 February 2020
doi: 10.3389/feart.2020.00034

Using Ultrasonic Waves to Determine the Microstructure of Snow

Ross Lieblappen[1,2]*, *John M. Fegyveresi*[1,3], *Zoe Courville*[1] *and Donald G. Albert*[1]

[1] US Army Corps of Engineers Cold Regions Research and Engineering Laboratory, Hanover, NH, United States, [2] Vermont Technical College, Randolph Center, VT, United States, [3] School of Earth and Sustainability, Northern Arizona University, Flagstaff, AZ, United States

Acoustic signals interact with the physical structure of porous media, are particularly sensitive to porosity and tortuosity, and can be used to measure physical properties in a non-destructive manner. Given the fragile nature of freshly fallen snow, non-contact, non-destructive characterization methods made possible via acoustic signals, are desirable. High frequency wave propagation methods can be used to determine *in-situ*, near-surface, micro-pore geometry parameters in snow using methods demonstrated on cohesive porous materials, including manufactured foams, porous metals, and sintered glass beads. High frequency (90 kHz), oblique-angle and near vertical reflection measurements were conducted on snow samples in a cold room to demonstrate the feasibility of acoustic characterization. A nonlinear least squares regression to the theoretical reflection response was used to derive the best-fitting values for the porosity and tortuosity. We compared the acoustically-derived snow physical parameters, including porosity and tortuosity, with values determined from X-ray micro-computed tomography (μCT) for different snow types. The μCT-measured and acoustically-derived methods demonstrated strong agreement for porosity with differences averaging 8% for all samples. Tortuosity values, however, had average differences of roughly 20% for all samples. The different error rates might be caused by the stronger dependence of the acoustic reflection on porosity than on tortuosity. For both parameters, the small grain snow and large grain firn samples had errors much larger than the fresh or 1 day samples. Fresh snow has the lowest reflection coefficients and demonstrates a steady decrease from <0.1 at normal incidence as the angle increases. Aging fresh snow for 1 day caused detectable changes in acoustic response, from slight decreases in porosity, and slight increases in tortuosity that occurred from sintering.

Keywords: snow, microstructure, ultrasonic acoustic waves, micro-computed tomography, porosity, tortuosity

OPEN ACCESS

Edited by:
Pascal Hagenmuller, UMR3589 Centre National de Recherches Météorologiques (CNRM), France

Reviewed by:
Henning Löwe, WSL Institute for Snow and Avalanche Research SLF, Switzerland
Amaelle Adeline Landais, Centre National de la Recherche Scientifique (CNRS), France

***Correspondence:**
Ross Lieblappen
ross.lieblappen@vtc.edu

Specialty section:
This article was submitted to Cryospheric Sciences, a section of the journal Frontiers in Earth Science

Received: *29 July 2019*
Accepted: *31 January 2020*
Published: *19 February 2020*

Citation:
Lieblappen R, Fegyveresi JM, Courville Z and Albert DG (2020) Using Ultrasonic Waves to Determine the Microstructure of Snow. Front. Earth Sci. 8:34. doi: 10.3389/feart.2020.00034

INTRODUCTION

In the 1950s, Maurice Biot published a comprehensive mathematical theory of wave propagation in porous materials (Biot, 1956). The theory predicted that two compressional waves and one shear wave would propagate in the bulk media. While the motion of all three waves are coupled to the motion of both the solid frame and the fluid in the pores, the first compressional wave (P1) traveled mainly in the solid frame, and the second (P2) mainly in the pore fluid. The first experimental measurements to confirm the existence of the two compressional waves were published in 1980 (Plona, 1980; Smeulders, 2005), and since then, many modifications have been made to the theory

(e.g., Allard and Atalla, 2009). Perhaps the earliest application of Biot's theory to snow was Johnson (1982), followed by many other studies that have used this theory (Albert et al., 2009; Maysenhölder et al., 2012; Sidler, 2015) for predictions and analysis of snow measurements.

Properties of specific porous materials can be determined from reflected or transmitted acoustic waves using a classical inverse scattering mathematical approach (Horoshenkov, 2017). For example, the interaction of sound energy with the ground is an important effect in understanding sound propagation in a natural setting, and is governed in part by the porous properties of the surface materials (Attenborough et al., 2011). Previous experimental work to determine soil and ground conditions was typically performed in the audio frequency range of 100–10,000 Hz, with wavelengths of 3 m−3 cm (e.g., Nagy et al., 1990; Hickey and Sabatier, 1997; Iversen et al., 2001; Attenborough et al., 2011, 2014). Continuous waves are broadcast with a loudspeaker and recorded by microphones located a few meters away to determine the ground impedance as a function of frequency. Other ground properties that can be determined using this method are effective flow resistivity, permeability, porosity and shallow layer depth. Pulses produced by firearms or explosives can be used to extend the surface area sampled to tens or hundreds of meters (Cramond and Don, 1984; Don and Cramond, 1987; Albert M. R., et al., 2008).

Standard acoustic analysis methods frequently depend on a rigid-porous theoretical treatment of the ground to interpret the results and derive porous medium parameters from the acoustic measurements. In the case of air-filled porous materials, the theory is considerably simplified by assuming that the solid frame is rigid (that is, without motion), an approach used for many applications, including the ground effect on outdoor sound propagation (e.g., Albert, 2001; Allard and Atalla, 2009; Attenborough et al., 2011; Horoshenkov, 2017). These analyses do not include vibration and seismic wave effects.

In the ultrasonic range, pore waves become non-dispersive and simple relationships exist between reflection coefficients and porous material properties, including tortuosity and permeability (Fellah et al., 2003a,b; Allard and Atalla, 2009). Previous studies (e.g., Fellah et al., 2003a,b, 2006; Allard and Atalla, 2009) have applied high frequency, rigid porous theory to cohesive porous materials, including sintered glass beads, porous metals, and fused manufactured foams. Most of the measurements were conducted at normal incidence, but oblique high frequency (200 kHz) measurements have also been reported (Fellah et al., 2003b). In these studies, a physical scattering process is generally modeled first, which results in a synthetic response for initially assigned parameters. These parameters are then adjusted so that the modeled output agrees well with the observed measurement data. Two important parameters that are therefore generally evaluated and often appear in studies of sound propagation in porous materials (e.g., Fellah et al., 2003a) are porosity (a measure of volume of the pore space to the volume of the solid frame material) and tortuosity (the ratio of the shortest distance through the pore space to the straight line distance).

Fresh natural snow is a difficult material to characterize, even with special techniques (Shimizu, 1970), as any mechanical interaction is likely to damage the fragile pores and grain bonds. Because acoustic waves are sensitive to the microstructural properties of porous materials, they can be used to measure snow properties in a non-destructive manner. The acoustic properties of snow have been investigated in the past for a variety of applications, including understanding the attenuation of snow covered ground (Oura, 1952; Ishida, 1965; Yamada et al., 1974), understanding the acoustic response of snow to explosives used in avalanche mitigation (Gubler, 1977), predicting the stability of a natural snowpack (Sommerfeld and Gubler, 1983), monitoring the location of avalanches (Suriñach et al., 2001; Van Herwijnen and Schweizer, 2011; Lacroix et al., 2012), and estimating snow water equivalent (SWE) (Kinar and Pomeroy, 2009). Low frequency acoustic waves can be used to determine snow depth and effective flow resistivity (air permeability) over distances of tens of meters (Albert, 2001; Albert D. G., et al., 2008).

There have been limited ultrasonic or high frequency measurements reported on real geological materials, including snow. Air-coupled transmission measurements through thin (1–2 mm thick) sintered glass beads and sandstone samples at high frequencies (100–500 kHz) at normal incidence have been reported (Nagy et al., 1990). Past work on the acoustic response of snow in the ultrasonic range has employed contact sensors buried in snow samples and natural snowpacks using a range of waveguides and coupling materials (Kapil et al., 2014; Reiweger et al., 2015; Capelli et al., 2016) or on ice cores in the laboratory (Bennet, 1972; Kohnen and Gow, 1979; Herron et al., 1985).

An *in situ* method to determine the characteristics of extremely fragile porous materials would be very helpful for studies of fragile natural snow covers. For this purpose, we examine the potential of ultrasonic reflections and avoid the use of wave transmission techniques suitable for stronger materials (Umnova et al., 2005). A newly-designed test apparatus was used to conduct ultrasonic reflection measurements in a cold room to derive the porosity and tortuosity of various snow samples. The ultrasonic measurements were validated by comparison with standard laboratory techniques (that may disturb the sample), with parameters derived from X-ray micro-computed tomography (μCT) scanning, and with previous laboratory measurements reported in the literature. These measurements are intended to validate the ultrasonic method and to provide insight for the development of a new, non-destructive, and field-portable device for providing real-time *in situ* measurements of pore characteristics and properties of snow. Such a device will also allow for better modeling of outdoor sound propagation, provide an opportunity to apply the methods to other fragile real-Earth materials, including sand, soil, and leaf litter, and would be of great interest for a wide range of potential applications in cold environments for the analysis and characterization of numerous snow, firn, and ice physical properties. While acoustic transmission measurements can improve the determination of porous material properties, they were not employed here because of the desire to develop a non-destructive, surface method.

For clarity, we define the porosity of a porous material as the ratio of the pore volume to the total volume. Tortuosity is a parameter to describe the increased path length between two points within the pores of a porous material compared to the straight-line path in open air. However, two definitions of tortuosity appear in the acoustic literature. One is the average point to point path length through the porous medium divided by the straight line path (in open air) ($L_{pore}/L_{straight}$). The other is the path length ratio squared $(L_{pore}/L_{straight})^2$. We use the latter definition in this paper (e.g., Fellah et al., 2003b; Allard and Atalla, 2009), so care is needed in comparing values from different techniques or references. In the next sections, we describe the methods and equipment used to prepare the snow samples, perform μCT scanning, and conduct the acoustic measurements. A discussion and conclusions follows.

METHODS

Snow Sample Preparation

Four distinct types of snow samples were prepared from (1) artificial snow, synthesized in a laboratory cold-room with small, relatively homogeneous rounded snow grains, designated SGA and SGB; (2) polar firn with large grains sieved so that grain sizes were between 0.85 and 1.2 mm, designated LGA and LGB; (3) freshly fallen natural snow with decomposing particles, very low density collected as fallen, designated FSA, FSB, FSC; and (4) the same freshly fallen snow, but allowed to age for 1 day, designated ASA and ASC. Samples sizes of 25 × 30 × 10 cm were prepared from each sample within an aluminum tray.

μCT Methods

Samples used for all μCT measurements were centrally-cut from the larger prepared snow samples noted above. Samples were trimmed into cylindrical shapes and were subsequently scanned using a Bruker SkyScan 1173 desktop μCT scanner. The SkyScan 1173 is equipped with a Hamamatsu 130/300 tungsten X-ray source that produces a fixed conical, polychromatic beam with a spot size of <5 μm and a flat panel sensor camera detector with 2240 × 2,240 pixels. We set the maximum accelerating voltage of the X-ray beam at 40 kV with a current of 200 μA. Samples were rotated 180° in 0.3° steps, with 4-frame averaged attenuation images captured at each step using a camera exposure of 310–360 msec. We used a 2 × 2 binning protocol to create X-ray radiographs 1120 × 1120 pixels. We completed reconstruction of the resulting radiographs using Bruker SkyScan's NRECON software that uses a modified Feldkamp cone-beam algorithm to produce a vertical stack of gray-scale cross-section images. As part of image post-processing, we performed ring artifact reduction, post-alignment correction, beam hardening correction, and a two-pixel Gaussian kernel smoothing to reduce noise. The resulting images had a spatial resolution of 15 μm per voxel, except for samples SGA and FSA that had 20-μm voxels, and a 16-bit gray-scale dynamic range. The final scanned volume was 1.7 cm in diameter × 1.7 cm high (2.2 cm × 2.2 cm for SGA and FSA).

We selected a cylindrical internal volume of interest (VOI) measuring 1.6 cm in diameter from each sample to eliminate edge effects and gaps. Using a histogram shape-based approach, we set critical thresholds to segment the air/void phase from the snow phase. We performed three-dimensional analysis on the resulting segmented images using Skycan's CTAn software to calculate the object total porosity and surface to volume ratio, which is inversely related to grain size. We then calculated the structure thickness, a metric used for measuring the size of an object (Lieb-Lappen et al., 2017). First, the medial axes of all structures of a given phase were identified. For each point along this axis, a sphere was fit such that it was both entirely inscribed within the phase of interest and encompassed the given starting point. The structure thickness was then calculated as the mean diameter of all spheres over the entire volume. Similarly, the structure separation calculated the average size of pores by performing the same analysis on the inverse phase (i.e., pore space).

The *tortuosity* of a porous medium can be defined geometrically as the tortuous path through a sample vs. a straight-line path, or in terms of the relative transport of some phenomenon (e.g., electrical current, heat transfer, or mass transport) through the medium vs. open air. 2D and 3D tortuosity are often determined through subjective estimation or empirically, although means to quantify tortuosity have been more recently developed. In this work, the air-phase tortuosity of the samples was calculated from the μCT data using TauFactor (Cooper et al., 2016), an open source, MATLAB-based application. The application determines tortuosity quantitatively from the modeled reduction in steady state diffusive transport caused by the geometry of heterogeneous media, as defined by the μCT image data. The tortuosity factor, τ is defined by $D^{eff} = D\frac{\varepsilon}{\tau}$ where ε is the volume fraction of the conductive phase, D is the diffusivity of the conductive phase in open air, and D^{eff} is the diffusivity through the porous volume. The TauFactor application simulates diffusion through the μCT reconstructed image using the voxels from the image as the mesh elements in order to avoid errors produced by smoothing or imposing other geometric distortions that can be caused by meshing (Cooper et al., 2016). Tortuosity in × (horizontal), y (horizontal) and z (vertical) directions was calculated as tortuosity is not typically isotropic; the reported value for tortuosity was the average of these directional tortuosities. On average, the directional tortuosities calculated were within 2% (an average of 1.7% for the entire sample set) of one another because these particular samples were mostly isotropic, composed of new snow and artificial snow with rounded grains.

Ultrasonic Acoustic Theory and Methods

The measurements were analyzed using a high-frequency, rigid-frame simplification of Biot's acoustic propagation model (Fellah et al., 2003a), in which the acoustic P2 wave traveling in the pore space is decoupled from the wave traveling in the skeleton frame of the porous material (i.e., seismic motion is ignored). The simplified theory allows the acoustic properties of the snow samples to be determined in a relatively straightforward way when compared to the full Biot's theory, a physical model that would require many more material properties to be known. Previous laboratory (Buser, 1986) and field measurements (Albert, 2001) have shown that a simplified rigid-porous model

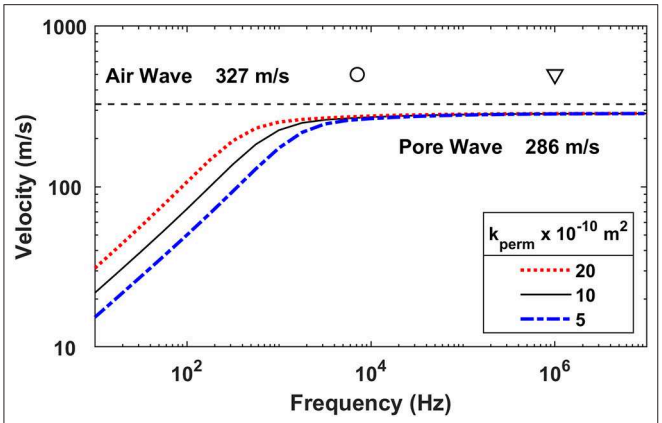

FIGURE 1 | Theoretical behavior of the Biot pore wave, showing the lack of frequency dependence above a critical frequency given by Equation (1), and indicated by the circle at 754 Hz. The calculations assumed a porosity of 0.45 and a tortuosity of 1.30. The three lines show the calculated velocity of the pore wave for different values of the snow permeability (5×10^{-10} m^2, 10×10^{-10} m^2, and 20×10^{-10} m^2). Our measurements were conducted at 90 kHz (indicated by the triangle), well above the frequency dependent band for any snow type.

is sufficient to accurately characterize airborne acoustic waves interacting with snow.

We have adapted the experimental methods of Fellah et al. (2003a) to determine the porosity and tortuosity of cohesive porous materials from reflection measurements at two (or more) oblique angles of incidence. At low frequencies, the propagation of the P2 (pore) wave in air is highly dependent on frequency, but becomes constant above a certain approximate critical frequency

$$f_c = \frac{v\phi}{k_{perm}} \tag{1}$$

where ϕ is the porosity, k_{perm} the permeability of the snow [m^2], and v is the kinematic viscosity of cold −8°C air ($1.23 \times 10^{-5} m^2$/s) with a speed of sound $c = 326$ m/s. To calculate a rough example we assume that $\phi = 0.45$, and the acoustic tortuosity $\alpha = \left(\frac{L_{pore}}{L_{open}}\right)^2 = 1.3$. Snow permeability is quite variable, so we use three values typical of temperate snow covers, $k_{perm} = (5, 10, 20) \times 10^{-10}$ m^2. These parameters were used to calculate the approximate behavior of a P2 pore wave and **Figure 1** shows the resulting P2 wave velocity as a function of frequency. The velocity becomes constant above about 10 kHz, and the theoretical asymptotic wave speed $V_{P2} = \frac{c}{\sqrt{\alpha}} = 286$ m/s. We use a frequency of 90 kHz for our measurements, well into the frequency band where the acoustic behavior of the P2 wave (and reflections from the porous surface) become constant and independent of frequency.

For these very high frequency ultrasonic waves, Fellah et al. (2003a,b) have shown that the porosity and tortuosity can be calculated from a series of oblique reflection measurements, $i = 1 \ldots n$, where $r_i(\Theta)$ is the reflection coefficient, θ is the angle of incidence, ϕ is the porosity, and α_∞ is the tortuosity.

$$r_i(\theta) = \frac{\alpha_\infty cos\theta_i - \phi\sqrt{\alpha_\infty - sin^2\theta_i}}{\alpha_\infty cos\theta_i + \phi\sqrt{\alpha_\infty - sin^2\theta_i}} \tag{2}$$

At normal incidence, the reflection coefficient Equation (2) reduces to $(1 - B)/(1 + B)$ where $B = \phi/\alpha_\infty^{1/2}$. The above equation can be rearranged to isolate the porosity ϕ:

$$\phi = \frac{\alpha_\infty (1 - r_i)\, cos\theta_i}{(1 + r_i)\sqrt{\alpha_\infty - sin^2\theta_i}} \tag{3}$$

If two reflections at two different angles (θ_i and θ_j) are measured, Equation (3) for reflection 1(r_i) can be divided by Equation (3) for reflection 2 (r_j) and the result solved for the tortuosity α_∞

$$\alpha_\infty = \frac{Asin^2\theta_i - sin^2\theta_j}{A^2 - 1} \tag{4}$$

$$\text{where } A = \left(\frac{(1 - r_j)(1 + r_i)\, cos\theta_j}{(1 + r_j)(1 - r_i)\, cos\theta_i}\right). \tag{5}$$

The tortuosity can be obtained from Equations (4) and (5) since they depend only on the measured angles and reflection amplitudes. The tortuosity value can then be substituted into Equation (3) to obtain the porosity. This is the method used by Fellah et al. (2003a,b) to deduce the porous parameters from two reflection coefficients at two oblique angles.

We used a more robust data reduction method to obtain the acoustic parameters. Instead of substituting pairs of measured reflection coefficients into Equations (2–5) to obtain individual parameter estimates, we used a non-linear, least squares method to directly fit Equation (2) to all of the measured reflection coefficients for a particular snow sample. The numerical method constrained the porosity in the range from 0 to 1, and the tortuosity to the region ≥1. This method produced parameter estimates along with confidence intervals for the parameters based on the goodness-of-fit.

Figure 2 illustrates the theoretical reflection coefficient calculated using Equation (2) for parameter values of porosity $\phi = 0.80$ and tortuosity $\alpha = 1.20$. This calculation and others show that variations in porosity have a larger effect on the normal reflection coefficient than similar variations in the tortuosity. The tortuosity lines also "cross-over" at some point as the incident angle increases; for this example at an angle of about 50°. The theory also predicts that at normal incidence, a decrease in porosity or increase in tortuosity results in a higher reflection coefficient.

Two non-contact (air coupled) Ultran Model NGC100-D25 transducers were used, one as a source and the other as a receiver. These transducers are designed to work in air, and have a diameter of 25 mm and a measured resonant frequency of 90 kHz. An Agilent Model 33120A function generator was programmed to continuously output three 90 kHz square wave pulses at a rate of 1 kHz and a peak-to-peak amplitude of 10 volts to drive the source transducer. The function generator also sent a synchronized pulse to the digital

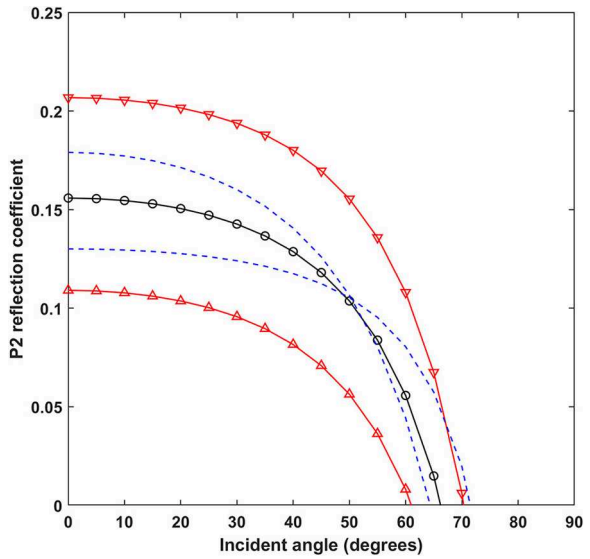

FIGURE 2 | Theoretical reflection coefficient calculated using Equation (2). The black line with circles is the reflection coefficient calculated as a function of angle for parameter values of porosity $\phi = 0.80$ and tortuosity $\alpha = 1.20$. Red solid lines with triangles pointing up/down have porosity values increased/decreased by 10% (0.80, 0.72). Blue dashed lines have modified tortuosity values of (1.32, 1.08).

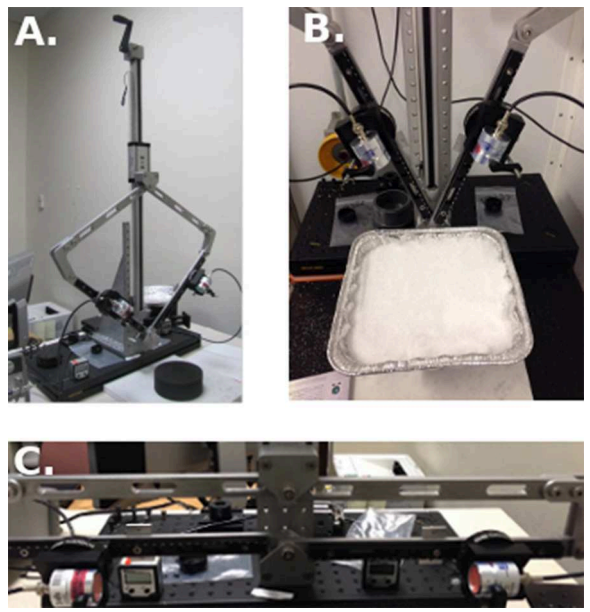

FIGURE 3 | (A) Ultrasonic transducer positioning rig following the methods of Pialucha and Cawley (1994). **(B)** Photo of ultrasonic transducer positioning rig being used to record reflections in a cold room. **(C)** Ultrasonic transducer positioning rig with transducers in horizontal position.

oscilloscope, a Tektronix Model DPO 2014, that recorded the signal detected by the receiver transducer after reflection from the snow surface. The received signals were on the order of tens of millivolts, so 512 repeated ultrasonic pulses were summed by the oscilloscope to improve the signal quality. The digital waveforms and peak-to-peak signals were saved for later analysis.

Following Pialucha and Cawley (1994), a mechanical rig was constructed to position the two ultrasonic transducers at various angles (measured with a Wixey digital angle gauge) as shown in **Figure 3**. The distance from the transducer to the snow surface was fixed for each sample measurement at 20 cm for each ray of the reflection path. Before the snow samples were measured, a direct measurement was conducted through the air to align the transducers and to determine the direct wave amplitude. We found that although signal could be detected off-axis laterally, the best alignment of the transducers was within a small deviation on the order of 0.5 cm or smaller. Reflection measurements were made in a cold room with a temperature of −8°C at 15 specific angles from 7.5° (the smallest measurable angle due to geometric limitations with the experimental set-up—namely the thickness of the transducers themselves), nominally at 5° increments to 75°. For each angle, the total peak voltage of the transmitted and reflected waveform were recorded. A representative series of reflected waveforms for angles of 7.5°-60° is shown in **Figure 4** for a fresh snow sample FSC. The reflection coefficients are defined as the reflected signal amplitude divided by the direct horizontal path signal amplitude. The porosities and tortuosities were calculated from the reflected wave peak-to-peak voltage values measured at oblique incidences using the non-linear regression of Equation (2) as discussed above.

RESULTS AND DISCUSSION

μCT Characterization and Determination of Snow Type

Three-dimensional (3D) binary (black and white) reconstructions of representative examples for each of the four general classes of snow are shown in **Figure 5** in order of age of snow (fresh snow, snow aged 1 day, small grained artificial snow and large grained firn). The fresh and 1-day-old snow samples had needle-like grains, while the other samples were much more rounded and compact.

We completed a 3D morphometric analysis on the binary images for all samples. The surface to volume (S/V) ratio, average structure thickness, and average structure separation are recorded in **Table 1**. As would be expected, the large grain firn had the smallest S/V ratio with an average of 8.8 $mm^{-1} \pm 0.2$ mm^{-1}, while fresh snow had the highest S/V ratio with an average of 63.8 $mm^{-1} \pm 5.4$ mm^{-1}. Aging of fresh snow over 1 day resulted in reduced S/V ratios by roughly 17%.

The software calculates structure thickness by first creating a skeletonization of the binarized snow phase to identify the medial axes of all structures. As described above, at each point along the axes, it then fits the maximal sphere fitting entirely within the object and records the diameter of the sphere. This results in a distribution of thicknesses shown in **Figure 6** with an average value for each sample recorded in **Table 1**. We note that the thickness distributions fall into three

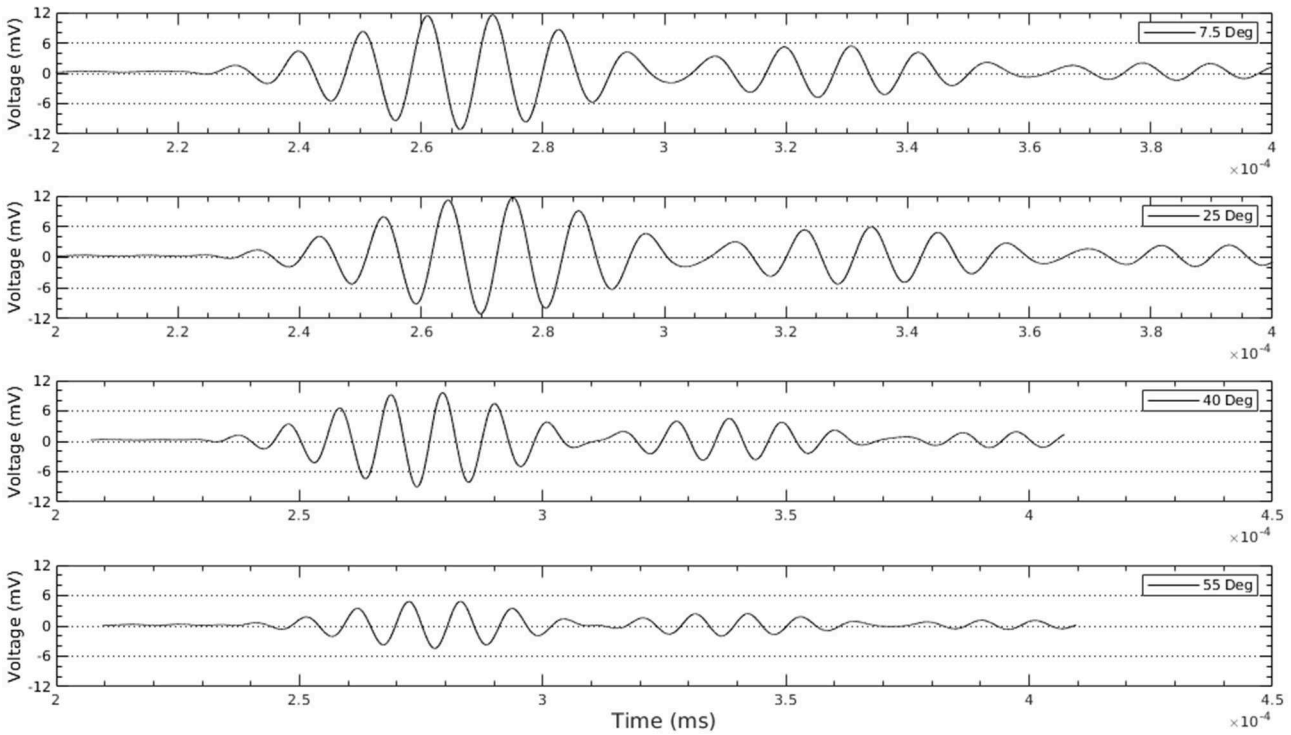

FIGURE 4 | Representative series of reflected acoustic waveforms ranging from angles 7.5° to 60°. The series shown is for fresh snow sample FSC.

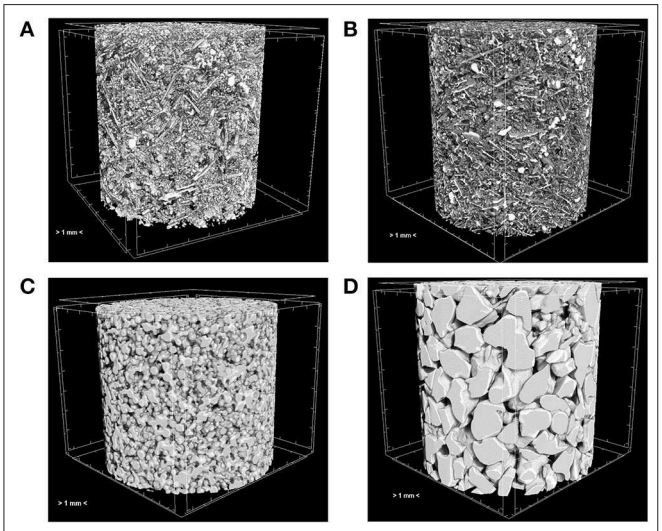

FIGURE 5 | 3D binary reconstructions of μCT data for **(A)** fresh snow (FSB), **(B)** snow aged 1 day (ASA), **(C)** small grained artificial snow (SGB), and **(D)** large grained firn (LGA). Samples **(A,B)** are 170 mm in height and diameter; samples **(C,D)** are 220 mm.

TABLE 1 | 3D μCT morphometric analysi.

Sample name	S/V ratio (mm^{-1})	Average structure thickness (mm)	Average structure separation (mm)
SGA: small grain snow A	22.3	0.19	0.27
SGB: small grain snow B	20.0	0.22	0.24
LGA: large grain firn A	8.72	0.58	0.39
LGB: large grain firn B	8.96	0.53	0.31
FSA: fresh snow A	57.8	0.087	0.42
FSB: fresh snow B	68.2	0.078	0.34
FSC: fresh snow C	65.4	0.065	0.27
ASA: FSA sample aged 1 day	48.0	0.098	0.24
ASC: FSC sample aged 1 day	54.4	0.077	0.26

distinct classes: (1) Very thin "needles" with most structures <0.1 mm thick for fresh snow (0.08 mm ± 0.01 mm) and snow aged 1 day (0.09 mm ± 0.01 mm), (2) structures having Gaussian distribution of thicknesses centered roughly around 0.2 mm for small grain snow (0.21 mm ± 0.02 mm), and 3) large structures with a wide range of thicknesses with a peak roughly around 0.6 mm for large grain firn (0.56 mm ± 0.04 mm).

A similar structure separation was calculated for each sample by running the same analysis but for the air/void phase. The distribution of separations is shown in **Figure 7** and the average values for each sample are recorded in **Table 1**. We observe

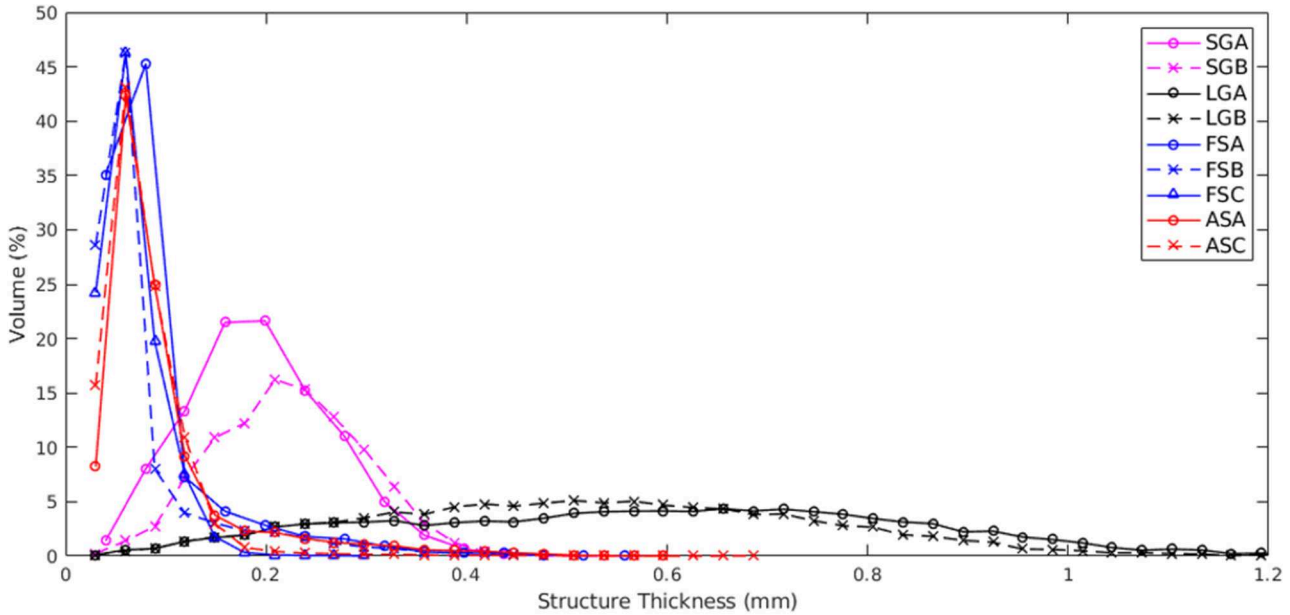

FIGURE 6 | Structure thickness distributions for all samples. We note that samples fall into three classes: (1) fresh snow and snow aged 1 day, (2) small grained snow, and (3) large grain firn.

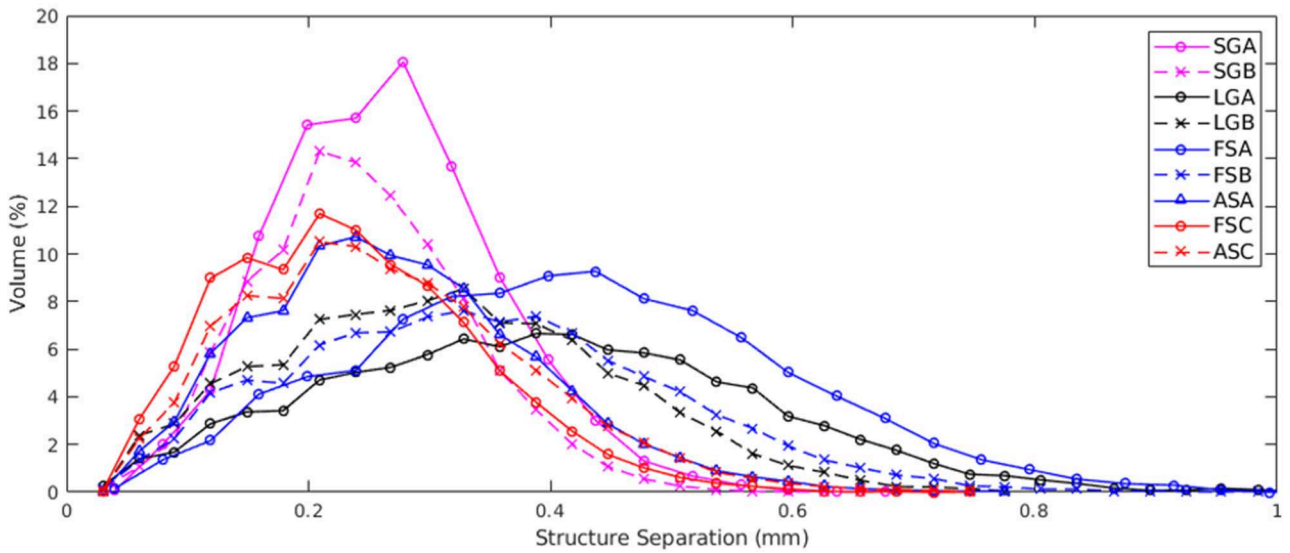

FIGURE 7 | Structure separation distributions for all samples. We note that samples generally fall into two classes: (1) fresh snow and large grain firn and (2) small grained snow and snow aged 1 day.

that there appears to be distinct classes separating the snow types again, but they are different from the structure thicknesses. The small grain snow (0. 26 mm ± 0.01 mm) generally has the same separation distributions as the snow aged 1 day (0.25 mm ± 0.01 mm), while the large grain snow (0.35 mm ± 0.06 mm) generally has the same separation distributions as the fresh snow (0.34 mm ± 0.08 mm) with FSC being an outlier.

Ultrasonic Wave Determination of Porosity and Tortuosity

The angular dependence of the reflection coefficient according to snow type is shown in **Figure 8**. The shape of the curves roughly falls into the four classes of snow types. Large grain snow has the highest reflection coefficients (>0.20) for low angles and falls dramatically for oblique angles >45°. Small grain snow actually shows an increase in reflection angle up to roughly 50°

before plummeting to zero around 70°. Fresh snow has the lowest reflection coefficients and demonstrates a steady decrease from <0.1 at normal incidence as the angle increases. Aging the fresh snow 1 day significantly increases the reflection coefficient for all angles. Using the points from these curves, we determined the porosity and tortuosity values of the samples by fitting Equation (2) to the measurements as discussed above. **Figure 9** shows the results for the fresh snow sample FSC2. The smooth theoretical line fits the measurements reasonably well, and the method also provides confidence intervals for the fitting parameters. In this case the derived porosity is 0.89 ± 0.02 and tortuosity 1.23 ± 0.05. Acoustically-derived parameter values for the other samples are listed in **Table 2**. The confidence width on the mean porosity for all the samples is 2% (with the worst error 7% for LGB) and for the tortuosity 4% with 11% maximum error bounds. The μCT-measured porosity and tortuosity values are also listed in **Table 2**. In addition, the square root of the μCT tortuosity is also given; it is this value that is compared to the acoustic tortuosity. The square root is needed because the μCT is based on diffusion, where the temperature disturbance travels a distance proportional to the square root of time, rather than directly proportional to time as for acoustic propagation. This difference in time dependence leads to μCT tortuosity values that are squared compared to acoustic values.

Porosity and tortuosity values calculated from the acoustic measurements are shown in **Figure 10**. The μCT-measured porosity and tortuosity values are plotted shown as red triangles and the acoustic estimates as circles with the confidence interval indicated for each snow sample. Insets for each graph show a scatter plot of μCT-measured values vs. acoustically-derived values, along with the 1:1 line. The two techniques, μCT-measured and acoustically-derived, demonstrated strong agreement for porosity with differences averaging 8% for all samples. Tortuosity values, however, had average differences of roughly 20% for all samples. For both parameters, the small grain snow and large grain firn samples had errors much larger than the fresh or 1 day samples. For the LG and SG samples, the acoustic porosity was higher and the acoustic tortuosity lower than the μCT results. The techniques had better agreement for fresh snow and snow aged 1 day with differences below 5% for porosity, but as much as 17% for tortuosity. This suggests that both techniques can detect which samples have more tortuous paths, but the accuracy of the methods is moderate. Bonfiglio and Pompoli (2013) reported similar relative tortuosity errors of 13–41% for measurements on porous foam and other materials. The porosity and tortuosity values measured with acoustics and μCT are summarized in **Table 2**.

Many of the field experiments on snow reported in the literature were conducted at low frequencies; however in recent years a few higher frequency laboratory measurements have been published. These studies were often centered on determining the absorption coefficient of various snow types, and so are not easily compared to our present work. Capelli et al. (2016) show in their **Figure 1** pore wave velocity measurements in the literature as a function of snow density. However, unless the measurements were made at frequencies above about 10 kHz (depending on snow properties), the pore wave velocity has a very strong frequency dependence as shown in our **Figure 1**. At high frequencies, the pore wave velocity will be given by $V_{P2} = \frac{c}{\sqrt{\alpha}}$ as mentioned earlier.

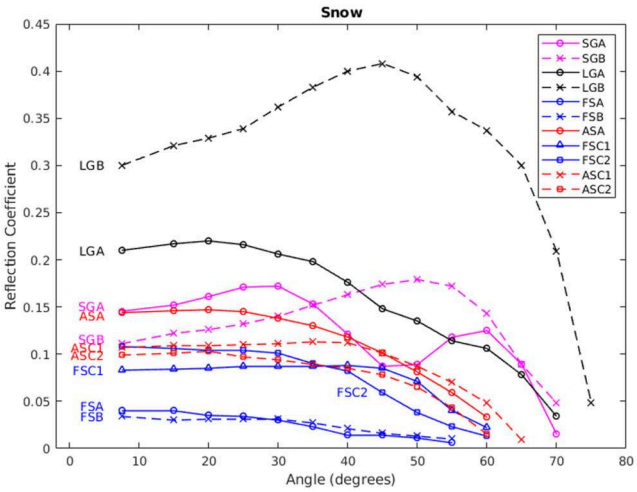

FIGURE 8 | Measured ultrasonic reflection coefficients as a function of incident angle for a variety of snow samples.

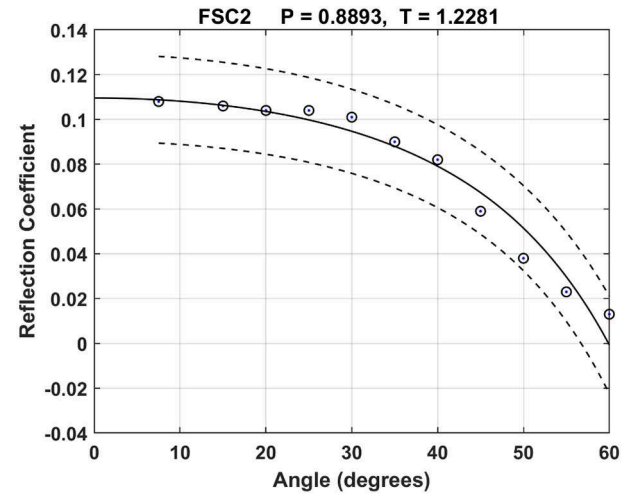

FIGURE 9 | Results of a nonlinear least squares fit of theoretical Equation (2) to the FSC2 snow sample reflection data. The best fit (solid line) is obtained for a porosity of 0.89 and a tortuosity of 1.23. Confidence intervals are shown as dashed lines.

Maysenhölder et al. (2012) measured and modeled the absorption coefficient of snow using measurements in an impedance tube over a frequency band of 125–1,600 Hz, but this band is likely within the frequency-dependent regime as shown in our **Figure 1**, so it is difficult to compare with the measurements reported here. For high porosity snow ($\phi > 0.8$), they report tortuosities of 1.36–1.56 that are higher than our determinations of 1.07–1.27, and their pore wave speeds would be lower. Datt et al. (2016) also reported on impedance tube measurements over a higher frequency range from 63 to 6,300 Hz. Their samples

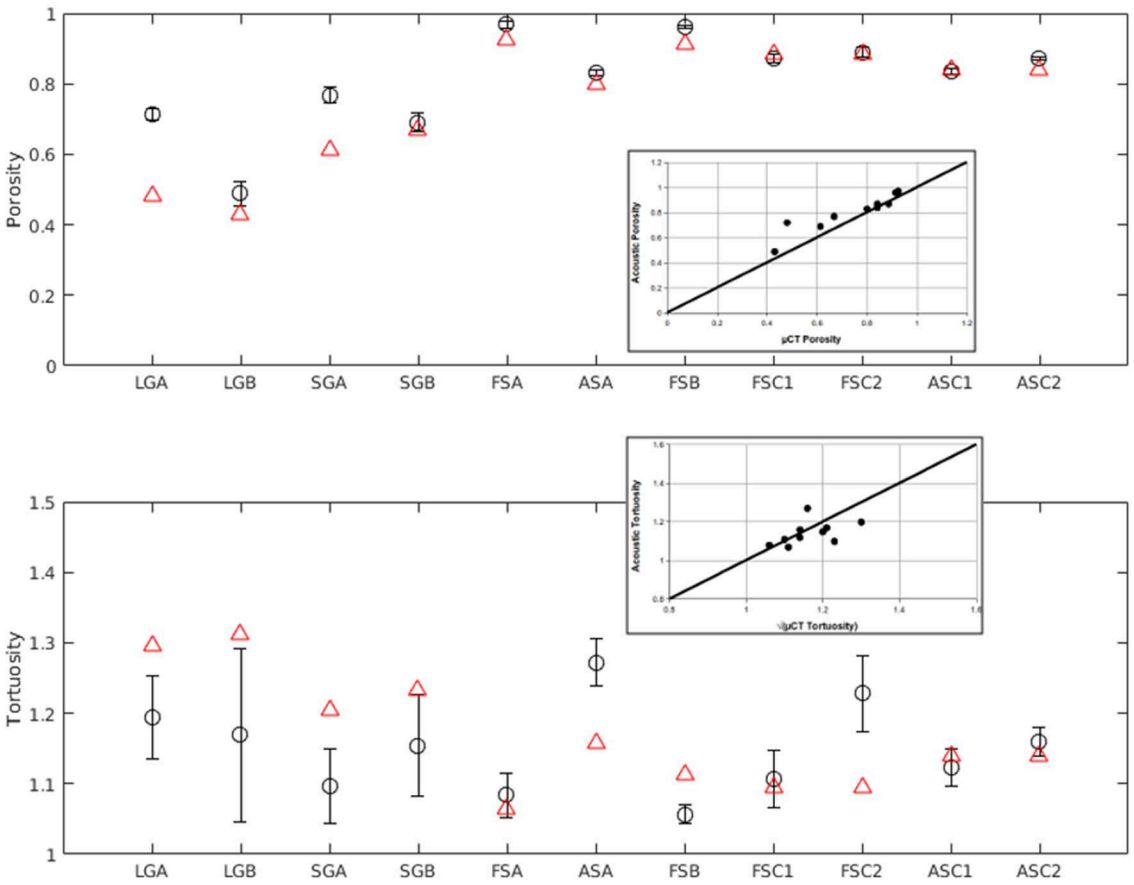

FIGURE 10 | Comparison of porosity and tortuosity values calculated from the acoustic measurements relative to μCT-measured values. For each graph, acoustic estimates are shown as black circles with the confidence interval indicated for each snow sample. μCT-measured values are plotted as red triangles. Insets for each graph show a scatter plot of μCT-measured values vs. acoustically-derived values, along with the 1:1 line.

TABLE 2 | Comparison of μCT and acoustic measured porosity and tortuosity results.

Sample name	μCT porosity	Acoustic porosity	μCT tortuosity	Sqrt (μCT tort)	Acoustic tortuosity	Pore wave speed (m/s)
SGA: small grain snow A	0.668	0.77	1.52	1.23	1.10	311
SGB: small grain snow B	0.613	0.69	1.45	1.20	1.15	304
LGA: large grain firn A	0.480	0.72	1.68	1.30	1.20	298
LGB: large grain firn B	0.430	0.49	1.72	1.21	1.17	301
FSA: fresh snow A	0.925	0.97	1.13	1.06	1.08	314
FSB: fresh snow B	0.913	0.96	1.24	1.11	1.07	315
FSC1: fresh snow 1	0.886	0.87	1.20	1.10	1.11	309
FSC2: fresh snow 2		0.89		1.10	1.23	294
ASA: FSA sample aged 1 day	0.799	0.83	1.34	1.16	1.27	289
ASC1: FSC sample aged 1 day	0.841	0.84	1.30	1.14	1.12	308
ASC2: FSC sample aged 1 day	0.841	0.87	1.30	1.14	1.16	303

were generally lower porosity (with one exception) but most of their tortuosities were near 1.0, with two samples at 1.2 and 1.7. Capelli et al. (2016) did make measurements of attenuation at high frequencies, using a pencil-lead-fracture as an impulsive acoustic source. Their measurements were in the 10–35 kHz band, but they reported only on the attenuation behavior of these waves.

All of these studies were done in containers or with contact transducers, while the method reported here used non-contact transducers and propagation, leaving the samples completely

undisturbed. We have only found one other paper (Gudra and Najwer, 2011) using a similar approach, and also at high frequencies. These researchers made vertical reflection measurements on snow samples at 40 kHz, recording the reflection from the snow surface and from the bottom of the container. They report reflection values of 0.2–0.5 for snow porosities from 0.89 to 0.5. Their values are higher than our measurements of 0.11 and 0.3 at the same endpoints, but tortuosity also plays a role [see the equation immediately after Equation (2)] and could be responsible for some of the differences.

CONCLUSION

The angular dependence of the reflection coefficient for various distinct snow types was shown to have a large, measurable signal that varied considerably with type of snow and porosity. A regression procedure on the set of reflection coefficients at all of the oblique angles of incidence produced porosity and tortuosity values with confidence intervals. The measurements showed that aging snow (sintering) 1 day causes detectable changes in acoustic response, slight decrease in porosity, and slight increase in tortuosity.

Porosity values determined from acoustic measurements were within 5% of porosity values determined from μCT data, overall. Tortuosities determined from acoustic waveforms shows the same trend as tortuosities calculated based on μCT data, but absolute values different by 8–30%, with best agreement found in fresh snow. Normal reflection has stronger dependence on porosity than on tortuosity.

These measurements show the potential utility of ultrasonic measurements as a method to determine fragile snow cover properties *in situ*. To do so, the acoustic positioning rig could be simplified and constructed as a metal half-arc capable of holding two transducers. Indentations could be made along the arc to "snap" the transducers into position at a few predetermined angles for measurement. A provision to make a vertical reflection should also be included, and a separate measurement at normal incidence with a metal plate on the ground could be used to determine the source transducer output. We were able to obtain reflection measurements from highly porous snow surfaces using only a 10 V PP output from a standard function generator, in contrast to most other studies that used hundreds of volts to excite the ultrasonic transducer, something we are too cowardly to try outdoors in wet snow!

DATA AVAILABILITY STATEMENT

The raw data supporting the conclusions of this article will be made available by the authors without undue reservation, to any qualified researcher upon request.

AUTHOR CONTRIBUTIONS

DA designed the project and contributed to the acoustic analysis. ZC prepared snow samples and wrote the introduction. JF conducted the ultrasonic acoustic experiments, prepared corresponding graphs, and wrote corresponding sections. RL conducted the μCT measurements, prepared corresponding graphs, wrote corresponding sections, and compiled all components of project. All authors edited and gave feedback on the manuscript.

FUNDING

This research was supported by the ERDC basic research program. DA and RL were supported in part by an appointment to the Environmental Management Participation Program at the U. S. Army Engineer Research and Development Center–Cold Regions Research and Engineering Laboratory (ERDC-CRREL) administered by the Oak Ridge Institute for Science and Education through an interagency agreement between the U. S. Department of Energy and ERDC. Permission to publish was granted by the Director of the Cold Region Research and Engineering Laboratory.

ACKNOWLEDGMENTS

The authors thank the two reviewers for many helpful comments which substantially improved the manuscript.

REFERENCES

Albert, D. G. (2001). Acoustic waveform inversion with application to seasonal snow covers. *J. Acoust. Soc. Am.* 109, 91–101. doi: 10.1121/1.1328793

Albert, D. G., Decato, S. N., and Carbee, D. L. (2008). Snow cover effects on acoustic sensors. *Cold Reg. Sci. Technol.* 52, 132–145. doi: 10.1016/j.coldregions.2007.05.009

Albert, D. G., Decato, S. N., and Perron, F. E. (2009). "*Experimental measurements of the Biot slow wave in natural snow covers*," *Paper Presented at Proceedings of the Fourth Biot Conference on Poromechanics* (New York, NY).

Albert, M. R., Albert, D. G., Perron, F. E., Ramos, I. (2008). *Acoustic Determination of Near-Surface Soil Properties.* US Army Cold Regions Research and Engineering Laboratory. Techincal Report.

Allard, J. F., and Atalla, N. (2009). *Propagation of Sound in Porous Media: Modelling Sound Absorbing Materials 2e*. Chichester: John Wiley & Sons.

Attenborough, K., Bashir, I., and Taherzadeh, S. (2011). Outdoor ground impedance models. *J. Acoust. Soc. Am.* 129, 2806–2819. doi: 10.1121/1.3569740

Attenborough, K., Li, K. M., and Horoshenkov, K. (2014). *Predicting Outdoor Sound.* New York, NY: Taylor and *Francis*.

Bennet, H. F. (1972). *Measurments of Ultrasonic Wave Velocities in Ice Cores From Greenland and Antarctica*. US Army cold regions research and engineering laboratory. *Research Report* 237.

Biot, M. (1956). The theory of propagation of elastic waves in a fluid-saturated porous solid, I. *Low-frequency range, II. Higher frequency range. J. Acoust. Soc. Am.* 28, 168–191. doi: 10.1121/1.1908239

Bonfiglio, P., and Pompoli, F. (2013). Inversion problems for determining physicial parameters of porous materials: overview and comparison between different methods. *Acta Acust. United Ac.*, 99, 341–351. doi: 10.3813/AAA.918616

Buser, O. (1986). A rigid frame model of porous media for the acoustic impedance of snow. *J. Sound Vib.* 111, 71–92. doi: 10.1016/S0022-460X(86)81424-9

Capelli, A., Kapil, J. C., Reiweger, I., Or, D., and Schweizer, J. (2016). Speed and attenuation of acoustic waves in snow: laboratory experiments and modeling with Biot's theory. *Cold Reg. Sci. Technol.* 125, 1–11. doi: 10.1016/j.coldregions.2016.01.004

Cooper, S. J., Bertei, A., Shearing, P. R., Kilner, J. A., and Brandon, N. P. (2016). TauFactor: an open-source application for calculating tortuosity factors from tomographic data. *SoftwareX*. 5, 203–210. doi: 10.1016/j.softx.2016.09.002

Cramond, A. J., and Don, C. G. (1984). Reflection of impulses as a method of determining acoustic impedance. *J. Acoust. Soc. Am.* 75, 382–389. doi: 10.1121/1.390482

Datt, P., Kapil, J. C., Kumar, A., and Srivastava, P. K. (2016). Experimental measurements of acoustical properties of snow and inverse characterization of its geometrical parameters. *Appl. Acoust.* 101, 15–23. doi: 10.1016/j.apacoust.2015.07.015

Don, C. G., and Cramond, A. J. (1987). Impulse propagation in a neutral atmosphere. *J. Acoust. Soc. Am.* 81, 1341–1349. doi: 10.1121/1.394540

Fellah, Z. E. A., Berger, S., Lauriks, W., Depollier, C., Aristegui, C., and Chapelon, J. (2003a). Measuring the porosity and the tortuosity of porous materials via reflected waves at oblique incidence. *J. Acoust. Soc. Am.* 113, 2424–2433. doi: 10.1121/1.1567275

Fellah, Z. E. A., Berger, S., Lauriks, W., Depollier, C., Trompette, P., and Chapelon, J. (2003b). Ultrasonic measurement of the porosity and tortuosity of air-saturated random packings of beads. *J. Appl. Phys.* 93, 9352–9359. doi: 10.1063/1.1572191

Fellah, Z. E. A., Fellah, M., Sebaa, N., Lauriks, W., and Depollier, C. (2006). Measuring flow resistivity of porous materials at low frequencies range via acoustic transmitted waves. *J. Acoust. Soc. Am.* 119, 1926–1928. doi: 10.1121/1.2179749

Gubler, H. (1977). Artificial release of avalanches by explosives. *J. Glaciol.* 19, 419–429. doi: 10.3189/S0022143000029440

Gudra, T., and Najwer, L. (2011). Ultrasonic investigation of snow and ice parameters. *Acta Phys. Pol. A* 120, 625–629. doi: 10.12693/APhysPolA.120.625

Herron, S. L., Langway, C. C., and Brugger, K. A. (1985). Ultrasonic velocities and crystalline anisotropy in the ice core from Dye 3, Greenland. *Greenland Ice Core Geophys. Geochem. Environ.* 33, 23–31. doi: 10.1029/GM033p0023

Hickey, C. J., and Sabatier, J. M. (1997). Measurements of two types of dilatational waves in an air-filled unconsolidated sand. *J. Acoust. Soc. Am.* 102, 128–136. doi: 10.1121/1.419770

Horoshenkov, K. V. (2017). A review of acoustical methods for porous material characterization. *Int. J. Acoust. Vib.* 22, 92–103. doi: 10.20855/ijav.2017.22.1455

Ishida, T. (1965). Acoustic properties of snow. *Contrib. Inst. Low Temp. Sci.* 20, 23–63.

Iversen, B. V., Schjonning, P., Poulsen, T. G., and Moldrup, P. (2001). *In-situ*, *on-site* and laboratory measurements of soil air permeability: boundary conditions and measurement scale. *Soil Sci.* 166, 97–106. doi: 10.1097/00010694-200102000-00003

Johnson, J. B. (1982). On the application of biot's theory to acoustic wave propagation in snow. *Cold Reg. Sci. Technol.* 6, 49–60. doi: 10.1016/0165-232X(82)90044-1

Kapil, J., Datt, P., Kumar, A., Singh, K., Kumar, V., and Satyawali, P. (2014). Multi-sensor couplers and waveguides for efficient detection of acoustic emission behavior of snow. *Cold Reg. Sci. Technol.* 101, 1–13. doi: 10.1016/j.coldregions.2014.01.003

Kinar, N. J., and Pomeroy, J. W. (2009). Automated determination of snow water equivalent by acoustic reflectometry. *IEEE T. Geosci. Remote.* 47, 3161–3167. doi: 10.1109/TGRS.2009.2019730

Kohnen, H., and Gow, A. J. (1979). Ultrasonic velocity investigations of crystal anisotropy in deep ice cores from Antarctica. *J. Geophys. Res.* 84, 4865–4874. doi: 10.1029/JC084iC08p04865

Lacroix, P., Grasso, J. R., Roulle, J., Giraud, G., Goetz, D., Morin, S., et al. (2012). Monitoring of snow avalanches using a seismic array: location, speed estimation, and relationships to meteorological variables. *J. Geophys. Res. Earth.* 117:F01034. doi: 10.1029/2011JF002106

Lieb-Lappen, R. M., Golden, E. J., and Obbard, R. W. (2017). Metrics for interpreting the microstructure of sea ice using X-ray micro-computed tomography. *Cold Reg. Sci. Technol.* 138, 24–35. doi: 10.1016/j.coldregions.2017.03.001

Maysenhölder, W., Heggli, M., Zhou, X., Zhang, T., Frei, E., and Schneebeli, M. (2012). Microstructure and sound absorption of snow. *Cold Reg. Sci. Technol.* 83, 3–12. doi: 10.1016/j.coldregions.2012.05.001

Nagy, P. B., Adler, L., and Bonner, B. P. (1990). Slow wave propagation in air-filled porous materials and natural rocks. *Appl. Phys. Lett.* 56, 2504–2506. doi: 10.1063/1.102872

Oura, H. (1952). Sound velocity in the snow cover. *Contrib. Inst. Low Temp. Sci. Ser. A* 9, 171–178.

Pialucha, T., and Cawley, P. (1994). The detection of thin embedded layers using normal incidence ultrasound. *Ultrasonics* 32, 431–440. doi: 10.1016/0041-624X(94)90062-0

Plona, T. J. (1980). Observation of a second bulk compressional wave in a porous medium at ultrasonic frequencies. *Appl. Phys. Lett.* 36, 259–261. doi: 10.1063/1.91445

Reiweger, I., Mayer, K., Steiner, K., Dual, J., and Schweizer, J. (2015). Measuring and localizing acoustic emission events in snow prior to fracture. *Cold Reg. Sci. Technol.* 110, 160–169. doi: 10.1016/j.coldregions.2014.12.002

Shimizu, H. (1970). Air permeability of deposited snow. *Contrib. Inst. Low Temp. Sci. Ser. A* 22, 1–32.

Sidler, R. (2015). A porosity-based Biot model for acoustic waves in snow. *J. Glaciol.* 61, 789–798. doi: 10.3189/2015JoG15J040

Smeulders, D. M. (2005). Experimental evidence for slow compressional waves. *J. Eng. Mech.* 131, 908–917. doi: 10.1061/(ASCE)0733-9399(2005)131:9(908)

Sommerfeld, R., and Gubler, H. (1983). Snow avalanches and acoustic emissions. *Ann. Glaciol.* 4, 271–276. doi: 10.3189/S0260305500005590

Suriñach, E., Furdada, G., Sabot, F., Biesca, B., and Vilaplana, J. (2001). On the characterization of seismic signals generated by snow avalanches for monitoring purposes. *Ann. Glaciol.* 32, 268–274. doi: 10.3189/172756401781819634

Umnova, O., Attenborough, K., Shin, H. C., and Cummings, A. (2005). Deduction of tortuosity and porosity from acoustic reflection and transmission measurements on thick samples of rigid-porous materials. *Appl. Acoust.* 66, 607–624. doi: 10.1016/j.apacoust.2004.02.005

Van Herwijnen, A., and Schweizer, J. (2011). Monitoring avalanche activity using a seismic sensor. *Cold Reg. Sci. Technol.* 69, 165–176. doi: 10.1016/j.coldregions.2011.06.008

Yamada, T., Hasemi, T., Izumi, K., and Sato, A. (1974). On the dependencies of the velocities of P- and S-waves and thermal conductivity of snow upon the texture of snow. *Contrib. Inst. Low Temp. Sci. Ser. A* 32, 71–80.

Conflict of Interest: The authors declare that the research was conducted in the absence of any commercial or financial relationships that could be construed as a potential conflict of interest.

frontiers in Earth Science

ORIGINAL RESEARCH
published: 19 March 2020
doi: 10.3389/feart.2020.00063

Experimental Study of Cone Penetration in Snow Using X-Ray Tomography

Isabel Peinke[1], Pascal Hagenmuller[1], Edward Andò[2], Guillaume Chambon[3], Frederic Flin[1] and Jacques Roulle[1]*

[1] Univ. Grenoble Alpes, Université de Toulouse, Météo-France, CNRS, CNRM, Centre d'Études de la Neige, Grenoble, France, [2] Univ. Grenoble Alpes, CNRS, Grenoble INP, 3SR, Grenoble, France, [3] Univ. Grenoble Alpes, INRAE, UR ETNA, Grenoble, France

The cone penetration test is widely used to determine the mechanical properties of snow and to delineate snow stratigraphy. Precise knowledge of the snow stratigraphy is essential for many applications such as avalanche forecasting or estimating the snowpack energy budget. With the development of sophisticated, high-resolution digital penetrometers such as the SnowMicroPenetrometer, the cone penetration test remains one of the only objective methods to measure snow stratigraphy. An accurate interpretation of the measured hardness profiles requires to understand the interaction between the cone tip and the snow material. In this study, we measured the displacement induced by the penetration of a conic tip with a radius of 2.5 mm in eight different snow samples using X-ray tomography. The experiments were conducted at a temperature of −10°C. To recover the full three-dimensional displacements between the tomographic images measured before and after the test, we specifically designed a tracking algorithm which exploits the unique shape of each snow grain. The tracking algorithm enables to recover most of the granular displacements and accurately captures the volumetric strain directly derived from density changes. The measured displacements are shown to be oriented downwards below the tip apex, upwards close to the snow surface, and nearly only radially in between. We observed and quantified the development of a compaction around and below the tip. Surprisingly, we also observed dilation of the snow material close to the snow and tip surfaces in very high-density samples. The radial extent of the compaction zone ranged between 1.6 and 2.3 times the tip radius. These results were compared to existing interpretative models. Although limited to relatively small samples and short penetration depths, these results provide new insights on snow deformation during a cone penetration test, and the validity of these models.

Keywords: snow, cone penetration test, CPT, image correlation, grain tracking, X-ray tomography

OPEN ACCESS

Edited by:
Michael Lehning, Federal Institute of Technology in Lausanne, Switzerland

Reviewed by:
Juerg Schweizer, WSL Institute for Snow and Avalanche Research SLF, Switzerland
Henning Löwe, WSL Institute for Snow and Avalanche Research SLF, Switzerland

***Correspondence:**
Pascal Hagenmuller
pascal.hagenmuller@meteo.fr

Specialty section:
This article was submitted to Cryospheric Sciences, a section of the journal Frontiers in Earth Science

Received: *20 September 2019*
Accepted: *20 February 2020*
Published: *19 March 2020*

Citation:
Peinke I, Hagenmuller P, Andò E, Chambon G, Flin F and Roulle J (2020) Experimental Study of Cone Penetration in Snow Using X-Ray Tomography. Front. Earth Sci. 8:63. doi: 10.3389/feart.2020.00063

1. INTRODUCTION

The cone penetration test (CPT) is widely used to determine the geotechnical engineering properties of soils and to delineate soil stratigraphy. This test consists of driving an instrumented tube with a conic tip into the ground and recording the forces required for penetration. In general, the recorded forces can include cone penetration resistance, sleeve friction and pore

pressure (e.g., Schmertmann, 1978; Mayne, 2007). Many investigations aimed to establish a frame to interpret CPT results. Most of them are based on empirical relations (Mayne, 2007). For instance, Robertson (2009) developed soil classification charts using the cone resistance and friction ratio based on empirical relations. Theoretical approaches have also been proposed and provided a useful framework of understanding. In particular, Bishop et al. (1945) introduced the cavity expansion model to retrieve the material properties of clay and sand from a CPT. Many of the current CPT inversion models in soil mechanics derive from this initial model, due to its ease of implementation and capability of describing elastic and plastic material deformation during CPT (e.g., Yu and Mitchell, 1998; Ruiz et al., 2016). However, Baligh (1986) showed that the cavity expansion model does not correctly account for the strain paths followed by soil elements, which could lead to inconsistencies in the subsequent test interpretation. Many studies have thus investigated the strain and stress paths at specific locations in a soil around a penetrating tip (e.g., White and Bolton, 2004). More recently, a full three-dimensional analysis of the deformation field was proposed by Paniagua et al. (2013) using X-ray tomography and digital image correlation.

The CPT, widely used and studied in geomechanics, was first adapted to snow with the ramsonde in the 1930's (Bader et al., 1939; Gubler, 1975). The ramsonde is a very simple and robust probe driven into the snow by mechanical hammer blows on its top. It is commonly used, e.g., by the observers of avalanche warning services to record snow hardness profiles. Ramsonde profiles provide an overall indication of snowpack structure, which can be used, for instance, to classify the snowpack as either potentially stable or potentially unstable with respect to avalanche release (Schweizer and Wiesinger, 2001). Several digital snow penetrometers have been developed to overcome the limited resolution of the ramsonde, e.g., the SnowMicroPenetrometer (SMP, Schneebeli and Johnson, 1998), the SABRE penetrometer (Mackenzie and Payten, 2002), or the SP2 (Avatech, see Hagenmuller et al., 2018). In addition, digital penetrometers initially designed for soils were also directly used to characterize the snowpack stratigraphy in Antarctica (McCallum, 2014). These instruments accurately determine the penetration resistance of thin layers and are able to capture numerous stratigraphic features of the snow cover (e.g., Pielmeier and Schneebeli, 2003). They can generally detect the presence of a weak layer of snow below a cohesive slab (Hagenmuller et al., 2018), which is an avalanche prone configuration (Schweizer et al., 2003). Reuter et al. (2015) derived promising quantitative indicators of snowpack stability directly from a SMP profile. Proksch et al. (2015) estimated the main snow structural parameters, namely density, correlation length, and specific surface area (SSA), solely from SMP profiles.

Snow differs from typical soils in two main aspects. Firstly, compared to soils, snow is a very fragile and porous material with a void ratio up to 90%. Thanks to the resulting low resistance, the CPT in snow can be performed at a constant speed (driven by a light-weight motor) with a small conic tip. Typically, the size of CPT tip radius in snow is of a few millimeters, and the typical snow grain size is about 0.1–1 mm. The penetration resistance is measured at high resolution in terms of force (around 0.01 N for the SMP) and vertical position (around 4 μm for the SMP) (Schneebeli and Johnson, 1998). The high-frequency fluctuations of penetration force with depth contain valuable information about snow microstructure, as they are directly linked to failure at bond scale (e.g., Löwe and Herwijnen, 2012). Secondly, snow exists on Earth at a high homologous temperature. Its mechanical behavior is therefore highly rate-dependent because of very rapid sintering processes and ice viscosity (e.g., Narita, 1983; Blackford, 2007; Peinke et al., 2019), in contrast to typical soils. In general, CPTs in snow are conducted with a penetration speed of a few centimeters per second. Reuter et al. (2019) estimated the induced strain rate to be about 100 s^{-1}. At this strain rate, snow mechanical behavior can be assumed to be brittle (Narita, 1983; Floyer and Jamieson, 2010) and numerical tests showed that inertial effects can be neglected (Hagenmuller et al., 2015).

Several specific models were proposed to interpret CPTs in snow (e.g., Johnson and Schneebeli, 1999; Marshall and Johnson, 2009). Löwe and Herwijnen (2012) used the framework of Homogeneous Poisson Processes to relate the measured force signal to the mechanical properties of individual bonds between snow grains. In particular, they assumed that the overall penetration force results from the superposition of spatially uncorrelated ruptures. These ruptures are supposed to be elastic brittle and to occur at the contact with the cone tip. This approach was generalized to the case of spatially inhomogeneous rupture intensities by Peinke et al. (2019). Ruiz et al. (2017) applied the cavity expansion model to analyse CPT in snow and to derive the elastic modulus and yield strength of the material.

These two classes of models are based on very different approaches. On the one hand, the cavity expansion model considers snow as a continuum material and describes the cone penetration by the formation of a cavity, with elastic and plastic zones surrounding the cavity. Further, only radial forces acting on the cone tip are considered. The typical cone-to-grain ratio for the SMP in snow is in the range 5–50 (Herwijnen and Miller, 2013), while after Bolton et al. (1993), the continuum media assumption reaches its limit for a ratio lower than 20. On the other hand, the Homogeneous Poisson Process model aims to identify the contribution of individual bond ruptures occurring directly next to the tip. This model accounts for the discrete nature of bond failures. However, experimental studies showed the formation of a significant compaction zone around the cone tip (e.g., Herwijnen, 2013; LeBaron et al., 2014), which challenges the assumptions of the Homogeneous Poisson Process model. In particular, the effective radius of the cone tip is increased by the compaction zone, and the rupture events may be spatially correlated. Knowledge of the strain paths around the penetrating tip are thus essential to interpret the measured force profiles.

Different studies aimed at investigating the displacement of snow grains induced by a CPT. Herwijnen (2013) used particle image velocimetry to quantify the displacement around the tip. With a digital video camera, they recorded images of the front face of a snow box via a viewing window through which the progression of the SMP tip could be observed. They also acquired micro-tomographic images of snow samples after the SMP tests to measure the radial density field from mean pixel intensity.

They observed a compaction zone with a radius equal to twice the cone radius, on average. The radius of this zone was shown to increase with snow density. Further, they observed that the size of this zone stabilizes after about 40 mm of penetration. LeBaron et al. (2014) also used particle image velocimetry on two-dimensional images of a split-axis snow micro-penetrometer along a viewing window. They observed a compaction zone diameter of about three times the tip diameter. Its radial cross-section area was estimated to be about 10 times larger than that of the SMP tip. Assuming axial symmetry, the compaction zone volume was estimated to be about 1 cm^3, with nearly 50% of the volume ahead of the tip. Floyer and Jamieson (2006, 2010) measured the extension of compaction and deformation zone with particle image velocimetry on a rounded-tip penetrometer. They observed a characteristic spike in the force signal during the initial stage of deformation and showed that this spike corresponds to the development of the compaction zone below the penetrometer tip.

The goal of this study is to quantify the three-dimensional deformation field in snow around the CPT tip, which is critical to interpret the recorded force signals. To this end, we combined micro-tomography and CPT, and developed a novel tracking method based on digital image correlation and matching of grain characteristics. The displacements at grain scale can then be recovered, from which the deformation around the tip is evaluated. The method was applied to samples spanning different snow types, thereby providing new insights and valuable information to assess the consistency of existing models.

2. METHODS

2.1. Experiments

We conducted CPT in eight samples of different snow types, and measured the induced deformation through micro-tomography (μCT).

2.1.1. Sample Preparation

The snow samples were prepared by sieving natural snow into sample holders dedicated to tomography and letting them rest by, at least, 24 h before conducting the measurements. The preparation of the samples and the experiments were performed in a regulated cold room at a constant temperature of $-10°C$. The samples covered a variety of seasonal snow types, namely rounded grains (RG), large rounded grains (RGlr), depth hoar (DH) and precipitation particles (PP), with bulk densities between 90 and 560 kg m^{-3} and specific surface areas between 10 and 54 m^2 kg^{-1} (**Table 1**). The sample holders were aluminum cylinders, which have the advantage of high thermal conductivity and relatively low X-ray absorption. Their size was limited to 2 cm height and 2 cm diameter, in order to enable μCT imaging with a pixel size small enough to resolve snow microstructure.

2.1.2. Micro-Tomography (μCT)

Two tomographic images of each sample were acquired: one before (pre-CPT image) and one after (post-CPT image) the CPT. The samples were scanned at a pixel size of 15 μm pix^{-1} with an X-ray tomograph (RX Solutions). The X-ray tube was powered by a voltage of 80 kV and a current of 100 μA. Each scan consisted of 1,440 radiographs covering a 360° rotation. In order to maintain a constant and uniform temperature of $-10°C$, a cryogenic cell (CellDyM) was used (Calonne et al., 2015).

TABLE 1 | Overview of the eight snow sample properties.

Sample name	Snow type	Sieve size (mm)	Density (kg m^{-3})	SSA (m^2 kg^{-1})
RG1	Rounded Grains (RG)	1.6	289	23.0
RG2	Rounded Grains (RG)	1.6	304	23.7
RGlr1	Large Rounded Grains (RGlr)	1	530	10.1
RGlr2	Large Rounded Grains (RGlr)	1	544	10.3
RGlr3	Large Rounded Grains (RGlr)	1	557	9.86
DH1	Depth Hoar (DH)	1.6	345	16.9
DH2	Depth Hoar (DH)	1.6	364	15.9
PP1	Precipitation Particles (PP)	1.6	91.3	53.5

Snow types are classified according to Fierz et al. (2009). Sample density and specific surface area (SSA) were derived from the μCT images.

The sets of radiographs were reconstructed into three-dimensional grayscale images representing the attenuation coefficients of the different materials composing the samples. Marks on the sample holder permitted us to register the pre- and post-CPT images, and correct unavoidable shifts due to movements of the tomograph elements with a sub-voxel accuracy. The aluminum sample holder was then masked in the images, and the ice was segmented from the air using the energy-based segmentation developed by Hagenmuller et al. (2013). Local density in the pre-CPT image (ρ_{pre}) and in the post-CPT image (ρ_{post}) were computed on the binary images by voxel counting. Surface areas were computed on the segmented images by Crofton approach, which showed good accuracy on anisotropic structures (Hagenmuller et al., 2016). The ratio between the area of the air/ice interface and the mass of ice defines the specific surface area (SSA).

2.1.3. Cone Penetration Tests (CPT)

The CPTs were conducted by inserting a cylinder of radius $R = 2.5$ mm with a conic tip of 60° apex angle, into the snow samples (**Figures 1A,B**). Note that the cylinder radius is the same as the cone maximum radius. The tip used here is thus slightly different from that classically used with the SnowMicroPenetrometer (SMP), for which penetrating cone has a slightly larger diameter than the driving cylinder (see Schneebeli and Johnson, 1998). This cylinder with a conic tip was mounted on the SMP (version 4, Schneebeli and Johnson, 1998) to control the vertical displacement and measure the penetration force. The SMP force sensor (Kistler 9207) measures forces in the range of [0, 40] N with a resolution of 0.01 N. The samples were placed on a micrometric positioning plate, which allowed us to perfectly center the tip in the snow sample (**Figure 1C**). After the acquisition of the first μCT image of the sample, the cone was inserted vertically at a constant speed of 20 mm s^{-1}. The penetrometer was not removed from the sample directly after the test, to let the loosened snow grains sinter. This waiting

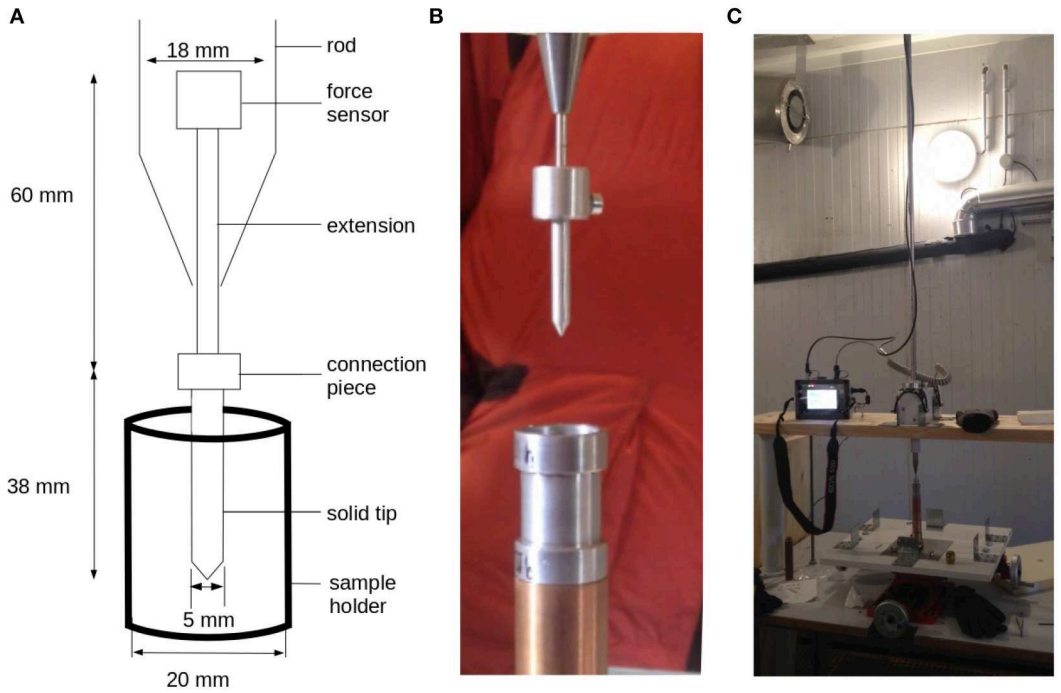

FIGURE 1 | Set-up of cone penetration tests: **(A)** scheme of the cone tip, **(B)** photo of the cone tip, and **(C)** photo of the whole experimental setup with the positioning plate.

time avoided any grain to fall into the cavity created by the cone removal. In our tests, the cone tip reached an average depth of 10–15 mm, corresponding to an approximate distance of 5–10 mm to the sample bottom.

2.2. Displacement Analysis

Snow mechanical behavior is highly rate-dependent, in particular due to very active sintering between grains. Hence, incremental CPTs followed by μCT, as conducted in sand (e.g., Paniagua et al., 2013), are not suitable for snow. The advantage of incremental CPTs is to have small grain displacements between two successive μCT scans (e.g., Andò et al., 2012). Here, we measured only the initial, intact snow microstructure and its final state after CPT. Characterizing the large grain displacements between these two images is a notoriously challenging task. However, at the considered penetration rate, snow behaves as a brittle material (e.g., Narita, 1983; Floyer and Jamieson, 2010) and can reasonably be considered as a granular assembly, i.e., we can assume that each grain moves as a solid body (Johnson and Hopkins, 2005; Hagenmuller et al., 2015). This feature was exploited to retrieve the displacement fields by combining: (1) tracking of individual grains (ID-track, Andò et al., 2012) based on their geometrical properties to obtain an initial displacement guess, and (2) digital image correlation (DIC) to refine this guess and achieve high accuracy and resolution (Hall et al., 2010).

2.2.1. Grain Segmentation

In order to track individual grains between the pre- and post-CPT images, a first identification of snow grains in the binary images of ice and air is required. Individual grains were segmented by applying a curvature-based algorithm developed by Hagenmuller et al. (2014). This algorithm detects preferential zones of mechanical weakness based on two geometrical criteria: negative minimal principal curvature and low contiguity between the grains. A threshold of $\kappa_t = 1.0$ on normalized curvature was used, as suggested by Hagenmuller et al. (2014). A contiguity parameter of $c_t = 0.1$ was chosen, to limit the number of grains by detecting only the thinnest bonds (see details in Hagenmuller et al., 2014).

2.2.2. ID-Track

The ID-Track follows the approach of Andò et al. (2012). The main idea is to pair grains in the pre- and post-CPT images which have similar geometrical properties and whose derived displacement is consistent. To this end, we considered three criteria on grain geometry: (i) similar grain volume (relative difference less than 50%), (ii) similar grain elongation (relative difference less than 50%), and (iii) large overlap (grains overlapping by at least 70%) between the grains aligned along their principle axis of moment of inertia. In addition, we considered two criteria on the resulting displacement between the paired grains: (i) small distance between the grain centers of mass in the two images (<20 voxels), and (ii) a globally outward displacement vector with respect to the cone center (i.e., the grain moves away from the cone). For each grain in the pre-CPT image, several grains of the post-CPT image may satisfy these five criteria. To select the best candidate out of this grain set, digital image correlation is used (see section 2.2.3).

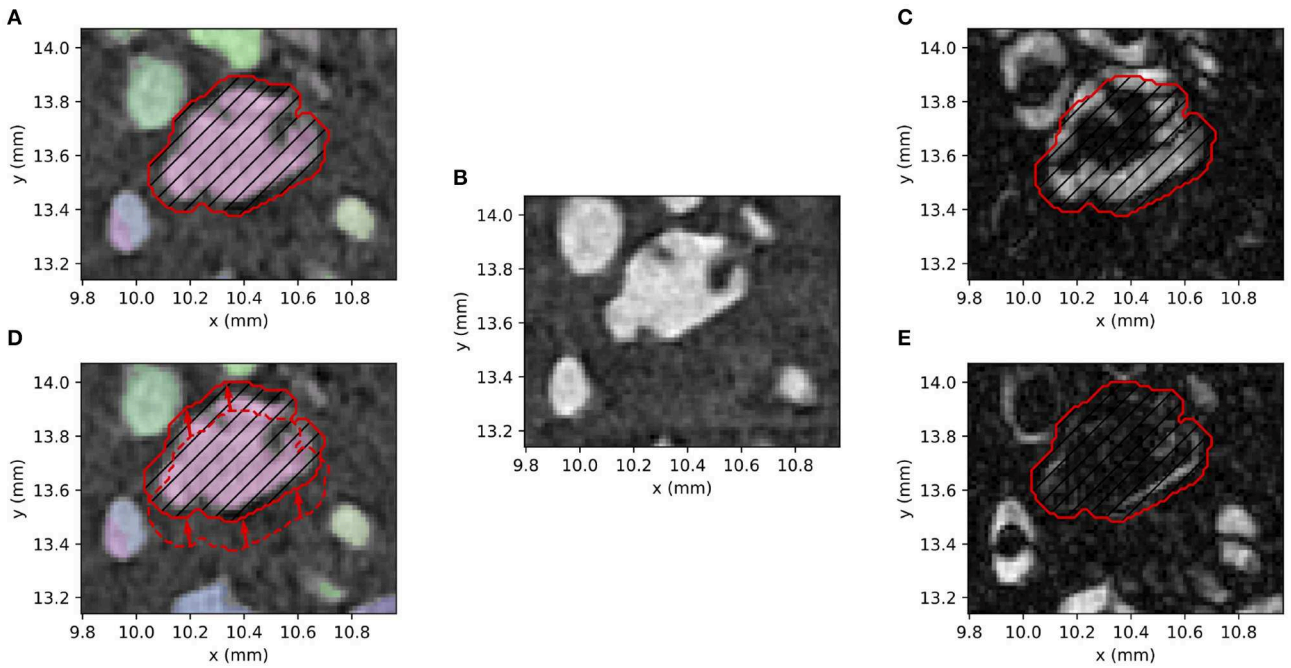

FIGURE 2 | Digital image correlation technique: **(A)** selection of one grain in the pre-CPT image and associated analysis window (dashed area), **(B)** post-CPT image, **(C)** grayscale difference of the pre- and post-CPT images with the analysis windows, **(D)** displaced pre-CPT image with the displaced (red, solid line) and initial analysis windows (red, dashed line), **(E)** grayscale difference of the displaced pre-CPT and post-CPT images.

2.2.3. Digital Image Correlation

The digital image correlation method follows the approach of Hall et al. (2010). The main idea is to perform digital image correlation between the pre- and post-CPT grayscale images on numerous analysis windows corresponding to each individual grain of the initial image. **Figure 2** shows the main steps of these three-dimensional method in a simplified two-dimensional scheme for one grain. First, an analysis window surrounding the grain of interest is defined (**Figure 2A**). The window corresponds to the grain volume dilated in the air (but not in neighboring grains) by three voxels. Then, a standard image registration is performed to find the transformation that best matches the pre- and post-CPT images masked on the analysis windows (**Figure 2E**). The quality of this match is quantified by the cross-correlation between the transformed pre-CPT image and the post-CPT image. The possible transformations were limited to solid displacements (6 degrees of freedom: 3 translations, 3 rotations). If the final value of the registration metric exceeded $CC_{max} = 0.75$, the registration was considered successful, i.e., the grain in the pre-CPT image is correctly detected in the post-CPT image. Python package SimpleITK (Yaniv et al., 2018) (module ImageRegistrationMethodv4 with gradient descent optimization and linear interpolation) was used to perform this image registration.

The example presented in **Figure 2** shows a grain with a small displacement between the pre- and post-CPT images. In case of larger displacements, the registration optimizer does not necessarily find the optimum of the registration metric in the complex domain of solid transformations. In that case, the displacements estimated by the ID-track method were used to seed the digital image correlation (see section 2.2.4).

2.2.4. Application to Experiments

To optimize computing costs, ID-track and digital image correlation were combined as follows. First digital image correlation was performed with a null displacement as seed. This first pass detects most of the small displacements under 10 voxels magnitude (corresponding to about 80% of the total grains). The successfully matched grains in the pre- and the post-CPT images are then masked before applying the ID-track, which significantly reduces the computing cost. ID-track is then used with relatively restrictive criteria to detect potential pairs of grains and the associated displacement seeds. Finally, digital image correlation is applied with these seeds to find the best image of the moved grains, and refine the displacement seeds to sub-voxel accuracy. If the best result (quantified by the coefficient of correlation between the grayscale images) exceeds the threshold of $CC_{max} = 0.75$, the grain is assumed to be successfully matched. In addition, a last method was applied to the remaining unmatched grains. We used the idea that a grain most likely moves like its neighbors, and seeded the image correlation method for these remaining grains with the displacements of the seven closest grains whose displacements were already detected.

2.2.5. Additional Metrics of Snow Deformation

The proposed methodology provides the full 3D displacement field $\boldsymbol{u}(r, \theta, z)$ at grain scale during a CPT in snow. However, some grains may not be successfully tracked between the pre- and

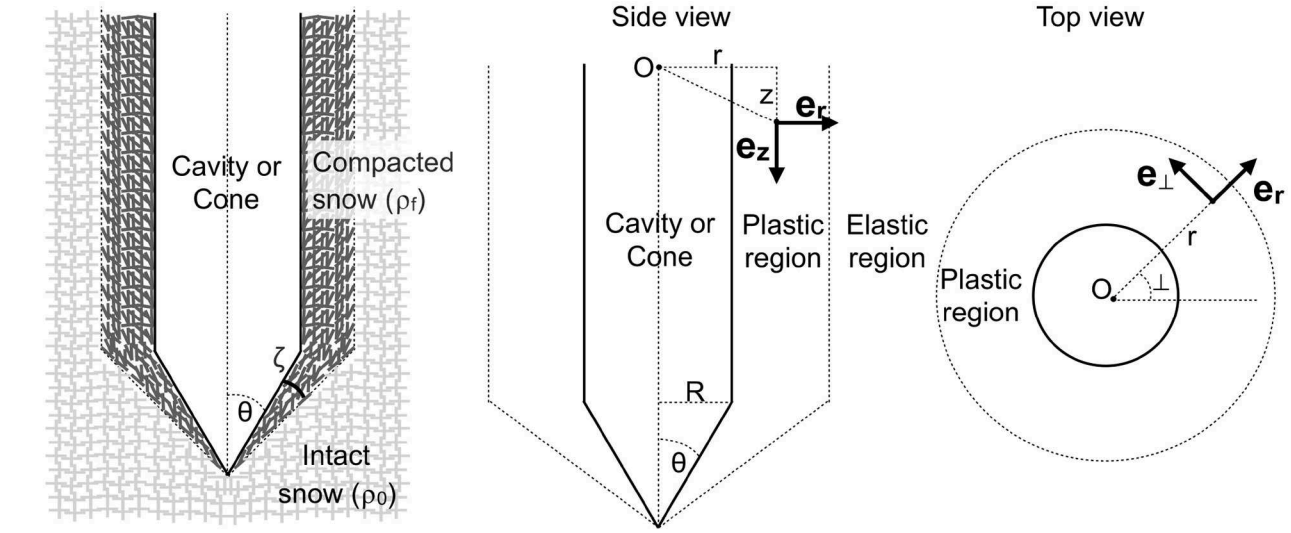

FIGURE 3 | (A) Compaction angle model and **(B)** different regions and coordinate system used in the cavity expansion model.

post-CPT images, and variability at the grain scale might hide the overall behavior. Therefore, in addition to the 3D displacement at grain scale, we computed averaged displacements in the (r, z) plane and along the radial position (**Figure 3**). To this end, we defined a grid with a vertical step $dz = 0.6$ mm and radial step $dr = 0.45$ mm. Assuming that the displacement is invariant with rotation around the cone axis, we defined the average vertical and radial displacements $(\overline{u_z}(r,z), \overline{u_r}(r,z))$ as the averages of u_z and u_r over all azimuthal positions, respectively. The radial profiles $\overline{\overline{u_z}}(r)$ and $\overline{\overline{u_r}}(r)$, were defined as vertical averages of $\overline{u_z}$ and $\overline{u_r}$ over the cylindric part of the penetrometer and up to a height equal to tip radius (**Figure 3**).

The evolution of density next to the cone can be directly derived from the tomographic images (see section 2.1.2) but also from the displacement field. With the assumption of small strain and axial symmetry, the density in the post-image $\rho_{post,disp}$ can be related to the density in the initial image ρ_{pre} via the volumetric strain (defined as the trace of the strain tensor, here expressed in cylindrical coordinates) as:

$$\rho_{post,disp} = \left(1 + \frac{\partial \overline{u_r}(r,z)}{\partial r} + \frac{\overline{u_r}(r,z)}{r} + \frac{\partial \overline{u_z}(r,z)}{\partial z}\right) \times \rho_{pre} \quad (1)$$

Finally, we defined the deformation zone as the zone where displacement magnitude is larger than 30 μm (about 20% of typical grain size, see **Table 1**) and the compaction zone as the zone where density change is larger than 5%, i.e., $0.95 < \rho_{post}/\rho_{pre} < 1.05$. The deformation zone is thus defined from the tracking results and the compaction zone solely from the local densities directly derived from the pre- and post-CPT images.

2.3. Theoretical Displacement Field Analysis

In this section, we present two existing, mechanically-based, interpretation models for CPT: the first is based on the angle of compaction around a penetrating cone, and the second is based on the cavity expansion model.

2.3.1. Angle of Compaction

Johnson (2003) defines the angle of compaction ζ as the angle of the compaction zone relative to the cone surface (**Figure 3A**). The model assumes that grains inside the compaction zone have the same size and microstructural properties as outside the zone. It is also assumed that grain bonds can only fail at the interface between the compaction zone and intact snow. Before failure is reached, the snow grains deform elastically in a direction normal to the penetrometer surface. After failure, the grains compact until they lock up, also in normal direction (**Figure 3A**). Johnson (2003) showed that the angle of compaction ζ depends on the half cone angle θ of the penetrometer tip, the initial density ρ_0 and the density ρ_f in the compaction zone as follows:

$$\zeta = \tan^{-1}\left[\tan\theta\left(\frac{1}{\sqrt{\beta}} - 1\right)\right] \quad (2)$$

where β is defined as the average volumetric strain in the compacted zone, i.e., $\beta = (1 - \rho_0/\rho_f)$. Equation (2) is easily applicable to our measurements, as density is directly measured on the tomographic images. The value of ρ_0 and ρ_f were computed in the area close to the cone tip, namely for radial positions in the range $[1, 1.5]R$ (with R the cone radius, see **Figure 3B**), on the pre- and post-CPT images, respectively.

2.3.2. Cavity Expansion Model

Bishop et al. (1945) first pointed out the possibility to compute an approximate value for the load required to force a cone deep into an elasto-plastic continuum material. We consider here a cylindrical (given the shape of the tip) cavity expansion model in an infinite medium, with a zero initial cavity radius. Snow is described as a cohesive-frictional material with a non-associated Mohr-Coulomb model. The analytical approximate solution of the cavity expansion problem proposed by Yu and Carter (2002) is used.

The Mohr-Coulomb model for snow involves the following material parameters: Young's modulus E, Poisson's ratio ν, angle of friction ϕ, angle of dilation ψ, and cohesion C. Typical values for these parameters were chosen according to Mellor (1975) (**Table 2**). The boundary conditions far from the cavity are characterized by a hydro-static pressure p_0, that was here set to 0. Similarly to Ruiz et al. (2017), an interfacial friction coefficient $\mu = 0.5$ between the tip and the snow was considered.

The cavity expansion model distinguishes three zones: the cavity (position of the penetrating cone), a surrounding plastic zone, and an outer elastic zone (**Figure 3B**). Yu and Carter (2002) showed that the radial and orthoradial normal stress components σ_r and $\sigma_\perp$ in the elastic region can be obtained from the equilibrium equation and elastic stress-strain relations as follows:

$$\sigma_r = -p_0 - Br^{-2}$$
$$\sigma_\perp = -p_0 + \frac{B}{2}r^{-2}$$

where r is the radial coordinate (**Figure 3B**) and B is a constant of integration (see Equation 54 in Yu and Carter, 2002). In the plastic region, Yu and Carter (2002) found that the stress components satisfying the equilibrium equation and the yield condition are:

$$\sigma_r = \frac{Y}{a-1} + Ar^{-\frac{a-1}{a}}$$
$$\sigma_\perp = \frac{Y}{a-1} + \frac{A}{a}r^{-\frac{a-1}{a}}$$

where $Y = \frac{2C\cos\phi}{1-\sin\phi}$ is the yield stress, $a = \frac{1+\sin\phi}{1-\sin\phi}$, and A is a constant of integration (see Equation 53 in Yu and Carter, 2002). The resulting penetration force F_p acting on the cone is computed similarly to Ruiz et al. (2017). The radial force acting on the conical tip is given by:

$$F_r = 2\pi\cot(\theta)\int_0^R \sigma_r(r)r dr$$

where R is the maximal cone radius. The resulting axial force required for cone penetration is, in the frictionless case:

$$F_z = F_r\tan(\theta)$$

By adding frictional effects, the resulting total penetration force is:

$$F_p = F_z(1 + \mu\cot(\theta)) \quad (3)$$

TABLE 2 | Material parameters describing snow as a Mohr-Coulomb material, and results of sensitivity analysis on force and displacement computed by the cavity expansion model.

Property	Symbol	Chosen value	Range	Displacement change (%)	Force change (%)
Young's modulus (Pa)	E	10^8	$[10^5, 10^{10}]$	22	152
Poisson's ratio	ν	0.2	[0.1, 0.4]	0.2	3
Angle of friction (°)	ϕ	20	[10, 30]	0.03	44
Angle of dilation (°)	ψ	−30	[−20, −40]	125	91
Cohesion (Pa)	C	10^3	$[10^2, 10^4]$	0.6	192

The model prescribes a purely radial displacement field. The displacement in the elastic zone is given by:

$$u = \delta r\left(\frac{c}{r}\right)^2$$

with δ and c depending on the material parameters (see Equations 40 and 55 in Yu and Carter, 2002). The displacement in the plastic zone depends on the plastic flow rule. With a non-associated Mohr-Coulomb flow rule, the explicit expression of the radial displacement is complex. Displacement in this zone was computed by numerically integrating the so-called incremental velocity V (derivative of radial displacement with respect to cavity radius expansion), whose analytical expression is:

$$V = \gamma\left(\frac{c}{r}\right)^{-\frac{1}{a}} + [2\delta - \gamma]\left(\frac{c}{r}\right)^{\frac{k}{\beta}}$$

where β and γ are constants defined in Equations (39) and (74) in Yu and Carter (2002).

Figure 4 shows the displacement field computed for the parameter values indicated in **Table 2**, as well as the corresponding density changes (computed from Equation 1) and force profile. Most of the displacement and density changes take place in a region of about $1.5R$ (**Figures 4A,B**). The force profile shows a parabolic increase with depth until the conical part of the tip has completely penetrated the snow material, followed by a linear increase with depth due to friction (**Figure 4C**).

We evaluated the sensitivity of the computed displacements and forces on the material parameters (**Table 2**). To this end, each parameter was varied in a realistic range (see column "range" in **Table 2**), while the other parameters were kept constant (see column "chosen value" in **Table 2**). The impact of the parameter values was evaluated on the radial force at the interface between the plastic and the cavity regions, and on the mean displacement for radial positions in the range $[1, 4]R$. In both cases, **Table 2** reports relative differences with respect to values obtained with the "chosen value" of the parameter. Results show that the displacement field is almost only controlled by the angle of dilation ψ. In contrast, the force mainly depends on the cohesion C, Young's modulus E, and angle of dilation ψ.

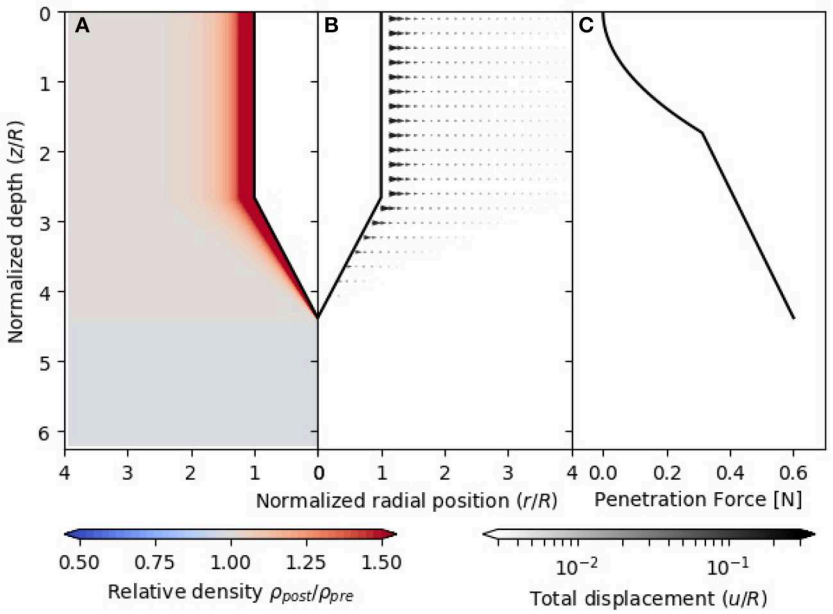

FIGURE 4 | Analytical solution of the cavity expansion model by Yu and Carter (2002): **(A)** relative density change, **(B)** displacement field normalized by tip radius R, and **(C)** penetration force profile. The relative density change is defined as the ratio between the density ρ_{post} after the CPT and the density ρ_{pre} before the CPT.

3. RESULTS

In this section, we first evaluate the performance of the tracking algorithm on the experimental data. The CPT-induced displacement field and compaction zone are then analyzed. Finally, the measured displacement and force are compared to the predictions of the mechanical models presented in section 2.3.

3.1. Tracking of Snow Grains

Figure 5 displays the grains in the pre-CPT image and the displacements induced by cone penetration for sample RG1. Similar figures for other samples can be found in **Figure S2**. We observe significant displacements in a region of about twice the cone radius. In general, movements are directed outwards and downwards, but also upwards close to snow surface. Note that displacements are here plotted as straight lines between the initial and final positions, which might not correspond to the exact grain trajectory, especially for large displacements.

The tracking algorithm fails to recover the displacement of all grains (see white grains in **Figure 5**). Nevertheless, as shown in **Table 3**, 90% of the grains, at least, were successfully tracked. Most of grains did hardly move, and were thus easy to track. However, in the zone of radius $2R$ where the largest displacements are observed, about 40–80% of the grains were still successfully tracked. If we only consider the grains initially located in the cavity, i.e., the zone occupied by the cone tip after the CPT, about 10–50% of the grains were successfully tracked.

The percentage of tracked grains depends on snow type. The algorithm detects the largest percentage of grains in samples composed of large rounded grains (RGlr), followed by depth hoar (DH) and rounded grains (RG). The lowest percentage of detection is obtained for samples composed of precipitation particles (PP). The grains composing the RGlr and DH samples are large and exhibit relatively unique shapes (see **Figure S1**), which makes the ID-track particularly efficient. Additionally, the tracking method also relies on the consistency of the grain segmentation. Grains can be efficiently tracked only if they are segmented in the same way in pre- and post-CPT image, without over- or under-segmentation. On RGlr or DH snow types, individual grains can generally be unambiguously identified, whereas the definition of grains in the PP type strongly depends on the chosen segmentation thresholds and can be affected by potential noise at the ice-air interface (Hagenmuller et al., 2014).

Accuracy of the computed displacement field was evaluated through two different approaches. Let us first recall that a grain is considered as successfully tracked when a correlation coefficient larger than $CC_{max} = 0.75$ is obtained between the pre- and post-CPT images (see sections 2.2.3 and 2.2.4). While this threshold indicates that the associated grains are similar, it does not guarantee that the association is physically correct. Hence, we checked visually the computed displacements on some selected grains, which appeared to be correct according to the displacements of the neighboring grains (**Figure 5**). More quantitatively, the obtained displacements were used to compute the density $\rho_{post,disp}$ in the post-CPT image (see Equation 1), which can be compared to the density directly measured on the post-CPT image ρ_{post}. This calculation provides a quantitative evaluation of the tracking method accuracy. In details, volumetric strain was computed only in regions with small displacements (radial and vertical displacements smaller than 30 voxels, i.e., 0.45 mm), so that the assumption of infinitesimal strain remains valid. As shown in **Figure 6**, values of $\rho_{post,displ}$ and ρ_{post}

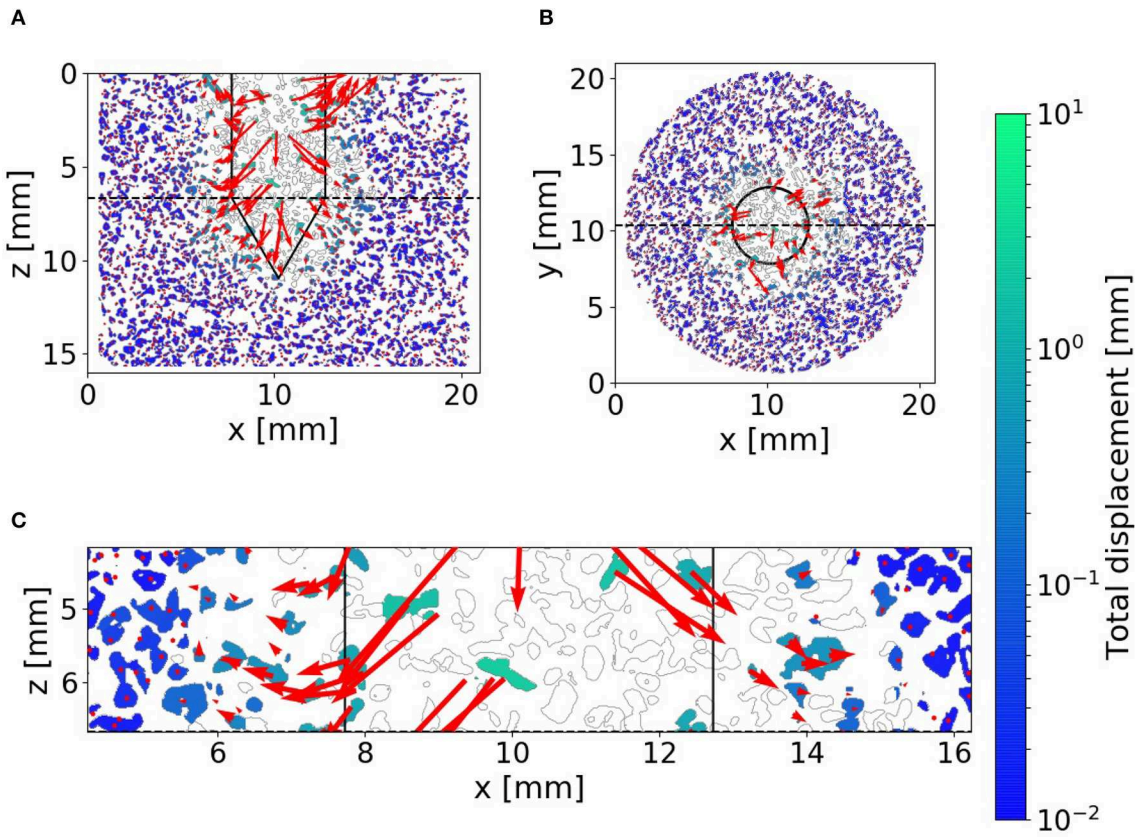

FIGURE 5 | Tracked displacement field for sample RG1 shown on **(A)** a vertical slice, **(B)** a horizontal slice, and **(C)** a zoom on the vertical slice. The dotted line in the vertical slice shows the position of the horizontal slice and vice versa. The contours of the grains in the pre-CPT image are shown in gray. Colors indicate the absolute displacement, and arrows show displacement components in the slice plane.

generally follow the 1:1 line, which indicates the consistency of the computed displacement field. The deviations tend to increase with the total displacement, which indicates that their might partially be due to the small strain assumption used for density calculation from the displacement field. Small deviations may also originate from segmentation errors of the ice, which can cause variations of the density of up to 5% according to Hagenmuller et al. (2016). Finally, some outliers can be observed, especially for DH and RGlr snow types, which exhibit the lowest relative compaction.

3.2. Analysis of the Deformation Around the Cone

3.2.1. Deformation and Compaction Zones

Figure 7 shows density changes and averaged displacement fields in the (r, z) plane for samples RG1 and DH2 (corresponding plots for the other samples are provided in **Figure S2**). Both radial and vertical displacements are observed. Vertical displacements are oriented upwards close to the surface, and tend to be downwards close to the tip apex. Upward movements close to snow surface tend to be more pronounced for snow types RGlr and DH, whereas downward movements close to the apex are more pronounced for snow type RG. The displacement field generally varies with both r and z, precluding the existence of solid blocks of compacted snow moving downwards or radially with the tip. The deformed zone rather progressively forms and evolves with cone penetration. Cone penetration is associated to compaction next to the tip in moderately dense samples (samples RG1, RG2,

TABLE 3 | Total number of grains and percentage of tracked grains in the different snow samples.

		Percentage (%) of tracked grains in a zone corresponding to		
Sample	**Total number of grains**	**The whole sample**	**Twice the tip radius**	**The cavity**
RG1	68,880	92	50	17
RG2	90,316	90	39	13
RGlr1	16,314	97	77	51
RGlr2	17,846	92	54	41
RGlr3	18,026	93	51	13
DH1	27,738	90	39	13
DH2	27,263	95	68	42
PP1	34,901	90	39	11

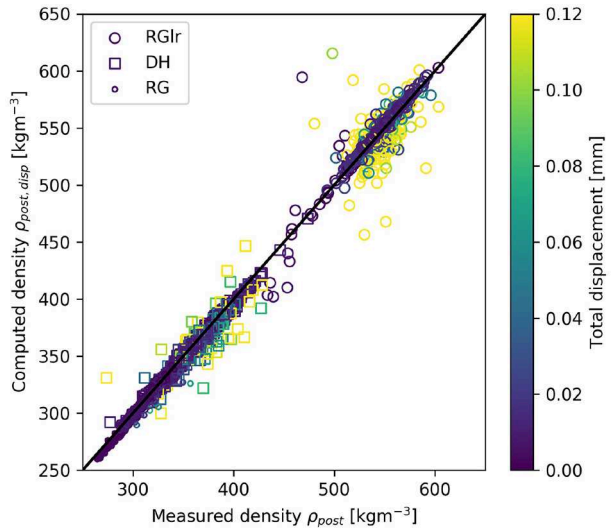

FIGURE 6 | Comparison between the post-CPT density computed from the displacement field $\rho_{post,disp}$ and the post-CPT density directly measured on the tomographic image ρ_{post} for the seven snow samples of type RG, RGlr and DH. Snow type is distinguished by point symbol. The points are colored according to their total displacement. Computed density is considered as representative, and shown on the figure, only if more than 30% of the grains are successfully tracked in the considered sub-volume.

PP), but to dilation in denser samples (samples RGlr1, RGlr2, RGlr3, DH1, DH2).

Figure 7 shows (black contour) the deformation zone and the compaction zone for two samples. Recall that these zones are based on thresholds on the volumetric deformation and absolute density change, respectively (see section 2.2.5). The radial and vertical extents of these two zones depend on the considered sample. **Table 4** summarizes the average values obtained for all samples. For sample PP1, we did not track enough grains to derive the deformation zone. Sample RGlr2 showed an upward movement in the whole cylinder, probably due to the deformation zone reaching sample bottom. In this case, no relevant deformation zone can be determined. In general, the radial extent of this zone varies between $1.8 - 2.7R$, with the highest values for snow type DH, followed by RGlr and RG (**Table 4**). The radial size of the deformation and compaction zones are similar for RG samples, while the compaction zone is slightly smaller than the deformation zone for RGlr and DH samples. Lastly, RG and PP samples show compaction zones of similar radial extents (about $2R$). The vertical extents of the deformation and compaction zones are similar, and smaller or equal than $1R$, for all samples.

3.2.2. Radial Profiles

A fast decay of the vertical and radial displacements with the radial position is observed for the different samples (**Figure 8**). The definition of the deformation zone (see section 2.2.5) is thus not very sensitive to the chosen displacement threshold. The vertical displacements are the smallest for RG samples, and the largest for RGlr and DH samples. They are positive (downwards) for RG samples and negative (upwards) for the other snow types. Radial displacements are of the same magnitude for all snow types.

Density change profiles (**Figure 9**) clearly show that compaction or dilation is located in a zone whose radius is about $2.5R$. As expected, largest density changes are observed close to the cone tip. Clear compaction is observed for snow types RG and PP, with maximal compaction values between 1.4 and 1.5. In addition, the strongest relative compaction is observed for the less dense samples. For samples with larger initial densities (DH and RGlr), dilation next to the tip is observed. However, DH samples, which are less dense than RGlr samples, show less dilation and even slight compaction in one case. RGlr samples show maximal dilation values (0.6).

3.3. Comparison Between Measurements and Models

3.3.1. Compaction Angle Model

Table 4 presents the theoretical compaction angle computed from Equation (2) on all samples. We recall that the compaction angle model also provides the radial extent of the compaction zone as the transition between the theoretically uniform compacted snow and the intact snow. The derived radial extent is smaller than the size of the sample (less $4R$) for only four samples. The smallest radial extent ($2.1R$) is obtained for PP, followed by RG ($2.8R$) and DH ($4.0R$). The extent of the compaction zone derived from the model is in agreement with the measured values for sample PP1 (see **Table 4**), but is over-estimated for the other snow types. Indeed, Johnson (2003)'s compaction model assumes an abrupt transition between intact snow and snow compacted to its critical density, which is not observed in our experiments (**Figure 9**). The samples either exhibit dilation next to the tip, or progressive compaction from the intact snow to the interface of the cone.

3.3.2. Cavity Expansion Model

Figure 10 compares the measured radial displacement profiles and the displacements predicted by the cavity expansion model. We recall that the model predicts null vertical displacements, while all tested samples (besides PP, for which we were not able to retrieve a displacement field) display a vertical displacement component (**Figures 8A–C**). The radial displacements (**Figure 10**) for the RG and DH snow types show relatively good agreement with the model. Best agreement was obtained for $\psi = -30^o$, with values of $R^2 > 0.9$. However, no value of the dilation angle ψ enabled to fit the model over the whole range of r values. For radial positions in $[1, 1.5]R$, the best fit is obtained with $\psi \in [-25, -30]^\circ$, but the faster displacement decay for larger r is better captured with $\psi = -35^\circ$. For RGlr snow type, radial displacements decay to zero much faster than the model regardless of the considered value of ψ, and for one sample (RGlr3) there is almost no radial displacement observed.

Figure 11 compares the force measured during the CPT to the solutions of the cavity expansion model. All material properties of the model, except for cohesion, were chosen according to typical snow properties (**Table 1**). Cohesion C was varied between 500 and 1,500 Pa. The general shape (parabolic) of the force profile

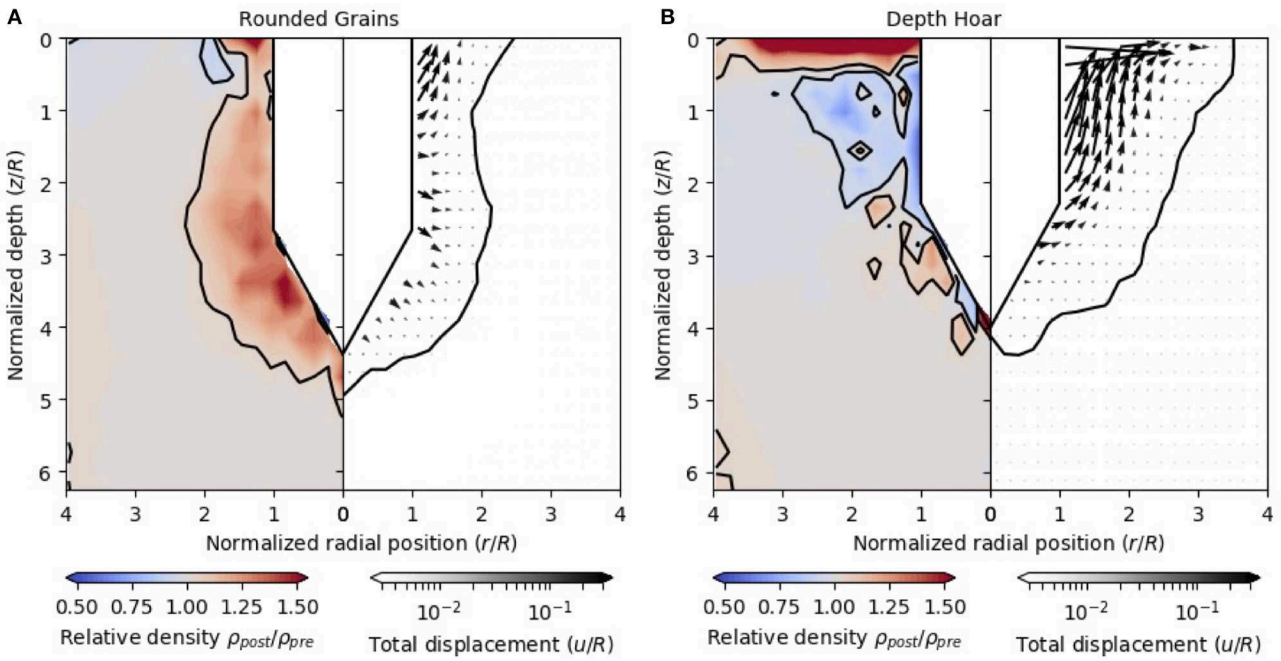

FIGURE 7 | Averaged density change (left side) and displacement field normalized by tip radius *R* (right side) around cone tip for two snow types: **(A)** RG (sample RG1), **(B)** DH (sample DH2). Contours show the compaction and deformation zones around the tip. Displacements are plotted only if more than 30% of the grains in the corresponding sub-volume are successfully tracked.

TABLE 4 | Size of the compaction and deformation zones normalized by tip radius *R* and compaction angle according to the model of Johnson (2003), for all samples.

Sample	RG1	RG2	RGlr1	RGlr2	RGlr3	DH1	DH2	PP1
Penetration depth	4.38	4.80	4.12	5.49	3.48	4.42	4.01	5.35
Compaction zone								
Height	0.90	0.84	0.23	>0.75	0.9	1.0	0.44	0.51
Radius	1.81	1.95	1.69	1.64	1.72	1.89	2.28	1.99
Std of radius	0.21	0.08	0.09	0.23	0.15	0.1	0.2	0.05
Deformation zone								
Height	0.62	0.77	0.34	>0.98	0.93	0.99	0.44	–
Radius	1.86	1.95	1.96	–	2.22	2.38	2.70	–
Std of radius	0.09	0.10	0.01	–	0.07	0.03	0.15	–
Compaction angle (°)	27	30	57	56	59	35	44	20

The radii of the compaction and deformation zones are defined as averages computed from the tip base (transition between cone and cylinder) up to about 2.5 mm beneath snow surface. Their height are defined as the distances between the tip and the deepest point in the compaction or deformation zones. The total penetration depth of the CPT scaled by tip radius R is also indicated.

appears to be well reproduced by the model. Obviously the cavity expansion model, which is based on the assumption of a continuum material, fails to reproduce the discrete nature of bond failures resulting in force fluctuations with depth. The recorded force profiles for the RG, RGlr, and DH snow samples agree with theoretical estimates obtained for cohesion values in the range [250, 1,500] Pa, while the force recorded for the PP sample appears to correspond to a lower cohesion.

4. DISCUSSION

4.1. High-Resolution Three-Dimensional Measurements of Snow Deformation

A novel method for three-dimensional tracking of individual grains around a CPT in granular materials was presented. It was applied to μCT images of eight snow samples, covering four different snow types. For each sample, two images were measured, one before and one after the CPT. The main challenge consisted in identifying the large displacements. Indeed, the highly rate-dependent mechanical behavior of snow did not allow us to conduct incremental CPT. However, compared to previous experimental studies of CPT in sand or soils (e.g., Paniagua et al., 2013; Silva et al., 2015), the relatively unique shape of each snow grain renders tracking applicable on such large displacements.

Our study provides the first observation of the full 3D displacement field at grain scale during a CPT in snow. Some grains could not be successfully tracked between the pre- and post-CPT images (**Figure 5**). However, assuming invariance of the displacement with rotation around the cone axis, we were able to reconstruct the displacement field everywhere outside the cavity (**Figure 7**). While direct validation of the tracking algorithm is out of reach, due to the absence of reference, the chosen methodology (high threshold on correlation coefficient

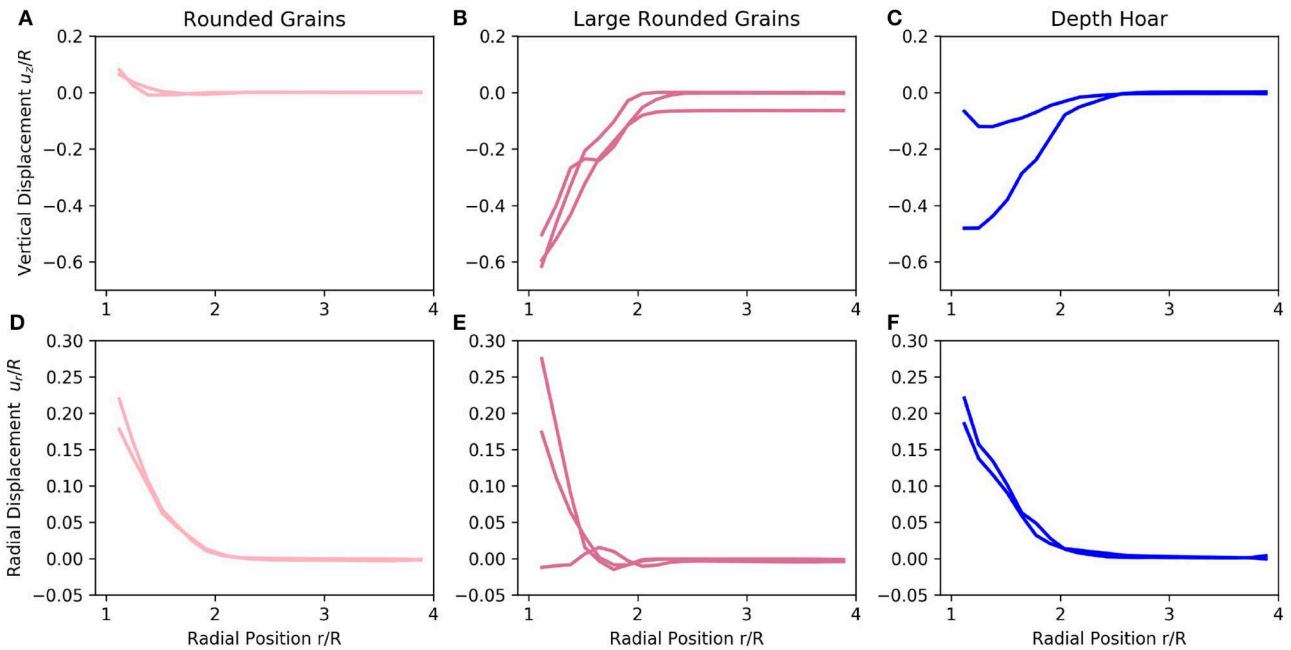

FIGURE 8 | Radial profiles of vertical **(A–C)** and radial displacement **(D–F)** normalized by tip radius *R* for RG **(A,D)**, RGlr **(B,E)**, and DH **(C,F)** snow types. In all plots, the different profiles correspond to the different samples for each snow type.

to consider a successful tracking) and indirect validation on the density field (**Figure 6**) provide good confidence in the obtained results.

The use of X-Ray tomography at a resolution of 15 μm inherently limited the size of the snow samples. The samples were cylinders of diameter and height of 20 mm ($4R$), confined in aluminum holders. Cone penetration reached an average depth of 10 mm, corresponding to an approximate distance of 7 mm ($\approx$ $2.5R$) to sample bottom. Herwijnen (2013) showed that a steady-state penetration behavior is reached on average after 40 mm of penetration depth in homogeneous snow samples. In this study, this steady-state regime could not be reached and we clearly observed different displacements close to snow surface, in comparison to larger depths (**Figure 7** and **Figure S2**). However, on samples RG or PP (**Figure 9** and **Table 4**), we did not observe any evidence of an increase or decrease of compaction zone radius with depth below the snow surface (depth $>$ 1 mm).

For low-density snow, the confinement of the samples is expected to have little influence on the measured displacements and forces. Some tested samples (RGlr1, 2 and 3) do however exhibit a high initial density, up to about 560 kg m^{-3}. In this case, the confinement may affect the CPT, in comparison to a test performed in a infinite medium. This impact was obvious on sample RGlr2, for which the largest penetration depth was reached and an overall upward movement of the sample was observed. Nevertheless, it has to be recalled that previous studies (e.g., Herwijnen, 2013; LeBaron et al., 2014), principally based on 2D imaging of snow samples through a viewing window, may also be affected by some boundary effects. In addition to sample confinement, the removal of the cone before the second tomographic scan may also affect the observed displacement field. Even if the cone was removed after about 2 h of sintering to solidify the cavity, we could observe that some grains were eroded from the sample and deposited on the top surface because of residual friction with the cone, particularly on samples characterized by a high initial density (**Figure 7** and **Figure S2**).

4.2. Analysis of CPT Deformation in Snow

Snow deformation around the cone was analyzed using the displacements retrieved by the tracking algorithm and the density evolution directly computed from the tomographic images. These two techniques are complementary. Tracking provides the full 3D, vectorial displacement field at grain scale, but fails to identify all the grains, especially when displacements are large. Density evolution can be directly computed on the whole volume and is more robust, but it is a scalar value and its resolution is limited to several grains.

In general, downwards movements were observed at tip apex, and upwards movements close to sample surface (e.g., **Figure 7**). In the literature, similar displacement patterns are reported for granular soils and clays (e.g., Ni et al., 2010; Arshad et al., 2014). Similar displacement patterns were also observed by Jiang et al. (2006) on numerical experiments with a discrete element model. Our experiments showed a dependence of the displacement pattern with snow type. In particular, the vertical displacement component was the smallest for RG samples, and the strongest upward movements were observed for DH and RGlr samples (**Figure 8**). These two latter snow types are characterized by the largest initial densities, which may be the origin of the upward movement. This interpretation is in agreement with the

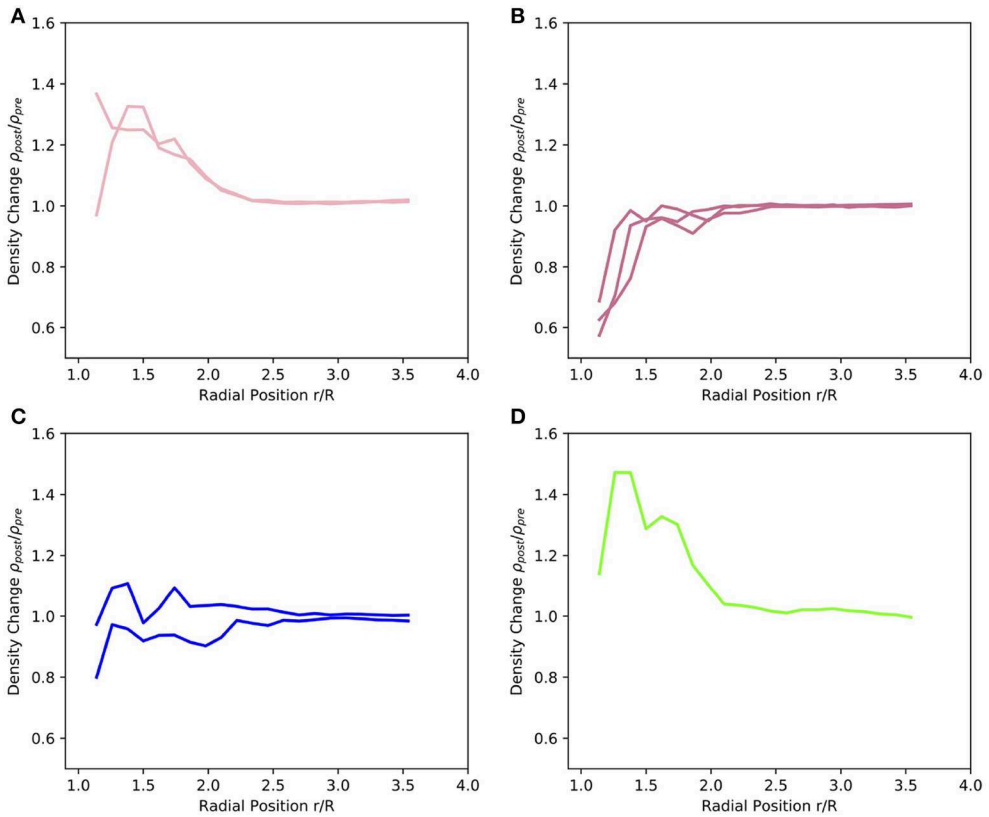

FIGURE 9 | Radial profiles of density changes for RG **(A)**, RGlr **(B)**, DH **(C)**, and PP **(D)** snow types. In all plots, the different profiles correspond to the different samples for each snow type.

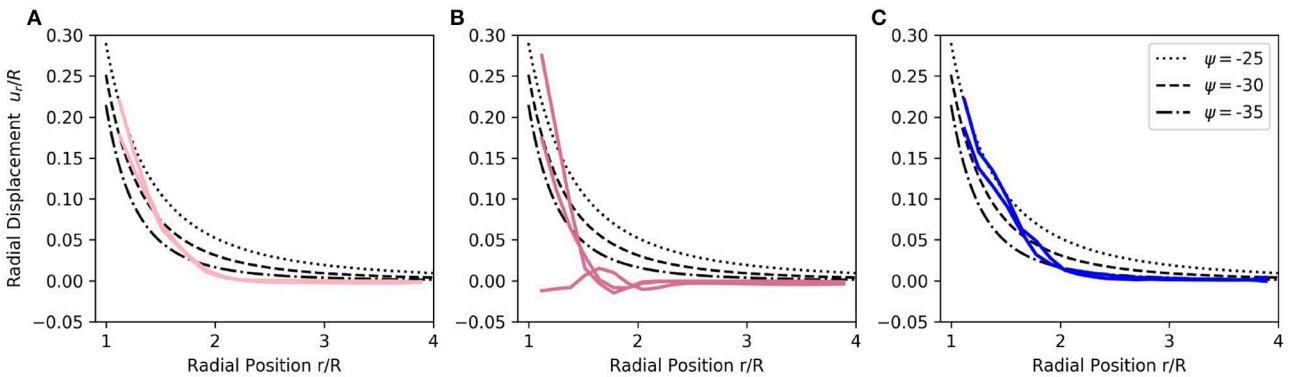

FIGURE 10 | Comparison between measured radial displacement profiles and predictions of cavity expansion model for different snow types: **(A)** RG, **(B)** RGlr, **(C)** DH. Predicted profiles are shown for three different dilation angles ψ, which is the only material parameter that significantly affects the computed displacements (**Table 2**).

observed density fields, which show almost no compaction for these samples. Hence the grains, instead of being compacted, are pushed upwards to let the cone penetrate.

Close to the cone tip, we observed compaction for snow types RG and PP and dilation for snow types RGlr and DH. These two groups differ by their initial density (denser RGlr/DH than PP/RG) and grain size (smaller PP/RG than RGlr/DH). These findings are consistent with observations of Riche and Schneebeli (2010), who investigated the perturbation induced by the penetration of a needle probe (1.2 mm diameter) into snow. They observed that samples with small structures develop a densified zone up to 0.2 mm surrounding the needle, while samples with larger structures (e.g., depth hoar) show a marked decrease of the volume fraction up to 0.5 mm from the needle, and a much smaller and less distinct densified zone.

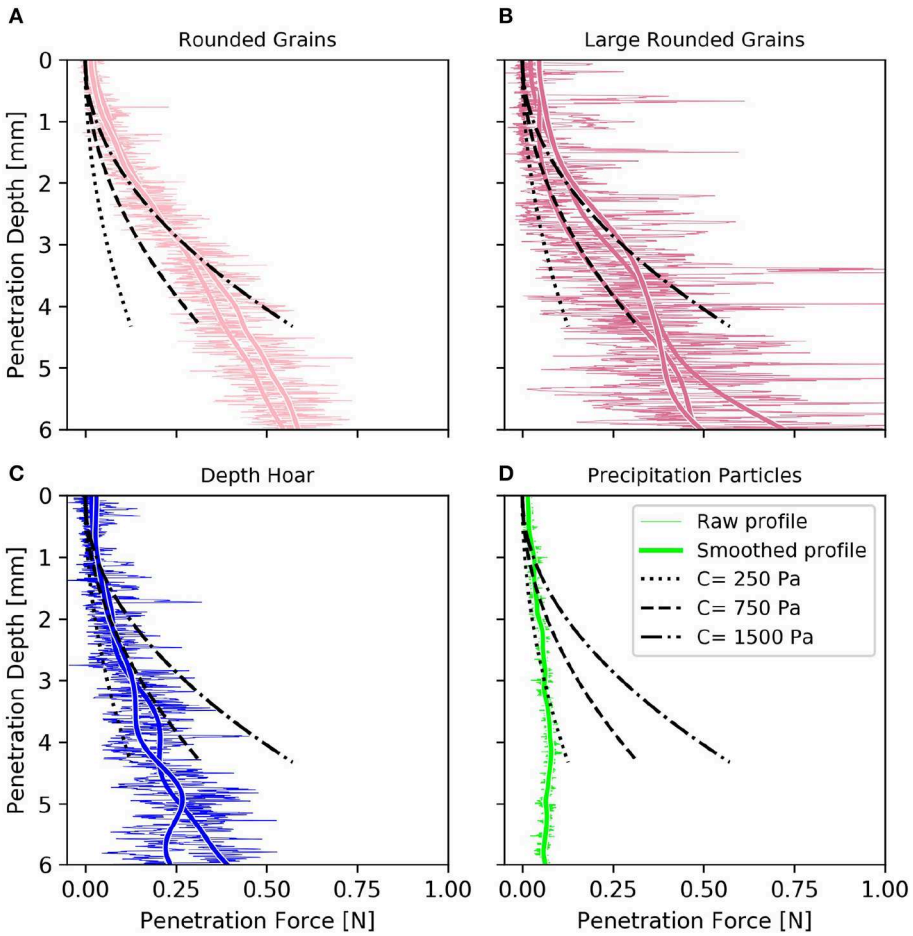

FIGURE 11 | Measured and computed CPT force profiles for the different snow types: **(A)** RG, **(B)** RGlr, **(C)** DH, **(D)** PP. The measured profiles are smoothed with a Gaussian filter of standard deviation equal to twice the equivalent optical radius (see **Table 1**). Computed profiles are obtained from Equation (3) with different values of cohesion C.

Deformation and compaction zones were defined on the base of thresholds on displacement magnitude and absolute density change. Unlike Floyer (2008), however, we did not observe significant differences between the two zones, i.e., grain displacements were systematically associated to density changes (compaction or dilation). Specifically, we did not observe any solid bulb of snow grains moving with the tip. Instead, the compaction zone appears to continuously reform with depth. The radius of the compaction zone obtained from our experiments appears to be smaller than values found in previous studies (**Table 4**). LeBaron et al. (2014) reported radii of about $3R$. Herwijnen (2013) measured an average ratio of 2 between the compaction zone radius and the tip radius, with values up to 4.7 for dense snow (390 kg m^{-3}). Floyer (2008) obtained a radial extent of the compaction zone of about $2R$. Here, we observed values in the range $[1.6, 2.3]R$ (see **Table 4**), which might be due to a not fully developed compaction zone. Indeed, Herwijnen (2013) (Figure 11 therein) showed a slight increase of the compaction zone radius with depth: from $1.5R$ for a penetration depth of 15 mm to $2R$ for a depth of 40 mm.

4.3. Applicability of CPT Interpretation Models

We used our experimental data to evaluate the displacement field predicted by the compaction angle model of Johnson (2003) and the cavity expansion model (Yu and Carter, 2002; Ruiz et al., 2017). The compaction angle model assumes that the compacted material around the cone tip reaches a uniform critical density. We showed that this assumption is not valid for snow (e.g., **Figure 7**), and leads to wrong predictions of compaction zone size (**Table 4**).

The cavity expansion model relies on the assumption of a continuum material. Bolton et al. (1993) showed that the continuum assumption reaches its limit when the ratio of cone penetrometer size to grain size is lower than 20. In our case, this corresponds to a mean grain radius larger than 0.125 mm. Samples of DH and RGlr are clearly above this limit, which may explain deviations from the model. A relatively good agreement was nevertheless observed between the measured and predicted radial displacement profiles for samples of DH. The RG samples are characterized by much smaller grains, and the assumption of

a continuum medium is more justified in this case. Accordingly, a good agreement was observed with the model in terms of radial and vertical (null) displacements. For both DH and RG snow types, the best fit was obtained for a dilation angle of -30°. The modeled force reproduced relatively well the parabolic shape of the measured profiles. The values of cohesion (about 1,000 Pa, see **Figure 11**), required to model the force, are in agreement with literature (Chandel et al., 2014; Reiweger et al., 2015). In our samples, the lowest cohesion is obtained for the PP sample, followed by DH, while the largest values were reported for RG and RGlr samples (see **Figure 11**).

5. CONCLUSION

A reliable interpretation of CPT force profiles requires a correct estimation of the displacement around the cone tip. We measured this displacement on snow with X-ray tomography, and proposed a novel method for recovering large displacements between two μCT scans. The method was applied to our data consisting of pre- and post-CPT tomographic images for eight snow samples. Most of the grains were successfully tracked between the two images. The volumetric strain is correctly reproduced by the tracking algorithm, giving confidence in the accuracy of the presented methodology. Measured displacements were oriented downwards at tip apex, upwards close to sample surface, and nearly radially in between. Displacements were shown to be sensitive to the initial sample density. In particular, upward movements were particularly pronounced for high density samples. CPT generally caused snow compaction around the tip but, surprisingly, dilation was also observed for the highest density ($>$ 350 kg m^{-3}) samples. However, sample confinement and shallow penetration depths might affect this behavior. Extension of these results to larger sample diameters and to penetration depths greater than 10 mm remains to be investigated. The radial extent of the compaction zone ranged between $[1.6, 2.3]R$, while its vertical extent below the tip ranged between $[0.2, 1.0]R$. We did not observe a clear variation of the size of the compaction zone with density.

Our results show that the size of the compaction zone cannot be accurately estimated by the simple model of Johnson (2003) for snow, as density progressively increases from intact snow to the snow in contact with cone tip. The cavity expansion model captures this progressive compaction. Moreover, force profiles predicted by the cavity expansion model for relevant material properties are in good agreement with measured profiles. Clearly, however, this model fails to reproduce force fluctuations due to the discrete nature of bond failures, and is unable to capture the vertical movement of snow particles during CPT.

Our results also provide an indirect evaluation of Poisson shot noise models (Löwe and Herwijnen, 2012; Peinke et al., 2019) for CPT. These models assume the force to be the sum of independent elastic brittle failures, and that grains do not contribute to the overall force once their bonds are broken, thus effectively disregarding the existence of the compaction zone. Consistently with Herwijnen (2013) and LeBaron et al. (2014), our measurements show that the compaction zone is not negligible and may play an important role for the force interpretation, even in very low density samples.

DATA AVAILABILITY STATEMENT

The datasets for this study are available upon request to the corresponding author.

AUTHOR CONTRIBUTIONS

IP, PH, and GC wrote the article with contributions of all co-authors. IP and JR conducted the cold-room CPT. IP, FF, PH, JR, and EA performed the tomographic measurements. IP, EA, and PH developed the tracking algorithm.

FUNDING

CNRM/CEN and ETNA were part of LabEX OSUG@2020 (ANR10 LABX56). ETNA was part of LabEX TEC21 (ANR11 LABX30). This work was partly supported by the European Space Agency under ESTEC Contract No. 4000112698/14/NL/LvH.

ACKNOWLEDGMENTS

We would like to thank S. Rolland du Roscoat, P. Charrier, L. Pézard, and P. Lapalus for their help with tomographic measurements and experiment design.

SUPPLEMENTARY MATERIAL

The Supplementary Material for this article can be found online at: https://www.frontiersin.org/articles/10.3389/feart.2020.00063/full#supplementary-material

REFERENCES

Andò, E., Hall, S. A., Viggiani, G., Desrues, J., and Bésuelle, P. (2012). Grain-scale experimental investigation of localised deformation in sand: a discrete particle tracking approach. *Acta Geotech.* 7, 1–13. doi: 10.1007/s11440-011-0151-6

Arshad, M., Tehrani, F., Prezzi, M., and Salgado, R. (2014). Experimental study of cone penetration in silica sand using digital image correlation. *Géotechnique* 64, 551–569. doi: 10.1680/geot.13.P.179

Bader, H., Haefeli, R., Bucher, E., Neher, J., Eckel, O., and Thams, C. (1939). Der Schnee und seine Metamorphose. Beiträge zur Geologie der Schweiz. Schweizerische Schnee- und Lawinenforschungskommission (Snow and its metamorphism). *SIPRE Trans.* 14:1954.

Baligh, M. (1986). Undrained deep penetration, I: shear stresses. *Geotechnique* 36, 471–485. doi: 10.1680/geot.1986.36.4.471

Bishop, R. F., Hill, R., and F Mott, N. (1945). The theory of indentation hardness tests. *Proc. Phys. Soc.* 57:321. doi: 10.1088/0959-5309/57/3/301

Blackford, J. (2007). Sintering and microstructure of ice: a review. *J. Phys. D Appl. Phys.* 40, R355–R385. doi: 10.1088/0022-3727/40/21/R02

Bolton, M. D., Gui, M. W., and Phillips, R. (1993). "Review of miniature soil probes for model tests," in *Proceedings of the 11th Southeast Asian Geotechnical Conference* (Singapore), 85–90.

Calonne, N., Flin, F., Lesaffre, B., Dufour, A., Roulle, J., Puglièse, P., et al. (2015). CellDyM: a room temperature operating cryogenic cell for the dynamic monitoring of snow metamorphism by time-lapse X-ray microtomography. *Geophys. Res. Lett.* 42, 3911–3918. doi: 10.1002/2015GL063541

Chandel, C., Srivastava, P. K., and Mahajan, P. (2014). Micromechanical analysis of deformation of snow using X-ray tomography. *Cold Reg. Sci. Technol.* 101, 14–23. doi: 10.1016/j.coldregions.2014.01.005

Fierz, C., Armstrong, R. L., Durand, Y., Etchevers, P., Greene, E., McClung, D. M., et al. (2009). "The international classification for seasonal snow on the ground," in *Tech. Doc. Hydrol. 83* Paris: UNESCO.

Floyer, J. (2008). *Layer detection and snowpack stratigraphy characterisation from digital penetrometer signals* (Ph.D. thesis). Department of Geoscience, University of Calgary, Calgary, AB, Canada.

Floyer, J., and Jamieson, J. (2010). Rate-effect experiments on round-tipped penetrometer insertion into uniform snow. *J. Glaciol.* 56, 664–672. doi: 10.3189/002214310793146322

Floyer, J. A., and Jamieson, J. B. (2006). "Empirical analysis of snow deformation below penetrometer tips," In *Proceedings of the International Snow Workshop* (Telluride, CO), 555–561.

Gubler, H. U. (1975). On the ramsonde hardness equation. *IAHS-AISH Publ.* 114, 110–121.

Hagenmuller, P., Chambon, G., Flin, F., Morin, S., and Naaim, M. (2014). Snow as a granular material: assessment of a new grain segmentation algorithm. *Granular Matt.* 16, 421–432. doi: 10.1007/s10035-014-0503-7

Hagenmuller, P., Chambon, G., Lesaffre, B., Flin, F., and Naaim, M. (2013). Energy-based binary segmentation of snow microtomographic images. *J. Glaciol.* 59, 859–873. doi: 10.3189/2013JoG13J035

Hagenmuller, P., Chambon, G., and Naaim, M. (2015). Microstructure-based modeling of snow mechanics: a discrete element approach. *Cryosphere* 9, 1969–1982. doi: 10.5194/tc-9-1969-2015

Hagenmuller, P., Matzl, M., Chambon, G., and Schneebeli, M. (2016). Sensitivity of snow density and specific surface area measured by microtomography to different image processing algorithms. *Cryosphere* 10, 1039–1054. doi: 10.5194/tc-10-1039-2016

Hagenmuller, P., van Herwijnen, A., Pielmeier, C., and Marshall, H.-P. (2018). Evaluation of the snow penetrometer avatech SP2. *Cold Reg. Sci. Technol.* 149, 83–94. doi: 10.1016/j.coldregions.2018.02.006

Hall, S., Bornert, M., Desrues, J., Pannier, Y., Lenoir, N., Viggiani, G., et al. (2010). Discrete and continuum analysis of localised deformation in sand using X-ray CT and volumetric digital image correlation. *Géotechnique* 60, 315–322. doi: 10.1680/geot.2010.60.5.315

Herwijnen, A., and Miller, D. A. (2013). Experimental and numerical investigation of the sintering rate of snow. *J. Glaciol.* 59, 1–6. doi: 10.3189/2013JoG12J094

Herwijnen, A. V. (2013). Experimental analysis of snow micropenetrometer (SMP) cone penetration in homogeneous snow layers. *Can. Geotech. J.* 50, 1044–1054. doi: 10.1139/cgj-2012-0336

Jiang, M., Yu, H.-S., and Harris, D. (2006). Discrete element modelling of deep penetration in granular soils. *Int. J. Numer. Anal. Meth. Geomech.* 30, 335–361. doi: 10.1002/nag.473

Johnson, J. (2003). A statistical micromechanical theory of cone penetration in granular materials. *ERDC/CRREL. Technical Report 03-3.* 51, 1–12.

Johnson, J., and Hopkins, M. (2005). Identifying microstructural deformation mechanisms in snow using discrete-element modeling. *J. Glaciol.* 51, 432–442. doi: 10.3189/172756505781829188

Johnson, J., and Schneebeli, M. (1999). Characterizing the microstructural and micromechanical properties of snow. *Cold Reg. Sci. Technol.* 30, 91–100. doi: 10.1016/S0165-232X(99)00013-0

LeBaron, A., Miller, D., and van Herwijnen, A. (2014). Measurements of the deformation zone around a split-axis snow micropenetrometer tip. *Cold Reg. Sci. Technol.* 97, 90–96. doi: 10.1016/j.coldregions.2013.10.008

Löwe, H., and Herwijnen, A. (2012). A Poisson shot noise model for micro-penetration of snow. *Cold Reg. Sci. Technol.* 70, 62–70. doi: 10.1016/j.coldregions.2011.09.001

Mackenzie, R., and Payten, W. (2002). "A portable, variable-speed, penetrometer for snow pit evaluation," in *Proceedings of the International Snow Workshop* (Penticton, BC), 294–300.

Marshall, H.-P., and Johnson, J. (2009). Accurate inversion of high-resolution snow penetrometer signals for microstructural and micromechanical properties. *J. Geophys. Res.* 114:F04016. doi: 10.1029/2009JF001269

Mayne, P. (2007). *In-situ* test calibrations for evaluating soil parameters. *Characterisat. Eng Propert. Natural Soils* 3, 1601–1652. doi: 10.1201/noe0415426916.ch2

McCallum, A. (2014). A brief introduction to cone penetration testing (CPT) in frozen geomaterials. *Ann. Glaciol.* 55, 7–14. doi: 10.3189/2014AoG68A005

Mellor, M. (1975). A review of basic snow mechanics. *IAHS Publ.* 114, 251–291.

Narita, H. (1983). An experimental study on tensile fracture of snow. *Contribut. Inst. Low Temperat. Sci.* A32, 1–37.

Ni, Q., Hird, C., and Guymer, I. (2010). Physical modelling of pile penetration in clay using transparent soil and particle image velocimetry. *Geotechnique* 60:121. doi: 10.1680/geot.8.P.052

Paniagua, P., Andò, E., Silva, M., Emdal, A., Nordal, S., and Viggiani, G. (2013). Soil deformation around a penetrating cone in silt. *Géotechnique Lett.* 3, 185–191. doi: 10.1680/geolett.13.00067

Peinke, I., Hagenmuller, P., Chambon, G., and Roulle, J. (2019). Investigation of snow sintering at microstructural scale from micro-penetration tests. *Cold Reg. Sci. Technol.* 162, 43–55. doi: 10.1016/j.coldregions.2019.03.018

Pielmeier, C., and Schneebeli, M. (2003). Stratigraphy and changes in hardness of snow measured by hand, ramsonde and snow micro penetrometer: a comparison with planar sections. *Cold Reg. Sci. Technol.* 37, 939–405. doi: 10.1016/S0165-232X(03)00079-X

Proksch, M., Löwe, H., and Schneebeli, M. (2015). Density, specific surface area, and correlation length of snow measured by high-resolution penetrometry. *J. Geophys. Res. Earth Surf.* 120, 346–362. doi: 10.1002/2014JF003266

Reiweger, I., Gaume, J., and Schweizer, J. (2015). A new mixed-mode failure criterion for weak snowpack layers. *Geophys. Res. Lett.* 42, 1427–1432. doi: 10.1002/2014GL062780

Reuter, B., Proksch, M., Löwe, H., Van Herwijnen, A., and Schweizer, J. (2019). Comparing measurements of snow mechanical properties relevant for slab avalanche release. *J. Glaciol.* 65, 55–67. doi: 10.1017/jog.2018.93

Reuter, B., Schweizer, J., and van Herwijnen, A. (2015). A process-based approach to estimate point snow instability. *Cryosphere* 9, 837–847. doi: 10.5194/tc-9-837-2015

Riche, F., and Schneebeli, M. (2010). Microstructural change around a needle probe to measure thermal conductivity of snow. *J. Glaciol.* 56, 871–876. doi: 10.3189/002214310794457164

Robertson, P. (2009). Interpretation of cone penetration tests - a unified approach. *Can. Geotechn. J.* 46, 1337–1355. doi: 10.1139/T09-065

Ruiz, S., Capelli, A., van Herwijnen, A., Schneebeli, M., and Or, D. (2017). Continuum cavity expansion and discrete micromechanical models for inferring macroscopic snow mechanical properties from cone penetration data. *Geophys. Res. Lett.* 44, 8377–8386. doi: 10.1002/2017GL074063

Ruiz, S., Straub, I., Schymanski, S. J., and Or, D. (2016). Experimental evaluation of earthworm and plant root soil penetration-cavity expansion models using cone penetrometer analogs. *Vadose Zone J.* 15, 1–14. doi: 10.2136/vzj2015.09.0126

Schmertmann, J. (1978). *Guidelines for Cone Penetration Test: Performance and Design*. Report FHWA-TS-78-209. Washington, DC: Federal Highway Administration, 146.

Schneebeli, M., and Johnson, J. (1998). A constant-speed penetrometer for high-resolution snow stratigraphy. *Ann. Glaciol* 26, 107–111. doi: 10.3189/1998AoG26-1-107-111

Schweizer, J., Jamieson, J. B., and Schneebeli, M. (2003). Snow avalanche formation. *Rev. Geophys.* 41:1016. doi: 10.1029/2002RG000123

Schweizer, J., and Wiesinger, T. (2001). Snow profile interpretation for stability evaluation. *Cold Reg. Sci. Technol.* 33, 179–188. doi: 10.1016/S0165-232X(01)00036-2

Silva, M., Doreau-Malioche, J., and Combe, G. (2015). "Champs cinématiques dans un sable lors de l'enfoncement d'un pieu par tomographie RX: comparaison des corrélations numérique continue et discrète," in *CFM 2015, 22ème Congrès Français de Mécanique* (Lyon).

White, D. J., and Bolton, M. D. (2004). Displacement and strain paths during plane-strain model pile installation in sand. *Geotechnique* 54, 375–397. doi: 10.1680/geot.2004.54.6.375

Yaniv, Z., Lowekamp, B. C., Johnson, H. J., and Beare, R. (2018). Simpleitk image-analysis notebooks: a collaborative environment for education and reproducible research. *J. Digit. Imaging* 31, 290–303. doi: 10.1007/s10278-017-0037-8

Yu, H. S., and Carter, J. (2002). Rigorous similarity solutions for cavity expansion in cohesive-frictional soils. *Int. J. Geomech.* 2, 233–258. doi: 10.1061/(ASCE)1532-3641(2002)2:2(233)

Yu, H. S., and Mitchell, J. K. (1998). Analysis of cone resistance: Review of methods. *J. Geotech. Geoenviron. Eng.* 124, 140–149. doi: 10.1061/(ASCE)1090-0241(1998)124:2(140)

Conflict of Interest: The authors declare that the research was conducted in the absence of any commercial or financial relationships that could be construed as a potential conflict of interest.

frontiers in Earth Science

ORIGINAL RESEARCH
published: 17 April 2020
doi: 10.3389/feart.2020.00101

A Micro-Mechanical Model for the Transformation of Dry Polar Firn Into Ice Using the Level-Set Method

Kévin Fourteau, Fabien Gillet-Chaulet*, Patricia Martinerie and Xavier Faïn*

Univ. Grenoble Alpes, CNRS, IRD, Grenoble INP, IGE, Grenoble, France

Interpretation of greenhouse gas records in polar ice cores requires a good understanding of the mechanisms controlling gas trapping in polar ice, and therefore of the processes of densification and pore closure in firn (compacted snow). Current firn densification models are based on a macroscopic description of the firn and rely on empirical laws and/or idealized geometries to obtain the equations governing the densification and pore closure. Here, we propose a physically-based methodology explicitly representing the porous structure and its evolution over time. In order to handle the complex geometry and topological changes that occur during firn densification, we rely on a Level-Set representation of the interface between the ice and the pores. Two mechanisms are considered for the displacement of the interface: (i) mass surface diffusion driven by local pore curvature and (ii) ice dislocation creep. For the latter, ice is modeled as a viscous material and the flow velocities are solutions of the Stokes equations. First applications show that the model is able to densify firn and split pores. Using the model in cold and arid conditions of the Antarctic plateau, we show that gas trapping models do not have to consider the reduced compressibility of closed pores compared to open pores in the deepest part of firns. Our results also suggest that the mechanism of curvature-driven surface diffusion does not result in pore splitting, and that ice creep has to be taken into account for pores to close. Future applications of this type of model could help quantify the evolution and closure of firn porous networks for various accumulation and temperature conditions.

Keywords: firn densification, pore closure, modeling, Level-Set, finite element, porous material

OPEN ACCESS

Edited by:
Johan Gaume,
Federal Institute of Technology in Lausanne, Switzerland

Reviewed by:
Martin Rückamp,
Alfred Wegener Institute Helmholtz Centre for Polar and Marine Research (AWI), Germany
Martin Truffer,
University of Alaska Fairbanks, United States

****Correspondence:***
Kévin Fourteau
kevin.fourteau@univ-grenoble-alpes.fr
Fabien Gillet-Chaulet
fabien.gillet-chaulet@univ-grenoble-alpes.fr

Specialty section:
This article was submitted to Cryospheric Sciences, a section of the journal Frontiers in Earth Science

Received: *28 August 2019*
Accepted: *23 March 2020*
Published: *17 April 2020*

Citation:
Fourteau K, Gillet-Chaulet F, Martinerie P and Faïn X (2020) A Micro-Mechanical Model for the Transformation of Dry Polar Firn Into Ice Using the Level-Set Method. Front. Earth Sci. 8:101. doi: 10.3389/feart.2020.00101

1. INTRODUCTION

Polar ice cores are important natural archives to study past climate dynamics. Indeed, ice cores are the only archive to encapsulate bubbles of air from past atmospheres, enabling direct measurements of past concentrations of greenhouse gases. The parallel study of ice core bubbles and isotopic composition of the ice matrix (which is used to reconstruct past temperatures: Dansgaard, 1953; Johnsen et al., 1989) has highlighted the strong link between greenhouse gases and climate (Barnola et al., 1987; Lüthi et al., 2008). In order to properly interpret the gas records of ice cores in terms of atmospheric concentrations, it is necessary to understand how atmospheric air gets embedded in ice. Gas trapping is the result of the slow compaction of snow near the surface of polar ice sheets.

The surface snow is a highly porous material, and its interstitial air can freely exchange with the above atmosphere. Due to the continuous deposition of new snow at the surface, snow strata

are buried and compressed by the weight of the overlying column (Herron and Langway, 1980; Wilkinson, 1988; Arnaud et al., 2000). This buried snow is referred to as firn. In response to the compression, the firn medium densifies and the interstitial porous network shrinks in size. When density reaches relative values to pure ice of about 0.9 (corresponding to 10% porosity in volume), the pores start to pinch and encapsulate the interstitial air in airtight bubbles (Schwander and Stauffer, 1984; Stauffer et al., 1985; Schaller et al., 2017). The transformation of firn into airtight ice happens at depths ranging from 50 to 120 m depending on the site and the local climatic conditions (Witrant et al., 2012). The mechanism of gas trapping has impacts for the interpretation of the gas records. First, as the closure of pores happens after the deposition of snow (from a few decades to a few millennia, e.g., Schwander et al., 1993; Bazin et al., 2013; Veres et al., 2013), the air is always younger than the surrounding ice. To temporally synchronize the measurements performed in the ice matrix and in the gaseous phase it is thus necessary to quantify the duration of the firn densification (Shakun et al., 2012; Parrenin et al., 2013). Moreover, the closure of pores in a single stratum at the bottom of the firn takes place over a period of time, rather than instantaneously (Schwander and Stauffer, 1984; Stauffer et al., 1985). It induces a smoothing of the fast atmospheric variations in ice core records (Spahni et al., 2003; Joos and Spahni, 2008; Fourteau et al., 2017).

The trapping of atmospheric gases in polar ice is usually modeled with the combination of a firn densification model (providing the evolution of density with depth; Lundin et al., 2017), coupled with a parametrization of pore closure with density (Goujon et al., 2003; Buizert et al., 2012; Witrant et al., 2012). A variety of firn densification models have been proposed in the literature (e.g., Herron and Langway, 1980; Arnaud et al., 2000; Arthern et al., 2010), with original applications covering topics from ice core interpretation to ice-sheet mass balance. These models represent the entirety of the firn column as a continuous material, from the surface to the firn/ice transition. The 3D microstructure of the firn is not explicitly represented, but can be partially taken into account with variables such as the coordination number of ice aggregates (Arnaud et al., 2000) or the size of ice crystallographic grains (Arthern et al., 2010). Similarly, several parameterizations relating the closure of pores to the density of firn have been proposed, based on measurements performed on firn cores (Goujon et al., 2003; Mitchell et al., 2015; Schaller et al., 2017). However, these measurements only take into account a few conditions of temperature and accumulation, and it is not clear how well they apply to firns undergoing different climatic conditions. In particular, it remains unclear how the progressive closure of bubbles took place in the firns of the very cold and arid conditions of the East Antarctic plateau during glacial periods. This is an issue as East Antarctic ice cores are the oldest known ice cores and are thus of crucial importance for paleoclimatology (Barnola et al., 1987; Loulergue et al., 2008; Lüthi et al., 2008). It thus appears important to be able to quantify how the pores progressively close in firns for a wide range of temperature and accumulation conditions. A potential way to answer this question is to develop physics-based micro-mechanical models of dry firn, explicitly representing the 3D structure of pores and their closure.

With these questions in mind, we began implementing a general micro-mechanical model able to handle the closure and splitting of pores in a firn layer. Contrary to other models, ours explicitly represents the 3D microstructure of the ice and pore phases of the firn layer, and their evolutions over time. However, we only represent a single firn layer and not the entire firn column. Therefore, this type of micro-mechanical model should be seen as complementary to macro-scale models representing the whole firn column. In order to model the coalescence and splitting of pores, we rely on a Level-Set representation of the ice/pore interface. The idea of this method is to replace the biphasic nature of firn by a scalar field, whose zero-value level marks the position of the interface (Osher and Sethian, 1988; Osher and Fedkiw, 2001). Indeed, the Level-Set method naturally handles the topological changes of the ice and pores phases, that happen when pores split or coalesce. Level-set approaches have already been used in the field of glaciology to track large scale glacier geometry features (Pralong and Funk, 2004; Bondzio et al., 2016). To our knowledge, we present here its first use to model firn microstructure evolution. The model takes into account the mechanisms of polycrystalline ice dislocation creep (Duval et al., 1983) and curvature-driven surface diffusion (Maeno and Ebinuma, 1983). Yet, it has been developed in a modular fashion so that other mechanisms can be implemented. The emphasis of this paper is to demonstrate the capability of the developed micro-mechanical model to handle the densification of deep firn, including pore closure, rather than address a specific scientific question. In section 2.1 of the article, we present the general principles of the model, while the specific implementation is detailed in the following section 2.2. In section 3.1, we asses the capability of the model to conserve mass. We then propose two applications of the model. In section 3.2, we quantify the impact of the building pressure of closed pores in the deepest part of firns. Finally, in section 3.3 we study the contributions of dislocation creep and curvature-driven surface diffusion to the closure of pores.

2. DESCRIPTION OF THE MODEL

The aim of the model presented in this article is to simulate the evolution of a centimeter scale firn sample under the compression imposed by the overlying firn column, as represented in **Figure 1**. In particular, we aim to explicitly represent the 3D porous microstructure, and its transformation over time.

2.1. General Principles

This section aims to describe the general principles behind our 3D model, independent of their specific numerical implementation. First, we describe the two physical mechanisms taken into account in the model, namely the ice dislocation creep and surface curvature-driven diffusion. Note that other mechanisms, such as the sublimation and deposition of water molecules with transport through the pore phase (Calonne et al.,

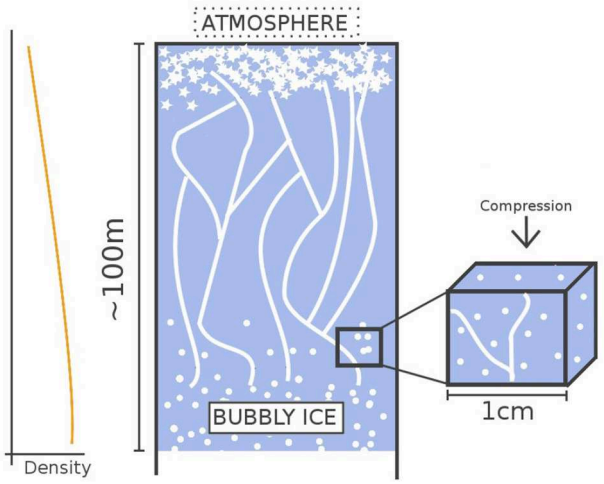

FIGURE 1 | Scheme of a firn column with a decreasing porosity with depth (white inclusions in the firn) until it transforms into airtight ice. The scheme shows the transformation of the open porosity (long connected white channels) into closed bubbles. This paper focuses in modeling small scale firn samples originating from the bubble closure zone in deep firn, similarly to the zoomed box on the right side.

2014) could be added in the future. We then present the Level-Set method, that is used to represent the position of the ice/pore interface in the model.

2.1.1. Ice Dislocation Creep

The first physical mechanism taken into account for the deformation of the porous network is the dislocation creep of the ice phase, due to the compression forces of the firn column above (Wilkinson and Ashby, 1975; Arzt et al., 1983). In the model we consider that the ice matrix can be represented as polycrystalline ice, neglecting the influence of individual crystallographic grains. The creep deformation of the ice is a viscoplastic motion with a low Reynolds number. The equations governing the motion of the ice matrix are the Stokes equations:

$$\begin{aligned} \nabla \cdot \bar{\bar{\sigma}} + \rho_{\text{ice}}\, \mathbf{g} &= 0 \\ \nabla \cdot \mathbf{v}^{\text{c}} &= 0 \end{aligned} \tag{1}$$

where $\nabla\cdot$ is the divergence operator, $\bar{\bar{\sigma}}$ is the stress tensor, ρ_{ice} is the density of ice, $\mathbf{g}$ is the gravity acceleration vector, and $\mathbf{v}^{\text{c}}$ is the ice creep velocity. To fully characterize the deformation of the ice matrix, the Stokes equations have to be completed with a constitutive law, describing the rheology of the ice material. Here, the creep of ice is represented by a Norton-Hoff power law (also referred to as Glen's law in glaciology; Duval et al., 1983; Schulson and Duval, 2009; Cuffey and Paterson, 2010):

$$\dot{\epsilon}_{ij} = A \tau^{n-1} \sigma'_{ij} \tag{2}$$

where i and j represent Cartesian coordinates (x, y, or z), $\dot{\epsilon}_{ij} = \frac{1}{2}\left(\frac{\partial v_{\text{i}}^{\text{c}}}{\partial x_{\text{j}}} + \frac{\partial v_{\text{j}}^{\text{c}}}{\partial x_{\text{i}}}\right)$ is the strain rate tensor (v_{i}^{c} being a Cartesian component of the creep velocity), $\sigma'_{ij} = \sigma_{ij} - 1/3\,\text{Tr}(\sigma)\delta_{ij}$ is the deviatoric stress tensor, with σ_{ij} being a component of the stress tensor $\bar{\bar{\sigma}}$ and δ_{ij} the Kronecker delta, and $\tau^2 = \frac{1}{2}\sigma'_{ij}\sigma'_{ij}$ is the effective shear stress. The parameter n is set to 3 (Schulson and Duval, 2009; Cuffey and Paterson, 2010). For the rest of the article, the pre-factor A is set to $0.08\,\text{MPa}^{-n}\,\text{yr}^{-1}$ which is the expected value for ice around the $-50°$C temperature. However, the model could be run at other temperatures by taking into account the documented dependence of A to temperature (Schulson and Duval, 2009; Cuffey and Paterson, 2010).

2.1.2. Surface Diffusion

The second mechanism implemented in the model is the diffusion of ice molecules due to gradients of chemical potential created by local curvature conditions. There are several mechanisms for the diffusion of water molecules as a response to these curvature differences (Ashby, 1974; Maeno and Ebinuma, 1983). Diffusive mechanisms transport mass from regions of high curvature toward regions of low curvature. As it has already been successfully implemented in Level-Set simulations (Bruchon et al., 2010, 2012), we implemented the specific mechanism of surface diffusion in which water molecules diffuse at the surface of the ice/pore interface. Following the work of Bruchon et al. (2010) and Bruchon et al. (2012), the equation governing the velocity of the interface is:

$$\mathbf{v}^{\text{d}} = -C_0(\triangle_s K)\mathbf{n} \tag{3}$$

with C_0 being a parameter representing the effectiveness of the diffusive mechanism, K the curvature of the interface, $\mathbf{n}$ the normal vector to the interface pointing in the ice phase, and Δ_{s} is the "surface Laplacian" (the Laplace-Beltrami operator).

The value of the parameter C_0 governing surface diffusion depends on the thickness in which diffusion occurs, the free energy of the ice surface, and the diffusion coefficient of water molecules at the ice surface (Bruchon et al., 2010). Unfortunately, these quantities are not well constrained, leading to a large uncertainty on the value of C_0 and its dependence to temperature (Petrenko and Whitworth, 1999). To overcome this issue, we evaluated that the mechanism of diffusion results in interface velocities similar to ice creep for $C_0 \simeq 10^{-6}\,\text{mm}^4\,\text{yr}^{-1}$. Therefore, in the rest of the study the parameter C_0 will be set to the values 10^{-6} or $10^{-7}\,\text{mm}^4\,\text{yr}^{-1}$ to, respectively represent the presence of a strong or mild influence of the diffusion process, relatively to ice creep.

Finally, as the mechanism of surface diffusion redistributes mass from some regions to others, it is mass conserving and does not modify the density of firn layers. A mathematical proof of this mass conservation, involving the generalized divergence theorem over closed surfaces, is presented in Bruchon et al. (2010).

2.1.3. The Level-Set Method

The goal of this model is to explicitly simulate the evolution of the ice/pore interface in firn. This evolution notably includes topological changes, resulting from pore closure or coalescence (Burr et al., 2019). In the model, the bi-phasic nature of the firn is replaced by a mono-phasic medium with the addition of a characteristic function retaining the position of the ice/pore

interface, the so called Level-Set (LS) function ϕ (Osher and Sethian, 1988; Gibou et al., 2018). This Level-Set framework naturally handles topological changes, which is needed to model the closure or coalescence of pores (Osher and Sethian, 1988). A typical choice for the LS function is the signed distance to the interface.

Considering a 3D domain D of firn the LS function ϕ is given by:

$$\phi(x) = \begin{cases} +\,\mathrm{dist}(x, \Sigma) & \text{if } x \in \text{ice} \\ -\,\mathrm{dist}(x, \Sigma) & \text{if } x \in \text{pore} \\ 0 & \text{if } x \in \Sigma \end{cases} \tag{4}$$

where x is a point of D, Σ is the interface between the ice and pore phases, and $\mathrm{dist}(x, \Sigma)$ is the distance of point x to the interface. The position of the interface is thus captured by the zero-level of the LS function, as one can retrieve it with $\Sigma = \{x \mid \phi(x) = 0\}$. The evolution of the porous network is therefore represented by the evolution of the zero-level of the LS function.

The velocity $\mathbf{v}^{\mathrm{tot}}$ of the ice/pore interface is the sum of the velocities induced by each individual physical mechanism. This velocity is then used to advect the LS function by solving the transport equation (Olsson and Kreiss, 2005; Bernacki et al., 2008):

$$\frac{\partial \phi}{\partial t} + \mathbf{v}^{\mathrm{tot}} \cdot \nabla \phi = 0 \tag{5}$$

2.2. Numerical Implementation

For our specific implementation, we rely on the Finite Element Method (FEM) to solve the equations involved in the model. The FEM allows us to use unstructured tetrahedral meshes, that can be adapted to the represent the 3D geometries of the ice and pore phases. In our case, we use first order tetrahedral elements.

Moreover, we rely on the open source Finite Element software Elmer[1] (Gagliardini et al., 2013), that notably provides a module to compute the deformation of the ice matrix, as well as a general framework to solve equations with the FEM. In Elmer, we use Biconjugate Gradient Stabilized iterative solvers, with the standard Incomplete LU factorization for preconditioning. When transient equations are used in Elmer, we rely on the Backward Difference Formula (second order) for time-stepping. Furthermore, in our implementation all vectorial equations are treated with 3D Cartesian coordinates.

To compute the evolution of the firn microstructure our model goes through three main stages at each time-step Δt: (i) the tetrahedral mesh is adapted to the firn microstructure given by the LS function, (ii) the interface velocities for each physical mechanisms are computed, (iii) the LS function is advected to represent the movement of the interface. The overall algorithm, with the mesh adaptation, computation of velocities, advection steps, as well as the initialization of the model, is summarized in **Figure 2**.

2.2.1. Mesh Adaptation

The mesh is adapted to the LS function at the beginning of each time-step. The first goal of the mesh adaptation is to improve the computational efficiency of the model by keeping a refined mesh near the ice/pore interface and a coarser resolution away, where a high density of elements is not needed (Olsson et al., 2007; Bruchon et al., 2010). The second goal is to produce two sub-meshes, referred to as $\mathcal{M}_{\mathrm{i}}$ and $\mathcal{M}_{\mathrm{p}}$. The first one is meant to cover the ice phase only, and the second one the pore phase only. Note that an equivalent model could have been developed using passive elements instead of producing the sub-meshes $\mathcal{M}_i$ and $\mathcal{M}_p$. However, we chose the latter method as it simplifies the visualization of the results.

At the end of the nth time-step, the LS function is defined on a tetrahedral mesh $\mathcal{M}_D^n$ covering the whole domain. Its zero-value level gives the position of the ice/pore interface for the following time-step. At the start of the new time-step, the mesh adaptation procedure produces three meshes $\mathcal{M}_D^{n+1}$, $\mathcal{M}_i^{n+1}$, and $\mathcal{M}_p^{n+1}$ that cover the whole domain, the ice phase and the pore phase. The ice mesh is composed of the elements of $\mathcal{M}_D^{n+1}$ that lie in the ice phase region, and similarly for the pore mesh. The vertices of $\mathcal{M}_i^{n+1}$ and $\mathcal{M}_p^{n+1}$ are thus also vertices of $\mathcal{M}_D^{n+1}$. Mathematically, $\mathcal{M}_D^{n+1}$ is thus the union of $\mathcal{M}_i^{n+1}$ and $\mathcal{M}_p^{n+1}$, while the intersection of $\mathcal{M}_i^{n+1}$ and $\mathcal{M}_p^{n+1}$ defines the ice/pore interface.

To mesh the domain according to the LS function, we rely on the remeshing library MMG[2] (based on Dapogny et al., 2014), that we have interfaced with Elmer. The library yields a tetrahedral mesh that is refined around the ice/pore interface, with tetrahedral elements either in the ice or pore phase, and tagged accordingly. The boundaries between the elements of the ice and pore regions thus lie on the zero-value level of the LS function. The MMG library includes parameters to adjust the mesh refinement. The main ones are the h_{grad} and h_{ausd} parameters, that respectively set the gradation of element sizes and the maximal distance between the ideal interface (defined by the LS function) and the interface captured by the tetrahedral mesh.

The mesh obtained with the MMG library is used as the domain mesh $\mathcal{M}_D^{n+1}$. Furthermore, the sub-meshes $\mathcal{M}_i^{n+1}$ and $\mathcal{M}_p^{n+1}$ are derived using the element-tag provided by the MMG library. The different variables defined at the nodes of $\mathcal{M}_D^n$ are finally interpolated on the new nodes of $\mathcal{M}_D^{n+1}$. This includes the LS function.

In order to facilitate the transfer of variables between the $\mathcal{M}_D^{n+1}$, $\mathcal{M}_i^{n+1}$, and $\mathcal{M}_p^{n+1}$ meshes, permutations tables that link a vertex in $\mathcal{M}_D^{n+1}$ to its equivalent in $\mathcal{M}_i^{n+1}$ and/or $\mathcal{M}_p^{n+1}$ are saved under the form of two arrays of integers. For a given node of index i in the domain mesh, the ith value of the permutation table is the index of the corresponding node in the ice mesh (respectively pore mesh) or 0 if the node does not lie in the ice phase (respectively pore phase). This allows to transfer variables from one mesh to another without interpolation, and with a

[1] https://www.csc.fi/web/elmer/elmer

[2] https://www.mmgtools.org

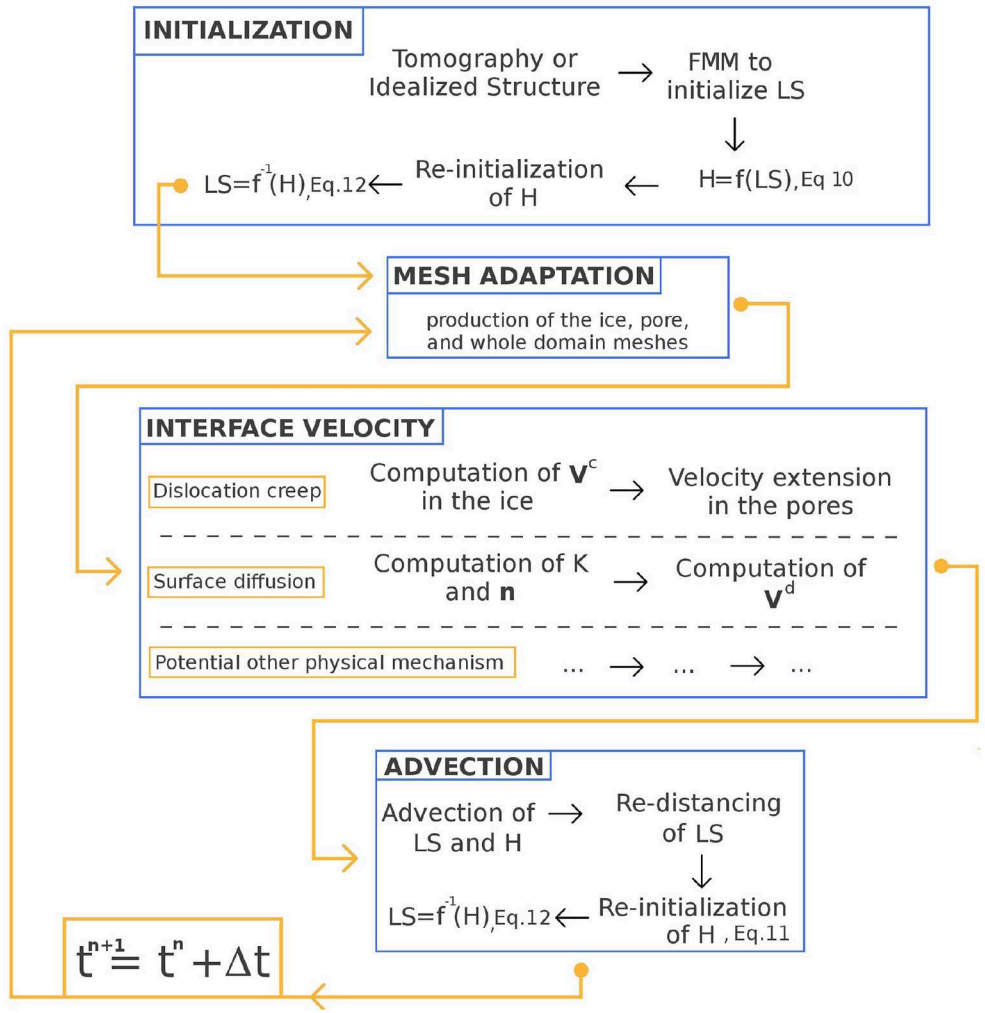

FIGURE 2 | Scheme of the model algorithm. Each blue box represents a core stage of the simulation.

good numerical efficiency. The complete mesh adaptation step procedure is summarized in **Figure 3**.

2.2.2. Computation of the Ice Creep Velocity

To compute the deformation of the ice matrix a numerical oedometric compression is performed, where the ice is compressed at the top and retained on all other sides. The enforced boundary conditions are therefore ones of non-penetration on all the domain sides ($\mathbf{v}^c \cdot \mathbf{n} = 0$, where $\mathbf{n}$ is the normal vector to the boundary), except for the top side where a normal stress is enforced on the ice ($\bar{\bar{\sigma}}\mathbf{n} = -P\mathbf{n}$, where P is the pressure imposed by the overlying column and the atmosphere). This overburden pressure increases with time according to the accumulation rate. The difference between high and low accumulation sites can therefore be modeled with appropriate choices for the increase of the overburden pressure over time. Finally, the force exerted by the air pressure in the pores is applied at the ice/pore interface. The Stokes equations are solved on the ice mesh $\mathcal{M}_i$ using the module readily available in Elmer.

The output velocity field of this oedometric compression produces a lot of displacement at the top of domain and practically none at the bottom. This means that at the top of the domain, the LS function would have to be advected over a long distance during a single time-step, which is numerically detrimental as it increases the Courant number (Courant et al., 1967). In order not to have all the displacement concentrated in one zone, we subtracted its average vertical value to the oedometric ice creep velocity field. This results in a field with the same strain and thus the same deformation of the porous network, but with a vertical velocity field distributed between the top and bottom parts of the sample, as seen in the left panel of **Figure 4**. This distributed velocity field is the velocity used in the model for the creep movement of the ice matrix. Note that performing an oedometric compression and subtracting the average vertical velocity, is equivalent to enforcing a Dirichlet condition of null vertical velocity in the middle of the domain.

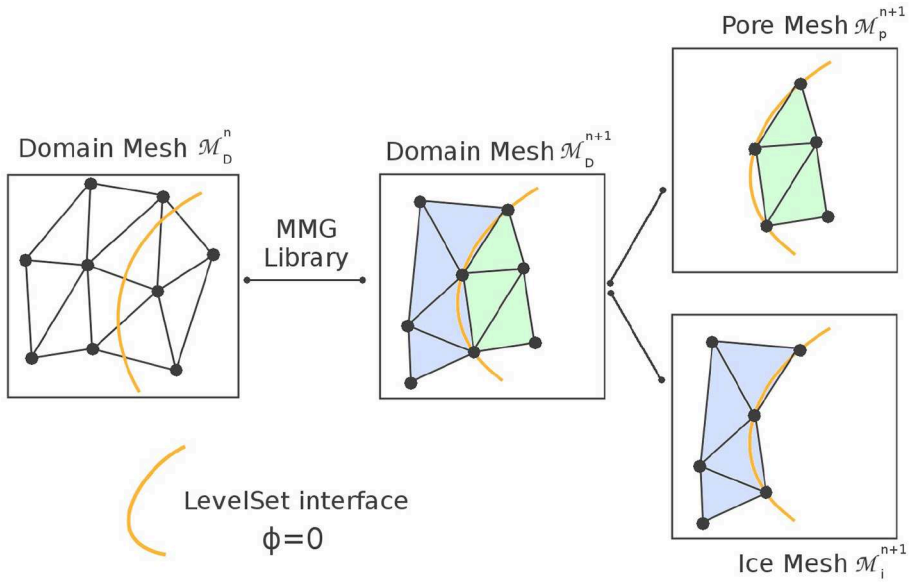

FIGURE 3 | Mesh adaptation of the domain following the LS function. The submeshes of the ice and pore phases $\mathcal{M}_i$, and $\mathcal{M}_p$ are also produced during mesh adaptation.

After solving Equation (1) and subtracting the average vertical value, the creep velocities are known within the ice material. However, to advect the LS function it is necessary for the advection velocity field to be defined on each side of the interface, and thus also inside the pore phase. This is a classical problem of the Level-Set method that can be solved with the aid of velocity extension methods (Adalsteinsson and Sethian, 1999). Here, the ice velocity is extended to the pore phase by solving the Equation:

$$-\alpha\Delta\mathbf{v}^{\text{ext}} + \mathbf{v}^{\text{ext}} = 0 \tag{6}$$

where Δ is the Laplace operator, $\mathbf{v}^{\text{ext}}$ the extended velocity, and α a smoothing parameter. The equation is solved on the pore mesh $\mathcal{M}_p$, with the boundary condition setting the extended velocity equal to the dislocation creep velocity on the ice/pore interface. The solution of Equation (6) is a smooth velocity field, that is equal to the ice creep velocity at the ice/pore interface.

The creep velocity on the ice mesh, and the extended velocity on the pore mesh are then transferred to the domain mesh $\mathcal{M}_D$. This results in a continuous velocity field defined on the whole domain D, that matches the ice creep in the ice region. An example of ice creep velocity extension is given in **Figure 4**.

2.2.3. Computation of the Surface Diffusion Velocity

To compute the surface diffusion velocity using Equation (3), one requires the curvature K and the normal vector $\mathbf{n}$. They can be calculated using:

$$\mathbf{n} = \frac{\nabla\phi}{\|\nabla\phi\|} \tag{7}$$

and

$$K = -\nabla\cdot\mathbf{n} \tag{8}$$

However, Equations (3) and (8) require second-order derivatives, which are not easily computed using first order elements. To reduce numerical noise, Equations (3) and (8) are stabilized with the introduction of diffusion parameters A_{k} and A_{v}:

$$\begin{aligned} K + A_{\text{k}}\Delta K &= -\nabla\cdot\mathbf{n} \\ v^{\text{d}} + A_{\text{v}}\Delta v^{\text{d}} &= C_0(\Delta_s K) \end{aligned} \tag{9}$$

where v^{d} is the norm of $\mathbf{v}^{\text{d}}$.

To compute the diffusion velocity vector $\mathbf{v}^{\text{d}}$, the normal vector $\mathbf{n}$ is first computed using Equation (7). The curvature K is then computed by solving the first equation of Equations (9). The norm v^{d} of $\mathbf{v}^{\text{d}}$ is computed by solving the second equation of Equations (9). The vector $\mathbf{v}^{\text{d}}$ is finally obtained by applying the norm v^{d} to the direction supported by $\mathbf{n}$. These computations are performed using Elmer modules specifically developed for this firn model.

2.2.4. Advection of the Level-Set

Once the total velocity of the interface (the sum of the creep and diffusion velocities) is computed, it is used to modify the porous structure of the firn material by advecting the LS function. However, the sole advection of the LS function using the velocity field is not sufficient to ensure a good representation of the evolution of the interface. Indeed, the property of the LS function to be a signed distance function is lost during the advection step, although it is fundamental for the computation of normal vectors and curvatures (Equation 7 for instance). That is why the LS function is regularly re-distanced, meaning that it is recomputed to remain a signed distance (Osher and Fedkiw, 2001). However, the re-distancing introduces errors and numerical diffusion in the model, that results in unphysical gain or loss of volume (Olsson and Kreiss, 2005). To overcome this issue, Zhao et al. (2014a)

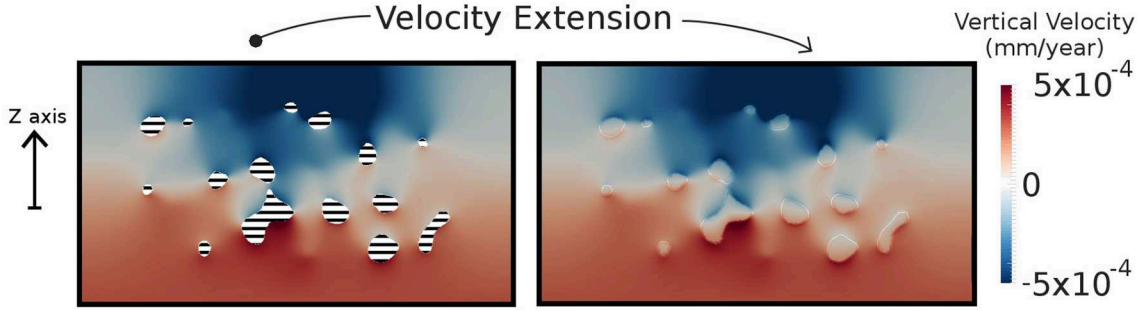

FIGURE 4 | Cut-views of a 3D firn sample (∼ 100 m deep, 7.57 × 3.75 mm dimensions). **(Left)** Vertical creep velocities computed in the ice phase. The pores are filled with black horizontal stripes. **(Right)** Vertical creep velocities extended to the whole domain.

introduced the Improved Conservative Level-Set (ICLS) method following the work of Olsson et al. (2007) on the Conservative Level-Set method. To ensure volume conservation, we have implemented the ICLS method for the advection stage.

The ICLS method introduces a new scalar field H, similar to the LS function ϕ, defined as:

$$H = \frac{1}{2}(1 + \tanh(\frac{\phi}{2\epsilon})) \tag{10}$$

It is a smeared Heaviside function, with a width of the order of ϵ. Similarly to the LS function, H captures the position of the ice/pore interface, that is located at $H = 1/2$. Moreover, H can also be used to compute the normal vector to the interface using Equation (7).

The implementation of the ICLS method works as follows. The LS and H functions are both advected on the mesh $\mathcal{M}_D$ using the total interface velocity. The advection is performed using the Advect software[3]. The LS function is then re-distanced to remain a signed distance function, using the mshdist software[4] (based on Dapogny and Frey, 2012). Next, the normal vectors to the new interface are computed. Near the interface the normal vector $\mathbf{n}$ is computed using the H function, and far from it is computed using the re-distanced LS function. This choice was made because using the H function to compute the normal vectors far from the interface yields spurious oscillations, a problem that does not arise with the LS function (Zhao et al., 2014a,b; Zhao L.-H. et al., 2014). A point of the domain is considered to be in the vicinity of the interface if its distance to the interface is smaller than twice the parameter ϵ in Equation (10). Then, the shape and the width of the H function are maintained thanks to a re-initialization step (Olsson et al., 2007; Zhao et al., 2014a,b; Zhao L.-H. et al., 2014). It consists in solving the equation:

$$\frac{\partial H}{\partial T} + \nabla \cdot [H(1-H)\mathbf{n}] = \nabla \cdot [\epsilon(\nabla H.\mathbf{n})\mathbf{n}] \tag{11}$$

In this equation, T is non-dimensionalized fictional time, distinct from the actual time, that is solely used to relax the equation to equilibrium (Olsson et al., 2007). The term on the left-hand side of Equation (11) compresses the width of the H function, while the right-hand side term expands it. The equation should be solved until the two terms balance, and a steady-state is reached (Olsson et al., 2007; Zhao et al., 2014a,b; Zhao L.-H. et al., 2014). In our model, the fictional time-step is set $\Delta T = 1$, and the equation is solved for a total 15 fictional time-steps, which is enough to reach a steady state (Olsson et al., 2007). Once the H function has been re-initialized, the LS function ϕ is updated in the vicinity of the interface using:

$$\phi = 2\,\epsilon\,\tanh^{-1}(2H - 1) \tag{12}$$

The advection step is then finished and the LS function defines the interface for the following time-step.

2.2.5. Initialization of the Model

The model needs to be initialized with a LS function, representing either a real firn porous structure or an idealized geometry. The initial porous structure can be derived from 3D voxel models obtained with Xray tomography of firn samples (Barnola et al., 2004; Gregory et al., 2014; Burr et al., 2018). To simplify the boundary conditions, the tomography models are padded with ice material on all sides, meaning that the ice/pore interface lies away from the boundaries of the domain D.

Starting from a 3D voxel model, the signed distance is computed on a Cartesian grid using the Fast Marching Method (FMM; Sethian, 1999). It is performed using the scikit-fmm[5] python package. The signed distance is then smoothed using a gaussian filter to remove the jags of the interface. The resulting signed distance defines the initial LS function, and is interpolated on the initial mesh $\mathcal{M}_D^0$. Since, the position of the ice/pore interface is not known in advance, $\mathcal{M}_D^0$ is finely resolved over the whole domain to properly capture its initial position.

Next, the H function is determined using Equation (10). In order to further smooth the interface and remove remaining jags, we perform a re-initialization step of H solving Equation (11) to equilibrium, followed by a LS function update using Equation (12). At this stage, the simulation can start with a mesh adaptation step.

[3]https://github.com/ISCDtoolbox/Advection
[4]https://github.com/ISCDtoolbox/Mshdist
[5]https://pypi.org/project/scikit-fmm/

3. NUMERICAL EXPERIMENTS

In this part we present a few numerical experiments, performed with the 3D firn model presented before. The aim of section 3.1 is to assess the capability of our model to conserve mass thank to the ICLS method. In section 3.2, we then use the model to quantify the impact of building pressure on the compressibility of closed pores in deep firn. Finally, section 3.3 discusses the contribution of individual physical mechanisms to the splitting of pores.

3.1. Mass Conservation

The goal of the ICLS method (Equation 11) and of the re-initialization is to ensure mass and volume conservation (Olsson et al., 2007; Zhao et al., 2014a,b; Zhao L.-H. et al., 2014). Similarly to Zhao et al. (2014b), we test the mass conservation of our micro-mechanical model by considering the advection of an idealized structure, in our case a sphere.

The domain is composed of a column of ice with dimensions 1 $\times 1 \times 4$ mm. The LS function is initialized to represent a spherical pore of radius 0.25 mm at the bottom of the column (see the left panel of **Figure 5**). This sphere is advected upward with a constant velocity of 10^{-3} mm yr^{-1}. Note that this advection velocity is imposed and does not depend on the computation of the mechanisms of surface diffusion or ice dislocation creep. Pictures of the sphere at the beginning and the end of the simulation are shown in **Figure 5**. The volume of the sphere is computed at the end of each time-step using the volume enclosed by the LS function.

With several sets of parameters, we tested the influence of the h_{grad} (mesh size gradation), h_{ausd} (controlling the mesh size at the interface), and ϵ (width of the H function) parameters on mass conservation. The different parameters of the simulations are listed in **Table 1**. The volume error evolutions are displayed in **Figure 6**. In the two best experiments (Exp2 and Exp7), the volume error does not exceed 2.5% after 20 time-steps and a total displacement of the sphere of 2 mm. These two cases are represented as orange pentagons and gray rhombuses in both panels of **Figure 6**. The results of the experiments show that smaller time-steps do not necessarily imply a better mass conservation. Indeed, comparing the blue dots ($\Delta t = 100$ yr, Exp1) and the yellow crosses ($\Delta t = 50$ yr, Exp8) points in **Figure 6** indicates a larger error at the end of the total advection in the case of the smaller time-step. Our understanding is that each time-step introduces volume errors during the advection step, and that multiplying time-steps accumulates the errors.

Moreover, it appears that a poor choice of parameters can lead to an important accumulation of errors over time, as seen with Exp3, 4, and 5 in **Figure 6**. It is however not straightforward to estimate the ideal parameters for a given simulation, as they depend on the specific geometry and velocity field of the problem. To limit problems of mass conservation, the rest of the simulations of this paper will not be run for more than 10 time-steps. **Figure 6** indicates that this should result in total errors of $<5\%$. In contrast, a simulation without the ICLS results in a $\sim$ 10% volume error after three time steps (black squares in **Figure 6**). This experiment highlights the necessity of the ICLS method to maintain small volume errors. For the rest of the article, the mesh adaptation parameters are set to $h_{\text{ausd}} = 0.01$ mm, $h_{\text{grad}} = 1.15$, and $\epsilon = 0.1$ mm. This results in boundary triangle elements with an average side of about 0.06 mm.

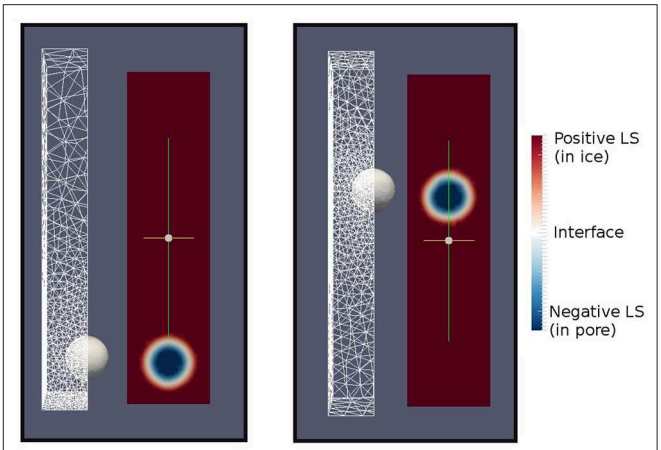

FIGURE 5 | Advection of a sphere. The left and right panels, respectively display the start and end the simulation. In each panel: the left part is the side view of the structure with the surface of the sphere in gray and the mesh of the exterior ice in white. The right part is a cross section of the column showing the LS function. Red colors represent the ice phase and blue colors the pore phase.

Zhao et al. (2014b) report a similar mass conservation experiment for a 2D case using an advected circle. They manage to maintain a relative error below 2%, for a total advection of about 250 diameters of the circle. Even though the 3D and 2D cases cannot be directly compared, it suggests that the model could be improved to obtain a better mass conservation. Moreover, there is a broad scientific literature on the implementation of conservative advection schemes for the Level-Set method (e.g., Kees et al., 2011; Owkes and Desjardins, 2013; Chiodi and Desjardins, 2017), that could benefit to the mass conservation capacity of our model in the future.

3.2. Effect of Internal Pressure on Pore Compression

As a first application of the model, we quantify the impact of internal pressure on the compression of closed pores. Indeed, current gas trapping models assume that in deep firn, open, and already closed pores compress in a similar fashion (Rommelaere et al., 1997; Buizert et al., 2012; Witrant et al., 2012). In real firn, the increased pressure in the already closed bubbles might slow their compression compared to open pores. A recent study by Fourteau et al. (2019) has shown that reducing the compressibility of closed pores by an amount of 50% in gas trapping models could explain a discrepancy between model results and direct measurements of air content in ice cores. It is however not clear if this reduced compressibility of 50% is physically sound or not.

To answer this question, we simulate the densification of a layer of the Lock-In firn, on the East Antarctic plateau. This site is characterized by an accumulation rate of

TABLE 1 | Parameters used for the sensitivity test of mass conservation.

h_{grad}	ϵ (mm)	h_{ausd} (mm)	Time-step (yr)	Experiment number
1.1	0.1	0.01	100	1
1.05	0.1	0.01	100	2
1.2	0.1	0.01	100	3
1.1	0.05	0.01	100	4
1.1	0.2	0.01	100	5
1.1	0.1	0.005	100	6
1.1	0.1	0.02	100	7
1.1	0.1	0.01	50	8
1.1	0.1	0.01	200	9
1.1	n.a.	0.01	100	10, No ICLS

3.9 cm yr^{-1} (ice equivalent), a surface temperature of $-53°C$, and a surface pressure evaluated at 0.0645 MPa (645 mbar) (Fourteau et al., 2019). The model is initialized with the microstructure obtained with a 2.5 × 2.5 × 2.5 mm tomography image, and selected at 80 m depth, near the start of the pore closure zone.

Two distinct simulations are performed. In the first one, the internal pressure of the pores is set to 0.065 MPa, the pressure of open pores found ∼ 100 m below surface. This thus corresponds to the compression of open pores. In the second case, the internal pressure of the pores increases according to its reduction of volume, following an ideal gas law. This represents the compression of closed pores. In both cases, the compression forces of the overlying column start at 0.62 MPa and increases over time due to the surface accumulation rate of 3.9 cm of ice equivalent per year. Furthermore, the mechanism of surface-diffusion is removed from the simulations. As this mechanism does not theoretically modify the total volume of the porosity, it should not influence the effect of pore pressure on their compressibility. The time-step is set to 200 yr, which results in a maximum displacement of the interface that does not exceed a few percents of the characteristic size of the pores.

The relative volume evolutions of the pores for 10 time-steps are displayed in **Figure 7**. The volume variations are larger than the uncertainties reported in section 3.1, and cannot be explained solely by mass conservation errors. It appears that the effect of building pressure does not have a strong impact on pore volume until more than 500 years have passed. At that point, the building pressure in the closed pores reaches 0.16 MPa, more than twice the initial value. The measured thickness of the pore closure zone at Lock-In is of about 20 m (Fourteau et al., 2019). With an accumulation of 3.9 cm per year, a given firn stratum takes about 500 yr to cross the pore closure zone. Therefore, this simulation suggests that the effect of building pressure in closed bubbles does not play a major role in the pore closure zone.

To better quantify this effect, we computed the compression speed of the porosity in each case (building pressure and no pressure building cases). The compression speed is defined here as $\partial_t V/V$, where V is the volume of the porosity and $\partial_t V$ is its temporal derivative. **Figure 8** shows the reduction of compression speed due to the building of internal pressure, compared to the case with pressure kept constant. Within the pore closure zone ($t \leq 500$ years), the compression speed with increasing pressure is reduced on average by 10%. The discrepancy between modeled and measured air content values in ice cores reported by Fourteau et al. (2019) cannot therefore be explained solely by the reduced compressibility of closed pores.

3.3. Contributions of Dislocation Creep and Surface Diffusion to Pore Splitting

In a recent article, Burr et al. (2019) performed different types of cold-room experiments to study the decoupled contributions of ice creep and curvature-driven diffusion to the evolution of firn and its porosity. They conclude that both compression and diffusive mechanisms contribute to the separation of pores.

In this section, we modeled the equivalent of Burr et al. (2019) experiments to study the individual contributions of dislocation creep and surface diffusion to the densification of firn and the closure of pores. In total, we run four different experiments, all initialized with the same porous network. The structure is extracted from the tomography image of a real firn sample excavated around the 100 m depth in the Lock-In firn core, described in the previous section. A 5.35 × 5.35 × 3.75 mm rectangular cuboid was extracted from a tomography image and used for initialization. The initial structure is shown in the left side of **Figure 9**. The compression imposed by the overlying firn column starts at 0.66 MPa and increases over time according to the 3.9 cm of ice per year accumulation rate. The internal pressure of the pores is maintained at 0.065 MPa, as we have seen that the building pressure in closed pores is small in the pore closure zone. All simulations are performed with a 100 years time-step, for a maximum of 10 time-steps.

3.3.1. Surface Diffusion Only

In the first simulation, the process of ice creep is removed and only the curvature-driven surface diffusion is taken into account. The parameter C_0 is set to 10^{-6} mm^4 yr^{-1}. The evolution of the initial firn structure after 700 years of evolution with surface diffusion only is displayed in **Figure 9A**. As seen in the figure, the mechanism of surface diffusion leads to a rounding of pores over time. This is consistent with a mass transport occurring from regions of high curvature toward regions of low curvature, as exemplified in **Figure 10**. While Burr et al. (2019) report that letting firn samples evolve at rest in a relatively high-temperature environment ($-2°C$) without compression leads to pore splitting, we did not observe such phenomenon in our simulation.

As the LS function gives the position of the ice/pore interface, it is possible to convert the output of the simulation into binary images, similar to tomographic images. We performed this conversion for the time-steps $t = 0$ and $t = 700$ years. The binary images can then be analyzed as tomographic images, and the number of individual pores in the medium can be counted (using the ImageJ plug-in Analysis_3D here; Boulos et al., 2012). It reveals that the simulation starts with 39 individual pores in

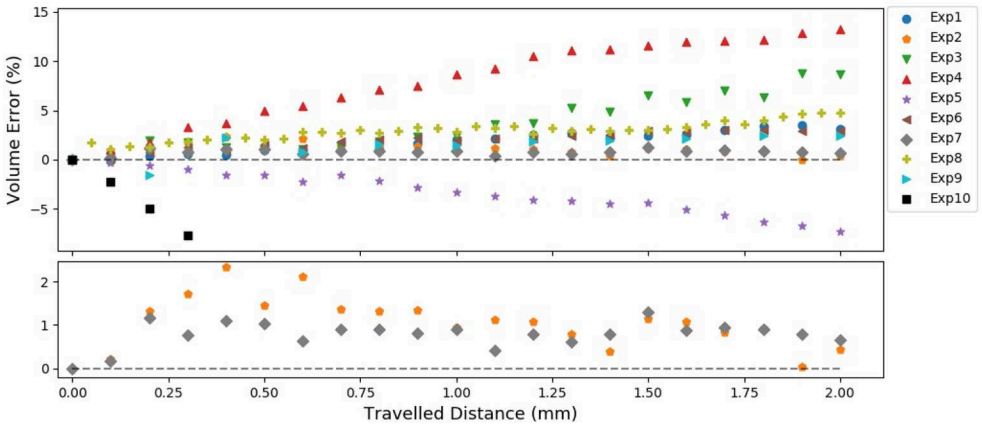

FIGURE 6 | Volume error of the advected sphere, expressed in percent of its initial volume. The orange pentagons and gray rhombuses correspond to the best parameterizations for mass conservation, and the black squares to an advection experiment without the ICLS method. The specific parameters of the other simulations are given in **Table 1**. The lower panel is a zoom to the best simulation results.

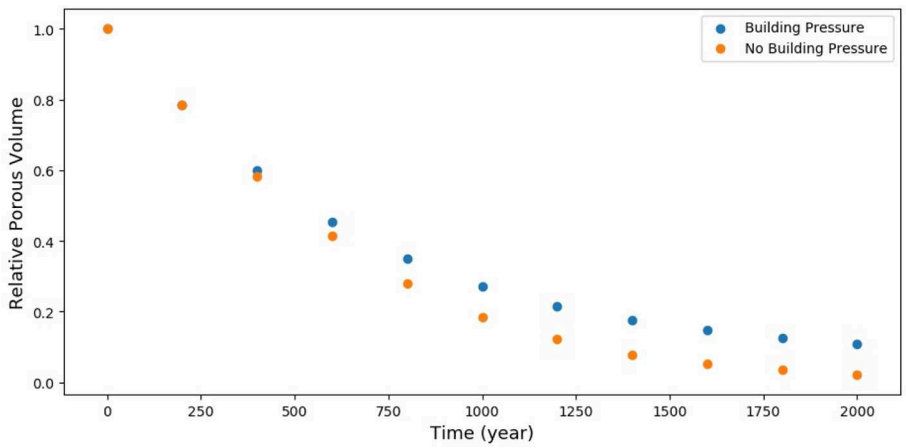

FIGURE 7 | Relative volume as a function of time, with or without building of internal pressure.

the volume and drops to only 9 individual pores after 700 years. This highlights that pore coalescence happened multiple times during the simulation. Thanks to the LS function, the density of the medium during the simulation can be quantified. The initial ice volume fraction is 0.902, and drops to 0.884 after 700 years, that is to say a decrease of about 2%. However, the mechanism of surface diffusion should theoretically not modify the density of the medium (Bruchon et al., 2010). This drop in ice volume fraction could be explained by the insufficient mass conservation of the model, as it is of the order of the volume error reported in section 3.1. Furthermore, a closer look at the surface diffusion velocity field in **Figure 10**, indicates that despite the stabilization of the equations (introduced in Equations 9) the velocity field exhibits a lot of variability that is likely related to numerical noise, rather than physically-relevant variability. We might therefore expect our representation of surface diffusion to introduce some numerical noise in the results, which could also contribute to the decrease in density.

3.3.2. Ice Creep Only

The second simulation is performed with solely the mechanism of ice creep. The evolution of the initial structure after compression is displayed in **Figure 9B**. As seen in the figure, this simulation leads to a densification of the medium, with a smaller porous network. This observation is confirmed by the analysis of the ice volume fraction, that increased from 0.902 to 0.960 after 700 years. This increase is larger than the uncertainties reported in section 3.1, and cannot therefore be solely explained by a mass conservation problem.

The simulation also visually exhibits pore splitting. This is confirmed by counting the number of individual pores before and after the compression. This number increased from 39 to 57 pores, showing the ability of the ice creep mechanism to split and isolate pores from the atmosphere. The same observation of pore splitting was made by Burr et al. (2019). They report pore separations of a sample during ongoing densification that is subject to solely mechanical loading.

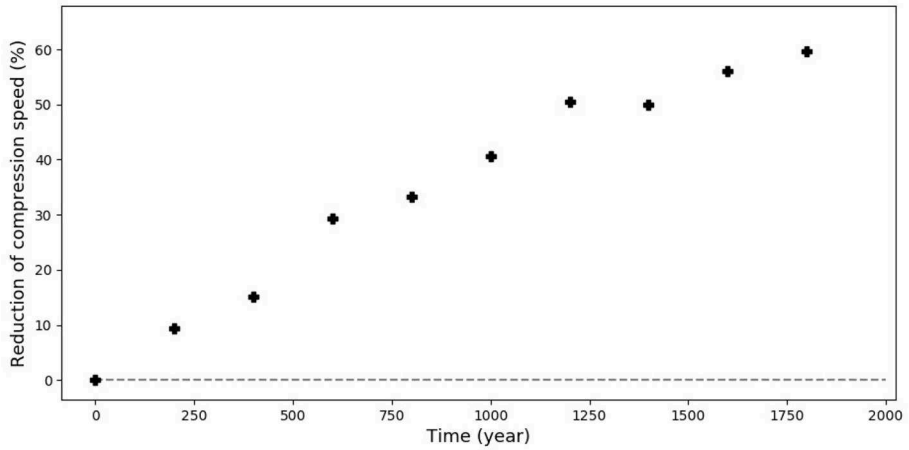

FIGURE 8 | Reduction of the compression speed of closed pores due to the building of pressure. The dashed line represents a non reduced compression speed, as in the constant pressure case.

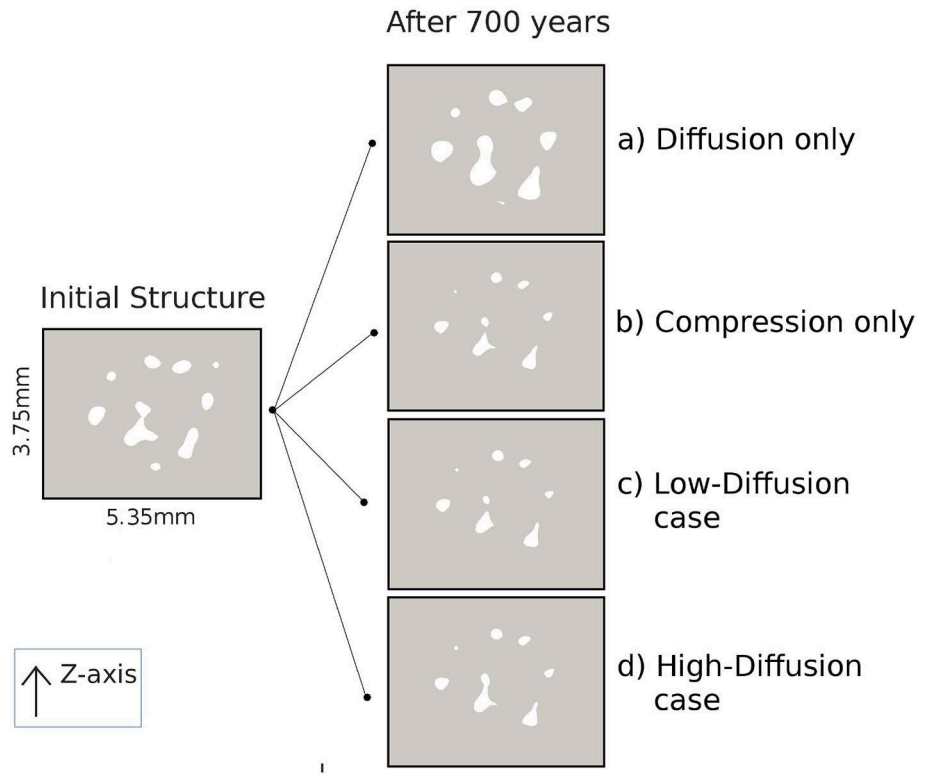

FIGURE 9 | 2D cut-views of the firn material. The gray medium is the ice matrix, and the white spaces are the pores. The slice on the left shows the initial porous structure used in all the simulations, and the four slices on the right show the results of the four different simulations after 700 years. **(A)** Diffusion only, **(B)** compression only, **(C)** Low-diffusion case, **(D)** High-diffusion case.

3.3.3. Combined Ice Creep and Surface Diffusion

The third and fourth simulations take into account the combined effects of curvature-driven surface diffusion and ice creep. The parameter C_0 is set to values of 10^{-6} and $10^{-7}\,\mathrm{mm^4\,yr^{-1}}$, to represent different levels of curvature-driven diffusion, respectively referred to as the high-diffusion and low-diffusion cases for the rest of the section.

2D cut-views of both simulations after 700 years are displayed in **Figure 9C** (low-diffusion case) and **Figure 9D** (high-diffusion case) in the right side of **Figure 9**. The results show an increase

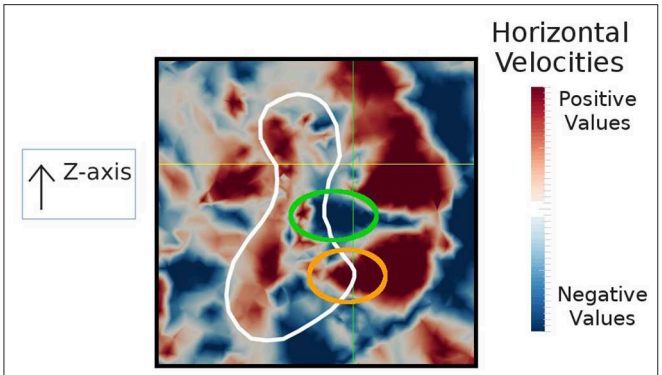

FIGURE 10 | 2D cut-view of the firn material showing the surface-diffusion velocity field in the horizontal direction. Blue colors stand for negative values and red colors for positive values. The interface of a pore is highlighted in white in the middle of the section. The green and orange circles, respectively, show the regions where the interface is receding in the ice phase and growing in the pore phase. This leads to the rounding of the pore.

in ice volume fraction from 0.902 to 0.959 for the low-diffusion case, and to 0.953 for the high-diffusion case. Increasing the role of diffusion in the simulation leads to a slightly smaller density. This is consistent with the 0.960 value reported in the absence of surface diffusion. Moreover, observation of the Lock-In firn core shows that ice volume fractions of 0.95 are found around the 130 m depth. This is consistent with the 700 years sinking time of the simulation, which corresponds to about 30 m of depth increase.

Analysis of the results also shows an increase in the number of individual pores from 39 to 61 and 50 for the low and high-diffusion, respectively. It appears that in the high-diffusion case, the mechanism of surface diffusion slows down the splitting of pores. Our understanding is that the diffusive mechanism leads to a rounding of the pores, preventing the development of small necks that would eventually lead to pore splitting. Surprisingly, the low-diffusion case displays a little more pore splitting than the case without any surface diffusion, that resulted in 57 individual pores after 700 years. It is not clear if this is related to a specific inter-play between the diffusion and creep mechanisms that would accelerate the splitting of pores, or simply numerical noise.

4. DISCUSSION

Combining the Finite Element and Level-Set methods is a promising modeling approach to simulate the topological evolution of firn under compression. Notably, the use of a mesh for the ice phase enables to easily compute deformation velocities as response to mechanical compression. This velocity field can then be used to simulate the evolution of the ice/pore interface with the LS function.

Yet, several optimizations and improvements of the model are still required before its operational application to study the closure of pores in polar firn. First, the model is currently fully sequential. Running a 10 steps simulation on a single processor and for a $5.35 \times 5.35 \times 3.75$ mm firn sample requires roughly a day of computation. The parallelization of the model would curb down this time, and allow to use the model on several-centimeter large domains, which have been shown to be more representative of real firn (Schaller et al., 2017; Burr et al., 2018). Moreover, parallelization would allow to use finer meshes and more complex numerical schemes that could improve the mass conservation and numerical stability of the model. The current version of the model cannot indeed ensure a mass conservation better than about 5% after ten time steps. This limits the ability of the model to perform simulations covering large time periods, and to accurately quantify the density increase of firn samples. Future work on the model should improve this mass conservation problem, potentially with the use of other mass-conserving advection schemes from the literature (e.g., Kees et al., 2011; Owkes and Desjardins, 2013; Chiodi and Desjardins, 2017). Finally, as shown in section 3.3.1, the current implementation of the surface diffusion mechanism leads to a noisy velocity field that might deteriorate the robustness of the results. The use of a very fine mesh near the interface could help resolve this problem, but would lead to a sharp increase in the computation time. On the other hand, the use of more sophisticated stabilization techniques (such as in Bruchon et al., 2010) could resolve this issue without an additional computational cost. Another solution could be the use of second-order elements for the computation of the second-derivatives required for the diffusive mechanism. As diffusion appears to play a significant role in the morphology of pores (Burr et al., 2019), it seems important to implement a fast and robust representation of diffusive mechanisms in the model. This would help to decipher the relative contributions of ice creep and diffusion to the evolution of the porous network, and provide insights on the evolution of pores at very low temperature.

In the article we first use our model to assess the impact of internal building pressure on the compressibility of closed pores. This allows to test the proposed hypothesis of Fourteau et al. (2019) that a lower compressibility of closed pores could explain a discrepancy between modeled and measured air content values in ice cores. Our results indicate that the compressiblity of closed pores is only reduced by an amount of $\sim$ 10%, much lower than the reduction needed to fully explain the model/data mismatch of Fourteau et al. (2019). Other potential mechanisms advanced by Fourteau et al. (2019) to explain this discrepancy are the brittle reopening of pores under pressure or the effusion of gases trough small capillaries not visible with Xray tomography or pycnometry measurements. Further work on the physical processes at play at the microstructural scale in firn is needed to resolve this question.

Then, we compare results of the model with cold-room experiments performed by Burr et al. (2019). While they report that both diffusive mechanisms and ice dislocation creep contribute to the separation of pores, we did not observe such a phenomenon in the simulations. In the model, the creep of the ice matrix leads to the separation of pores, but on the other hand the mechanism of surface diffusion leads to the rounding and even coalescence of pores. As seen in **Figure 10**, the surface diffusion velocity field exhibits numerical noise. This noise might lead to an unphysical movement of the ice/pore interface in the model, explaining some of the discrepancy with

the experiment of Burr et al. (2019). However, we expect the mechanism of surface diffusion to transport mass from zones of high curvature to zones of low curvature. This would lead to the rounding of the pores, rather than the pore separation observed by Burr et al. (2019). Another potential explanation could be that the mechanism of surface diffusion implemented in the model is not representative of the diffusive mechanisms at play during (Burr et al., 2019) experiments. It is indeed possible that the dominant diffusive mechanism is the sublimation and redeposition of water molecules at the ice/pore interface, rather than the surface diffusion implemented in our model (Maeno and Ebinuma, 1983). However, the diffusion of water molecules through sublimation and redeposition would also transport matter from regions of higher curvature to regions of lower curvature. We might therefore also expect a rounding of the pores, hindering the formation of necks and their separation.

5. CONCLUSION

This article presents the development and implementation of a 3D micro-mechanical model of firn compression. In order to handle the topological changes occurring in the porous network of deep firn (such as pore splitting or pore coalescence) the model relies on the Level-Set framework to represent the position of the ice/pore interface. The model is able to determine the movement of the interface due to the creep of the ice matrix as a response to the mechanical stress imposed by the overlying firn column. Moreover, mechanisms of curvature-driven diffusion (in our case surface diffusion) can be added to the model. Finally, we implemented the Improved Conservative Level-Set Method (ICLS, Zhao et al., 2014a,b; Zhao L.-H. et al., 2014) to improve the mass conservation properties of the model. Numerical experiments on an idealized case indicate that the implementation of the ICLS method greatly improves the mass conservation. Yet, errors of several percent after ten time-steps are still present.

As a first application, we assess the impact of internal pressure in the compression of closed pores near the firn/ice transition. In order not to rely on an idealized geometry we used a real porous network, extracted from a tomographic image, to carry out the simulations. Our results indicate that the increase of internal pressure can be ignored at the bottom of the firn column, as assumed by existing gas trapping models (Rommelaere et al., 1997; Buizert et al., 2012; Witrant et al., 2012). Finally, we study the contributions of ice dislocation creep and surface diffusion to the densification of a small firn sample and to the separation of pores. As expected the mechanical compression of the firn sample leads to an increase in density, as well as pore splitting reflected by an increase in the number of individual pores. On the other hand, the mechanism of surface diffusion appears to lead to pore rounding which hinders their separation.

Our results suggest that the Level-Set method, combined with Finite Element modeling, can be adequate to study polar firn densification and pore isolation from the atmosphere, although several improvements are still required.

DATA AVAILABILITY STATEMENT

The datasets generated for this study are available on request to the corresponding author.

AUTHOR CONTRIBUTIONS

The model was developed by KF with the help of FG-C, following an idea of KF, PM, and XF. The manuscript was written by KF, with the help of all co-authors.

FUNDING

This work was supported by the French INSU/CNRS LEFE projects NEVE-CLIMAT and HEPIGANE. The Lock-In drilling operation was supported by the IPEV project no. 1153 and the European Community's Seventh Framework Programme under grant agreement no. 291062 (ERC ICE&LASERS). The tomography images were obtained by the Institute for Snow and Avalanche Research SLF (Davos, Switzerland).

ACKNOWLEDGMENTS

We thanks Christophe Martin and Didier Bouvard for pointing to us the usage of Level-Set models in the sintering community. We thank Maurine Montagnat for the useful discussion on ice mechanics. We thank Olivier Gagliardini for his help with the Elmer software. We thank Charles Dapogny for the useful discussion on the Level-Set method, mesh adaptation, and advection of scalar field. We thank Martin Schneebeli, Henning Löwe, and Anouk Marsal for their involvement with the tomography images. The Lock-In drilling operation was conducted by Phillipe Possenti, Jérôme Chappellaz, David Colin, Philippe Dordhain, and PM. We are thankful to MT and MR for reviewing this article, and to JG for editing it.

REFERENCES

Adalsteinsson, D., and Sethian, J. (1999). The fast construction of extension velocities in level set methods. *J. Comput. Phys.* 148, 2–22. doi: 10.1006/jcph.1998.6090

Arnaud, L., Barnola, J.-M., and Duval, P. (2000). Physical modeling of the densification of snow/firn and ice in the upper part of polar ice sheets. *Phys. Ice Core Rec.* 285–305. Available online at: http://hdl.handle.net/2115/32472 (accessed March 06, 2020).

Arthern, R. J., Vaughan, D. G., Rankin, A. M., Mulvaney, R., and Thomas, E. R. (2010). *In situ* measurements of antarctic snow compaction compared with predictions of models. *J. Geophys. Res. Earth Surf.* 115:F03011. doi: 10.1029/2009JF001306

Arzt, E., Ashby, M. F., and Easterling, K. E. (1983). Practical applications of hot isostatic pressing diagrams: four case studies. *Metall. Trans. A* 14, 211–221. doi: 10.1007/BF02651618

Ashby, M. (1974). A first report on sintering diagrams. *Acta Metall.* 22, 275–289. doi: 10.1016/0001-6160(74)90167-9

Barnola, J.-M., Pierritz, R., Goujon, C., Duval, P., and Boller, E. (2004). 3D reconstruction of the vostok firn structure by x-ray tomography. *Data Glaciol. Stud.* 97, 80–84. Available online at: http://ftp.esrf.eu/pub/UserReports/21167_C.pdf (accessed March 06, 2020).

Barnola, J.-M., Raynaud, D., Korotkevich, Y. S., and Lorius, C. (1987). Vostok ice core provides 160,000-year record of atmospheric CO_2. *Nature* 329, 408–414. doi: 10.1038/329408a0

Bazin, L., Landais, A., Lemieux-Dudon, B., Toyé Mahamadou Kele, H., Veres, D., Parrenin, F., et al. (2013). An optimized multi-proxy, multi-site Antarctic ice and gas orbital chronology (AICC2012): 120-800 ka. *Clim. Past* 9, 1715–1731. doi: 10.5194/cp-9-1715-2013

Bernacki, M., Chastel, Y., Coupez, T., and Logé, R. (2008). Level set framework for the numerical modelling of primary recrystallization in polycrystalline materials. *Scr. Mater.* 58, 1129–1132. doi: 10.1016/j.scriptamat.2008.02.016

Bondzio, J. H., Seroussi, H., Morlighem, M., Kleiner, T., Rückamp, M., Humbert, A., et al. (2016). Modelling calving front dynamics using a level-set method: application to Jakobshavn Isbræ, West Greenland. *Cryosphere* 10, 497–510. doi: 10.5194/tc-10-497-2016

Boulos, V., Fristot, V., Houzet, D., Salvo, L., and Lhuissier, P. (2012). "Investigating performance variations of an optimized GPU-ported granulometry algorithm," in *Proceedings of the 2012 Conference on Design and Architectures for Signal and Image Processing* (Rhodes Island), 1–6.

Bruchon, J., Drapier, S., and Valdivieso, F. (2010). 3D finite element simulation of the matter flow by surface diffusion using a level set method. *Int. J. Numer. Methods Eng.* 86, 845–861. doi: 10.1002/nme.3079

Bruchon, J., Pino-Muñoz, D., Valdivieso, F., and Drapier, S. (2012). Finite element simulation of mass transport during sintering of a granular packing. Part I. Surface and lattice diffusions. *J. Am. Ceram. Soc.* 95, 2398–2405. doi: 10.1111/j.1551-2916.2012.05073.x

Buizert, C., Martinerie, P., Petrenko, V. V., Severinghaus, J. P., Trudinger, C. M., Witrant, E., et al. (2012). Gas transport in firn: multiple-tracer characterisation and model intercomparison for NEEM, Northern Greenland. *Atmos. Chem. Phys.* 12, 4259–4277. doi: 10.5194/acp-12-4259-2012

Burr, A., Ballot, C., Lhuissier, P., Martinerie, P., Martin, C. L., and Philip, A. (2018). Pore morphology of polar firn around closure revealed by X-ray tomography. *Cryosphere* 12, 2481–2500. doi: 10.5194/tc-12-2481-2018

Burr, A., Lhuissier, P., Martin, C. L., and Philip, A. (2019). *In situ* X-ray tomography densification of firn: the role of mechanics and diffusion processes. *Acta Mater.* 167, 210–220. doi: 10.1016/j.actamat.2019.01.053

Calonne, N., Geindreau, C., and Flin, F. (2014). Macroscopic modeling for heat and water vapor transfer in dry snow by homogenization. *J. Phys. Chem. B* 118, 13393–13403. doi: 10.1021/jp5052535

Chiodi, R., and Desjardins, O. (2017). A reformulation of the conservative level set reinitialization equation for accurate and robust simulation of complex multiphase flows. *J. Comput. Phys.* 343, 186–200. doi: 10.1016/j.jcp.2017.04.053

Courant, R., Friedrichs, K., and Lewy, H. (1967). On the partial difference equations of mathematical physics. *IBM J. Res. Dev.* 11, 215–234. doi: 10.1147/rd.112.0215

Cuffey, K., and Paterson, W. S. B. (2010). *The Physics of Glaciers, 4th Edition*. Academic Press. Available online at: https://www.elsevier.com/books/the-physics-of-glaciers/cuffey/978-0-12-369461-4

Dansgaard, W. (1953). The abundance of O^{18} in atmospheric water and water vapour. *Tellus A Dyn. Meteorol. Oceanogr.* 5, 461–469. doi: 10.1111/j.2153-3490.1953.tb01076.x

Dapogny, C., Dobrzynski, C., and Frey, P. (2014). Three-dimensional adaptive domain remeshing, implicit domain meshing, and applications to free and moving boundary problems. *J. Comput. Phys.* 262, 358–378. doi: 10.1016/j.jcp.2014.01.005

Dapogny, C., and Frey, P. (2012). Computation of the signed distance function to a discrete contour on adapted triangulation. *Calcolo* 49, 193–219. doi: 10.1007/s10092-011-0051-z

Duval, P., Ashby, M. F., and Anderman, I. (1983). Rate-controlling processes in the creep of polycrystalline ice. *J. Phys. Chem.* 87, 4066–4074. doi: 10.1021/j100244a014

Fourteau, K., Faïn, X., Martinerie, P., Landais, A., Ekaykin, A. A., Lipenkov, V. Y., et al. (2017). Analytical constraints on layered gas trapping and smoothing of atmospheric variability in ice under low-accumulation conditions. *Clim. Past* 13, 1815–1830. doi: 10.5194/cp-13-1815-2017

Fourteau, K., Martinerie, P., Faïn, X., Schaller, C. F., Tuckwell, R. J., Löwe, H., et al. (2019). Multi-tracer study of gas trapping in an East Antarctic ice core. *Cryosphere* 13, 3383–3403. doi: 10.5194/tc-13-3383-2019

Gagliardini, O., Zwinger, T., Gillet-Chaulet, F., Durand, G., Favier, L., de Fleurian, B., et al. (2013). Capabilities and performance of Elmer/Ice, a new-generation ice sheet model. *Geosci. Model Dev.* 6, 1299–1318. doi: 10.5194/gmd-6-1299-2013

Gibou, F., Fedkiw, R., and Osher, S. (2018). A review of level-set methods and some recent applications. *J. Comput. Phys.* 353, 82–109. doi: 10.1016/j.jcp.2017.10.006

Goujon, C., Barnola, J.-M., and Ritz, C. (2003). Modeling the densification of polar firn including heat diffusion: application to close-off characteristics and gas isotopic fractionation for Antarctica and Greenland sites. *J. Geophys. Res. Atmos.* 108:4792. doi: 10.1029/2002JD003319

Gregory, S. A., Albert, M. R., and Baker, I. (2014). Impact of physical properties and accumulation rate on pore close-off in layered firn. *Cryosphere* 8, 91–105. doi: 10.5194/tc-8-91-2014

Herron, M. M., and Langway, C. C. (1980). Firn densification: an empirical model. *J. Glaciol.* 25, 373–385. doi: 10.1017/S0022143000015239

Johnsen, S. J., Dansgaard, W., and White, J. (1989). The origin of Arctic precipitation under present and glacial conditions. *Tellus B Chem. Phys. Meteorol.* 41, 452–468. doi: 10.3402/tellusb.v41i4.15100

Joos, F., and Spahni, R. (2008). Rates of change in natural and anthropogenic radiative forcing over the past 20,000 years. *Proc. Natl. Acad. Sci. U.S.A.* 105, 1425–1430. doi: 10.1073/pnas.0707386105

Kees, C., Akkerman, I., Farthing, M., and Bazilevs, Y. (2011). A conservative level set method suitable for variable-order approximations and unstructured meshes. *J. Comput. Phys.* 230, 4536–4558. doi: 10.1016/j.jcp.2011.02.030

Loulergue, L., Schilt, A., Spahni, R., Masson-Delmotte, V., Blunier, T., Lemieux, B., et al. (2008). Orbital and millennial-scale features of atmospheric CH_4 over the past 800,000 years. *Nature* 453, 383–386. doi: 10.1038/nature06950

Lundin, J. M., Stevens, C. M., Arthern, R., Buizert, C., Orsi, A., Ligtenberg, S. R., et al. (2017). Firn model intercomparison experiment (FirnMICE). *J. Glaciol.* 63, 401–422. doi: 10.1017/jog.2016.114

Lüthi, D., Floch, M. L., Bereiter, B., Blunier, T., Barnola, J.-M., Siegenthaler, U., et al. (2008). High-resolution carbon dioxide concentration record 650,000– 800,000 years before present. *Nature* 453, 379–382. doi: 10.1038/nature06949

Maeno, N., and Ebinuma, T. (1983). Pressure sintering of ice and its implication to the densification of snow at polar glaciers and ice sheets. *J. Phys. Chem.* 87, 4103–4110. doi: 10.1021/j100244a023

Mitchell, L. E., Buizert, C., Brook, E. J., Breton, D. J., Fegyveresi, J., Baggenstos, D., et al. (2015). Observing and modeling the influence of layering on bubble trapping in polar firn. *J. Geophys. Res. Atmos.* 120, 2558–2574. doi: 10.1002/2014JD022766

Olsson, E., and Kreiss, G. (2005). A conservative level set method for two phase flow. *J. Comput. Phys.* 210, 225–246. doi: 10.1016/j.jcp.2005.04.007

Olsson, E., Kreiss, G., and Zahedi, S. (2007). A conservative level set method for two phase flow II. *J. Comput. Phys.* 225, 785–807. doi: 10.1016/j.jcp.2006.12.027

Osher, S., and Fedkiw, R. P. (2001). Level set methods: an overview and some recent results. *J. Comput. Phys.* 169, 463–502. doi: 10.1006/jcph.2000.6636

Osher, S., and Sethian, J. A. (1988). Fronts propagating with curvature-dependent speed: algorithms based on Hamilton-Jacobi formulations. *J. Comput. Phys.* 79, 12–49. doi: 10.1016/0021-9991(88)90002-2

Owkes, M., and Desjardins, O. (2013). A discontinuous galerkin conservative level set scheme for interface capturing in multiphase flows. *J. Comput. Phys.* 249, 275–302. doi: 10.1016/j.jcp.2013.04.036

Parrenin, F., Masson-Delmotte, V., Köhler, P., Raynaud, D., Paillard, D., Schwander, J., et al. (2013). Synchronous change of atmospheric CO_2 and antarctic temperature during the last deglacial warming. *Science* 339, 1060–1063. doi: 10.1126/science.1226368

Petrenko, V. F., and Whitworth, R. W. (1999). *Physics of Ice*. OUP Oxford.

Pralong, A., and Funk, M. (2004). A level-set method for modeling the evolution of glacier geometry. *J. Glaciol.* 50, 485–491. doi: 10.3189/172756504781829774

Rommelaere, V., Arnaud, L., and Barnola, J.-M. (1997). Reconstructing recent atmospheric trace gas concentrations from polar firn and bubbly ice data by inverse methods. *J. Geophys. Res. Atmos.* 102, 30069–30083. doi: 10.1029/97JD02653

Schaller, C. F., Freitag, J., and Eisen, O. (2017). Critical porosity of gas enclosure in polar firn independent of climate. *Clim. Past* 13, 1685–1693. doi: 10.5194/cp-13-1685-2017

Schulson, E. M., and Duval, P. (2009). *Creep and Fracture of Ice*. Cambridge University Press.

Schwander, J., Barnola, J.-M., Andrié, C., Leuenberger, M., Ludin, A., Raynaud, D., et al. (1993). The age of the air in the firn and the ice at Summit, Greenland. *J. Geophys. Res. Atmos.* 98, 2831–2838. doi: 10.1029/92JD02383

Schwander, J., and Stauffer, B. (1984). Age difference between polar ice and the air trapped in its bubbles. *Nature* 311, 45–47. doi: 10.1038/311045a0

Sethian, J. A. (1999). Fast marching methods. *SIAM Rev.* 41, 199–235. doi: 10.1137/S0036144598347059

Shakun, J. D., Clark, P. U., He, F., Marcott, S. A., Mix, A. C., Liu, Z., et al. (2012). Global warming preceded by increasing carbon dioxide concentrations during the last deglaciation. *Nature* 484, 49–54. doi: 10.1038/nature10915

Spahni, R., Schwander, J., Flückiger, J., Stauffer, B., Chappellaz, J., and Raynaud, D. (2003). The attenuation of fast atmospheric CH_4 variations recorded in polar ice cores. *Geophys. Res. Lett.* 30:1571. doi: 10.1029/2003GL017093

Stauffer, B., Schwander, J., and Oeschger, H. (1985). Enclosure of air during metamorphosis of dry firn to ice. *Ann. Glaciol.* 6, 108–112. doi: 10.3189/1985AoG6-1-108-112

Veres, D., Bazin, L., Landais, A., Toyé Mahamadou Kele, H., Lemieux-Dudon, B., Parrenin, F., et al. (2013). The Antarctic ice core chronology (AICC2012): an optimized multi-parameter and multi-site dating approach for the last 120 thousand years. *Clim. Past* 9, 1733–1748. doi: 10.5194/cp-9-1733-2013

Wilkinson, D. (1988). A pressure-sintering model for the densification of polar firn and glacier ice. *J. Glaciol.* 34, 40–45. doi: 10.1017/S0022143000009047

Wilkinson, D., and Ashby, M. (1975). Pressure sintering by power law creep. *Acta Metall.* 23, 1277–1285. doi: 10.1016/0001-6160(75)90136-4

Witrant, E., Martinerie, P., Hogan, C., Laube, J. C., Kawamura, K., Capron, E., et al. (2012). A new multi-gas constrained model of trace gas non-homogeneous transport in firn: evaluation and behaviour at eleven polar sites. *Atmos. Chem. Phys.* 12, 11465–11483. doi: 10.5194/acp-12-11465-2012

Zhao, L., Bai, X., Li, T., and Williams, J. (2014a). Improved conservative level set method. *Int. J. Numer. Methods Fluids* 75, 575–590. doi: 10.1002/fld.3907

Zhao, L., Mao, J., Bai, X., Liu, X., Li, T., and Williams, J. (2014b). Finite element implementation of an improved conservative level set method for two-phase flow. *Comput. Fluids* 100, 138–154. doi: 10.1016/j.compfluid.2014.04.027

Zhao, L.-H., Mao, J., Liu, X.-Q., Bai, X., and Williams, J. (2014). Improved conservative level set method for free surface flow simulation. *J. Hydrodyn.* 26, 316–325. doi: 10.1016/S1001-6058(14)60035-4

Conflict of Interest: The authors declare that the research was conducted in the absence of any commercial or financial relationships that could be construed as a potential conflict of interest.

frontiers in Earth Science

ORIGINAL RESEARCH
published: 29 April 2020
doi: 10.3389/feart.2020.00122

Microorganisms Associated With Dust on Alpine Snow

Zoe R. Courville[1], Ross M. Lieblappen[1,2], Alison K. Thurston[1], Robyn A. Barbato[1], John M. Fegyveresi[1,3], Lauren B. Farnsworth[1], Jeff Derry[4], R. M. Jones[1], Stacey J. Doherty[1] and Shelby A. Rosten[1]*

[1] US Army Corps of Engineers Engineer Research and Development Center, Cold Regions Research and Engineering Laboratory, Hanover, NH, United States, [2] Department of Science, Vermont Technical College, Randolph Center, VT, United States, [3] School of Earth and Sustainability, Northern Arizona University, Flagstaff, AZ, United States, [4] Center for Snow and Avalanche Studies, Silverton, CO, United States

We investigated snow microstructure and microbial composition from snow samples collected from western Colorado, a region that experiences frequent dust-on-snow deposition events. We developed a methodology to quantify the amount, size, and location of dust particles within the snow matrix through analysis of X-ray micro-computed tomography data. Concurrently, we determined the microbial composition in sampled dust layers through DNA sequencing. We found that dust particles were generally embedded in the snow grains, with a small fraction of the dust particles' surface area exposed to air. Microbial community composition varied more by alpine site rather than residence time of the dust within the snowpack, with the recently deposited dust layer harboring both the highest diversity and highest concentration of dust particles. The presence of microbiota in the dust-impacted snowpack has important implications for snowpack stability, melting, and biogeochemistry.

Keywords: dust, microbes, snow, micro-computed tomography, microstructure

OPEN ACCESS

Edited by:
Melody Sandells, Northumbria University, United Kingdom

Reviewed by:
Arwyn Edwards, Aberystwyth University, United Kingdom
Andrew Jonathan Hodson, The University Centre in Svalbard, Norway

****Correspondence:***
Zoe R. Courville
zoe.r.courville@usace.army.mil

Specialty section:
This article was submitted to Cryospheric Sciences, a section of the journal Frontiers in Earth Science

Received: *29 July 2019*
Accepted: *31 March 2020*
Published: *29 April 2020*

Citation:
Courville ZR, Lieblappen RM, Thurston AK, Barbato RA, Fegyveresi JM, Farnsworth LB, Derry J, Jones RM, Doherty SJ and Rosten SA (2020) Microorganisms Associated With Dust on Alpine Snow. Front. Earth Sci. 8:122. doi: 10.3389/feart.2020.00122

INTRODUCTION

Dust deposition on a snow surface accelerates snow melt primarily by causing the snow surface to become darker and secondarily through dry and wet snow metamorphic processes and snow grain growth that occur before the onset of melt (Conway et al., 1996; Skiles et al., 2018). Our study site, the Senator Beck Basin Study Area in the San Juan Mountains has been extensively studied (Painter et al., 2007, 2012; Skiles et al., 2015) with a focus on the radiative impacts on snowpacks due to dust deposition. Evidence including particle size, isotopic analysis, and remote sensing imagery points to the Colorado Plateau, and possibly the Mojave Desert, as the source regions for the dust deposited in this area (Lawrence et al., 2010; Skiles et al., 2015). The focus of our study was to investigate dust-associated microbial deposition on snowpack and structure and to examine aerosolized microbial communities through dust transport, including dust provenance within a larger project examining the ultimate contribution of dust deposition, and microbial component, to the timing and onset of melt within our study area. Our hypothesis driving this focused area of the larger work is that microbiota present on dust particles deposited on the snow could be linked to source regions.

The global estimate of dust lofting is 2–5 million metric tons per year (Perkins, 2001), providing a significantly large substrate for the transport of dust-associated microorganisms. During lofting events (short and long range) the microorganisms attached to dust can experience a wide range of stressors including UV radiation and dessication, resulting in variable viability (Meola et al., 2015; Schuerger et al., 2018). However, aerosolized dust particulates have been accepted as a major

source of microbes, particularly to remote regions (Harding et al., 2011). Bacteria attached to dust particles can be found deposited anywhere in the world (Miteva et al., 2009; Yamaguchi et al., 2012; Favet et al., 2013). For instance, microorganisms originating from the Saharan Desert have been found thousands of kilometers away in the Caribbean and European Alps (Kellogg and Griffin, 2006; Meola et al., 2015). This global transport of microorganisms has important implications for human-health, ecology, nutrient cycling, and melt (Weir-Brush et al., 2004; Comrie, 2005; Weil et al., 2017).

Of interest to this work was the deposition of microorganisms on snow, which seasonally accounts for 50% of the Earth's surface (Sevruk, 1992). In snow covered environments, once the dust is deposited, its associated microbes are in contact with other microbes inhabiting the snow and ice. In fact, snow and ice microbial communities have been described in the Canadian High Arctic, Iceland, Greenland, and European Alps (Harding et al., 2011; Lutz et al., 2014, 2015; Meola et al., 2015), with $\sim 10^3$-10^4 cells detected per milliliter of melted snow (Maccario et al., 2015; Wunderlin et al., 2016). The remote detection and impact of algae on the albedo of snow has been studied by Painter et al. (2001) and Dial et al. (2018) and modeled by Cook et al. (2017a,b).

One pressing question in the field is how geographically diverse dust-associated microbial populations are (Kellogg and Griffin, 2006; Grantham et al., 2015). A review by Anesio et al. (2017) highlighted that primary producers (e.g., photoautotrophs) found in snow and ice are much more similar across global glacial regions than heterotrophic bacterial communities. They note that limitations in molecular techniques for discriminating eukaryotic organisms may contribute to the lack of reported diversity (Anesio et al., 2017). Dust deposited on snow can be from local, regional or global sources. Therefore, there could be a small subset of microorganisms, which have adapted to the snow environment and are dispersed globally. Conversely, the microbial communities may be influenced more by dust origin and instead exhibit similar functions/processes, which allow for adaptation to snow environments (Kellogg and Griffin, 2006). Comparing the dust collected during dust deposition events to possible dust origins will shed light on this question. For example, it is predicted that a substantial amount of the dust deposited on snow in the San Juan Mountains is from Mojave Desert and the Colorado Plateau (Lawrence et al., 2010). The mechanisms responsible for microbial adaptability to desert conditions (sporulation and pigment production) have been suggested to enable adaptability to the challenging conditions in snow environments (Meola et al., 2015). Dust-associated microorganisms may have different metabolic requirements (Anesio et al., 2017), pigmentation production (Lutz et al., 2014, 2015) and growth rates when compared to microbiota that is native to the snow and ice environment.

METHODS

We investigated the identity of dust-associated microorganisms and their influence on the snow matrix immediately prior to the onset of melt season including microstructural analysis of dust and snow via X-ray micro-computed tomography (micro-CT), meteorological analysis and microbiology.

Alpine snow samples were aseptically collected using sterile gloves and bags in collaboration with the Center for Snow and Avalanche Studies during multiple dust events in the late winter and early spring of 2017 for microbial studies. Coincident snow samples for microstructural analysis were collected for micro-CT investigations non-aseptically. The samples were collected from two different locations: the Berthoud Pass Colorado Dust-on-Snow study site near Winter Park, Colorado and the Swamp Angel Study Plot in Senator Beck Basin near Silverton, Colorado (**Figure 1**). Microbial community composition was measured from the snow samples; coincident snow microstructural analysis and the meteorology of the dust deposition events were examined in order to determine potential impacts to the snow structure and to determine the dust source location. We collected dust-impacted snow samples both immediately following dust deposition events as well as merged snow layers formed at the end of the snow season to examine subsequent post-depositional processes. We sought to discern the aggregated effect of multiple dust deposition events on the snow structure and microbial taxa present.

Snow Sampling

Samples were collected from Berthoud Pass in the central Rocky Mountains near Winter Park, Colorado (39°47′52″N, 105°46′37″W, 3,446 m asl) and the Swamp Angel Study Plot, located in the Senator Beck Basin in the San Juan Mountains, near Silverton, Colorado (37°54′25″N, 107°42′40″W, 3,371 m asl) (**Figure 1**). These study sites are both flat, relatively open areas located within forested regions. For microbial characterization, three separate samples of each dust layer in the snow pack were collected ∼50–100 cm apart (**Table 1**) using sterile bags and collection equipment. Each individual sample consisted of an ∼3 L volume collected aseptically from surface snow immediately following new dust events and in snow pits, after the individual dust layers had merged. For sample collection immediately following dust deposition events, surface samples of the dust layer from the top 5 cm of the snow pack were collected. These samples are denoted as IDL (Individual Dust Layers). Over the course of the late-spring, individual dust deposition layers in the snow typically merge into single layers due to snow processes including melt, grain growth due to temperature gradients within the snowpack, and sublimation/condensation. We collected a snow sample of the buried, merged dust layers by collecting the same volume from the 4 cm thick merged dust layer at the Swamp Angel Study Site and the 3 cm thick merged dust layer at Berthoud Pass. We denote these samples as ALM (All Layers Merged).

Sampling was undertaken for microstructural characterization at the same time as microbial sampling, and included measurements of snow temperature, stratigraphy (via traditional means as well as recorded in near infrared (NIR) photography) and density. Snow samples for microstructural analysis were collected in large, 3,000 cm^3 volumes, 20 × 15 × 10 cm, placed in individual rigid samples containers, packaged securely to minimize movement, and shipped back to the lab in coolers packed in dry ice and eutectic packs. The outer edges of the

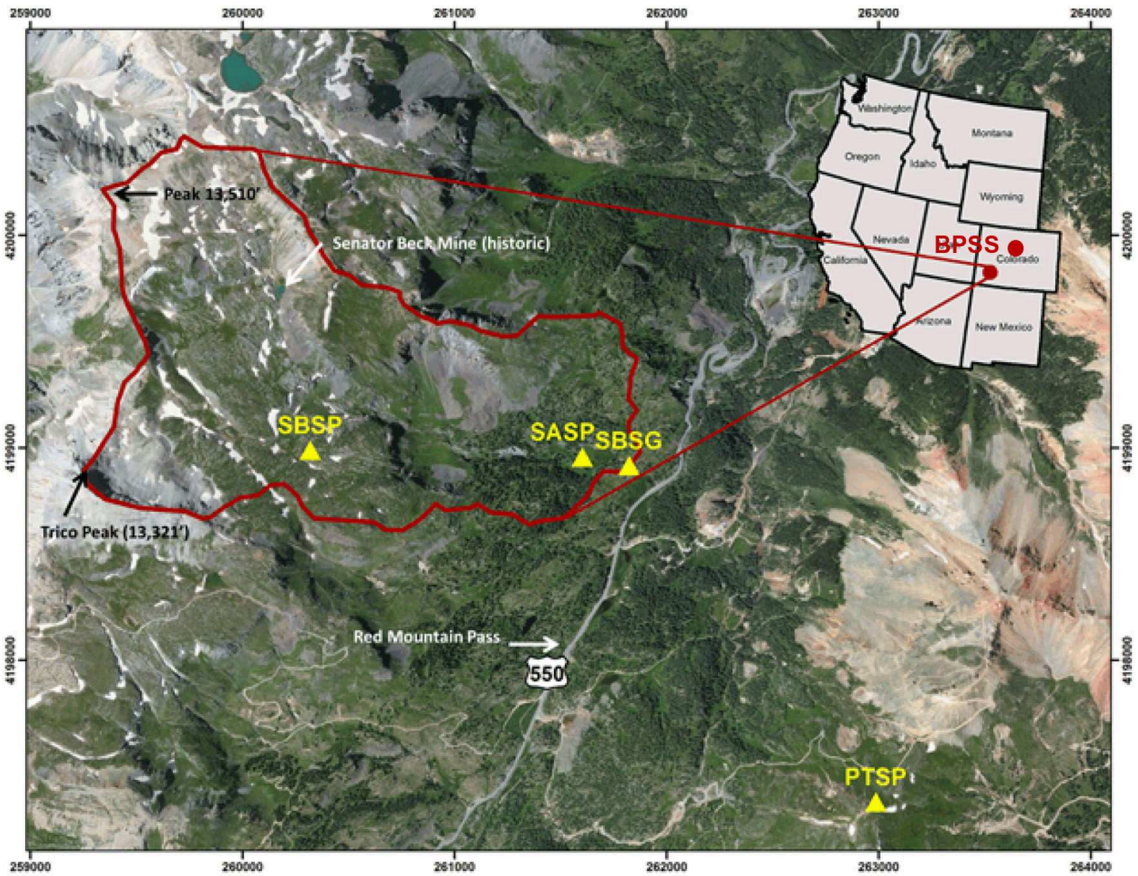

FIGURE 1 | Map from the Center for Snow and Avalanche Studies indicating sample site locations in Colorado, USA (http://snowstudies.org/sbbsa1.html). The Senator Beck Study Plot (SBSP), Swamp Angel Study Plot (SASP), and associated Senator Beck Stream Gauge (SBSG) and Putney Study Plot (PTSP) are indicated by yellow triangles within the Senator Beck Basin (SBB). Samples were collected at the Swamp Angel Study Plot and at the top of Berthoud Pass, in the northwest portion of the state, denoted by BPSS.

TABLE 1 | Samples collected in spring 2017 from Berthoud Pass (near Fraser, Colorado), and the Swamp Angel Study Plot in Senator Beck Basin.

Sample name	Study site	Date collected	Dust event
BP ALM	Berthoud Pass	May 1, 2017	Merged dust layer
SASP IDL	Swamp Angel Study Plot	April 10, 2017	Dust Event 4 (D4)
SASP ALM	Swamp Angel Study Plot	April 29, 2017	Merged dust layer

Each dust layer was sampled three separate times, with each sample spaced ∼50–100 cm apart.

samples were sacrificed so that the center sub volume of 5 × 2 × 2 cm of the sample was imaged. A volume of interest inside the imaged sample was further defined to remove edge effects caused by sample preparation.

Snow Microstructure

In order to determine the location of dust particles within the 3D snow matrix, we imaged snow samples using a Bruker Skyscan 1173 micro-CT scanner housed in a −10°C cold room. We focused on samples collected during the late spring from a merged layer at the Swamp Angel Study Plot, samples collected immediately after a dust event (D4) at Swamp Angeland a sample from a merged dust layer from a snow pit at Berthoud Pass. We examined three separate sub-samples for the individual dust event layer sample. Each sample was scanned with 40 kV X-rays at 200 mA and a nominal resolution of ∼15 μm as the sample was rotated 180° in 0.4° steps with an exposure time of 300–350 ms. X-rays were detected using a 5 Mp (2,240 × 2,240) flat panel sensor utilizing 2 × 2 binning, and projection radiographs were averaged over four frames. The resulting 1,120 × 1,120 radiographs were then reconstructed into 2-D gray-scale horizontal slices using the software package NRecon (Bruker), which utilizes a modified Feldkamp cone-beam algorithm. Image reconstruction processing included sample-specific post alignment, Gaussian smoothing using a kernel size of two, sample-specific ring artifact correction of dead pixels, beam hardening correction, and X-ray source thermal drift correction.

Grayscale images were segmented into three phases: air (lowest x-ray absorption), dust (highest x-ray absorption), and snow (intermediate x-ray absorption). Segmenting thresholds for each of the phases were determined by finding the local

minimum between peaks on the histogram showing all grayscale values. Dust and snow microstructural parameterizations were analyzed using the software package CTAn (Bruker's proprietary CT Analysis program). Microstructural parameters that we calculated using CTAn include the total porosity of the samples, the number of particles or objects of each phase, the surface to volume ratio (S/V) of each phase (which is inversely related to the grain size), and structure thickness, which provides an estimate of particle/pore size depending on the phase that is being examined. Theoretically, assuming the snow grains are spherical particles, S/V is related to the specific surface area (SSA) of snow by the relationship $SSA = S/\rho_i V$, where ρ_i is the density of ice. The SSA is in turn related to the optical grain size of ice (D_0), according to the relationship $D_0 = 6/(\rho SSA)$.

Meteorology

We compiled meteorological data from Swamp Angel Study Plot located within the Silverton Beck Basin near Silverton, Colorado, which was installed and maintained by the Center for Snow and Avalanche Studies, and a second weather station located near the summit of Berthoud Pass. Data captured at these stations include ambient air temperature, humidity, wind direction and wind speed. These measurements were used to evaluate wind direction and wind speed associated with a number of depositional events to better constrain the provenance of the deposited dust. Times reported are in Mountain Standard Time (ignoring Daylight Savings Time).

The Swamp Angel Study Plot is located in a sheltered clearing at the lower end of the Senator Beck Basin Study Area, at ∼3,371 m, below tree-line and surrounded by sub-alpine forest, and is the primary study location for snow sampling. This protected location provided an excellent location for measuring precipitation and snowpack accumulation, where wind speeds are very low (winter hourly average was <1 m/s), and wind redistribution of snow-cover is negligible. Because the site sits in a sheltered pocket at the lower end of the Senator Beck Basin watershed, air temperature and humidity data from the Swamp Angel Study Plot are strongly influenced by the surrounding terrain. The site consists of a 6-m pipe mast with an extensive array of instruments, a stand-alone precipitation gauge, and a surrounding 30 × 30 m snow profile plot. The site is generally level, sloping 3 degrees east-north-east. Air temperature (°C) and relative humidity (%) were measured every 5 s at a fixed height on the tower. Incoming short- and long-wave radiation values are measured (W m^{-2}) every 5 s by individual sensors at the top of the tower. Wind speed data for back trajectory modeling was collected from the Putney Study Plot, a nearby high alpine site, in order to represent basin-wide wind conditions, as opposed to the Swamp Angel Study Plot wind data, which reflects the relatively sheltered study site.

The weather station at Berthoud Pass is maintained by the US Department of Agriculture Natural Resources Conservation Service as part of the National Water and Climate Center (NWCC) at ∼3,446 m elevation. It is a sub-alpine site located below tree-line. Measurements were made hourly and included snow-water equivalent (Sensotec 100″ Transducer), air temperature (YSI extended range), snow depth, soil moisture (Hydraprobe Analog), soil temperature (Hydroprobe Analog), salinity, real dielectric constant, wind direction and speed, and solar radiation. Near real-time data are available on the NWCC website. A second, higher elevation met station is also located near Berthoud Pass, a Meteorological Terminal Aviation Routine (METAR) station, located at an elevation of 3,807 m. We used the wind data from the METAR station, which is the higher site, for back trajectory modeling.

We ran several transport and dispersion simulations using the Hybrid Single Particle Lagrangian Integrated Trajectory (HYSPLIT) model provided by the National Oceanic and Atmospheric Administration (Stein et al., 2015). The HYSPLIT model calculation method is a hybrid between a Lagrangian approach, using a moving frame of reference for the advection and diffusion calculations as the trajectories or air parcels move from their initial location, and an Eulerian approach, which uses a fixed three-dimensional grid as a frame of reference to compute pollutant air concentrations. In order to determine the storm trajectories of the dust deposition events, we ran back trajectory simulations for Senator Beck Basin using a grid-point statistical interpretation archive method, the Global Data Assimilation System, within HYSPLIT.

DNA Sequencing

To examine which microorganisms were associated with the dust deposited on snow, DNA was extracted using the MoBio PowerWater DNA Isolation Kit (MoBio, Carlsbad, California). Samples were prepared for DNA extraction in a −16°C cold room using sterile technique to limit any contamination. Samples were thawed at 4°C over a 3–5 days period and processed within 48 h of melting. Due to the low dust concentration in the samples, the extraction protocol was modified as follows: melted samples were filtered onto two sterile filters (MoBio Water Filters, 0.22 μM), and the resulting DNA was pooled after extraction. Care was taken to ensure the filter was not folded onto itself to maximize the exposure of dust to the beads in the bead tube. After filtration, samples were incubated at 65°C for 10 min and subjected to 30 min of vigorous vortexing (Luhung et al., 2015). DNA extraction controls were carried out in parallel with snow samples. Extraction controls consisted of 10 mL of sterile water undergoing the same protocol as the collected snow samples including the filtration step.

The V1-V2 region of the 16S rRNA gene was sequenced for bacteria and archaea using a Thermofisher Ion Torrent Personal Genome Machine sequencer at the Microbiome Analysis Center (MBAC) at George Mason University based on the manufacturer's protocols. Bioinformatic analysis and visualization of the 16S rRNA amplicon data was conducted using the R packages *dada2*, *phyloseq,* and *ggplot2* package in R (McMurdie and Holmes, 2013; Callahan et al., 2016; Wickham, 2016; R Core Team, 2018). In brief, Bam files were converted to FastQ files and demultiplexed prior to importing into R, resulting in 173,084 raw reads in nine samples. Adapter removal and barcode trimming were done in R prior to running the forward reads through the *dada2* (version 1.10.1) pipeline. Standard filtering parameters were used to filter out low quality reads, and the forward reads were trimmed to a consistent length

(300 base pairs) and estimated errors were calculated. After dereplication, an amplicon sequence variant (ASV) table was created and chimeras were removed. Taxonomy was assigned using RDP trainset 16 (doi: 10.5281/zenodo.801828) In *phyloseq* ASVs identified as chloroplast at the class level were removed. Additionally, the phylum Fusobacteria was removed because it had an ASV count of one, and genus *Propionibacterium* was removed as it is a published human contaminant (Sheik et al., 2018). Relative abundance was calculated and log transformed for normal distribution. Alpha diversity was calculated from the ASV counts using the Shannon diversity index (Shannon, 1948).

Statistical differences in the relative abundance of tested taxa and the Shannon diversity index values were determined using analysis of variance (ANOVA) and the Tukey multiple comparison test. To visualize differences is microbial taxonomy between sample types, Principal Coordinate Analysis (PCoA) dissimilarity plots were created using Bray-Curtis distances (Bray and Curtis, 1957).

After filtering 134,521 reads, nine samples (not including controls) remained. The extraction controls contained only 4% of the number of reads as the samples and had a significantly lower Shannon diversity index (**Figure 2**). Therefore, they were not included in the rest of the analysis.

To determine the dominant ASVs in our samples, the relative abundance for a unique ASV was averaged across site replicates. The top 10 ASVs, after averaging, for each sample were then referred to as dominant. To determine a closely related species, the dominant ASV DNA sequences were compared to sequences in the National Center for Biotechnology Information Basic Local Alignment Search Tool Nucleotide (blastn) suite (https://blast.ncbi.nlm.nih.gov/Blast.cgi) (Altschul et al., 1990). Default parameters were used for the inquiry except the 16S ribosomal RNA sequence (Bacteria and Archaea) database was selected for comparison with a max target sequences of 10. Only the top ranking alignment from a search was used for discussion and listed in **Supplement Table 1**.

RESULTS

Snow Microstructure

The snow microstructural data obtained via micro-CT imaging was examined with the primary objective of determining where, within the snow matrix, the dust particles reside. Dust was

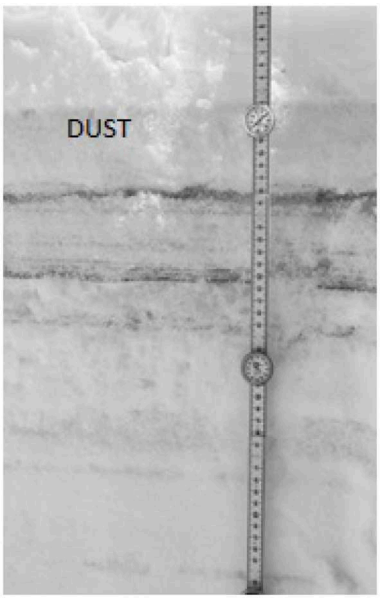

FIGURE 3 | Near infrared image of the snow pit sampled on May 1, 2017 at Swamp Angel Study Plot highlight the merged (ALM) layer at 11 cm depth, denoted by "dust" label.

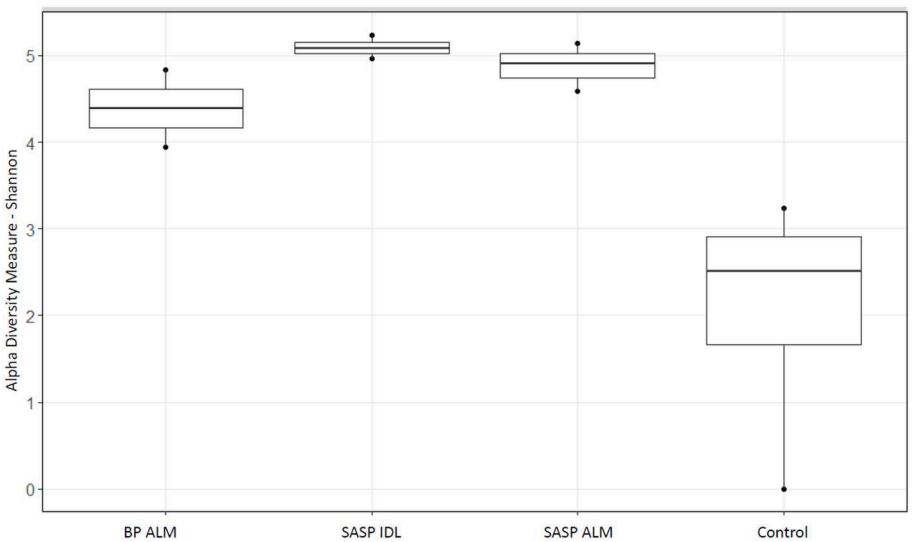

FIGURE 2 | Shannon diversity index of extraction controls vs. dust-impacted snow samples, with Berthoud Pass merged layer (BP ALM) showing less diversity than the Swamp Angel Study Plot individual dust event layer and merged layer (SASP IDL and ALM, respectively), vs. the control.

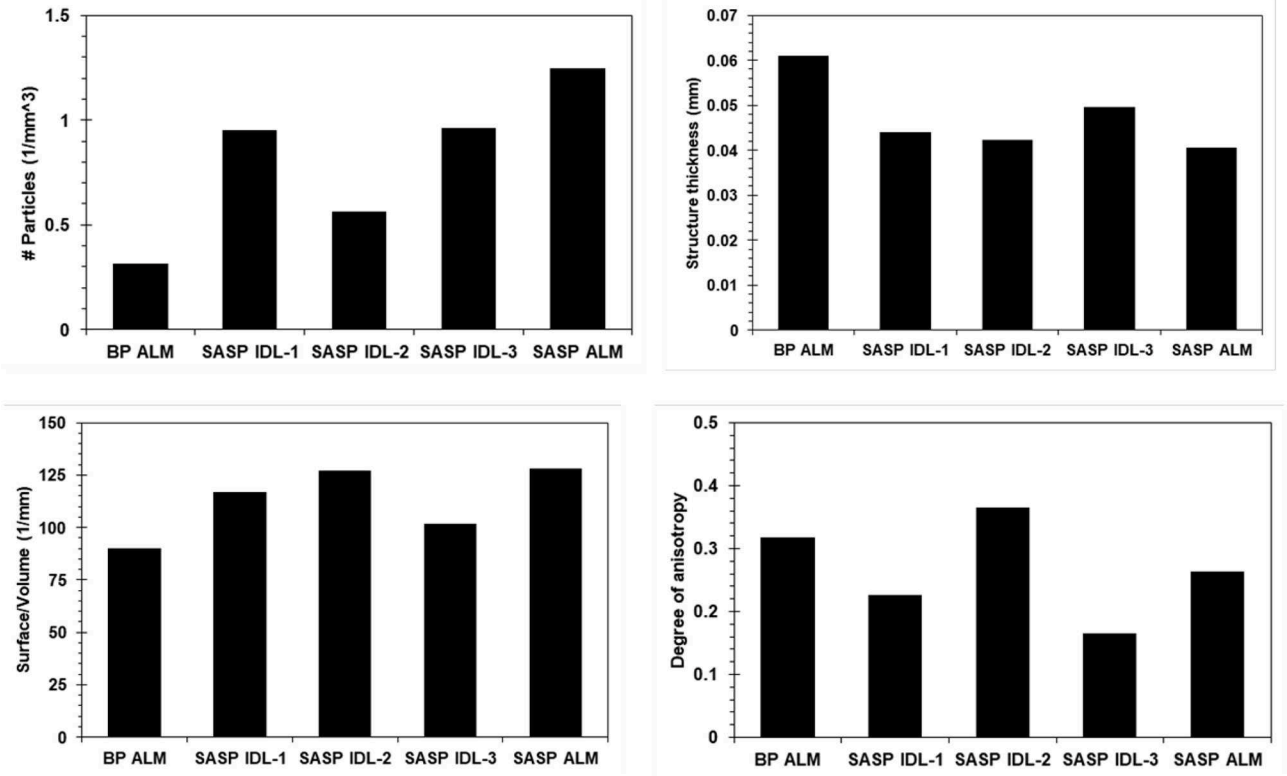

FIGURE 4 | Microstructural characterization of the dust particles in snow samples from Berthoud Pass and Swamp Angel Study Plot BP ALM (Berthoud Pass, all layers merged), SASP IDL (Swamp Angel Study Plot individual dust event layer, subsamples 1–3), and SASP ALM (Swamp Angel Study Plot all layers merged). The top panels show the number of particles per cubic millimeter and average thickness of the particles for all five samples containing noticeable quantities of dust. The bottom panels show the surface to volume ratio and degree of anisotropy.

most clearly identified on samples from the merged layer from Berthoud Pass, immediately after dust event D4 at the Swamp Angel Study Plot, and from the merged layer at Swamp Angel Study Plot, collected during the late spring. We examined three separate sub-samples for the individual dust event layer sample. After segmenting the snow, dust, and air phases (**Figure 3**), we quantified the microstructural parameters for each phase in 2-dimensional cross-sections (2D) and in bulk three dimensions (3D).

Dust layers were generally visible in snow pits excavated at the study sites, and can be readily seen in NIR images of the snow pit walls (**Figure 3**). The microstructural characteristics of the dust particles within the dust layer from the merged Berthoud Pass sample, post-dust event samples and the merged Swamp Angel samples are shown in **Figure 4**. The merged layer from Swamp Angel had the highest number of dust particles contained within the scanned sample, while merged layer from Berthoud Pass had the lowest number of dust particles. The structure thickness and surface to volume (S/V) ratio of the dust particles was relatively similar for all samples, which indicates that the dust grain sizes are consistent between both the dust event D4 from Swamp Angeland the merged layers from both Swamp Angel and Berthoud Pass. This consistency suggests that dust grains remain relatively isolated from one another in the snow matrix and do not group together as the late-season merged layer forms, which would be exhibited as differences between the microstructure of the samples from the individual dust event layer and all layers merged. Finally, we calculated the degree of anisotropy, where 0 indicates perfectly isotropic shapes and 1 indicates the theoretical completely anisotropic. Although there was some anisotropy in the shape of the grains observed, the lack of a temporal trend suggests that the dust grains do not rotate or shift in a consistent manner over time.

We note that the number of dust particles per unit volume is an inherently noisy number due to the size of the dust particles and the fact that some of the dust particles were similar in size to detector noise. For this reason, we were not able to despeckle the image beyond a low level Gaussian smoothing filter during image reconstruction. Therefore, the numerical value for dust particle density carries less validity than the relative number when comparing across samples. The Berthoud Pass sample of merged dust layers clearly had a much lower amount of dust particles compared to the merged dust layer sample from the Swamp Angel Study Plot. There is also a higher concentration of dust particles within the merged layer from Swamp Angel vs. the recently deposited snow sample collected just after the dust event D4.

We found that snow characteristics varied with sample, particularly with snow porosity. The Swamp Angel Study plot individual dust event layer snow sample had very low porosity,

5–20%, which is nearly the value of ice, while merged layers from Swamp Angel and Berthoud Passhad porosities of 54 and 62%, respectively. The Swamp Angel Study Plot merged layer sample had the highest concentration of dust particles according to the microstructural analysis, as well as the largest surface to volume ratio (S/V) value (**Figure 5**). The S/V values reported in **Figure 5** correspond to SSA values of 9.89 and 19.7 m^2/kg for the merged layers from Berthoud Pass and the Swamp Angel Study Plot, respectively, and an average of 3.00 m^2/kg for the Swamp Angel Study Plot individual samples. The merged dust layers from Swamp Angel and Berthoud Pass taken at the end of the season (April 29 and May 1, respectively) have higher S/V ratios and SSA values, and corresponding smaller snow grain sizes, than the snow collected April 10 from the D4 dust event at Swamp Angel. The small variability between samples examined from the same layer compared to layers merged after deposition shows consistency among snow samples of similar history.

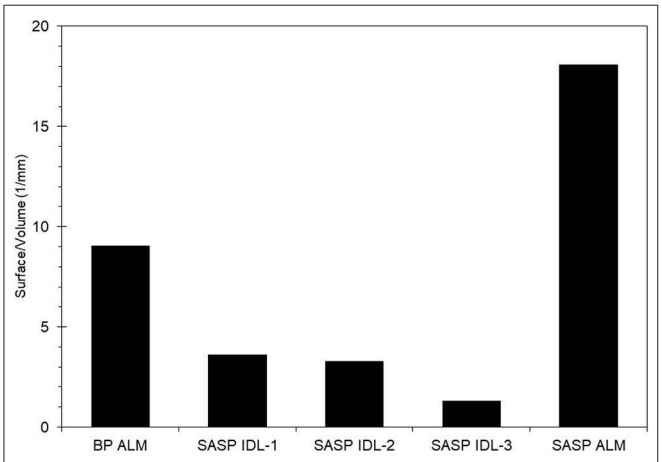

FIGURE 5 | Surface to volume ratios of the snow phase in the Berthoud Pass merged layer sample, and the Swamp Angel Study Plot individual dust layer and Swamp Angel Study Plot merged layer samples, denoted by BP ALM, SASP IDL, and SASP ALM, respectively. Subsamples of SASP IDL samples are denoted 1–3.

Dust was generally observed to be located toward the exterior of the snow grains (**Figure 6**) in micro-CT data. The percentage of dust particle surface embedded within the snow matrix was calculated by dividing the total surface area of the dust particles in contact with the air by the total surface area of the dust particles. A dust particle completely embedded in snow would have 0% exposure. Any value above 0% indicates the dust is on the surface of the snow grain. We note that there is an upper limit as it is impossible for a dust particle to be 100% exposed (i.e., free floating). Percentage of surface area exposed for various deposition events is shown in **Figure 7**. Although the percentages of the dust surface area exposed are small, they are above 0, indicating that a small portion of dust particle surface area resides on the surface of the snow grain.

Meteorological Data

In the Spring of 2017, four separate depositional events occurred within Senator Beck Basin, as evidenced by visible dust layers on the snow surface (**Table 2**). For each event, we examined

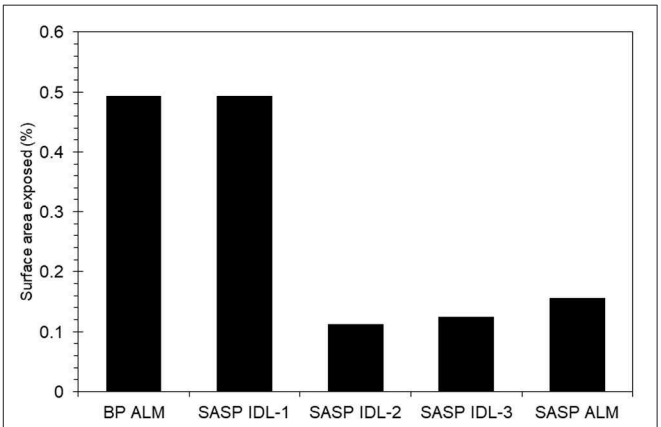

FIGURE 7 | Dust surface area exposed to air relative to embedded in the snow grain for samples from Berthoud Pass (merged layer, BP ALM), and the Swamp Angel Study Plot (both merged layer, SASP ALM, and individual dust event layer SASP IDL, with subsamples denoted 1–3).

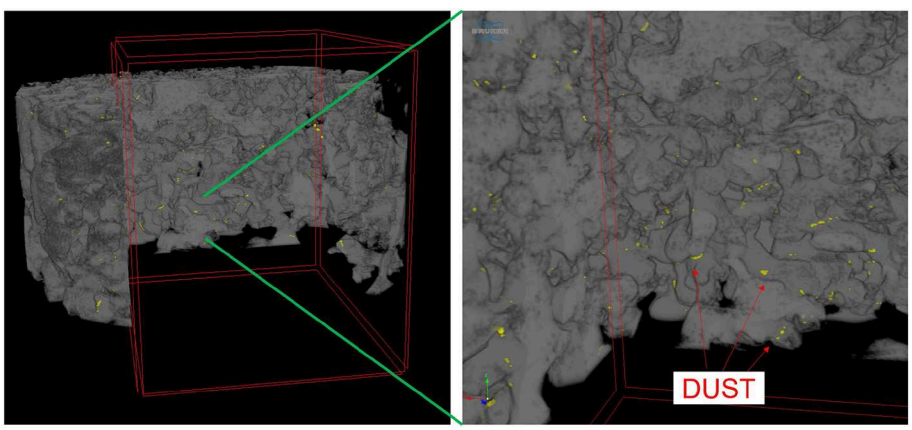

FIGURE 6 | Three-dimensional micro-CT image of dust particles within snow matrix, showing the dust located on the surface of snow grains. In the figure, dust is yellow and the snow grains are gray.

TABLE 2 | Description of weather events in which a dust deposition event occurred and snow samples were collected.

Dust event	Deposition type	Average wind direction (degrees)	Average wind speed (m s^{-1})	Peak gust (m s^{-1})	Start of event	End of event
D1	Wet	218	18	36	3/5/17 12:00	3/6/17 10:00
D2	Wet	N/A	N/A	N/A	3/23/17 N/A	N/A
D3	Wet	183	11	29	3/30/17 15:00	3/31/17 3:00
D4	Dry	228	13	27	4/8/17 13:00	4/9/17 9:00

Compiled data is from the Center of Snow and Avalanche Studies and the USGS (dust mass).

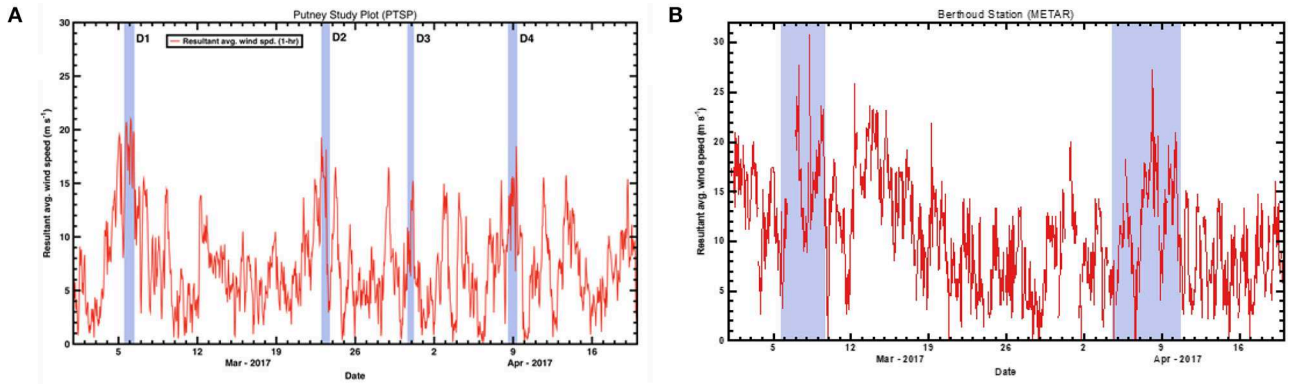

FIGURE 8 | Resultant average wind speeds during spring 2017 at the three study plot stations. **(A)** shows the 1-h average wind speeds (m s^{-1}) for Senator Beck Basin. Highlighted areas indicate four depositional events noted in **Table 2**. **(B)** shows wind data from Berthoud Pass METAR (Meteorological Terminal Aviation Routine) station collected during spring 2017. Highlighted areas indicate possible dust deposition events at Berthoud Pass.

the meteorological data captured in Senator Beck Basin as well as Berthoud Pass. Specifically, we evaluated wind direction and speed to better constrain the provenance of the deposited dust (**Figure 8**). In each plot, the highlighted areas indicate the four events noted in **Table 2**. Wind speeds are shown as 1-hr average resultant wind speeds (m s^{-1}).

HYSPLIT simulations were run for each of the dust events D1–D4 at Senator Beck Basin, which contributed to the merged layer in sample at the Swamp Angel Study Plot, and similarly the high wind events at Berthoud Pass. Unlike Senator Beck Basin, Berthoud Pass is not monitored regularly by on-site personnel, with dust events inferred based on depth of dust deposition layer and subsequent meteorology. The back trajectory results for each event in the Senator Beck Basin region and Berthoud Pass are shown in **Figure 9**. The results agree well with the average wind directions observed at the stations near Senator Beck Basin for each deposition event. In the majority of the events for the Senator Beck Basin site, the trajectories' highest frequency was found over the Four Corners region. Dust event 3 (D3) had the highest frequency of trajectories centered at the Swamp Angel Study Site. This is indicative of a weak event for which wind sources are difficult to identify accurately. Further evidence for this is reflected in low peak wind gust for D3. The back trajectory modeling for the Berthoud Pass area does not locate a specific source site as well, with the trajectories being more diffuse, particularly for the first dust deposition event (**Figure 9E**). Source regions are south-west of the study site, with storms originating further west than in the case of Senator Beck Basin.

DNA Sequencing

Our aim was to investigate whether there were differences in microbial community structure between locations. Using the Shannon diversity index, samples collected from the Swamp Angel Study Plot individual dust event layer had the highest diversity, while the Berthod Pass merged layer had the lowest diversity (**Figure 2**). Though the alpha diversity between samples was not significantly different (**Figure 2**), differences of beta diversity between locations were observed (**Figure 10**). The PCoA plot accounted for 55.7% of the variation in the dataset (**Figure 10**). In ordination space, samples that are closer together have similar microbial communities. The snow samples collected from the merged dust layer at Berthoud Pass cluster away from those collected from Swamp Angel Study Plot along PCoA axis 1, indicating that the microbial communities in the snow were different based on location (**Figure 10**). The microbial communities within the two Swamp Angel Study Plot samples cluster together. This was expected as the microbial communities from Swamp Angel Study Plot individual dust event layer contributed to the merged microbial community present in the Swamp Angel study plot merged layer samples. Interestingly, one of the Swamp Angel Study Plot merged layer replicates separated from the others along the PCoA axis 2 (**Figure 10**). Possible causes for a disparate microbial community in the replicate include the presence of microbes from other dusting events, community proliferation, or a combination of the two.

Investigation of microbial taxonomy revealed 14 phyla identified in the snow samples (**Figure 11**). Proteobacteria,

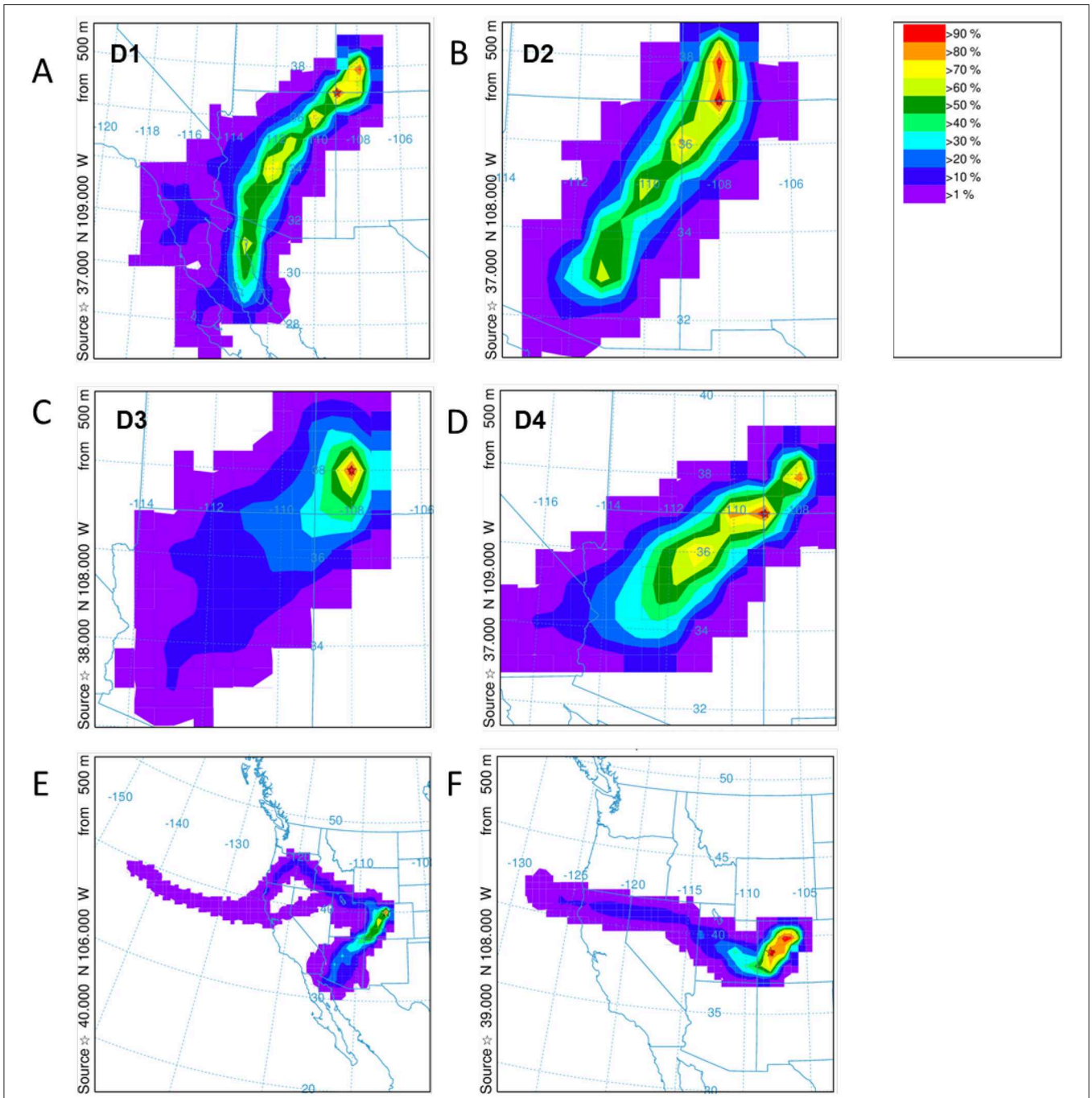

FIGURE 9 | HYSPLIT frequency backward trajectories for the dust deposition events D1–D4 for Swamp Angel Study Plot are shown in **(A–D)** and Berthoud Pass **(E,F)**. The storm systems for the identified Berthoud Pass dust events are more diffuse. Note the differences in area between panels.

Actinobacteria, Bacteriodetes, and Acidobacteria encompassed almost 98% of the identified taxa (**Figure 11**). Firmicutes and Cyanobacteria encompassed ∼1.0 and 0.7%, respectively (**Figure 11**). The abundance of Acidobacteria ($P < 0.001$) and Actinobacteria ($P = 0.009$) were significantly different between the Berthoud Pass merged layer and both Swamp Angel Study Plot samples, including the individual dust event layer and the merged dust layer. Additionally, the abundance of Bacteriodetes was significantly lower in the Berthoud Pass merged layer ($P = 0.018$). Further investigation at the class level revealed that the most abundant taxa were Alphaproteobacteria, Actinobacteria, Acidobacteria_Gp1, Betaproteobacteria, Cytophagia Sphingobacteriia, and Gammaproteobacteria (**Figure 12**). Actinobacteria were

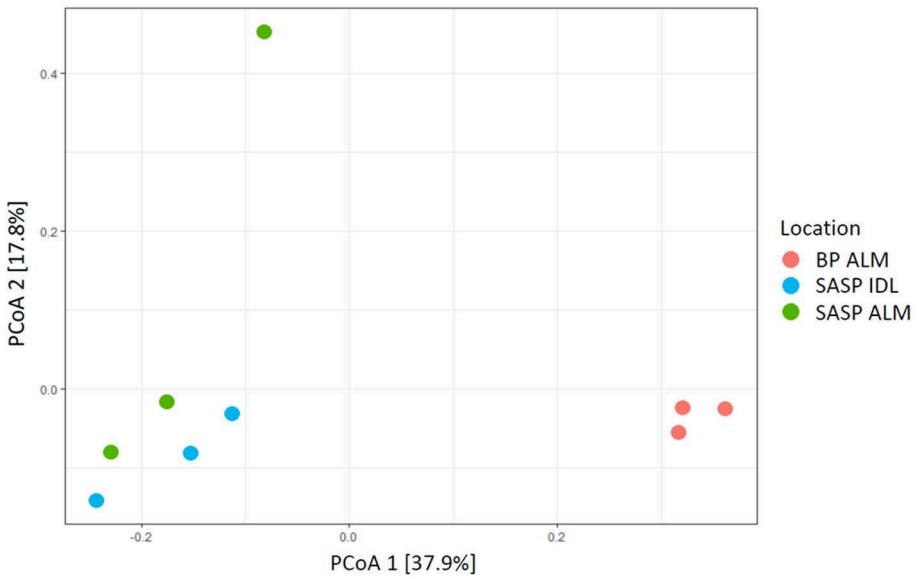

FIGURE 10 | PCoA plot of microbial communities from three snow samples (Bray-Curtis distances). The first principal coordinate accounts for differences in microbial communities based on location. The Samples Swamp Angel merged layer (SASP ALM) and Swamp Angel individual dust event layer (SASP IDL)–are more similar to one another than to the Berthoud Pass merged layer sample (BP ALM).

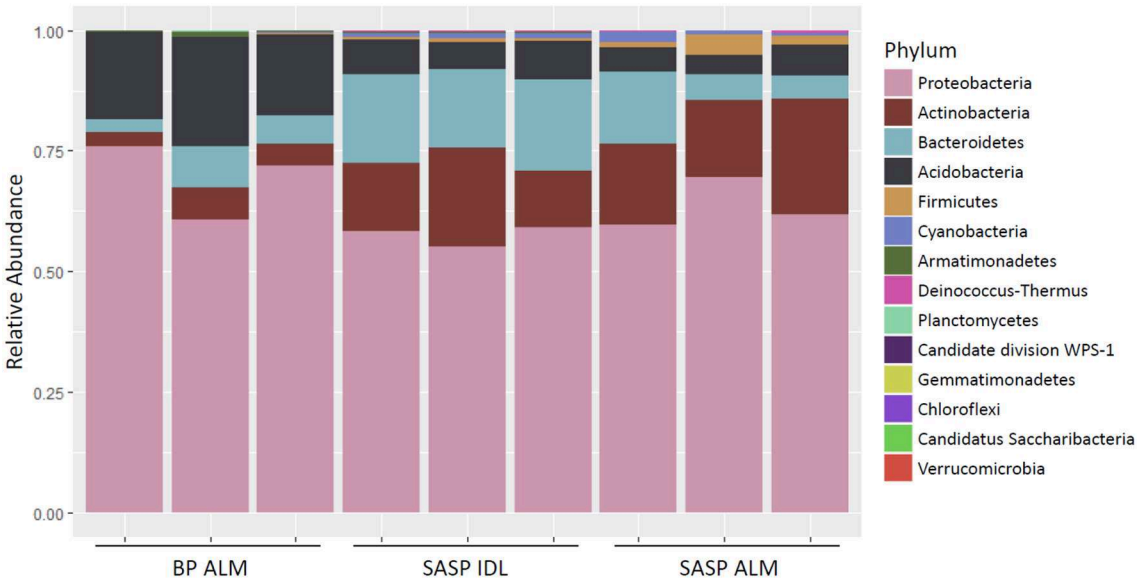

FIGURE 11 | Relative abundance of microorganism in each replicate at the phylum level. for samples from Berthoud Pass (merged layer BP ALM), and Swamp Angel Study Plot (SASP, individual deposited layers, IDL and all layers merged, ALM).

significantly more abundant in the Swamp Angel Study Plot snow samples ($P = 0.009$), whereas Acidobacteria ($P < 0.001$) were significantly more abundant in the Berthoud Pass samples (**Figure 12**). Cytophagia ($P = 0.008$) were significantly more abundant in the Swamp Angel Study Plot individual dust event layer samples when compared to the other samples tested (**Figure 12**). At the phylum or class taxonomic level, no significant differences were observed between the individual and merged dust event at the Swamp Angel Study Plot.

Of the 2,799 unique amplicon sequence variants (ASVs) in our dataset, we examined the top ten dominant (based on the average relative abundance across sample replicates) detected per sampling event (**Supplemental Table 1**). The majority of these dominant ASVs were Proteobacteria with a few occurrences of Actinobacteria, Bacteroidetes and Acidobacteria

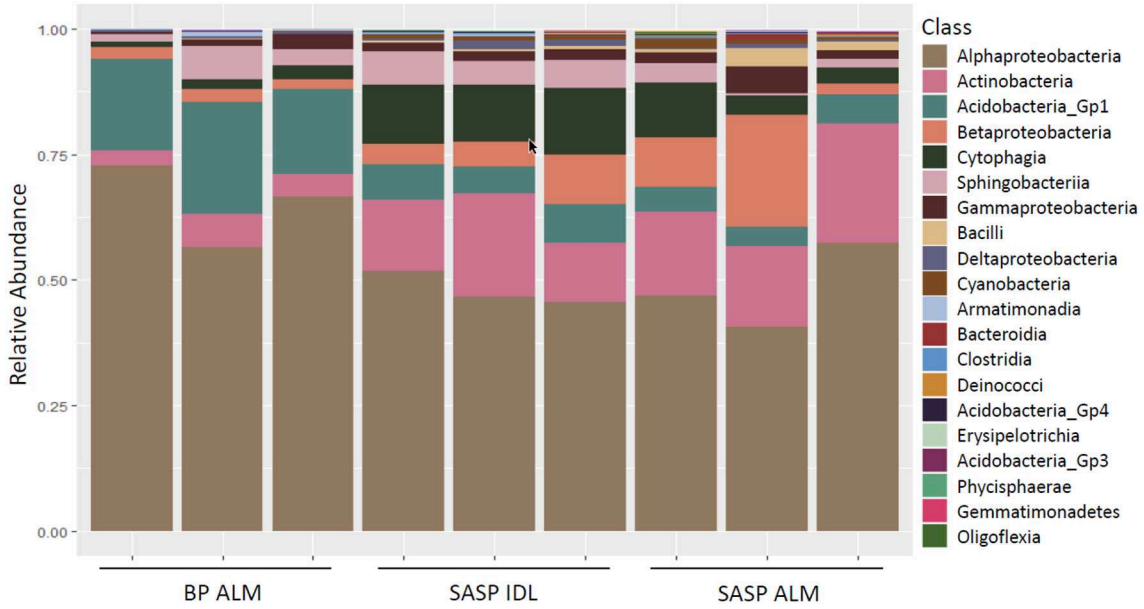

FIGURE 12 | Relative abundance of microorganism in each replicate at the class level for samples from Berthoud Pass (BP, all layers merged, ALM), and Swamp Angel Study Plot (SASP, individual deposited layers, IDL and all layers merged, ALM).

(**Supplemental Table 1**). Of the four dominant ASVs that were present in all three samples, two belong to the family *Acetobacteraceae* and two belong to the family of *Beijerinckiaceae*. Additionally, three ASVs were dominant in both Swamp Angel Study Plot samples from the individual dust event and the merged dust layer, but not in the Berthoud Pass merged layer; these belong to the families *Propionibacteriaceae*, *Cytophagaceae* and *Sphingomonadaceae* (**Supplemental Table 1**). The dominant ASV nucleotide sequences were compared against sequences in the NCBI 16S ribosomal RNA sequences (Bacteria and Archaea) nucleotide database using nBLAST (Altschul et al., 1990) and GenBank (Benson et al., 2017).

DISCUSSION

Our study provides some of the first analyses of coupled snowpack microbial and microstructural characteristics of deposited dust events and subsequent fate within the snowpack. We found that the dust particles embedded toward the outside of snow grains have a low percentage of surface area exposed to air. Microstructural analysis of the dust within the snow matrix suggests that dust particles reside at the snow/pore interface (and not the interior of the snow grains) so that a small portion of the dust particle surface is exposed to air, resulting in potential interactions between the dust particles and the microbes present in the pore space. Facilitation of these interactions could have important implications for activity and metabolism of snowpack microbes.

The increase in S/V, and corresponding SSA, of the Swamp Angel Study Plot merged layer collected April 29 when compared to the snow sample from the dust event at the same location, collected April 10, is not expected, as the typical predicted trend for snow entails the SSA decreasing over time due to temperature gradient-induced grain growth (Colbeck, 1982). Much more work is warranted, but our results do provide preliminary evidence that in some specific instances grain growth can be suppressed in the presence of dust—particularly on the micro-scale. In this instance, the formation of a melt-freeze layer shortly after dust event D4, as evidenced by the low porosities of the Swamp Angel Study Plot individual dust event layer samples, likely lead to the further formation of a crust layer then impacted by metamorphic processes. This suppression of grain growth is counterintuitive, but has been noted anecdotally by field observers at the study site. Other instances of decreases in SSA over time have been noted by Domine et al. (2009) for the case of melt-freeze layers being metamorphosed into hoar layers, and in the case of wind-induced reduction of snow grain sizes through mechanical processes.

Meteorology and subsequent back trajectory modeling suggests that the dust we examined for the Senator Beck region originated in the southern Colorado Plateau; with the wind trajectory coming from the southwest (**Figure 9**, top). The source region for the Berthoud Pass area is less clear (**Figure 9**, bottom) with two separate, and diffuse source areas, but the back trajectory modeling suggests dust originates in the Four Corners region for the first event and in central-west Colorado for the second event. These differences in dust origin may play a critical role in the microbial communities detected in the snowpack, with the differences in microbial composition being greater between sampling sites vs. in temporal differences.

Because the resolution of the micro-CT does not capture the small size of bacteria, we used a DNA sequencing approach

to understand microbial community structure in the dust-impacted snow. Alpha diversity ranged from 4 to 5, which is consistent with a median diversity index of 4.15 from surface snow microbes in the Australian Alps and Swiss Alps (Wunderlin et al., 2016). Our results that location was a strong driver in microbial community composition align with other studies in the Australian and Swiss Alps (Wunderlin et al., 2016) and in the USA in the mountains in Utah (Dastrup et al., 2018).

Proteobacteria, Actinobacteria, Bacteroidetes, and Acidobacteria accounted for the majority of the detected phyla in all samples. The same top four phyla also accounted for 72–98% of the total relative abundance from Australian and Swiss Alps (Wunderlin et al., 2016). This deviates slightly from the notion of a core snow microbiome of Proteobacteria, Bacteroidetes, Firmicutes, and Cyanobacteria (Hell et al., 2013; Hauptmann et al., 2014; Wunderlin et al., 2016). Proteobacteria was the most abundant phylum found in the Colorado snowpack from this study and from the Fennoscandian and Colorado snowpack in Brown and Jumpponen (2019). There, Acidobacteria_Gp1 and Actinobacteria were also detected (Brown and Jumpponen, 2019). Proteobacteria were also found in the Greenland Ice Sheet (Perini et al., 2019a) as well as clear ice and subglacial ice in Svalbard (Perini et al., 2019b). Cytophagia were detected in snow collected from Greenland, Iceland, Svalbard, and Sweden (Lutz et al., 2016). Interestingly, the abundance of Cyanobacteria was low in all samples, though they have been found in other cryosphere environments such as glaciers in west Greenland (Uetake et al., 2010) and snow in the Canadian High Arctic (Harding et al., 2011) and the Sierra Nevada, California (Carey et al., 2016).

Considering the top ten sequence amplicon variants per site, the most closely matched organisms were detected in a variety of environments, including arid areas such as the Colorado Plateau (*Sphingomonas desiccabilis*) (Gundlapally and Garcia-Pichel, 2006) and Saudi Arabia (*Microvirga arabica*) (Veyisoglu et al., 2015). Others were detected in cold regions such as Arctic ecosystems (*Huanghella arctica* and *Terriglobus saanensis SP1PR4*) (Rawat et al., 2012; Jiang et al., 2013), Antarctic soil (*Mucilaginibacter terrae)* (Sedláček et al., 2017), and permafrost (*Polymorphobacter fuscus*) (Jia et al., 2015). Those from more extreme environments may be better adapted to survive in the alpine environment of the Colorado Rockies throughout the winter.

Of important consideration is how the physical environment of the snowpack during melt either enhances or deters microbial growth and function. In this study, we evaluated a cold, young snow, which may be more influenced by source material. It is very likely that the composition of the soil microbial community will be dictated by dominant microbes capable of replicating at the onset of melt.

Our work leads to many further important questions for consideration, namely in the linked evolution of snow grains in the presense of dust particles and the implications for the microbiota present on the dust particles. The onset of melt will lead to a dramatically altered environment for those communities present in the snowpack, both in terms of temperature and moisture content. These effects will vary spatially depending on the persistence of snowcover and the residence times of deposited dust particles and the microbiomes they contain.

CONCLUSIONS

This work offers the link between snow microstructure and the microbial communities present in dust-laden snow. The presence of these microbes has important implications for ecosystem services such as nutrient release. A fundamental understanding of microbial location and activity combined with knowledge of how they contribute to melt would provide key data to more accurately project the stability of the snow pack. Furthermore, an assessment of environmental factors affecting microbial growth is critical to understand how microbial dust transport influences snow packs. Additionally, it serves as a way to characterize microorganisms that can survive and grow once deposited onto snow packs. Combining these data with specific microbial signatures could provide a robust tool to better understand the origin and fate of dust on snow. Our data set, while limited in temporal and spatial sampling, provides preliminary examination into coupled dust and microbial impacts on snowpack characteristics. On-going work seeks to extend our observations into the full melt season impacts of microbial and microstructure co-evolution, including clean vs. dusty snow evolution.

DATA AVAILABILITY STATEMENT

The raw sequences of the 16S rRNA genes generated for this study can be found in the NCBI SRA database (www.ncbi.nlm.nih.gov/sra) under the BioProject accession number PRJNA602710.

AUTHOR CONTRIBUTIONS

This project was conceived by ZC and RB in close collaboration, who both contributed to the overall manuscript, which was equally contributed to by numerous individuals. JD collected all of the microbial samples immediately following dust events and collected all of the meteorological data. ZC and LF conducted physical property field sampling. RL conducted the micro-CT analysis, including dust analysis, and wrote much of the methodology section and the microstructural analysis sections. AT and SR processed the snow and carried out the DNA extractions. AT, SR, SD, and RJ conducted the microbial analysis. AT and RB wrote the majority of the microbial section, with contributions from SD. JF completed the back trajectory modeling and met data analysis, and wrote the majority of those sections.

ACKNOWLEDGMENTS

The authors wish to acknowledge funding from the Army Basic Research Funding ASSALT 6.1 program, Geospatial Research and

Engineering (GRE) "Dark materials in snow and their impacts on preferential sublimation and surface roughness," the 6.2 program Geospatial Research and Engineering (GRE) Army Terrestrial-Environmental Modeling and Intelligence System Science Technology Objective-Research (ARTEMIS STO-R) "Dynamic Undisturbed Soils Testbed to Characterize Local Origins and Uncertainties of Dust (DUST-CLOUD)," and the Engineering Research and Development Center Future Investment Funding project "Environmental forensics for reverse point sourcing and attribution." The authors also wish to thank the Center for Snow and Avalanche Study for field support and a huge degree of help throughout this project and three reviewers whose comments and suggestions helped to greatly improve the manuscript.

SUPPLEMENTARY MATERIAL

The Supplementary Material for this article can be found online at: https://www.frontiersin.org/articles/10.3389/feart.2020.00122/full#supplementary-material

Supplemental Table 1 | Summary of the top 10 most abundant amplicon sequence variants per site/condition. Sample BP ALM refers to the Berthoud Pass merged layer, SASP ALM refers to the Swamp Angel Study Plot merged layer, and SASP IDL refers to the Swamp Angel Study Plot individual dust layer from dust event D4.

REFERENCES

Altschul, S. F., Warren, G., Webb, M., Myers, E. W., and David, J., L. (1990). Basic local alignment search tool. *J. Mol. Biol.* 215, 403–410. doi: 10.1016/S0022-2836(05)80360-2

Anesio, A. M., Lutz, S., Chrismas, N. A., and Benning, L. G. (2017). The microbiome of glaciers and ice sheets. *NPJ Biofilms Microbi.* 3:10. doi: 10.1038/S41522-017-0019-0

Benson, D. A., Mark, C., Karen, C., Karsch-Mizrachi, I., Lipman, D. J., James, O., et al. (2017). "GenBank." *Nucleic Acids Res.* 45, D37–D42. doi: 10.1093/nar/gkw1070

Bray, J. R., and Curtis, J. T. (1957). An ordination of the upland forest communities of Southern Wisconsin. *Ecol. Monogr.* 27, 325–349. doi: 10.2307/1942268

Brown, S. P., and Jumpponen, A. (2019). Microbial ecology of snow reveals taxa-specific biogeographical structure. *Microb. Ecol.* 77, 946–958. doi: 10.1007/s00248-019-01357-z

Callahan, B. J., Sankaran, K., Fukuyama, J. A., McMurdie, P. J., and Holmes, S. P. (2016). Bioconductor workflow for microbiome data analysis: from raw reads to community analyses. *F1000 Res.* 5:1492. doi: 10.12688/f1000research.8986.2

Carey, C. J., Hart, S. C., Aciego, S. M., Riebe, C. S., Blakowski, M. A., and Aronson, E. L. (2016). Microbial community structure of subalpine snow in the Sierra Nevada, California. *Arct. Antarct. Alp. Res.* 48, 685–701. doi: 10.1657/AAAR0015-062

Colbeck, S. (1982). An overview of seasonal snow metamorphism. *Rev. Geophys. Space GE.* 20, 45–61. doi: 10.1029/RG020i001p00045

Comrie, A. C. (2005). Climate factors influencing coccidioidomycosis seasonality and outbreaks. *Environ. Health Persp.* 113:688. doi: 10.1289/ehp.7786

Conway, H., Gades, A., and Raymond, C. F. (1996). Albedo of dirty snow during conditions of melt. *Water Resour. Res.* 32, 1713–1718. doi: 10.1029/96WR007212

Cook, J. M., Hodson, A. J., Gardner, A. S., Flanner, M., Tedstone, A., Williamson, C., et al. (2017b). Quantifying bioalbedo: a new physically based model and discussions of empirical methods for characterising biological influence on ice and snow albedo. *Cryosphere* 11, 2611–2632. doi: 10.5194/tc-2017-73

Cook, J. M., Hodson, A. J., Taggart, A. J., Mernild, S. H., and Tranter, M. (2017a). A predictive model for the spectral "bioalbedo" of snow. *J. Geophys. Res. Earth Surf.* 122, 434–454. doi: 10.1002/2016JF003932

Dastrup, D. B., Carling, G. T., Collins, S. A., Nelson, S. T., Fernandez, D. P., Tingey, D. G., et al. (2018). Aeolian dust chemistry and bacterial communities in snow are unique to airshed locations across northern Utah, USA. *Atmos. Environ.* 193, 251–261. doi: 10.1016/j.atmosenv.2018.09.016

Dial, R. J., Ganey, G. Q., and Skiles, S. M. (2018). What color should glacier algae be? An ecological role for red carbon in the cryosphere. *FEMS Microbiol. Ecol.* 94:fiy007. doi: 10.1093/femsec/fiy007

Domine, F., Taillandier, A.-S., Cabanes, A., Douglas, T. A., and Sturm, M. (2009). Three examples where the specific surface area of snow increased over time. *Cryosphere* 3, 31–39. doi: 10.5194/tc-3-31-2009

Favet, J., Lapanje, A., Giongo, A., Kennedy, S., Aung, Y. Y., Cattaneo, A., et al. (2013). Microbial hitchhikers on intercontinental dust: catching a lift in Chad. *ISME J.* 7, 850–867. doi: 10.1038/ismej.2012.152

Grantham, N. S., Reich, B. J., Pacifici, K., Laber, E. B., Menninger, H. L., Henley, J. B., et al. (2015). Fungi identify the geographic origin of dust samples. *PLoS ONE.* 10:e0122605. doi: 10.1371/journal.pone.0122605

Gundlapally, S. R., and Garcia-Pichel, F. (2006). The community and phylogenetic diversity of biological soil crusts in the colorado plateau studied by molecular fingerprinting and intensive cultivation. *Microb. Ecol.* 52, 345–57. doi: 10.1007/s00248-006-9011-6

Harding, T., Jungblut, A. D., Lovejoy, C., and Vincent, W. F. (2011). Microbes in high arctic snow and implications for the cold biosphere. *Appl. Environ. Microb.* 77, 3234–3243. doi: 10.1128/AEM.02611-10

Hauptmann, A. L., Stibal, M., Bælum, J., Sicheritz-Pontén, T., Brunak, S., Bowman, J. S., et al. (2014). Bacterial diversity in snow on North Pole ice floes. *Extremophiles* 18, 945–951. doi: 10.1007/s00792-014-0660-y

Hell, K., Edwards, A., Zarsky, J., Podmirseg, S. M., Girdwood, S., Pachebat, J. A., et al. (2013). The dynamic bacterial communities of a melting high Arctic glacier snowpack. *ISME J.* 7, 1814–1826. doi: 10.1038/ismej.2013.51

Jia, L., Xiaomin, F., Zhong, Z., Lu, H., Xiaocui, H., Zhenquan, L., and Jie, L. V. (2015). "Polymorphobacter fuscus sp. nov., isolated from permafrost soil, and emended description of the genus polymorphobacter." *J. Syst. Evol. Micr.* 65, 3920–3925. doi: 10.1099/ijsem.0.000514

Jiang, F., Mengchen, X., Lu, C., Wenjing, K., Fang, P., Jun, D., et al. (2013). Huanghella arctica gen. nov., sp. nov., a bacterium of the family cytophagaceae isolated from arctic tundra soil. *Int J. Syst. Evol. Micr.* 63, 696–702. doi: 10.1099/ijs.0.041533-0

Kellogg, C. A., and Griffin, D. W. (2006). Aerobiology and the global transport of desert dust. *Trends Ecol. Evol.* 21, 638–644. doi: 10.1016/j.tree.2006.07.004

Lawrence, C. R., Painter, T. H., Landry, C. C., and Neff, J. C. (2010). Contemporary geochemical composition and flux of aeolian dust to the San Juan Mountains, Colorado, United States. *J. Geophys. Res. Biogeo.* 115, 1–15. doi: 10.1029/2009JG001077

Luhung, I., Wu, Y., Ng, C. K., Miller, D., Cao, B., and Chang, V. W. C. (2015). Protocol improvements for low concentration DNA-based bioaerosol sampling and analysis. *PLoS ONE* 10:e0141158. doi: 10.1371/journal.pone.0141158

Lutz, S., Anesio, A. M., Edwards, A., and Benning, L. G. (2015). Microbial diversity on Icelandic glaciers and ice caps. *Front. Microbiol.* 6:307.doi: 10.3389/fmicb.2015.00307

Lutz, S., Anesio, A. M., Jorge Villar, S. E., and Benning, L. G. (2014). Variations of algal communities cause darkening of a Greenland glacier. *FEMS Microbiol. Ecol.* 89, 402–414. doi: 10.1111/1574-6941.12351

Lutz, S., Anesio, A. M., Raiswell, R., Edwards, A., Newton, R. J., Gill, F., et al. (2016). The biogeography of red snow microbiomes and their role in melting arctic glaciers. *Nat. Commun.* 7:11968. doi: 10.1038/ncomms11968

Maccario, L., Sanguino, L., Vogel, T. M., and Larose, C. (2015). Snow and ice ecosystems: not so extreme. *Res. Microbiol.* 166, 782–795. doi: 10.1016/j.resmic.2015.09.002

McMurdie, P. J., and Holmes, S. (2013). Phyloseq: an R package for reproducible interactive analysis and graphics of microbiome census data. *PLoS ONE* 8:e61217. doi: 10.1371/journal.pone.0061217

Meola, M., Lazzaro, A., and Zeyer, J. (2015). Bacterial composition and survival on Sahara dust particles transported to the European Alps. *Front. Microbiol.* 6:1454. doi: 10.3389/fmicb.2015.01454

Miteva, V., Teacher, C., Sowers, T., and Brenchley, J. (2009). Comparison of the microbial diversity at different depths of the GISP2 Greenland ice core in relationship to deposition climates. *Environ. Microbiol.* 11, 640–656. doi: 10.1111/j.1462-2920.2008.01835.x

Painter, T. H., Barrett, A. P., Landry, C. C., Neff, J. C., Cassidy, M. P., Lawrence, C. R., et al. (2007). Impact of disturbed desert soils on duration of mountain snow cover. *Geophys. Res. Lett.* 34, 1–6. doi: 10.1029/2007GL030284

Painter, T. H., Duval, B., Thomas, W. H., Mendez, M., Heintzelman, S., and Dozier, J. (2001). Detection and quantification of snow algaei with an airborne imaging spectrometer. *Appl. Environ. Microbiol.* 67, 5267–5272. doi: 10.1128/AEM.67.11.5267-5272.2001

Painter, T. H., Skiles, S. M., Deems, J. S., Bryant, A. C., and Landry, C. C. (2012). Dust radiative forcing in snow of the Upper Colorado River Basin: 1. A 6 year record of energy balance, radiation, and dust concentrations. *Water Resour. Res.* 48:7521. doi: 10.1029/2012WR011985

Perini, L., Gostinčar, C., Anesio, A. M., Williamson, C., Tranter, M., and Gunde-Cimerman, N. (2019b). Darkening of the greenland ice sheet: fungal abundance and diversity are associated with algal bloom. *Front. Microbiol.* 10:557. doi: 10.3389/fmicb.2019.00557

Perini, L., Gostinčar, C., and Gunde-Cimerman, N. (2019a). Fungal and bacterial diversity of Svalbard subglacial ice. *Sci. Rep.* 9:20230. doi: 10.1038/s41598-019-56290-5

Perkins, S. (2001). Dust, the thermostat: how tiny airborne particles manipulate global climate. *Sci. News.* 160, 2000–2002. doi: 10.2307/4012776

R Core Team (2018). *R: A Language and Environment for Statistical Computing (version R 3.5.2)*. Vienna: R Foundation for Statistical Computing.

Rawat, S. R., Minna, K., Männist, Ö., Valentin, S., Lynne, G., Matt, N., et al. (2012). Complete genome sequence of terriglobus saanensis type strain SP1PR4T, an acidobacteria from tundra soil. *Stand. Genomic. Sci.* 7, 59–69. doi: 10.4056/sigs.3036810

Schuerger, A. C., Smith, D. J., Griffin, D. W., Jaffe, D. A., Wawrik, B., Burrows, S. M., et al. (2018). Science questions and knowledge gaps to study microbial transport and survival in Asian and African dust plumes reaching North America. *Aerobiologia.* 34, 425–435. doi: 10.1007/s10453-018-9541-7

Sedláček, I., Roman P., Stanislava K., Ivana M., Pavla H., Eva S., et al. (2017). Mucilaginibacter terrae sp. nov., isolated from antarctic soil. *Int. J. Syst. Evol. Microbiol.* 67, 4002–4007. doi: 10.1099/ijsem.0.002240

Sevruk, B. (ed.). (1992). *Snow Cover Measurements and Areal Assessment of Precipitation And Soil Moisture*. Geneva: Secretariat of the World Meteorological Organization. p. 283.

Shannon, C. E. (1948). A mathematical theory of communication. *Bell Syst. Tech. J.* 27, 379–423. doi: 10.1002/j.1538-7305.1948.tb01338.x

Sheik, C. S., Reese, B. K., Twing, K. I., Sylvan, J. B., Grim, S. L., Schrenk, M. O., et al. (2018). Identification and removal of contaminant sequences from ribosomal gene databases: lessons from the census of deep life. *Front. Microbiol.* 9:840. doi: 10.3389/fmicb.2018.00840

Skiles, S. M., Flanner, M., Cook, J. M., Dumont, M., and Painter, T. H. (2018). Radiative forcing by light-absorbing particles in snow. *Nat. Clim. Change* 8, 964–971. doi: 10.1038/s41558-018-0296-5

Skiles, S. M., Painter, T. H., Belnap, J., Holland, L., Reynolds, R. L., Goldstein, H. L., et al. (2015). Regional variability in dust-on-snow processes and impacts in the Upper Colorado River Basin. *Hydrol. Process.* 29, 5397–5413. doi: 10.1002/hyp.10569

Stein, A. F., Draxler, R. R., Rolph, G. D., Stunder, B. J. B., Cohen, M. D., and Ngan, F. (2015). NOAA's HYSPLIT atmospheric transport and dispersion modeling system. *B. Am. Meteorol. Soc.* 96, 2059–2077. doi: 10.1175/BAMS-D-14-00110.1

Uetake, J., Naganuma, T., Hebsgaard, M. B., Kanda, H., and Kohshima, S. (2010). Communities of algae and cyanobacteria on glaciers in west Greenland. *Polar Sci.* 4, 71–80. doi: 10.1016/j.polar.2010.03.002

Veyisoglu, A., Tatar, D., Saygin, H., Inan, K., Cetin, D., Guven, K., et al. (2015). Microvirga makkahensis sp. nov., and Microvirga arabica sp. nov., isolated from sandy arid soil. *Antonie van Leeuwenhoek*. 109, 287–296. doi: 10.1007/s10482-015-0631-z

Weil, T., De Filippo, C., Albanese, D., Donati, C., Pindo, M., Pavarini, L., et al. (2017). Legal immigrants: invasion of alien microbial communities during winter occurring desert dust storms. *Microbiome* 5:32. doi: 10.1186/s40168-017-0249-7

Weir-Brush, J. R., Garrison, V. H., Smith, G. W., and Shinn, E. A. (2004). The relationship between gorgonian coral (*Cnidaria: Gorgonacea*) diseases and African dust storms. *Aerobiologia* 20, 119–126. doi: 10.1023/B:AERO.0000032949.14023.3a

Wickham, H. (2016). *Ggplot2: Elegant Graphics for Data Analysis. 2nd Edn. Use R*. Cham: Springer.

Wunderlin, T., Ferrari, B., and Power, M. (2016). Global and local-scale variation in bacterial community structure of snow from the Swiss and Australian Alps. *FEMS Microbiol. Ecol.* 92, 1–12. doi: 10.1093/femsec/fiw132

Yamaguchi, N., Ichijo, T., Sakotani, A., Baba, T., and Nasu, M. (2012). Global dispersion of bacterial cells on Asian dust. *Sci. Rep.* 2:525. doi: 10.1038/srep00525

Conflict of Interest: The authors declare that the research was conducted in the absence of any commercial or financial relationships that could be construed as a potential conflict of interest.

frontiers in Earth Science

METHODS
published: 10 June 2020
doi: 10.3389/feart.2020.00179

Application of a Magnetic Resonance Imaging Method for Nondestructive, Three-Dimensional, High-Resolution Measurement of the Water Content of Wet Snow Samples

Satoru Adachi[1]*, *Satoru Yamaguchi*[2], *Toshihiro Ozeki*[3] and *Katsumi Kose*[4]

[1] Shinjo Cryospheric Environment Laboratory, National Research Institute for Earth Science and Disaster Resilience (NIED), Shinjo, Japan, [2] Snow and Ice Research Center, National Research Institute for Earth Science and Disaster Resilience (NIED), Niigata, Japan, [3] Hokkaido University of Education, Faculty of Education, Sapporo, Japan, [4] MRI Simulations Inc., Tokyo, Japan

OPEN ACCESS

Edited by:
Guillaume Chambon, National Research Institute of Science and Technology for Environment and Agriculture (IRSTEA), France

Reviewed by:
Andreas Pohlmeier, Helmholtz-Verband Deutscher Forschungszentren (HZ), Germany
Kevin Hammonds, Montana State University, United States

***Correspondence:**
Satoru Adachi
stradc@bosai.go.jp

Specialty section:
This article was submitted to Cryospheric Sciences, a section of the journal Frontiers in Earth Science

Received: 09 October 2019
Accepted: 07 May 2020
Published: 10 June 2020

Citation:
Adachi S, Yamaguchi S, Ozeki T and Kose K (2020) Application of a Magnetic Resonance Imaging Method for Nondestructive, Three-Dimensional, High-Resolution Measurement of the Water Content of Wet Snow Samples. Front. Earth Sci. 8:179. doi: 10.3389/feart.2020.00179

The infiltration of melted snow water and rainwater into snow can drastically change the form of snow layers. This process is an important factor affecting wet snow avalanches. Accordingly, numerous field surveys and cold room experiments have been conducted to investigate the distribution of water in snow. The common methods of water content measurement (calorimetric and dielectric methods) are implemented by disturbing snow samples to measure them. However, the resolutions obtained are of the order of several centimeters, which hinders the continuous measurement of the water content of a particular sample. Magnetic resonance imaging (MRI), which is typically used in the medical field, can be used to generate a high-resolution three-dimensional (3D) image of the water distribution in samples without destructing them. The luminance of images produced by MRI depends on the volumetric water content of the sample, with luminance increasing with volumetric liquid water content. Therefore, the volumetric liquid water content of the sample can be estimated from its luminance value. Considering this concept, we developed a method to measure the volumetric liquid water content of wet snow samples using MR images. To evaluate the developed method, we prepared several wet snow samples and measured their various volumetric liquid water contents using MRI (θ_{MRI}) and the calorimetric method (θ_{cal}). θ_{MRI}, and θ_{cal} showed good correlation when compared, with values in the range 0.02–0.46. Therefore, our system can accurately and non-destructively measure water content. The developed method using MRI can measure 3D volumetric liquid water contents with a high resolution (2 mm). Using the developed method, we investigated the hysteresis of the water retention curve of snow based on the measurements of a wetting process (boundary wetting curve) and a drying process (boundary drying curve) of the water retention curve for each sample. Our results indicate the existence of hysteresis in the snow water retention curves and the possibility of modeling it by adopting contexts of soil physics.

Keywords: wet snow, Magnetic Resonance Imaging, liquid water content, inhomogeneity of water content, non-destructive visualization, hysteresis

INTRODUCTION

An accurate description of meltwater movements in snow covers is essential to improve the prediction of wet snow disasters. Penetrating water is sometimes ponded at the boundary of snow layers with different characteristics caused by capillary barriers (e.g., Khire et al., 2000; Waldner et al., 2004; Avanzi et al., 2016). A snow layer with a high water content can become the sliding surface of an avalanche as the shear strength of snow exponentially decreases as a function of the volumetric water content (Yamanoi and Endo, 2002). The ponding of water above a capillary barrier is prone to subsequent flow instability, which subsequently results in a preferential flow path. As a result, a heterogeneous water discharge occurs from the snowpack. This heterogeneous water discharge affects the timing of full-depth avalanches because they are sometimes triggered by water reaching the bottom of snow covers. Moreover, snow grain characteristics rapidly change in wet conditions, and snowpack mechanical properties, stability, and optical properties all change with the liquid water contents (Marshall et al., 1999; Baggi and Schweizer, 2008; Mitterer et al., 2011; Techel and Pielmeier, 2011; Dietz et al., 2012; Mitterer and Schweizer, 2013; Schmid et al., 2015). Therefore, knowledge on the distribution of liquid water contents in snow covers resulting from water movements is important to understand snow properties.

The water retention curve, which is also known as the "soil–water characteristic curve," "water content–matric potential curve," or "capillary pressure–saturation relationship," shows the relationship between the liquid water content and matric potential and is a fundamental aspect of hydraulic properties in porous media (Klute, 1986). A water retention curve can be classified as either a wetting process (boundary wetting curve) or a drying process (boundary drying curve). The liquid water content obtained along the boundary drying curve is generally greater than that obtained at the same suction along the boundary wetting curve of the same sample due to hysteresis. The mechanisms for this hysteretic response include the ink-bottle effect arising from the non-uniformity of interconnected pores, potential differences in advancing and receding solid–liquid contact angles, wetting- and drying-induced changes to pore structure, air entrapment, capillary condensation, and thixotropic or aging effects dependent on the wetting/drying history (Hillel, 1980; Lu and Likos, 2004). The hysteresis plays an important role in the development of preferential flow paths in soil. Because soil and snow are both porous media, the hysteresis in snow also plays an important role in the preferential flow path development in snow, considering that the water retention curve of snow shows hysteresis. Although several studies (Wankiewicz, 1978; Adachi et al., 2012) have implied the presence of hysteresis in the water retention curve of snow, it has not yet been proven.

Recently, Leroux and Pomeroy (2017) developed a model of water movements in snow based on the context of soil physics (Kool and Parker, 1987), with the assumption that the water retention curve of snow is subject to hysteresis. They succeeded in reproducing preferential flow paths in snow covers using their model. Their work was innovative as it first introduced the idea of hysteresis in the water retention curve to a water movement model in snow. However, room for discussion remains due to the lack of knowledge on hysteresis in snow water retention curves and the direct application of water retention curve hysteresis in soil physics to snow.

Experiments investigating the hysteresis of porous media are generally conducted by measuring the boundary wetting curve and boundary drying curve of the same sample. Therefore, measuring the boundary wetting curve and boundary drying curve using the same snow samples is necessary to investigate the hysteresis of the water retention curve. However, the common methods of measuring liquid water content, calorimetric (Akitaya, 1978; Kawashima et al., 1988), and dielectric measurements (Denoth et al., 1984; Sihvola and Tiuri, 1986), are implemented by melting the sample or inserting a device into the sample. However, making multiple measurements of the liquid water content of a single sample using these methods is difficult. Recently, Yamaguchi et al. (2010, 2012) measured the boundary drying curve of snow and found these measurements to be more sensitive to change than the boundary drying curve of sand. Their results imply that a high-resolution liquid water content measurement (<few centimeters) is required to detect the difference between the boundary wetting curve and the boundary drying curve; however, neither of the standard methods can provide such high-resolution data. Consequently, a new, non-destructive, high-resolution method is required to measure the liquid water content of snow for the investigation of hysteresis in the snow water retention curve.

Magnetic resonance imaging (MRI) is one of the measurement methods that are non-destructive and have high resolution (Lauterbur, 1973). MRI can image nuclear magnetic resonance (NMR) signals from protons in a liquid and has been commonly used in medical applications to image tissues, such as the brain and tendons, which have a high water content. MRI has also been used for the measurement of water in porous media. Amin et al. (1994) obtained measurements of the distribution of water in packed clay soil columns to study the static and dynamic water phenomena in soil with adequate liquid water content; Hollewand and Gladden (1995) continuously imaged the liquid in porous catalyst support pellets to investigate the relationship between the inhomogeneity of the porous structure and the diffusion of the liquid; and Ozeki et al. (2007) visualized brine channels in sea-spray icing to investigate the former's role in the development of the latter. These studies only focused on the water distribution in the porous media and did not discuss quantitative water distributions.

Recently, we have developed a specialized form of MRI, called Cryospheric MRI (C-MRI), to examine wet snow (Adachi et al., 2009, 2017, 2019). In this study, a new method to measure quantitative liquid water content in snow using C-MRI was developed. Subsequently, by employing the characteristics of MRI measurement (non-destructive and high resolution), an investigation of the boundary wetting curves and boundary drying curves with the same snow samples was conducted. Finally, the hysteresis of the water retention curve of snow was discussed using these data.

C-MRI

In this study, a compact MRI system, which employs a small permanent magnet and a small console (Haishi et al., 2001), was used (Adachi et al., 2009, 2017). The C-MRI hardware comprised four parts: a permanent 0.21 T magnet, a gradient coil set, an RF coil located in a cold room with a temperature of 0°C, and an MRI console located in the laboratory under uncontrolled temperature conditions (**Figure 1**). The C-MRI machine had a gap of 0.25 m, in which the permanent magnet homogeneity was 25 ppm over a 0.15 m diameter spherical volume at 26°C. As the permanent magnet homogeneity changes with temperature, a shim coil was installed to correct the distorted magnetic field (Tamada et al., 2011; Adachi et al., 2019) at 0°C. Two problems are associated with maintaining the temperature of the wet snow samples at 0°C in the system: warming due to the intermittent current flow in the coils and fluctuations in the temperature of the cold room. To maintain the sample at the correct temperature, an air flow cooling system and a water cooling system incorporated around the RF coil were introduced into our C-MRI system (Adachi et al., 2019).

MR images can be obtained in two main methods: spin echo and gradient echo. According to Bernstein et al. (2004), the gradient echo method is generally more suitable for fast imaging, due to its shorter imaging time than the spin echo method. On the contrary, the spin echo method has greater immunity to artifacts resulting from off-resonance effects, such as inhomogeneity of the main magnetic field and magnetic susceptibility variations. In this study, we selected the spin echo method because the C-MRI system had a small amount of inhomogeneity in its magnetic field, even though it was corrected by the shim coil system.

The normal matrix size of the obtained MR image of a three-dimensional (3D) spin echo sequence was 128 × 128 × 128 pixels with a voxel size of 1 mm^3. The imaging time of this matrix size was ∼330 min. The echo time, which is the time from the application of a pulse for exciting the NMR signal until its appearance, was 10 ms and the repetition time, which is the time from one excitation pulse to the next, was 1,200 ms. The repetition time was determined based on the result of the bulk water measurement using C-MRI. The spin–lattice relaxation time and spin–spin relaxation time of bulk water were 1,000 and 900 ms, respectively. In this study, the image intensity is dumped with a factor of 0.7 using these values. To obtain a stronger image intensity, an extension of repetition time is better; however, it is undesirable from the perspective of snow metamorphism, namely the snow grain characteristics rapidly change in wet conditions (Tusima, 1973; Brun, 1989). In this study, image intensity is predominantly weighted by spin–lattice relaxation time because echo time is significantly less than spin–spin relaxation time and repetition time is of the same order as spin–lattice relaxation time. Moreover, the spin–lattice relaxation time of the bulk water in the wet snow samples should not significantly change because the snow samples do not contain paramagnetic impurities. Under this condition, it is reasonable to consider that image intensity is proportional to its water content.

In the experiments, the voxel size was changed from 1 to 2 mm^3 (matrix size of 64 × 64 × 64 pixels) to reduce the imaging time. For these parameters, the imaging time was reduced from 330 to 80 min. Furthermore, the introduction of compressed sensing (Lustig et al., 2007), which is a technique for estimating the data required for imaging a small number of data samples and reconstructing the image, resulted in a final imaging time of 20 min. This value is sufficiently low to avoid the effects of rapid metamorphism of the snow grain in wet conditions (Tusima, 1973; Brun, 1989).

Figure 2 shows the examples of vertical cross-section images of a boundary drying curve of the snow samples taken by our C-MRI scanner. The snow samples were made of sieved snow (with particle diameters ranging from 1.0 to 1.4 mm) and was place into a column with a diameter and height of 80 and 150 mm, respectively. The column with the snow samples was placed in a plastic cup, which had a volume greater than that of the column, and was submerged in 0°C water. The column was allowed to settle until the snow samples were saturated with 0°C water. Next, the water was subsequently removed from the plastic cup until the water level was 10 mm from the bottom, and the snow samples were allowed to settle until a steady state of the water movement in the snow samples were reached. Finally, the sample was imaged with C-MRI (8-bit grayscale image, with a matrix size of 128 [height] × 128 [width] × 16 voxels [depth] and voxel size of 1 × 1 × 8 mm).

The distribution of the water content in the sample is shown by the grayscale value in the figure, where a brighter shade indicates that there is more water present. Generally, MRI can only detect the protons in the liquid. Therefore, the dark areas above the hydraulic head (broken line in **Figures 2A–C**) indicated a lack of liquid water (or less liquid water) in this area. **Figures 2A–C** are the seventh, eight, and ninth slices of the 16 slices in the depth direction, respectively, and each image has an 8 mm thickness in the depth direction. The water heads have a different shape in each image. They have an inhomogeneous distribution, even though they are taken only 8 mm apart along the depth direction. The 3D inhomogeneity of the hydraulic head may depend on the different locations resulting from the 3D inhomogeneity of the air gap size distribution, which controls the water retention capability. This result indicates that the water distribution in snow strongly depends on the snow's microstructure. However, collecting such detailed water distribution data using the common methods of liquid water content measurement has not been possible previously. Therefore, our C-MRI method can become a powerful tool to understand the dependency of water distribution in snow on the microstructure.

CALCULATION OF VOLUMETRIC LIQUID WATER CONTENT FROM MR IMAGES

Method

Kose et al. (2004) developed a method to measure the trabecular bone volume fraction of the calcaneus using MRI of the heel and a standard phantom, which was filled with a solution to compare proton densities. When the image of the heel was taken, bone marrow fluid in the calcaneus was imaged with

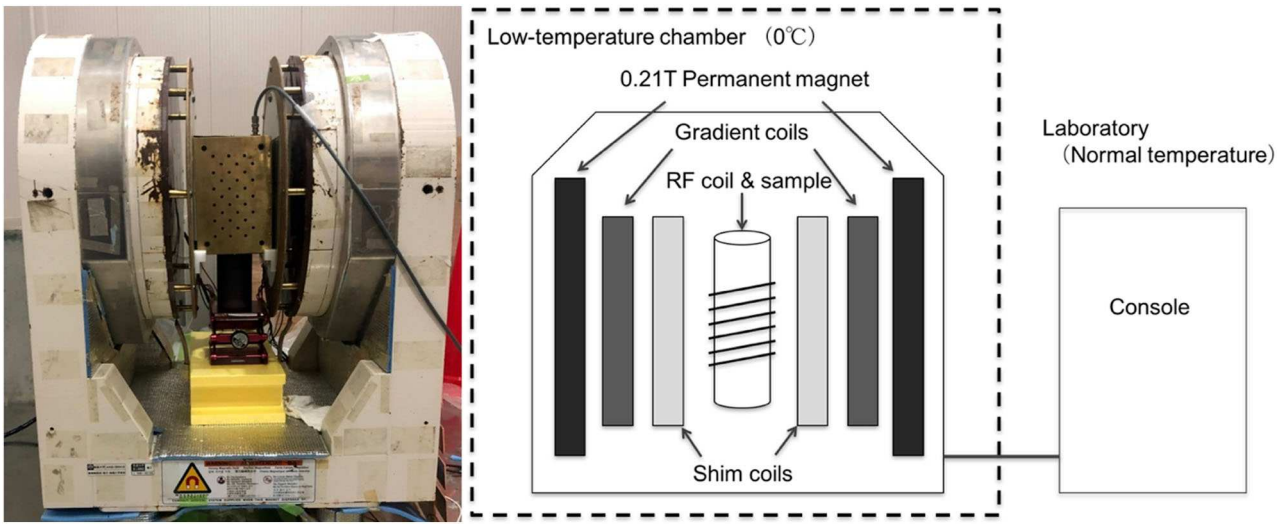

FIGURE 1 | Photograph and schematic diagram of a C-MRI.

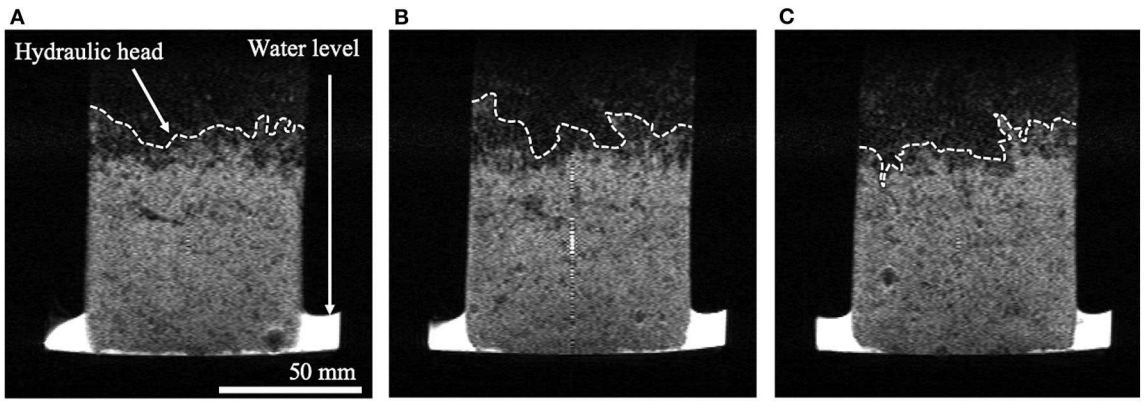

FIGURE 2 | Vertical images of MRI of wet snow sample. White area: water, Gray area: snow with a lot of water, Black area: low moisture snow or air gap. Broken lines are hydraulic head. **(A)** Image at 7th slice, **(B)** image at 8th slice, and **(C)** image at 9th slice.

certain luminance values, depending on the content of bone marrow fluid present. By comparing the luminance values of the calcaneus with the luminance values of the standard phantom, the volumetric content of bone marrow fluid in the calcaneus can be estimated, considering that the luminance values have a linear dependence on the content of marrow fluid. According to Kose et al. (2004), three conditions are necessary to use their method: First, the repetition time must be sufficiently longer than the echo time, which was followed in this study, as stated in section C-MRI. Second, the spin–spin relaxation time must be corrected for every sample. Our imaging target is always water, so this measure should be corrected for each sample. Third, a target sample and standard phantom image must both be present in the image. They can be checked with a device that takes a sample MR image. For these reasons, we concluded that the method reported by Kose et al. (2004) can be applied to calculate the volumetric liquid water content from an image of wet snow taken using MRI.

In our system, a reference phantom, consisting of a 100-mm-diameter plastic tube filled with pure water, was set close to the snow samples, so that the image included the reference phantom and snow samples (**Figure 3A**). If the magnetic field is perfectly homogeneous, then the volumetric liquid water content of the wet snow samples can be shown as the ratio of the image intensity averaged over a region of the sample at a certain height (R_s) and the image intensity averaged over a region of the reference phantom at the same height (R_{e1}) (**Figure 3B**). However, a realistic magnetic field has a certain spatial heterogeneity, and thus the ratio of R_s to R_{e1} needed to be corrected using an image of the standard phantom (**Figure 3C**). The cross-sectional area of the standard phantom included the areas of R_s and R_w. Here, the image intensity averaged over the same region of R_{e1} in the cross section of the standard phantom is shown as R_{e2} and that of R_s is shown as R_w (**Figure 3C**). If the magnetic field is perfectly homogeneous, then R_{e2} and R_w should be the same because the areas of R_{e2} and R_w are completely filled with water. In other words, the ratio of R_{e2} and R_w indicates the degree of influence of the magnetic field heterogeneity. On the basis of these concepts, the volumetric liquid water

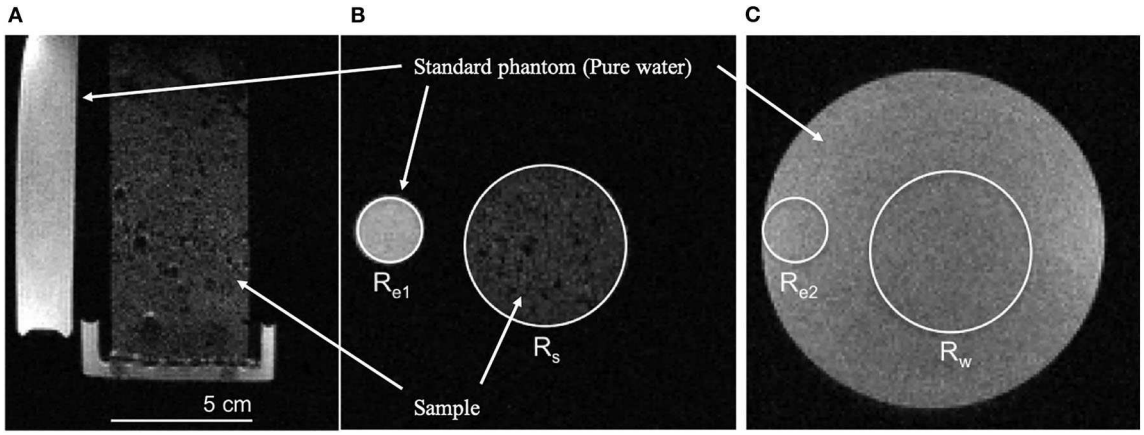

FIGURE 3 | Schematic diagram of the method for calculating volumetric water content from image of MRI. **(A)** Vertical sectional image of MRI, **(B)** horizontal sectional image of MRI, and **(C)** standard phantom filled with pure water only. R_s, region of interest of measuring water content of wet snow sample; R_{e1}, region of interest of standard phantom neighbor of wet snow sample; R_w, same region of interest as R_s in standard phantom; and R_{e2}, same region of interest as R_{e2} in standard phantom.

content of the samples using MRI (θ_{MRI}) was calculated using the following equation:

$$\theta_{MRI} = \frac{R_s}{R_{e1}} \times \frac{R_{e2}}{R_w} \quad (1)$$

As the magnet of our C-MRI machine had a large gap, the magnetic field heterogeneity may have depended on fluctuations in the environmental conditions, such as electric noise and temperature. To minimize these effects, the images of the standard phantom were taken once on each experimental day, and R_s, R_{e1}, R_{e2}, and R_w in Equation (1) were calculated using images obtained on the same day. Here, by using the data of the standard phantom taken on different days, we estimated the influence of this in Equation (1), which originates from the fluctuation of the magnetic field heterogeneity resulting from the changing environmental conditions. In the investigation, the ratios of R_{e2} and R_w were calculated and compared for every height of 2 mm for seven experimental days of the standard phantom data. The ratios showed small fluctuations between days, and the average standard deviation over all the heights was ± 0.05. The actual uncertainty of the water content calculation using (Equation 1), due to the fluctuation of the magnetic field heterogeneity, should be smaller than ± 0.05 because the images of the sample and the standard phantom were taken on the same day within several hours. Nonetheless, we concluded that the maximum uncertainty of the water content calculation using (Equation 1) was ± 0.05.

Procedure to Test the Method

To evaluate the accuracy of our method in calculating the volumetric liquid water content using (Equation 1) and MRI, comparisons between θ_{MRI} and measured volumetric liquid water contents using the calorimetric method (θ_{cal}) were conducted. The snow samples for the accuracy verification experiments were refrozen melt forms kept in a cold room at -10°C. The snow samples were screened to control the grain size, and three grain sizes (S, 1.0–1.7 mm; M, 1.7–2.0 mm; L, 2.8–3.4 mm) were selected. Snow from each sample was packed into a sample column that consisted of six acrylic rings (ring size: 20 mm in length, 50 mm in diameter) taped securely together. The bulk density was $\sim$500 kg m^{-3}, which was determined by the volume of the sample column and the weight of snow added and was controlled by tamping each snow sample. To create various volumetric liquid water contents, a gravity drainage column method (Yamaguchi et al., 2010, 2012) was adopted (**Figure 4**). First, the column holding the snow samples was set on a plate and subsequently set in a plastic cup with a height of 150 mm and diameter of 95 mm (**Figure 4A**). Water at 0°C was poured into the cup to submerge the sample column on the plate. Next, the column was allowed to settle until the snow samples were saturated with 0°C water (this process took 10 min) (**Figure 4B**). The water was subsequently removed from the cup until a defined water-table level in the plate was reached, and the sample column was allowed to settle again until a steady state of the water movement in the snow samples was reached (this process also took 10 min) (**Figure 4C**). Then, the sample column on the plate, which kept the water-table level, was moved from the plastic cup to the MRI machine, and an MR image was taken. Finally, using (Equation 1), the volumetric liquid water content was calculated at 2 mm height intervals. After the MRI measurement, the sample column on the plate was removed from the MRI scanner, and the volumetric liquid water content of each column was measured at 20 mm height intervals using a portable calorimeter (Kawashima et al., 1988). As the height resolution of θ_{MRI} was 2 mm and that of θ_{cal} was 20 mm, the measured θ_{MRI}s were averaged over every 10 pixels to obtain the same height resolution of θ_{cal} for comparison. To investigate the accuracy of θ_{MRI}, 71 volumetric liquid water content s with three different grain size samples (S, 16 cases; M, 22 cases; L, 33 cases) were measured using the MRI method (θ_{MRI}) and the calorimetric method (θ_{cal}).

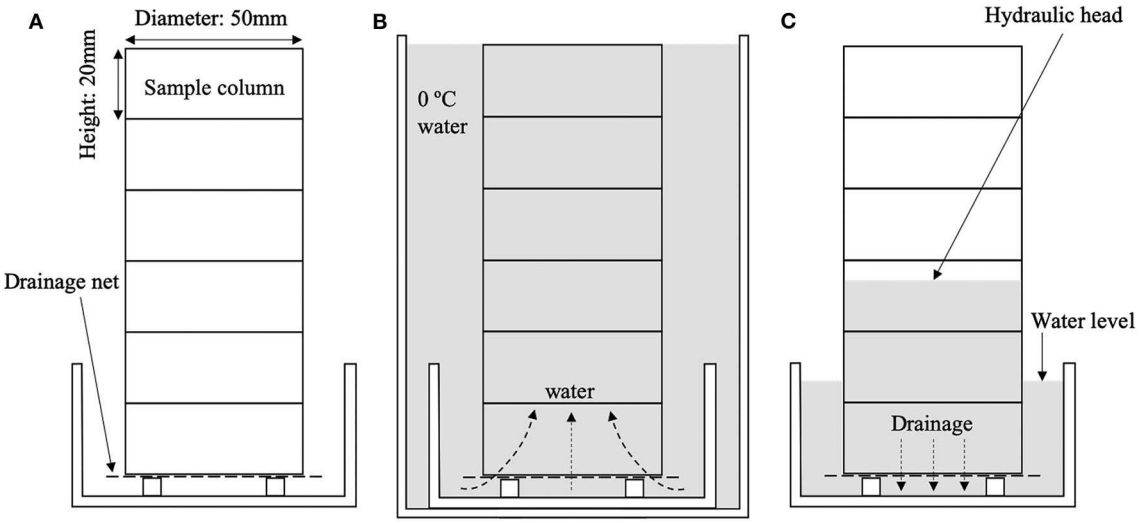

FIGURE 4 | Schematic diagram of measurement of the water retention curve of snow. **(A)** Initial state of sample column with dry snow. **(B)** The column submerged in water until the saturated condition. Water could go in the column only from the bottom. **(C)** The column settled in the low temperature room until the steady state of movement of water.

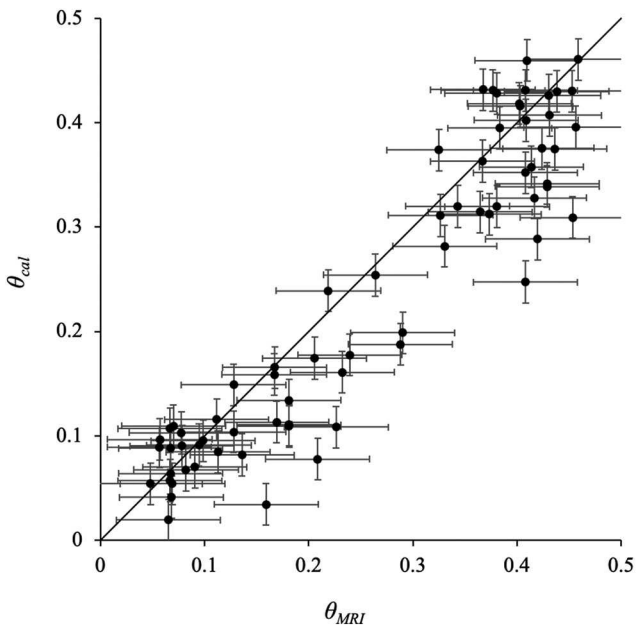

FIGURE 5 | Relationship of volumetric liquid water content between MRI method and calorimetric method. θ_{MRI}, volumetric liquid water content measured using image of MRI; θ_{cal}, volumetric liquid water content measured using the calorimetric method. The error range for each point is ±0.02 on the θ_{cal} and ±0.05 on the θ_{MRI}.

Accuracy Evaluation Results of the Method

Figure 5 compares the results of the θ_{MRI} and θ_{cal} methods. In this figure, each data point was plotted with an uncertainty range resulting from each method: ±0.02 on θ_{cal} (Kawashima et al., 1988) and ±0.05 on θ_{MRI} (see section Calculation of Volumetric Liquid Water Content From MR Images). The solid line is a 1:1 line. Although several θ_{MRI} data showed smaller values than θ_{cal}, θ_{MRI} values were mostly larger than θ_{MRI} values, and this trend did not depend on the grain size. This difference may be caused by the quality of the MR image due to external noise, but the reason why θ_{MRI} gave consistently larger values than θ_{cal} is unclear at present.

To correct the θ_{MRI} values, we assumed a linear dependency on θ_{cal} because both data sets essentially show the same trend. Equation (2) gives this parameterization with the least squares method:

$$\theta_{cal} = 0.9^{*}\theta_{MRI} \quad (R^2 = 0.9) \tag{2}$$

Using Equation (2), we can obtain the correct quantitative volumetric liquid water content with a residual standard error of ±0.05.

HYSTERESIS IN SNOW WATER RETENTION CURVES

Procedure to Measure the Hysteresis in Snow Water Retention Curves

To investigate the hysteresis of the snow water retention curves, the boundary wetting curve and boundary drying curve of the snow samples were measured using the MRI method. The snow samples for hysteresis measurements were similar to those described in section Procedure to Test the Method, namely, screened refrozen melt forms with three different grain sizes (S, 1.0–1.7 mm; M, 1.7–2.0 mm; L, 2.8–3.4 mm) were used. The snow samples were placed into a sample folder connected with several acrylic pipes (50 mm diameter), as presented in section

Procedure to Test the Method. Three sample sets for each grain size were made, and three experiments for each grain size were conducted using these sample sets. The details of these experiments are provided in **Table 1**, where the values were averaged over three sample sets for each grain size.

First, the boundary wetting curves were measured. The sample set on the plate was set into a plastic cup with a diameter and height that were sufficiently larger than those of the snow samples (**Figure 4**). Subsequently, 0°C water was poured into the plastic cup until the bottom few centimeters of the sample were submerged (**Figure 4**). Water infiltrated into the snow samples due to the capillary force of snow from the bottom of the sample. When the water movement in the sample reached a steady state (after 10 min), the distribution of the volumetric liquid water content was measured using the MRI method, and the measured values were corrected using (Equation 2). After the boundary wetting curve measurement, the same sample was fully submerged in the 0°C water in the plastic cup. After 10 min, water was drained from the plastic cup until a defined water-table level in the plate was reached, and the sample was subsequently maintained at 0°C until it reached a steady state (10 min in this study) (**Figure 4**). The distribution of the volumetric liquid water content was also measured using MRI and corrected using (Equation 2). These results were considered to represent the boundary drying curve.

Characteristics of the Hysteresis of Snow Water Retention Curves

Figure 6 shows the measurement results of the boundary wetting curve and boundary drying curve for three grain sizes. The data in the figure were averaged over three experimental results using different snow samples for each grain size. For all grain sizes, the volumetric liquid water content obtained along the boundary drying curve is greater than that obtained at the same suction (h) along the boundary wetting curve. This trend is similar to the hysteresis of a soil water retention curve. Therefore, we concluded that a snow water retention curve has hysteresis, which is similar to that of soil.

Yamaguchi et al. (2010, 2012) measured the boundary drying curve and analyzed measured data using the Van Genuchten equation (Van Genuchten, 1980), which is described as follows:

$$\psi = \frac{1}{\alpha}\left(S_e^{\frac{-1}{m}} - 1\right)^{\frac{1}{n}} \tag{3}$$

with

$$S_e = \frac{(\theta_w - \theta_r)}{(\theta_s - \theta_r)}$$

where Ψ is the pressure head, S_e is the effective saturation, and α, n, and m are parameters, with $m = 1–1/n$. θ_w, θ_r, and θ_s are the volumetric liquid water content, irreducible volumetric liquid water content, and saturated volumetric liquid water content, respectively. For detailed analyses, the obtained water retention curves in this study were fitted using the Van Genuchten equation using the Retention Curve (RETC) software (Van Genuchten et al., 1991). In this study, the value of θ_r was fixed as 0.02 (Yamaguchi et al., 2010, 2012) and θ_s was not fixed, although Yamaguchi et al. (2010, 2012) used a θ_s value of 90% of sample porosity. The straight lines in **Figure 6** show the fitting curve of the Van Genuchten equation determined using the RETC. The values of θ_s for grain sizes S and L showed almost the same values of 90% of the sample porosity, which corresponds to the results of Yamaguchi et al. (2010, 2012). By contrast, the values of θ_s for a grain size of M were slightly smaller (80% of the sample porosity).

To describe the boundary wetting curve and boundary drying curve using the results of Equation (3), the parameter vectors (θ_r^d, θ_s^d, θ_w^d, α^d, n^d) and (θ_r^w, θ_s^w, θ_w^w, α^w, n^w) are introduced, where superscripts w and d indicate wetting and drying, respectively. According to Kool and Parker (1987), the relationships between the parameter vectors of the boundary wetting curve and boundary drying curve in soil physics are as follows:

$$\begin{aligned} n^w &= n^d \\ \alpha^w &= \gamma\alpha^d \\ \theta_s^w &= \theta_s^d \\ \theta_r^w &= \theta_r^d \end{aligned} \tag{4}$$

where γ is a coefficient that varies from 1 to 5.66 depending on soil cohesiveness, with a mean value of 2.2 (Likos et al., 2013). First, Equation (4) can be applied to the analyses of the hysteresis of the snow water retention curve. $\theta_r^w = \theta_r^d$ should be completed because θ_r is fixed as 0.02 in this study. The assumption that $\theta_s^w = \theta_s^d$ seems to be also completed from the results in **Figure 6**. Therefore, two of the four conditions in Equation (4) are fulfilled by the hysteresis of the water retention curve of snow.

Yamaguchi et al. (2012) indicated that α^d and n^d can be described as functions of ρ_s/d as follows:

$$\alpha^d = 4.4 \times 10^6 \left(\frac{\rho_s}{d}\right)^{-0.98} \tag{5}$$

$$n^d = 1 + 2.7 \times 10^{-3} \left(\frac{\rho_s}{d}\right)^{0.61}$$

where ρ_s is the dry density of the snow samples (kg m^{-3}) and d is the grain size (m). **Figure 7** shows the relationship between α (α^d and α^w) and ρ_s/d and between n (n^d and n^w) and ρ_s/d. In the figures, the fitting curves of α and n, which were calculated using (Equation 5), are also shown.

Regarding n^d and n^w, **Figure 7** indicates two important results: First, the assumption that $n^w = n^d$ should be reasonable for the hysteresis of the snow water retention curve. Second, Equation (5) can efficiently reconstruct the values of n^w and n^d with ρ_s/d. For α^d and α^w, all of α^d were plotted near the curve

TABLE 1 | Information of snow samples for investigation of hysteresis of snow water retention curve.

Sample name	Grain size*	Density	Parameters in Van Genuchten model			
	(m) d	(kg m^{-3}) ρ_s	α^d	α^w	n^d	n^w
S	1.2×10^{-3}	492	15	22	8	8
M	1.9×10^{-3}	484	21	32	6	7
L	3.1×10^{-3}	526	39	54	5	5

Grain size was calculated from the averaged over the two mesh sizes.

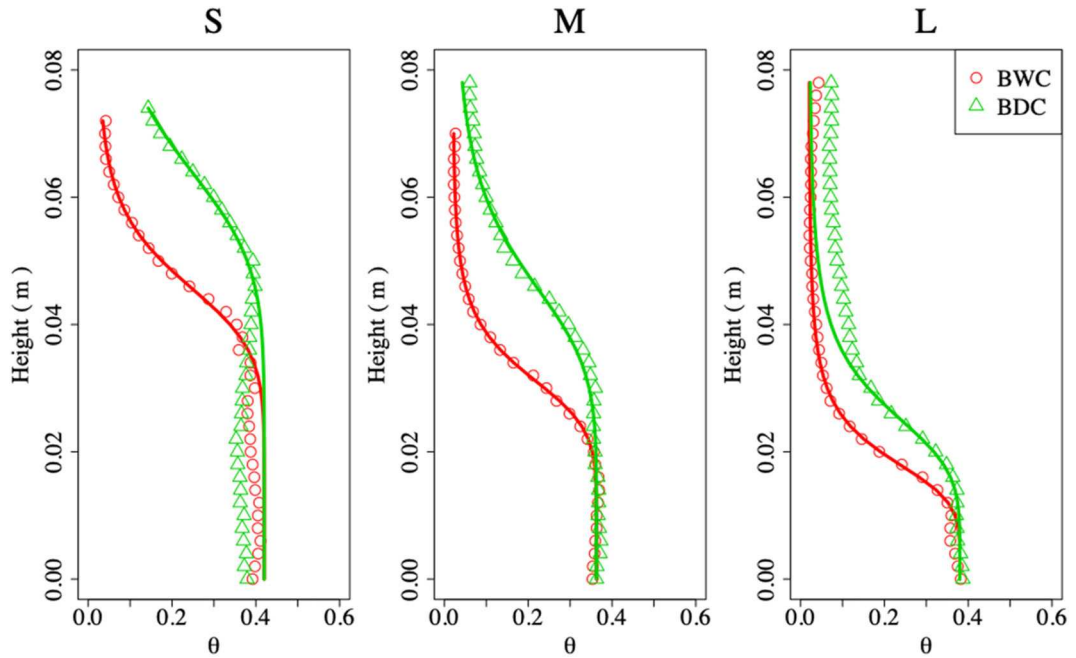

FIGURE 6 | Measurement results of boundary wetting curve and boundary drying curve for different grain sizes (S, M, L) (Equation 3). BWC, boundary wetting curve; BDC, boundary drying curve; θ, volumetric liquid water content. Red circles are measurement results of boundary wetting curve, and green triangles are measurement results of boundary drying curve. Red and green curves are fitting curves for Van Genuchten equation, respectively.

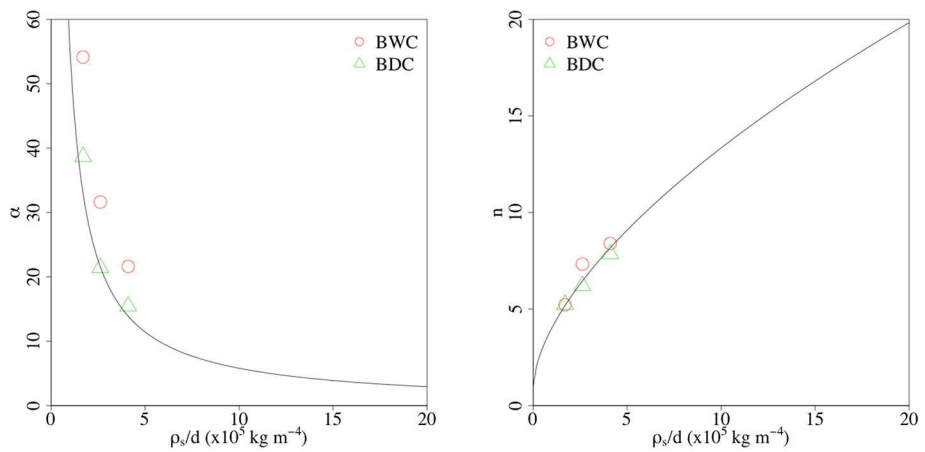

FIGURE 7 | Comparison results between α, n (Equation 5). Red circles are results of boundary wetting curve (BWC) and green triangles are results of boundary drainage curve (BDC). Black curves are calculated curves using the equation of Yamaguchi et al. (2012) with ρ_s/d. ρ_s/d, ratio of snow density and grain size.

calculated using (Equation 5) in **Figure 7**. Therefore, Equation (5) can also reconstruct the values of α^d in this study. On the contrary, all values of α^w are larger than α^d, that is, they are plotted at a higher position than the curve calculated using (Equation 5). This result indicates that the assumption that $\alpha^w = \gamma\alpha^d$ is valid. From these results, we finally conclude that the ideas of Kool and Parker (1987) regarding soil physics can be applied to the analyses of the hysteresis of the snow water retention curve.

Leroux and Pomeroy (2017) performed a sensitive analysis of γ in their model, and their results indicated that the water movement simulation was dependent on the value of γ. They concluded that the best simulation results were obtained when the value of γ was >2.0. On the contrary, the calculated values of γ for each sample in this study are 1.4, 1.5, and 1.4 for S, M, and L, respectively. These values are smaller than those obtained by Leroux and Pomeroy (2017). Because this study considered only three cases, the true value of γ could not be determined for the description of the hysteresis of snow water retention curves and also could not discuss the dependency of γ on snow characteristics. However, our results indicate that the water retention curve hysteresis of snow can be described using the equations of Yamaguchi et al. (2012) and the true value of γ.

CONCLUSION

In this study, we developed a method to calculate the volumetric water content of snow using MR images. Although the traditional methods of measuring volumetric liquid water contents destroy the sample in the process, our method can perform volumetric liquid water content measurements non-destructively. In addition, our method can measure volumetric liquid water content s with high resolution. To evaluate the efficacy of our method, we compared the volumetric liquid water contents of several snow samples calculated using MRI with those measured using a calorimeter. A good linear relationship was found between the results from θ_{MRI} and θ_{cal} for volumetric liquid water content values, ranging from 0.02 to 0.42. Therefore, we concluded that our method can be used to calculate volumetric liquid water content over a large range in wet snow samples.

Using our developed method, we measured the two types of water retention curve, namely the boundary wetting and drying curves, of each snow sample and modeled these data using the Van Genuchten equation (Van Genuchten, 1980). Our results indicated that the water retention curve of snow has a hysteresis similar to that of soil; that is, the volumetric liquid water content obtained along the boundary drying curve is greater than that obtained at the same suction along the boundary wetting curve. In accordance with the analyses of the ideas of Kool and Parker (1987) in soil physics, we obtained relationships similar to those of soil between the parameters (n, α, θ_r, and θ_s) of the Van Genuchten equation for the boundary wetting curve and the boundary drying curve. Therefore, the ideas of Kool and Parker (1987) can be applied to analyze the hysteresis of the water retention curves of snow. Our method to measure volumetric liquid water contents is non-destructive and provides a higher resolution of volumetric liquid water content than the existing methods. Therefore, it can help in the detailed understanding of the behavior of water in snow.

An issue to address in future studies is to reduce the imaging time using high-speed imaging sequence, such as multi-slice or multi-echo pulse sequence. Therefore, it is necessary to implement external noise by electric and magnetic shields for C-MRI considering air permeability. Moreover, owing to high-resolution measurements, a combination of our method and X-ray CT image analyses will pave the way to an innovative means that can help in investigating the relationship between the microstructure and the behavior of water in snow.

DATA AVAILABILITY STATEMENT

The raw data supporting the conclusions of this article will be made available by the authors, without undue reservation, to any qualified researcher.

AUTHOR CONTRIBUTIONS

SY supported on manuscript writing and analyzed hysteresis of snow water retention curves. TO gave advice and supported on the experimental method of wet snow samples. KK supported on the MRI imaging method and MRI image analysis method. All authors contributed to the article and approved the submitted version.

FUNDING

This study was part of the project research on combining risk monitoring and forecasting technologies for mitigation of diversifying snow disasters and was supported by JSPS KAKENHI, with Grant No. JP15H01733 (SACURA PJ).

ACKNOWLEDGMENTS

We would like to acknowledge members of the Snow and Ice Research Center for their participation in useful discussions. We also appreciate helpful comments and suggestions from two reviewers.

REFERENCES

Adachi, S., Ozeki, T., Shigeki, R., Handa, S., Kose, K., Haishi, T., et al. (2009). Development of a compact magnetic resonance imaging system for a cold room. *Rev. Sci. Instrum.* 80:054701. doi: 10.1063/1.3129362

Adachi, S., Yamaguchi, S., Ozeki, T., and Kose, K. (2012). "The water retention curve of snow measured using an MRI system," in *Proceedings to the 2012 International Snow Science Workshop* (Anchorage: *Alaska*), 918–922.

Adachi, S., Yamaguchi, S., Ozeki, T., and Kose, K. (2017). Current status of application of cryospheric MRI to wet snow studies (in Japanese with English abstract). *J. Jpn. Soc. Snow Ice* 79, 497–509. Available online at: https://www.seppyo.org/publication/seppyo/seppyo_archives/79_2017/79_06_2017/attachment/79-6_497

Adachi, S., Yamaguchi, S., Ozeki, T., and Kose, K. (2019). Development of a magnetic resonance imaging system for wet snow samples. *Bull. Glaciol. Res.* 37S, 43–51. doi: 10.5331/bgr.17SR01

Akitaya, E. (1978). Measurements of free water content of snow by calorimetric method. *Low Temp. Sci. A* 36,103–111.

Amin, M. H. G., Hall, L. D., Chorley, R. J., and Carpenter, T. A. (1994). Magnetic resonance imaging of soil-water phenomena. *Magn. Reson. imaging* 12, 319–321. doi: 10.1016/0730-725X(94)91546-6

Avanzi, F., Hirashima, H., Yamaguchi, S., Katsushima, T., and Michele, C. D. (2016). Observations of capillary barriers and preferential flow in layered snow during cold laboratory experiments. *Cryospere* 10, 2013–2026. doi: 10.5194/tc-10-2013-2016

Baggi, S., and Schweizer, J. (2008). Characteristics of wet-snow avalanche activity: 20 years of observations from a high alpine valley (Dischma, Switzerland). *Nat. Hazards* 50, 97–108. doi: 10.1007/s11069-008-9322-7

Bernstein, M. A., King,. K. F., and Zhou, X. J. (2004). *Handbook of MRI Pulse Sequence*. Burlington, MA: Elsevier Academic Press. doi: 10.1016/B978-012092861-3/50021-2

Brun, E. (1989). Investigation on wet-snow metamorphism in respect of liquid-water content. *Ann. Glaciol.* 13, 22–26. doi: 10.3189/S0260305500007576

Denoth, A., Foglar, A., Weiland, P., Mätzler, C., Aebischer, H., Tiuri, M., et al. (1984). A comparative study of instruments for measuring the liquid water content of snow. *J. Appl. Phsy.* 56, 2154–2160. doi: 10.1063/1.334215

Dietz, A. J., Kuenzer, C., Gessner, U., and Dech, S. (2012). Remote sensing of snow - a review of available methods. *Int. J. Remote Sens.* 33, 4094–4134. doi: 10.1080/01431161.2011.640964

Haishi, T., Uematsu, T., Matsuda, Y., and Kose, K. (2001). Development of a 1.0 T MR microscope using a Nd-Fe-B permanent magnet. *Magn. Reson. Imaging* 19, 875–880. doi: 10.1016/S0730-725X(01)00400-3

Hillel, D. (1980). *Fundamental of Soil Physics*. *New York*, NY*: Academic Press*. doi: 10.1016/B978-0-08-091870-9.50006-6

Hollewand, M. P., and Gladden, L. F. (1995). Transport heterogeneity in porous perellet-II. *NMR imaging studies under transient and steady-state conditions. Chem. Eng. Sci*. 50, 327–344. doi: 10.1016/0009-2509(94)00219-H

Kawashima, K., Endo, T., and Takeuchi, Y. (1988). A portable calorimeter for measuring liquid water-content of wet snow. *Ann. Graciol.* 26, 103–105. doi: 10.3189/1998AoG26-1-103-106

Khire, M. V., Benson, C., and Bosscher, P. J. (2000). Capillary barriers: design variables and water *balance. J. Geotech. Geoenviron. Eng.* 126. 695–708. doi: 10.1061/(ASCE)1090-0241(2000)126:8(695)

Klute, A. (1986). "Water retention: laboratory methods," in *Methods of Soil Analysis, Part 1, Physical and Mineralogical Methods*, ed A. Klute (ASA and SSSA: Madison), 635–662. doi: 10.2136/sssabookser5.1.2ed.c26

Kool, J. B., and Parker, J. C. (1987). Development and evaluation of closed-form expressions for hysteretic soil hydraulic properties. *Water Resourc. Res.* 23, 105–114. doi: 10.1029/WR023i001p00105

Kose, K., Matsuda, Y., Kurimoto, T., Hashimoto, S., Yamazaki, Y., Haishi, T., et al. (2004). Development of a compact MRI system for trabecular bone volume fraction measurements. *Magn. Reson. Med*. 52, 440–444. doi: 10.1002/mrm.20135

Lauterbur, P. C. (1973). Image formation by local induced interactions: examples employing nuclear magnetic resonance. *Nature* 242, 190–191. doi: 10.1038/242190a0

Leroux, N. R., and Pomeroy, J. W. (2017). Modelling capillary hysteresus effects on preferential flow through melting and cold layered snowpacks. *Adv. Water Resoures* 107, 250–264. doi: 10.1016/j.advwatres.2017.06.024

Likos, W., Lu, N., and Godt, J. (2013). Hysteresis and uncertainty in soil-water retention curve parameters. *J. Geotech. Geoenviron. Eng.* 140:4. doi: 10.1061/(ASCE)GT.1943-5606.0001071

Lu, N., and Likos, W. J. (2004). *Unsaturated Soil Mechanics 1st Edn*. Hoboken, NJ: Wiley.

Lustig, M., Donoho, D., and Pauly, J. M. (2007). The application of compressed sensing for rapid MR imaging. *Magn. Reson. Med.* 58, 1182–1195. doi: 10.1002/mrm.21391

Marshall, H. P., Conway, H., and Rasmussen, L. A. (1999). Snow densification during rain. *Cold Reg. Sci. Technol.* 30, 35–41. doi: 10.1016/S0165-232X(99)00011-7

Mitterer, C., Hirashima, H., and Schweizer, J. (2011). Wet-snow instabilities: comparison of measured and modelled liquid water content and snow stratigraphy. *Ann. Glaciol.* 52, 201–208. doi: 10.3189/172756411797252077

Mitterer, C., and Schweizer, J. (2013). Analysis of the snow-atmosphere energy balance during wet-snow instabilities and implications for avalanche prediction. *Cryosphere* 7, 205–216. doi: 10.5194/tc-7-205-2013

Ozeki, T., Yamamoto, R., Adachi, S., and Kose, K. (2007). "NMR imaging sea spray icing and ice adhesion tests of pliable polymer sheet for deicing," in *Proceedings of 12th International Workshop on Atmospheric Icing of Structures* (Yokohama), 6.

Schmid, L., Koch, F., Heilig, A., Prasch, M., Eisen, O., Mauser, W., et al. (2015). A novel sensor combination (upGPR-GPS) to continuously and nondestructively derive snow cover properties. *Geophys. Res. Lett*. 42, 3397–3405. doi: 10.1002/2015GL063732

Sihvola, A., and Tiuri, M. (1986). Snow fork for field determination of density and wetness profiles of asnow pack. *IEEE Trans. Geosci. Remote Sens*. GE-*24,* 717–721. doi: 10.1109/TGRS.1986.289619

Tamada, D., Terada, Y., and Kose, K. (2011). Design and evaluation of planar single-channel shim coil for permanent magnetic resonance imaging magnet. *Appl. Phys. Express* 4:066702. doi: 10.1143/APEX.4.066702

Techel, F., and Pielmeier, C. (2011). Point observations of liquid water content in wet snow -investigating methodical, spatial and temporal aspects. *Cryosphere* 5, 405–418. doi: 10.5194/tc-5-405-2011

Tusima, K. (1973). Grain coarsening of ice particles immersed in pure water. *J Jpn Soc Snow Ice* 40, 155–165. doi: 10.5331/seppyo.40.155

Van Genuchten, M. T. (1980). A closed-form equation for predicting the hydraulic conductivity of unsaturated soils. *Soil. Sci. Soc. Am. J.* 44, 892–898. doi: 10.2136/sssaj1980.03615995004400050002x

Van Genuchten, M. T., Leij, F. J., and Yates, S. R. (1991). *The RETC Code for Quantifying the Hydraulic Functions of Unsaturated soils, Version 1.0*. Riverside, CA: U.S. Salinity Laboratory, USDA, ARS, EPA Report 600/2-91/065.

Waldner, P. A., Schneebeli, M., Schultze-Zimmermann, U., and Flühler, H. (2004). Effect of snow structure on water flow and solute transport. *Hydrol. Process* 18, 1271–1290. doi: 10.1002/hyp.1401

Wankiewicz, A. (1978). "A review of water movement in snow," in *Modeling of Snow Cover Runoff*, eds S. C. Colbeck *and M. Ray (Hanover, NH: US Army Cold Regions Research and Engineering Laboratory*), 222–252.

Yamaguchi, S., Katsushima, T., Sato, A., and Kumakura, T. (2010). Water retention curve of snow with different grain sizes. *Cold Reg Sci Technol.* 64, 87–93. doi: 10.1016/j.coldregions.2010.05.008

Yamaguchi, S., Watanabe, K., Katsushima, T., Sato, A., and Kumakura, T. (2012). Dependence of the water retention curve of snow on snow characteristics. *Ann. Glaciol.* 53, 6–12. doi: 10.3189/2012AoG61A001

Yamanoi, K., and Endo, Y. (2002). Dependence of shear strength of snow cover on density and water content (in Japanese). *J. Jpn. Soc. Snow Ice*. 64, 443–451. doi: 10.5331/seppyo.64.443

Conflict of Interest: KK founded the company MRI Simulations Inc.

The remaining authors declare that the research was conducted in the absence of any commercial or financial relationships that could be construed as a potential conflict of interest.

frontiers in Earth Science

ORIGINAL RESEARCH
published: 16 September 2020
doi: 10.3389/feart.2020.00365

On the Birth of Structural and Crystallographic Fabric Signals in Polar Snow: A Case Study From the EastGRIP Snowpack

Maurine Montagnat[1,2]*, *Henning Löwe*[3], *Neige Calonne*[2], *Martin Schneebeli*[3], *Margret Matzl*[3] *and Matthias Jaggi*[3]

[1] Univ. Grenoble Alpes, CNRS, IGE, Grenoble, France, [2] Univ. Grenoble Alpes, Université de Toulouse, Meteo-France, CNRS, CNRM, Centre d'Études de la Neige, Grenoble, France, [3] WSL Institute for Snow and Avalanche Research SLF, Davos Dorf, Switzerland

The role of near-surface snow processes for the formation of climate signals through densification into deep polar firn is still barely understood. To this end we have analyzed a shallow snow pit (0-3 meters) from EastGRIP (Greenland) and derived high-resolution profiles of different types of mechanically relevant fabric tensors. The structural fabric, which characterizes the anisotropic geometry of ice matrix and pore space, was obtained by X-ray tomography. The crystallographic fabric, which characterizes the anisotropic distribution of the **c**-axis (or optical axis) orientations of snow crystals, was obtained from automatic analysis of thin sections. The structural fabric profile unambiguously reveals the seasonal cycles at EastGRIP, as a consequence of temperature gradient metamorphism, and in contrast to featureless signals of parameters like density or specific surface area. The crystallographic fabric profile unambiguously reveals a signal of cluster-type texture already at shallow depth. We make use of order of magnitude estimates for the formation time of both fabric signals and discuss potential coupling effects in the context of snow and firn densification.

Keywords: snow cover, structural fabric, crystallographic fabric, seasonal signal, metamorphism, densification, Greenland

OPEN ACCESS

Edited by:
Alun Hubbard,
Arctic University of Norway, Norway

Reviewed by:
Sumito Matoba,
Hokkaido University, Japan
Silvan Leinss,
ETH Zürich, Switzerland

***Correspondence:**
Maurine Montagnat
maurine.montagnat@univ-grenoble-alpes.fr

Specialty section:
This article was submitted to Cryospheric Sciences, a section of the journal Frontiers in Earth Science

Received: *16 October 2019*
Accepted: *07 August 2020*
Published: *16 September 2020*

Citation:
Montagnat M, Löwe H, Calonne N, Schneebeli M, Matzl M and Jaggi M (2020) On the Birth of Structural and Crystallographic Fabric Signals in Polar Snow: A Case Study From the EastGRIP Snowpack. Front. Earth Sci. 8:365. doi: 10.3389/feart.2020.00365

1. INTRODUCTION

The mechanical behavior of porous ice is controlled by different types of anisotropy. The anisotropic geometry of the ice matrix and pore space, characterized by *the structural fabric*, affects the macroscopic mechanical properties of snow, e.g., the elasticity tensor (Hagenmuller et al., 2015; Srivastava et al., 2016; Gerling et al., 2017). As snow is made of individual crystals of ice, another type of anisotropy comes into play that is the anisotropic distribution of the **c**-axis (or optical axis) orientations, characterized by *the crystallographic fabric*. The latter has been widely investigated for dense ice and its impact on the elastic, viscoplastic and large scale flow behaviors was shown (Nakaya and Marshall, 1954; Duval et al., 1983). Thus, a faithful mechanical description of the entire snow-firn-ice column requires understanding the origin, strength, and impact of both fabric signals.

In Antarctica and Greenland, snow transforms into firn and ice by compaction of subsequent seasonal layers whose mechanical properties may affect densification mechanisms at depth.

Processes occurring in near-surface Antarctic snow have been discussed as a potential origin of different features observed at depth. The variability reported in the O2/N2 ratios in the air trapped in the deep ice might reflect local (78S) summertime insolation (Bender, 2002; Lipenkov et al., 2011). Layering of firn properties would result into layered gas trapping "artifacts" that challenge the interpretation of gas concentrations in ice cores (Fourteau et al., 2017, 2020). As a result, how features of the snow cover (heterogeneities, anisotropy, layering, etc.) are transferred to firn and ice remains a key question to improve the interpretation of paleoclimatic signals extracted from ice cores (e.g., Steen-Larsen et al., 2011; Fourteau et al., 2019) and the modeling of densification.

Anisotropy in the structural fabric of near-surface snow can be caused by temperature gradient metamorphism (Calonne et al., 2012, 2017; Löwe et al., 2013; Leinss et al., 2020). In addition, indications for the evolution of structural anisotropy under mechanical deformations was found in laboratory experiments (Wiese and Schneebeli, 2017a) and suggested by polarimetric radar measurements in an Arctic snowpack (Leinss et al., 2016). The dielectric permittivity was also used to characterize the structural anisotropy in deep firn from the dielectric anisotropy (Fujita et al., 2009, 2014). Seasonal variations were revealed, with higher structural anisotropy in summer layers. This was attributed to the stronger summer-to-autumn metamorphism causing the development of vertically oriented ice structures layers that are mechanically stiffer and less sensitive to densification in contrast to the less metamorphosed, more isotropic winter layers. Very recently, Moser et al. (2020) analyzed the structural anisotropy of snow from Kohnen Station and reported the emergence of a seasonal pattern in the anisotropy that was attributed to the impact of a stronger daily temperature gradient and higher temperatures during the transition from summer to autumn. Comparatively, density signal measured in isolated firn cores is strongly perturbed by stratigraphic noise. Laepple et al. (2016) made an extensive data set of horizontal and vertical high resolution density measurements performed along 143 snow pits at Kohnen station, Antarctica, that ended revealing a seasonal signal.

In contrast to the long history of crystallographic fabric measurements in deep firn and ice (Perutz et al., 1939; Gow and Williamson, 1976), the crystallographic fabric of snow has only recently been studied. The evolution of the crystallographic fabric of a natural alpine snow sample subjected to a temperature gradient was analyzed from thin sections (Riche et al., 2013). They reported an initial cluster-type fabric in the freshly deposited snow that evolved toward a girdle-type during controlled temperature gradient metamorphism. Later, the same method was applied to characterize the vertical profile of crystallographic fabric along a three-meter deep snowpack at Point Barnola, Antarctica, a very low-temperature and low-accumulation site (-80 to -25°C, 25 kg $m^{-2}yr^{-1}$) (Calonne et al., 2017). While no trend with depth was observed, correlations between crystallographic fabric, density and specific surface area (SSA) were found, such that weak girdle-type fabrics were measured in layers of lower density, lower specific surface area, and larger grain size. The latter observation was assumed to be the result of a preferential crystal growth mechanism during temperature gradient metamorphism.

The role of crystallographic anisotropy on the mechanical properties (and densification) of low-density snow and firn was addressed by Theile et al. (2011), Rolland du Roscoat et al. (2011), and Burr et al. (2017). Due to the complexity of the snow microstructure, the local state of stress in a loaded snow sample is strongly heterogeneous. This was shown by Schneebeli (2004) and Hagenmuller et al. (2014) for elastic applications (neglecting the crystallographic orientations of individual grains). Hagenmuller et al. (2014) highlighted the potential role of crystal orientation to determine the strength at the local scale, between two bonds. Under creep conditions, Theile et al. (2011) simulated intragranular deformations and microstructural changes and concluded a measurable impact of the crystallographic anisotropy on the densification of structurally isotropic snow. Back to polar firn conditions, recent measurements of seismic diving waves at Kohnen (Schlegel et al., 2019) indicated the necessity of quantifying the crystallographic fabric alongside with the structural fabric to evaluate uncertainties in the inversion technique giving access to the elastic moduli in firn cores.

The present work is motivated by the abundant evidences showing the need to quantify the strength and variability of both structural and crystallographic fabric signals in snow and firn. We will provide measurements and detailed analyses of both fabric signals, including their variations with depth, in the natural snowpack at the EastGRIP ice core site, Greenland. The EastGRIP site (75.6268°N 35.9915°W) is located in the vicinity of the Northeast Greenland Ice Stream (NEGIS), the sole interior Greenlandic ice stream that initiates near the summit dome. Snow surface temperatures at EastGRIP range between about -10 and -40°C. A previous analysis of shallow cores (67 m depth) at that site showed relatively stable accumulations of 110 kg $m^{-2}yr^{-1}$ in average over the past 400 years, as well as a density profile very similar to the one at NorthGRIP [Greenland, Dahl-Jensen et al. (2002)], with values ranging from about 250 kg m^{-3} at the surface to about 850 kg m^{-3} at 67 m depth (Vallelonga et al., 2014). Due to the relatively high temperatures and high accumulations at EastGRIP, a stronger impact of metamorphism, settlement and compaction on the structural and crystallographic fabric can be expected in comparison to Point Barnola (Calonne et al., 2017).

Methodologically, we relied on established means. The crystallographic anisotropy was evaluated by performing thin sections of snow (Riche et al., 2013) and using the Automatic Ice Texture Analyzer (AITA, Wilson et al., 2003). For the structural anisotropy, we performed micro-computed (contrast) tomography (microCT) (Coléou et al., 2001; Schneebeli and Sokratov, 2004), which is presently the most direct way to compute structural fabric alongside with routinely evaluated properties of density and specific surface area. Our analysis confirms that a seasonal signal emerges in the structural anisotropy and that significant cluster-type textures are appearing with depth.

The paper is organized as follows. The measurements performed along the three-meter deep snow pit are described in

FIGURE 1 | Near-infrared picture (qualitative) of the snow wall that highlights the snowpack layering via differences in the specific surface area. Clearly visible is the melt event from 2012 as a (low specific surface area) marker.

section 2. Section 3 presents the analysis of the microstructure and texture parameters. Finally, section 4 provides an attempt to explain the origin of the structural and crystallographic fabric signals observed in the EastGRIP snowpack.

2. MATERIALS AND METHODS

2.1. Field Measurements

The data underlying this work were collected at the EastGRIP site (75.6268N 35.9915W) during a campaign conducted in May 2016 within the Greenland Climate Network (GC-Net) maintenance program. They comprise a deep profile (three meters) for excavating samples for post-campaign laboratory measurements, a shallow profile (130 cm, 300 m away from the deep profile) for standard *in-situ* snow measurements as a reference, and complementary automatic temperature measurements.

Three blocks of snow of one meter height were cut out from the deep pit. **Figure 1** shows a near-infrared (840–940 nm) picture of the pit, showing the locations of the snow blocks and illustrating qualitatively the snowpack layering. The blocks were then transported in insulated boxes of dimensions $0.5 \times 0.5 \times 1$ m^3 to the WSL-SLF cold labs in Davos under controlled temperature conditions ($-20°C$). The snow samples have not been impregnated in the field and some degree of metamorphism is expected to occur during transport.

To further characterize the snowpack at EastGRIP, snow pit measurements of the first 130 cm depth were performed on May 24, 2016, 11 p.m. local time at the shallow pit. Density and specific surface area (SSA) profiles were obtained from box cutter measurements (Proksch et al., 2016) and IceCube measurements (Zuanon, 2013), respectively, with a 3 cm vertical resolution. The *in-situ* temperature profile was measured with a 5 cm vertical resolution (**Figure 2**).

The *in-situ* measurements were complemented by automatic temperature data from the EastGRIP site that was provided through the EastGRIP surface measurement program (H-C. Steen-Larsen, personal communication). Automatic temperatures were measured by thermistors that were inserted into the snow the first year of the program and subsequently buried during accumulation. The measurements presented here are from May 2016 to May 2017, during which the amount of snow accumulation was evaluated between 40 and 50 cm. Available raw temperature measurements as a function of the initial sensor depths, not corrected for subsequent accumulation, are shown in **Figure 2**.

2.2. Laboratory Measurements

Each of the three snow blocks extracted along the EastGRIP snow pit were further sub-sampled in the laboratory for subsequent X-ray micro-computed tomography (microCT) and crystallographic orientation analyses (thin sections and Automatic Ice Texture Analysis, AITA). A schematic of the sampling procedure for both types of measurements is given in **Figure 3** and further detailed below. The exact location of the thin sections along the microCT sample is known only with a precision of a few millimeters. MicroCT measurements cover the entire profile length in a continuous way, whereas thin sections are not contiguous. Each orientation data extracted from the thin section automatic analysis integrates information over the full area of the thin section (2×3 cm^2).

2.2.1. Micro Computed Tomography Measurements

The microCT analysis was performed to obtain 3-D images of the snow microstructure and to derive the structural parameters. For that, two lines of parallel sampling were made from bottom to top along each of the one-meter-long snow block, in order to provide a 50% overlap between the samples, except at the transition between the one-meter-long blocks. Each sample had a diameter of about 30 mm, and a height of about 60 mm. The microCT analyses were performed in a micro-CT 40 scanner from ScancoMedical located in a cold-room at -15°C. After reconstruction the gray-scale images were filtered by a Gaussian filter (sigma = 1.5, support = 2) to remove the image noise, and segmented by using a fit of the histogram to three Gaussians as detailed in (Hagenmuller et al., 2013). The images have a voxel size of 18μm. By analyzing the microCT samples vertically in a moving region of interest (ROI) analysis (cubic window of 400 ×

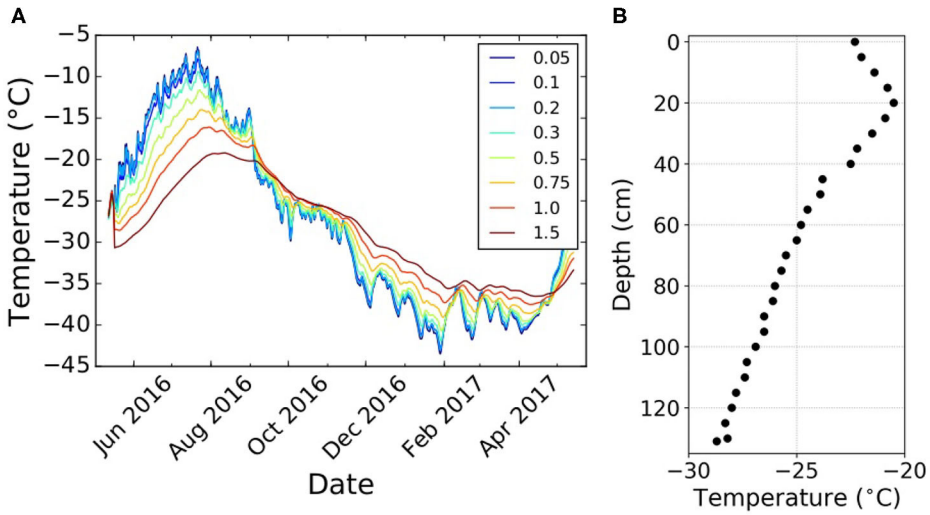

FIGURE 2 | (A) Temperature data (Courtesy of H-C. Steen-Larsen) measured from April 2016 to March 2017 at different depths in m (legend). **(B)** Temperature profile of the first 1.3 m depth of the snowpack measured at EastGRIP on May 24th, 2016.

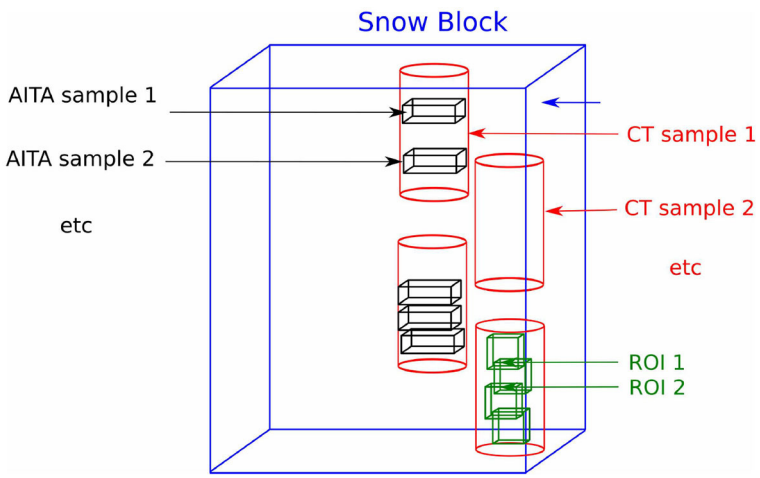

FIGURE 3 | Schematic showing the sub-sampling of the snow blocks for co-located microCT and AITA measurements. Typical dimensions of thin sections (from AITA samples) are 30×20 mm^2. MicroCT samples are about 60 mm height and 30 mm diameter.

400 × 400 voxels), continuous profiles of density, specific surface area and structural anisotropy were obtained. Immediately after the microCT scanning, each cylindrical sample was impregnated with diethyl phthalate (CAS No. 84-66-2) in a cold room at −4°C (Heggli et al., 2009) and kept at −60°C until thin sectioning.

2.2.2. Ice Texture Measurements

Distributions of **c**-axis crystallographic orientations (also called crystallographic fabrics or textures) were measured on thin sections of snow made along the impregnated microCT samples, following the technique described in Riche et al. (2012). Operating in a -15°C room, two to four thin sections were extracted from one microCT sample. Thin sections were cut and thinned down to a thickness of about 100 μm and were about 30×20 mm^2 in dimension. Most of them were cut vertically, compared to the microCT cylindrical sample, and therefore along the snow pit vertical (see **Figure 3**).

The **c**-axis crystallographic orientations were measured using the AITA, as performed in Riche et al. (2013) and Calonne et al. (2017). The analyzer provides the **c**-axis orientation $\mathbf{c}^k$ of every pixel k over the thin section surface. In our case, a pixel had a size of 10 μm and the entire area of the thin section was mapped.

Each orientation $\mathbf{c}^k$ is defined in a spherical coordinate system by an inclination θ_k (angle in the vertical plane between 0 and 90°) and an azimuth ϕ_k (angle in the horizontal plane between 0 and 360°) given in a local reference frame R with the third axis perpendicular to the thin section. The expression of $\mathbf{c}^k$ in this reference frame is:

$$\mathbf{c}^k = (\cos\phi_k \sin\theta_k, \sin\phi_k \sin\theta_k, \cos\theta_k) \quad (1)$$

Orientation measurements are provided together with a quality factor ranging from 0 to 100 for each pixel. Only pixels with a quality factor higher than 70 were considered here (Peternell et al., 2011). This automatically removes the non-ice pixels surrounding snow grains. To ensure that the samples are representative, analyzed thin sections contained at least 100 snow crystals.

2.2.3. Structural Fabric From microCT Data

Different types of structural fabric tensors can be computed from a two-phase microstructure (Moreno et al., 2014) to characterize the anisotropic distribution of ice and air in snow. For instance in Srivastava et al. (2016) a fabric tensor was computed from the mean intercept length to infer the stiffness tensor of snow. In the following, we used a definition of an orientation tensor that is based on the two-point correlation function of the microstructure (Löwe et al., 2013; Calonne et al., 2015; Leinss et al., 2016). Under the assumption of transverse isotropy and ellipsoidal symmetry of the correlation function, the structural orientation tensor takes the form

$$\boldsymbol{A}^{(2)} = \begin{bmatrix} Q(\epsilon) & 0 & 0 \\ 0 & Q(\epsilon) & 0 \\ 0 & 0 & 1-2Q(\epsilon) \end{bmatrix} \quad (2)$$

where $\epsilon = l_z/l_{xy}$ is the ratio between the vertical and horizontal correlation lengths obtained from the two-point correlation function. The function $Q(\epsilon)$ is explicitly given in Löwe et al. (2013, Equation 3). In this representation it follows that $\mathrm{Tr}(\boldsymbol{A}^{(2)}) = 1$ with eigenvalues given by $A_1^{(2)} = Q(\epsilon), A_2^{(2)} = Q(\epsilon), A_3^{(2)} = 1 - 2Q(\epsilon)$. As outlined in Torquato (2005, Chapter 17), "needle shaped microstructure" (i.e., preferential vertical orientations) correspond to $A_1^{(2)} = A_2^{(2)} = 1/2, A_3^{(2)} = 0$ (for $\epsilon \to \infty$) while "penny shaped microstructures" (i.e., preferential horizontal orientations) correspond to $A_1^{(2)} = A_2^{(2)} = 0, A_3^{(2)} = 1$ (for $\epsilon \to 0$). Practically, these extreme cases are never reached in snow where anisotropy values seem to be bounded by $0.7 < \epsilon < 2.1$ (Leinss et al., 2020). To characterize the structural fabric via $Q(\epsilon)$, the two-point correlation function $C(r)$ was calculated from segmented tomography images following Löwe et al. (2013) by means of fast Fourier transformation, and fitted to exponentials $C_\beta(r) = C_{\beta,0}\exp(-r/l_\beta)$ along the coordinate axes $\beta = x, y, z$ (z being the vertical direction along the snow pit). This procedure yields the correlation lengths l_z and $l_{xy} = (l_x + l_y)/2$, their ratio $\epsilon = l_z/l_{xy}$ and the orientation tensor via Equation (2).

2.2.4. Crystallographic Fabric From AITA Data

From the **c**-axis orientation measurements (Equation 1), a quantitative evaluation of the texture can be performed by means of the second order orientation tensor $\mathbf{a}^{(2)}$ and its eigenvalues as in e.g., (Thorsteinsson et al., 1997). The second order orientation tensor is defined as

$$\mathbf{a}^{(2)} = (1/N_p)\sum_{k=1}^{N_p} \mathbf{c}^k \otimes \mathbf{c}^k \quad (3)$$

with N_p the total number of pixels over which $\mathbf{c}^k$ is calculated, and $\otimes$ the tensor product. By construction, $\mathbf{a}^{(2)}$ is symmetric and a symmetry reference frame exists in which $\mathbf{a}^{(2)}$ is diagonal. Let $a_1^{(2)}$, $a_2^{(2)}$, and $a_3^{(2)}$ denote the three corresponding eigenvalues that satisfy $1 > a_1^{(2)} > a_2^{(2)} > a_3^{(2)} > 0$ and $a_1^{(2)} + a_2^{(2)} + a_3^{(2)} = 1$. These eigenvalues correspond to the length of the axes of the ellipsoid that best fits the distribution of the **c**-axis orientations. Three classical types of texture can be defined that are (1) the isotropic texture with **c**-axes oriented randomly in all directions leading to $a_1^{(2)} \simeq a_2^{(2)} \simeq a_3^{(2)} \simeq 1/3$, (2) the girdle texture with **c**-axes oriented randomly within a preferential plane, $a_1^{(2)} \simeq a_2^{(2)} > 1/3$, and (3) the cluster texture with **c**-axes oriented toward one direction and $a_2^{(2)} \simeq a_3^{(2)} < 1/3$.

In the following, the eigenvector direction, and the associated eigenvalues, are represented in the c-axis pole figure (stereographic projection of c-axes) for each thin section. The pole-figures are plotted in the plane of the thin section (see e.g., **Figure 4**).

As in Calonne et al. (2017), and following (Fisher et al., 1987), we defined the girdle index $n_G = \ln(a_2^{(2)}/a_3^{(2)})$ (the higher, the more girdle-type is the texture) and the cluster index $n_C = \ln(a_1^{(2)}/a_2^{(2)})$ (the higher, the more cluster-type is the texture).

3. RESULTS

3.1. Overview

The following **Figures 4–6** illustrate the snow microstructure (vertical slices from the microCT images and associated range of ϵ values) and the crystallographic fabric (c-axis orientation maps and associated pole figures) obtained at some representative depths along the three-meter deep snow pit. Note that due to the sampling procedure (cf. section 2.2) the match between microCT images and thin section areas analyzed by AITA is not exact. Thin section areas are nevertheless always located within the microCT sample volume.

A large part of the snowpack is characterized by medium to strong structural fabrics, as it can be detected on some of the microCT images showing a chain-like structure of the ice matrix, and with ϵ values larger than 1.2. This is the case for snow at 80 cm and 263 cm depth, shown in **Figure 4**, for which ϵ values are as high as 1.7. The weakest structural anisotropy is mostly found in the upper part of the pit, as shown in **Figure 6** (a) with an example from a sample extracted at 28 cm depth, with ϵ close to 0.8.

In contrast to what was observed in previous similar analyses performed on natural snow cover from Antarctica (Point Barnola) (Calonne et al., 2017) or the Alps (Riche et al., 2013), many thin sections show a (crystallographic) texture with a significant **c**-axis clustering. For the two examples shown in **Figure 5**, the crystallographic anisotropy is characterized by an eigenvalue $a_1^{(2)}$ of the second order orientation tensor as high as 0.68 and a strong cluster indexes of up to 1.4. Similar values were found at a depth of about 1,000 m along the Greenlandic NEEM ice core (Montagnat et al., 2014). The cluster positions on the pole figures (see e.g., **Figure 5**) reveal that their direction is very

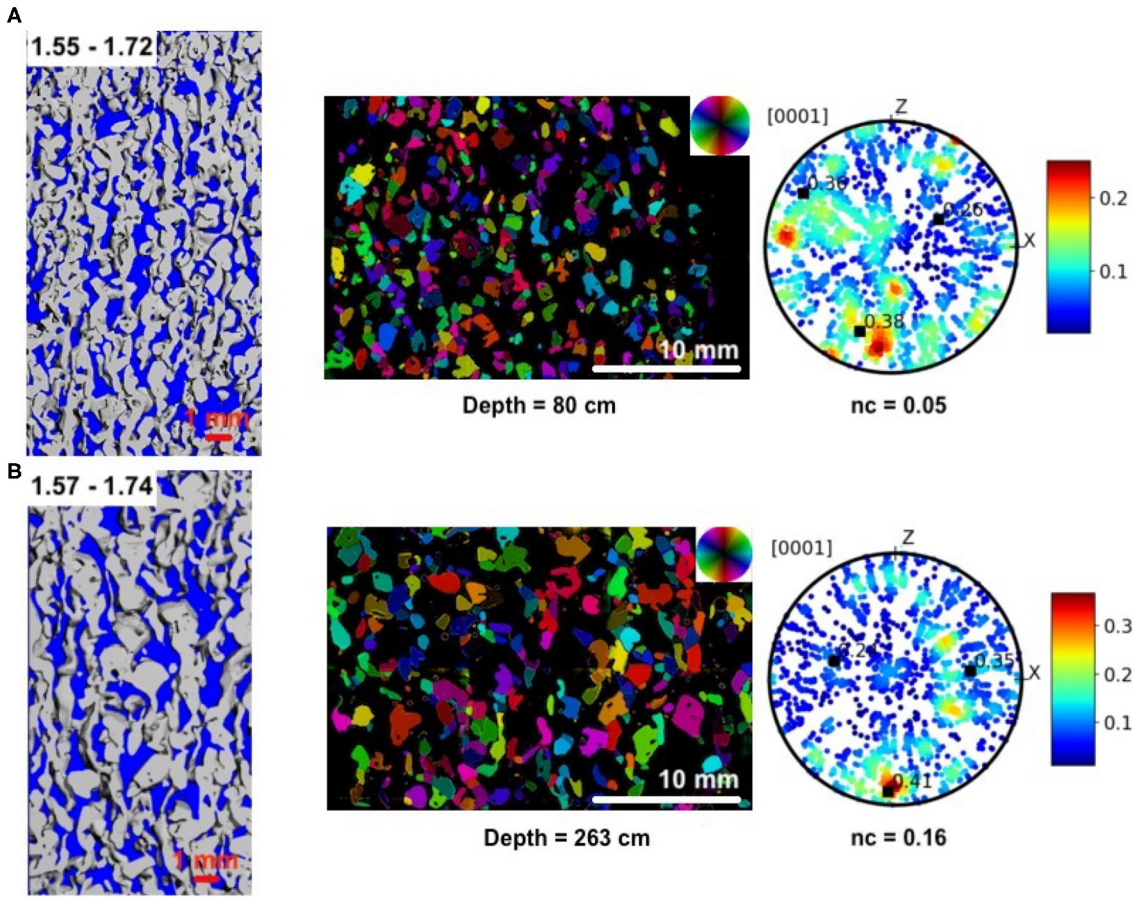

FIGURE 4 | MicroCT structure, microstructure and **c**-axis pole figure from samples extracted at 80 **(A)** and 263 **(B)** cm depth along the EastGRIP snow pit. The thin section was made in the microCT sample. A range of ϵ values is given in the microCT structure. The figures of microstructure are color-coded with the colorwheel that represents orientations of the c-axis. On the pole figures, 5,000 pixels are plotted. The black squares correspond to the location of the eigenvectors of $\mathbf{a}^{(2)}$, and the associated eigenvalues are given. nc is the cluster index. The z-axis is the same for the three images.

close to 0° or 180° (North or South) with a low inclination. As thin sections were cut out vertically, those cluster-type textures correspond to **c**-axes mostly oriented closed to the vertical. At a few specific depth, variability within the height of one single thin section (2 cm) is observed and the resulting eigenvalues thus reveal an "average" texture over a non-homogeneous vertical extent (see **Figure 6**).

3.2. Structural and Crystallographic Fabric Profiles

As the main result of the present study, we provide the vertical profiles of all the structural and crystallographic parameters in **Figure 7**.

In view of traditionally used snow parameters like density or specific surface area the snow at EastGRIP is unremarkable. The density (**Figure 7A**) shows a rather typical behavior of highly fluctuating values around an average density of about 370 kg m^{-3} without any apparent trend with depth in these first three meters, as expected for this location (Schaller et al., 2016). Most values are between 250 and 450 kg m^{-3}. The 2012 Greenland surface melt event is easily identified in a depth of around 1.64 m where the density reaches 818 kg m^{-3}. The *in-situ* density profile from cutter measurements, from the nearby snow pit, matches rather well with the microCT data, showing similar stratigraphic features in the first 1.3 m.

The profile of specific surface area (**Figure 7B**) shows a drop from near surface values of 15 m^2 kg^{-1} to about 8 m^2 kg^{-1} in the first 0.5 m. Below, specific surface area decreases more smoothly with depth, reaching about 6 m^2 kg^{-1} at 3 m. The *in-situ* IceCube measurements show a similar sharp decrease with depth in the first meter. Specific surface area values are however systematically higher than the ones from microCT, especially in the first 0.4 m (about 25 m^2 kg^{-1} vs. 15 m^2 kg^{-1}). Similar deviations were reported in Calonne et al. (2019), suggesting possible biases in the specific surface area measurement methods. In our case, the deviations might have been likewise caused by equi-temperature metamorphism in the snow blocks during transport and storage, leading to a specific surface area decrease, the higher the initial specific surface area, the higher the evolution rate.

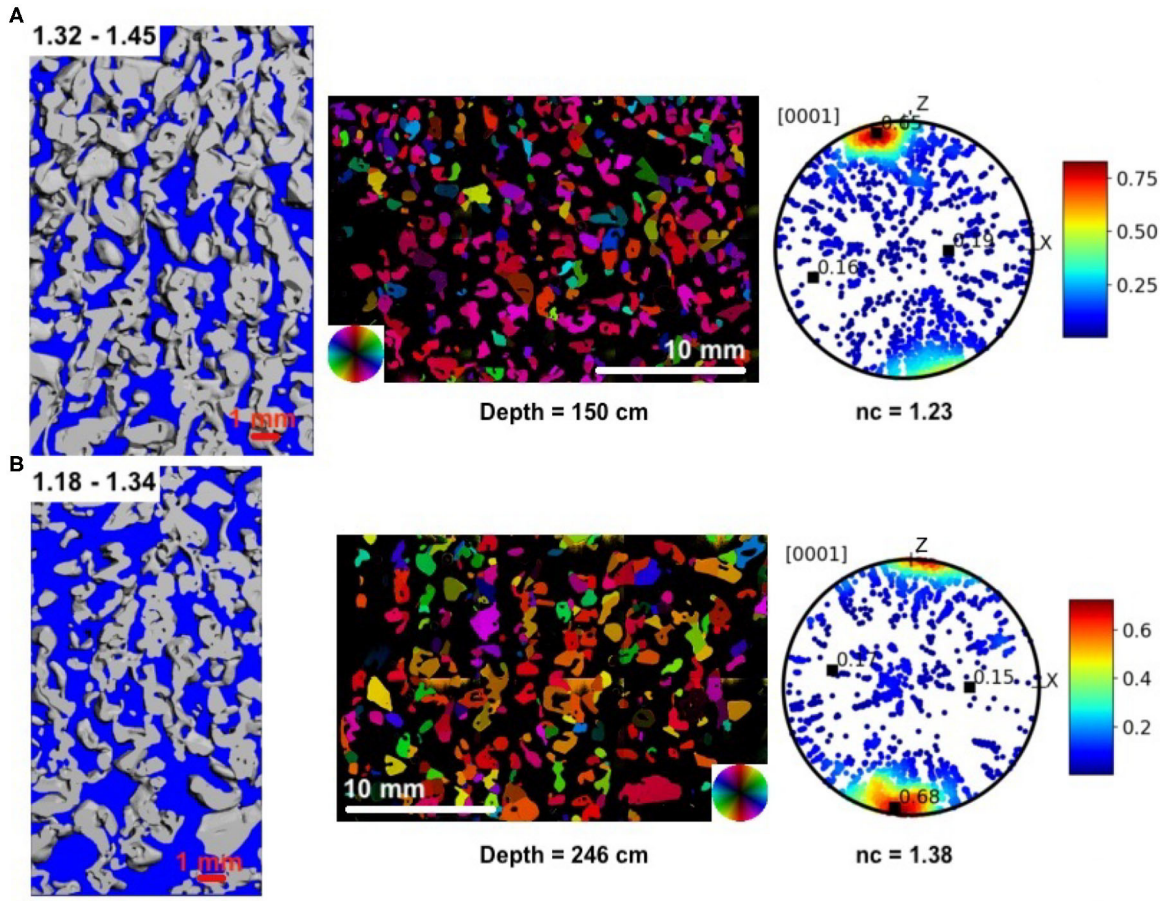

FIGURE 5 | MicroCT structure, microstructure and **c**-axis pole figure from samples extracted at 150 **(A)** and 246 **(B)** cm depth along the EastGRIP snow pit. The thin section was made in the microCT sample. A range of ϵ values is given in the microCT structure. The figures of microstructure are color-coded with the colorwheel that represents orientations of the c-axis. On the pole figures (right), randomly picked 5,000 pixels are plotted. The black squares correspond to the orientation of the eigenvectors of $\mathbf{a}^{(2)}$, and the associated eigenvalues are given. nc is the cluster index. The z-axis is the same for the three images.

In contrast, the structural fabric profile (**Figure 7D**) reveals an interesting signal with depth, where characteristic (saw-tooth-like) up-and-down variations are observed. These variations become more apparent when the data is smoothed (Gaussian filter with $\sigma = 14$ cm black line in **Figure 7D**): the structural anisotropy repeatedly shows abrupt increases followed by areas of gentle decrease with depth. The anisotropy signal can be used to define seasonal markers (Moser et al., 2020). To this end vertical dashed lines have been manually added at the locations of steepest increase of the anisotropy with depth. From the date the profile was taken (May 24 2016) and from the date of the 2012 melt event (early July), the observed offset of the (2016, 2012) markers from the surface and the melt-event, respectively, indicates that the steepest gradient of the anisotropy signal is created in the early summer season. Overall, these annual anisotropy markers are consistent with the thickness of mean annual layers of about 27 cm (given an average snow density of about 370 kg m^{-3}, and an average accumulation rate of 100 kg $m^{-2}yr^{-1}$).

The crystallographic fabric are shown in **Figure 7F**. Whereas, cluster indexes in the first meter are low (below 0.4) and little-scattered, indexes from 1 to 3 m depth strongly fluctuate and reach high values up to 1.4 (corresponding to $a_1^{(2)}$ eigenvalues of 0.7). A clustering trend is observed in the depth interval 1–1.5 m depth (above the melt-refrozen layer) as well as in the interval 1.7 to 2.5 m depth. In contrast, no significant evolution and trend are observed in the girdle index (not shown). For comparison, the eigenvalues of the structural and crystallographic fabric (eigenvalues) are shown in **Figures 7C,E**.

4. DISCUSSION

4.1. Near-Surface Signal of Structural Anisotropy

A key finding of the present study is a clear seasonal signal in the structural fabric (anisotropy) in the first three meters of snow at the EastGRIP site. This is in agreement with observations in the snowpack at Kohnen, Antarctica, that were recently published

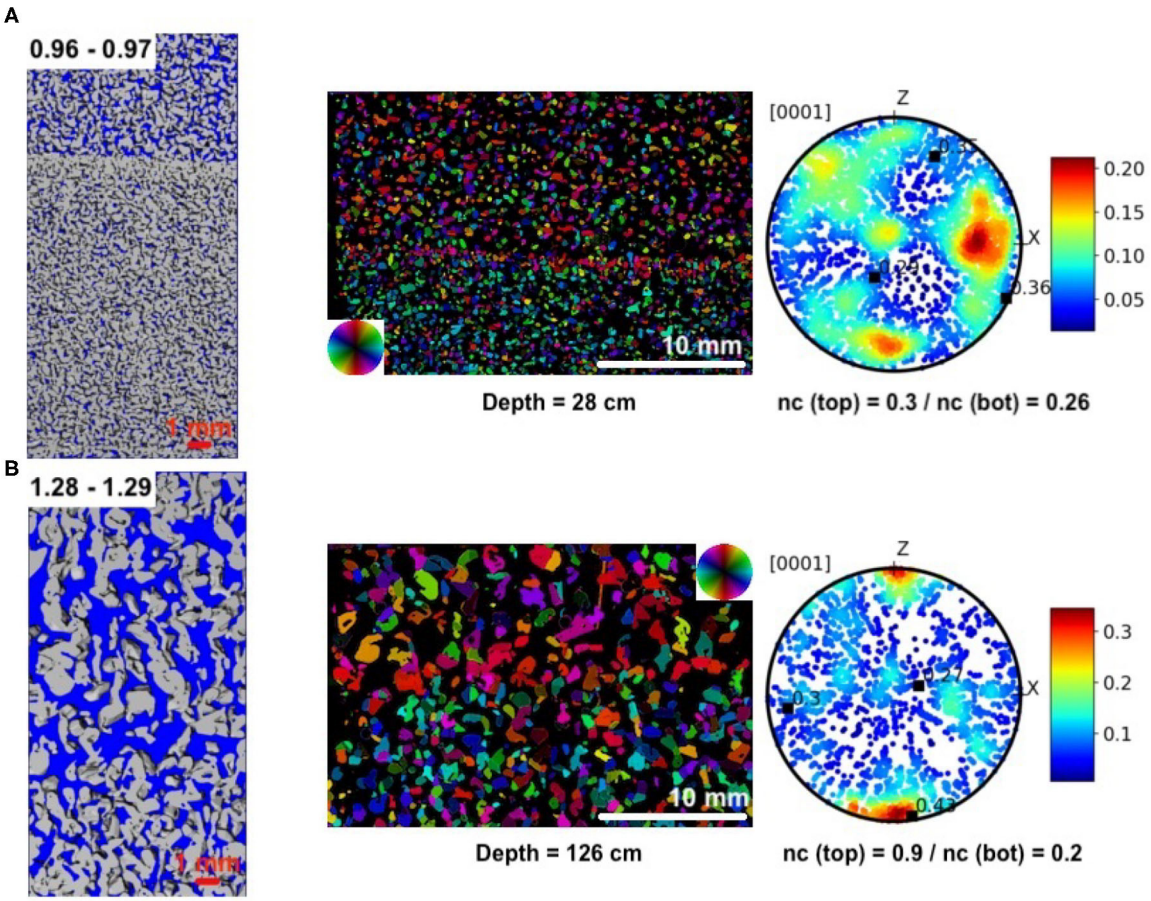

FIGURE 6 | MicroCT structure, microstructure and **c**-axis pole figure from samples extracted at 28 **(A)** and 126 **(B)** cm depth along the EastGRIP snow pit. A corresponding range of ϵ values is given in the microCT structure. The figures of microstructure are color-coded with the colorwheel that represents orientations of the c-axis. On the pole figures, 5,000 pixels are plotted. The black squares correspond to the location of the eigenvectors of $\mathbf{a}^{(2)}$, and the associated eigenvalues are given. nc is the cluster index. The z-axis is the same for the three images.

by Moser et al. (2020). The seasonal variations in the structural anisotropy emerge as a characteristic, asymmetric saw-tooth signal (**Figure 7D**) where the timing suggests that the steep edge is imprinted into the profile in early summer.

To quantify the expected range of anisotropy variations we have forced the model from Leinss et al. (2020) with the measured temperatures (**Figure 2**) in the absence of settling assuming a constant accumulation rate (presented in **Appendix A**). The results suggest that the order of magnitude of the structural fabric variations (seasonal jumps in ϵ of up to 0.3) can be well-explained by variations in the vapor flux during temperature gradient metamorphism caused by observed temperatures (cf. **Appendix A** and **Figure 8A**). The vapor flux is proportional to the temperature gradient and increases with temperature according to the temperature dependence of the equilibrium vapor pressure. The results shown in **Appendix A** and **Figure 8B** also indicate that for a realistic *mean* surface velocity $\dot{b} = 0.3$ m yr^{-1} (corresponding to a mean density of 370 kg m^{-3} and an accumulation rate of 100 kg m^{-2}yr^{-1}) the 4 peaks occurring in the structural anisotropy in the first 1.5 m (cf. **Figure 7D**) can be recovered.

The asymmetry of the saw-tooth-pattern is however not explained by the model when neglecting settling and seasonal variations in the accumulation rate. **Figure 8B** reveals the subtle impact of the accumulation rate on both, absolute magnitude and variability of the structural anisotropy with depth, even when using a constant accumulation throughout the year. The accumulation rate determines the timing and duration at which a material element, previously located at the surface, is advected through the (anisotropy forming) heat wave into the sub-surface. Accordingly, when the accumulation rate exhibits seasonality too, it can be expected that a lag between the maxima of temperature/temperature gradients (anisotropy forming period) and the maxima of accumulation (anisotropy burial period) contributes to the signal shape. To assess the seasonality of accumulation at EastGRIP, we considered re-analyses data from the model MAR (Modèle Atmosphérique Régional) (Fettweis et al., 2020) for the monthly averaged precipitation at EastGRIP

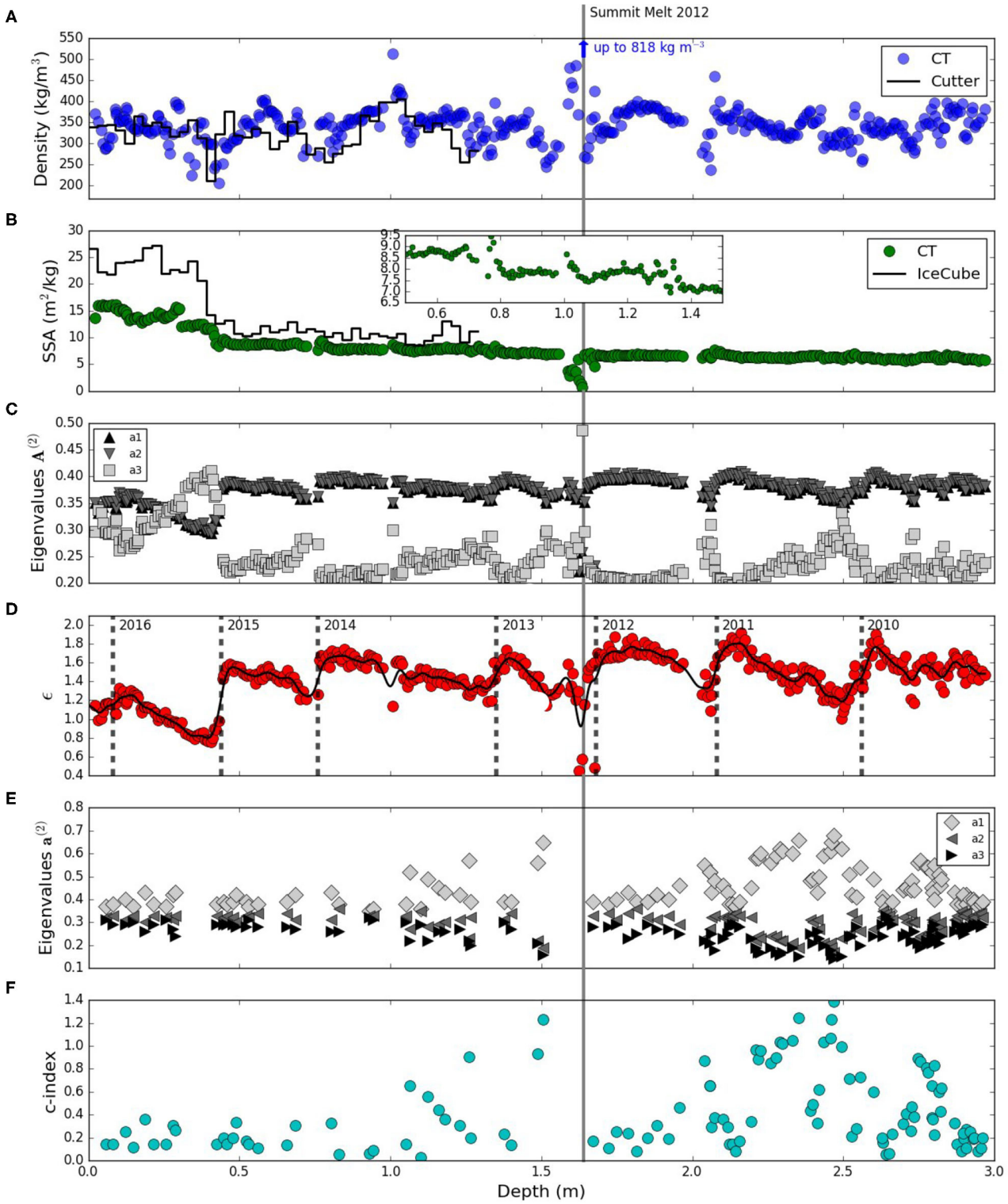

FIGURE 7 | Structural and crystallographic signals extracted from microCT and AITA from the snow profile taken at EastGrip. **(A)** Density (kg m^{-3}). **(B)** Specific Surface Area (m^2 kg^{-1}). **(C)** Eigenvalues of the structural fabric tensor $\mathbf{A}^{(2)}$. **(D)** Ratio of the vertical and horizontal correlation lengths. **(E)** Eigenvalues of the second order orientation tensor $\mathbf{a}^{(2)}$. **(F)** Cluster index n_C. The figure is complemented by a marker for the 2012 melt event and several anisotropy markers [2016-2011 in **(D)**] that correspond to the early summer season of the respective year (for details cf. text).

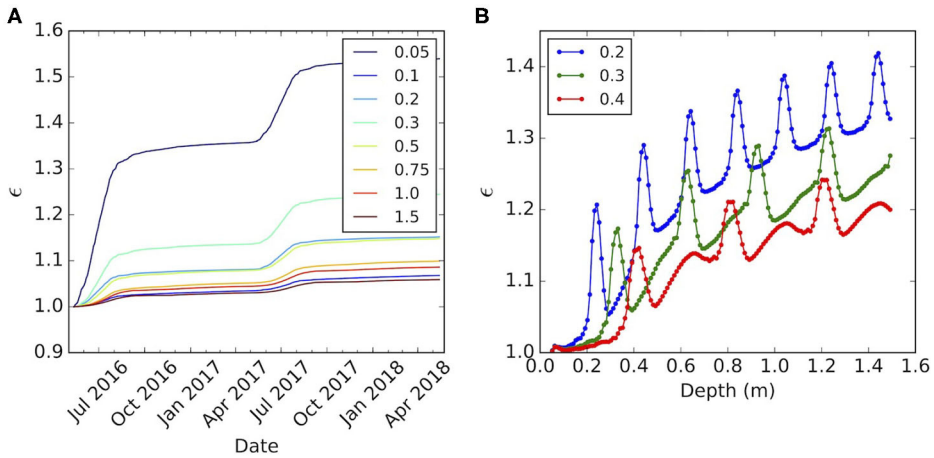

FIGURE 8 | (A): Modeled evolution of the structural anisotropy ϵ over 2 years with temperature and temperature gradient time series taken from the EastGRIP field measurements at fixed depth in m (legend). **(B)**: Modeled anisotropy profile using spatio-temporal interpolation of the measured temperatures and gradients for different (constant) accumulation rates in m/year (legend). The start of the time series in **(A)** and the surface **(B)** corresponds to May 12. For details see text.

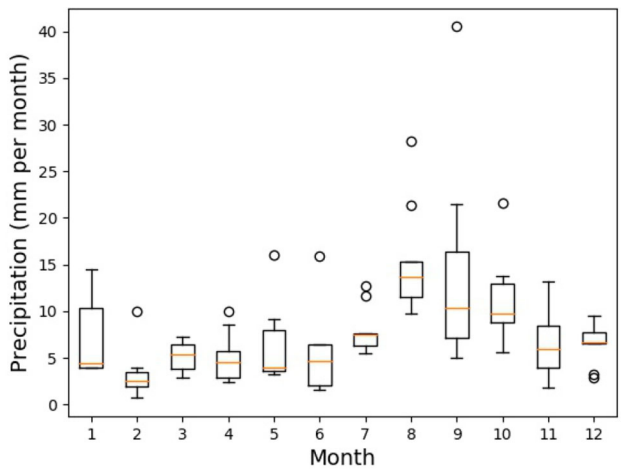

FIGURE 9 | Precipitation at EastGRIP obtained from model MAR re-analyses. Statistics over the period 2009–2017.

over the period 1979–2018. The averaged precipitation for the period of interest (2009–2017) is included in **Appendix B**, **Figure 9** suggesting a seasonal pattern in accumulation around an annual average of about 96 mm water equivalent (w.e.) ($\sim$ 8 mm w.e per month). Comparing **Figure 9** with **Figure 2** confirms that the maximum firn temperatures and temperature gradients (July) coincide with low accumulation in summer, and that the temperature maxima lag $\sim$2 months behind the accumulation maxima in fall.

From the considerations of the accumulation rate and from the results of the model above, we suggest the following mechanism for the creation of the asymmetric saw tooth pattern in anisotropy at EastGRIP: The steep edge is formed at the surface in early-to-mid summer as a consequence of three mechanisms. (i) The increase of temperatures and gradients in the sub-surface that considerably increase the rate of anisotropy formation, consistent in order of magnitude with Leinss et al. (2020). (ii) The onset of diurnal temperature variations in spring that likely inhibit anisotropy formation close to the surface due to alternating gradients at daily frequency. Such metamorphism under alternating gradients is known to lack common features of depth hoar formation (Pinzer and Schneebeli, 2009), even for high gradient magnitudes. But diurnal gradients may still effectively contribute to a reduction of the anisotropy through settling (Leinss et al., 2020). (iii) Lower summer accumulation which leaves the surface snow in conditions (i) and (ii). Later in the year, through increase of accumulation, the generated steep edge of the saw-tooth is buried without significant change in shape (steep edge still visible in the second cycle in (cf. **Figure 7D**) but with an overall gentle increase under the influence of persistent, seasonal temperature gradients. The latter shifts the anisotropy signal toward higher values by repeated metamorphism of consecutive years. Clearly, a confirmation of the hypothesized interplay of mechanisms would however require the implementation of all potential processes in a single model.

In our data, the initially imprinted asymmetric saw tooth is preserved down to the depth of 3 m corresponding to 6 year old snow. It is interesting to note that Fujita et al. (2014) reported measurable variations in the structural anisotropy down to a depth of 26 m in the NEEM firn using dielectric methods. Since our structural anisotropy parameter ϵ can be directly used to compute the dielectric anisotropy (Leinss et al., 2016) these findings are linked by exactly the same parameter. Fujita et al. (2014) attributed the signal as remainders of summer-to-winter variations in near-surface metamorphism, which would be consistent with our findings. It must be noted though, that at NEEM the details of accumulation, temperature and seasonality are different. Kuramoto et al. (2011) reported that the deposition

during the November-July period is greater than during July-October period by 10–20 mm w.e. (expressed here as a mass balance) for a mean annual mass balance of 176 mm w.e. An important conclusion drawn by Fujita et al. (2014) for NEEM was the preservation of the insolation-sensitive structural fabric signal all the way to the pore close-off. To assess the fate of the structural anisotropy in deep firn however requires to discuss the structural fabric alongside with the crystallographic fabric which is known to influence deep firn densification.

4.2. Near-Surface Signal of Crystallographic Anisotropy

In addition to the structural fabric signal, we also find indications of a crystallographic signal in the EastGRIP snow. Marked cluster-type textures are visible along the snow pit and occur more frequently with depth, with eigenvalues $a_1^{(2)}$ that locally exceed 0.6 in the last two meters. This contrasts with the measurements performed at Point Barnola, Antarctica (Calonne et al., 2017), where only weak girdle-type textures were observed along a similar three-meter deep snow pit ($T_{\mathrm{mean}} \sim -40^{\circ}$C). In addition, the significant anti-correlation of the crystallographic fabric (girdle-type) with density observed along the Point Barnola snow pit is absent here at EastGRIP.

Two hypotheses could explain the occurrence of clustered textures in the snowpack, namely (i) the temperature gradient metamorphism, at temperature conditions encountered in EastGRIP ($T_{\mathrm{mean}} \sim -20^{\circ}$C), favors a cluster-type texture or (ii) at the temperature conditions of EastGRIP, compression creep can not be neglected anymore and, within some specific layers, conditions could favor individual grains to rotate toward the vertical because of dislocation motion under a local stress resulting from the vertical overburden stress.

The first hypothesis can be tested by comparing the EastGRIP snowpack texture with the one measured during temperature gradient metamorphism experiments performed by Riche et al. (2013) on a natural alpine snowpack at a mean temperature of -20°C and under a constant gradient of 50 $^{\circ}$C m^{-1} (bottom temperature: -15°C; top temperature: -25°C). The texture evolved from an initial cluster-type fabric toward a weak girdle-type for a low-density natural snow sample. Thus, although the temperature and temperature gradient conditions in the EastGRIP snowpack are close to the conditions of these experiments, the texture evolution differs. The main differences between (Riche et al., 2013) experiments and the EastGRIP snowpack conditions are two-fold. First, the first 20 cm of the EastGRIP snowpack encounter temperatures higher than -10°C during the summer period, i.e., about 3 months. Around -10°C, there is a transition in ice crystal growth from a preferential prismatic growth to a preferential basal (**c**-axis) growth (Nakaya and Marshall, 1954; Lamb and Scott, 1972). From Calonne et al. (2017), one could expect these conditions to favor the growth of grains with c-axis oriented parallel to the temperature gradient (i.e., basal faces perpendicular to the vapor flux). Given that the temperature gradient is vertical, cluster-type fabric with **c**-axes oriented vertically would then developed preferentially. However, if this short duration of a cluster-favored temperature gradient metamorphism was sufficient, it would result in a positive correlation between structural anisotropy and cluster index (Riche et al., 2013; Calonne et al., 2017). This correlation is not observed, as pronounced structural anisotropy are found below 0.4 m depth ($\epsilon > 1.2$) whereas cluster index shows larger values only from 1 m depth and below. Second, whereas Riche et al. (2013) studied the effect of a constant temperature gradient during 3 months, the intensity and direction of the temperature gradient at EastGRIP vary with time due the seasonal temperature oscillations. The impact of an alternating gradient (diurnal oscillations) on snow microstructure was studied recently by Wiese and Schneebeli (2017b) but no analysis of crystallographic orientations was done. Overall, a firm conclusion about the role of temperature gradient metamorphism in the development of the observed cluster-type texture is presently not possible and confirming or rejecting this hypothesis would require further dedicated experiments.

The second hypothesis is based on the observation that the number of cluster-type textures increases with depth. In natural, slow deforming ice this type of cluster texture can be explained by dislocation-induced deformation under compression (Alley, 1988, 1992). Although the density at the surface and the mean overburden stress is relatively low, the stress distribution in snow is expected to be broad (Theile et al., 2011). Accordingly, the load bearing fraction of the microstructure exhibits significantly higher stresses than the mean (Schneebeli and Sokratov, 2004), in particular if grains are connected by small necks (Hagenmuller et al., 2014). Depending on the structural fabric of the layer, the strength and viscosity are expected to vary significantly impacting local stress concentrations (Wiese and Schneebeli, 2017b). In particular, we expect layers with a high vertical structural anisotropy to be stiffer to viscoplastic deformation under a vertical load, relative to the surrounding more isotropic layers. The following hypothesis is therefore based on the picture of a layered snowpack, where the induced strain is vertically heterogeneous and concentrated in layers with a low structural anisotropy.

To assess the potential impact of stress on texture formation in these layers we have conducted an order-of-magnitude estimate for the conditions encountered in the EastGRIP snowpack in **Appendix C**. By employing the so called Sachs approximation (Sachs, 1928), we computed the rotation of independent grains under a vertically homogeneous compressive stress corresponding to the weight of two-meters of snow with an average density of 350 kg m^{-3}. The rotation is computed from the stress-induced motion of dislocations following (Alley, 1988) and taking into account the temperature dependant dislocation velocity measured by Shearwood and Whitworth (1991). By considering the above mentioned local stress enhancement as estimated in snow, we show that an ensemble of independent grains evolves toward an anisotropic texture similar to the one measured along the EastGRIP snow pack [$a_1^{(2)} \sim 0.6$] after about 3,000 to 4,000 days ($\sim$ 8–11 yrs) in the temperature conditions of EastGRIP (see **Appendix C** and **Figure 10**). By doing the same modeling for colder temperature conditions (-40°C), no anisotropic texture could

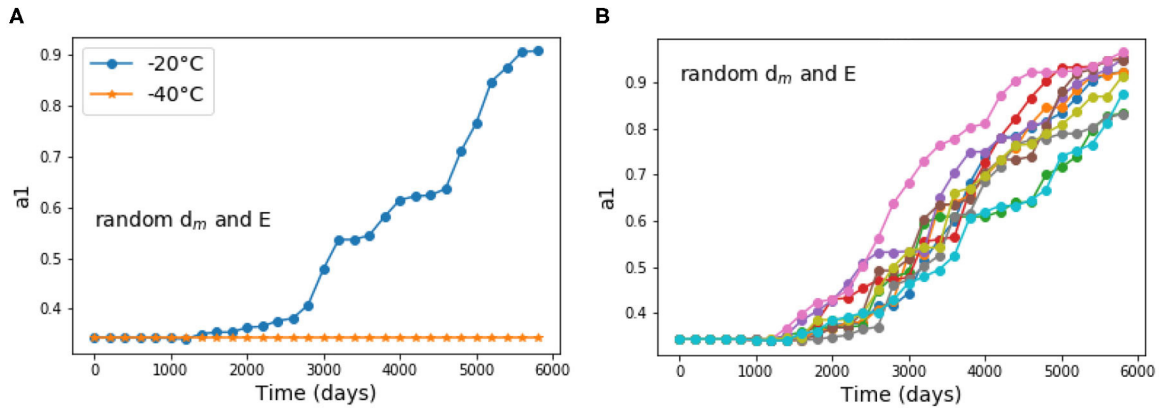

FIGURE 10 | Modeled evolution of $a_1^{(2)}$ as a function of time, based on 1000 random initial orientations, following the homogeneous stress hypothesis (Sachs), with initial density varying randomly between $d_m(min)$ and $d_m(max)$ (Table A1) and stress concentration E varying randomly between 1 and 10. **(A)** Comparison between the two temperature conditions of Point Barnola (−40°C) and EastGRIP (−20°C) for on single run. **(B)** Ten runs performed for EastGRIP conditions (−20°C). No variation between the runs is observed for Point Barnola conditions.

be generated. From Alley (1988) a texture characterized by an $a_1^{(2)}$ eigenvalue of 0.6 would correspond to a accumulated compressive strain of about 25%. The measured variation of density between adjacent layers can be as high as 100 kg m^{-3} (average density of 370 kg m^{-3}), and are therefore not incompatible with a creep driven local densification of 25%. Although a clear correlation could not be established owing to the limited numbers of texture measurements, the highest cluster indexes are found in layers characterized by a low structural anisotropy. This is coherent with the assumption of isotropic layers being more compliant to compressive stress than stiffer layers which are characterized by a strong vertical anisotropy.

This order-of-magnitude estimate shows that for the temperature conditions of EastGRIP, the overburden stress imposed by the upper two-meter snow column could activate dislocations in individual grains in some layers to an extent that induces significant crystallographic rotations after only 8 to 11 years. The resulting modeled textures are coherent with the textures measured in the third meter of the EastGRIP snowpack. That such a clustered texture is not observed at Point Barnola (Calonne et al., 2017) is consistent with the fact that plastic deformation is very dependent on temperature, and therefore no rotation is predicted at very low temperatures. This simple model predictably fails to predict the **c**-axis rotations at higher density for which interactions between neighboring grains must be taken into account. By neglecting the effect of strain incompatibilities between grains, the Sachs hypothesis considered here is expected to overestimate the kinematic of crystallographic rotations (Castelnau et al., 1996). In addition, metamorphism-induced recrystallization, grain re-arrangement and heterogeneous densification contribute to the evolution of microstructural (structural and crystallographic) heterogeneities [see for instance Fujita et al. (2009)] that would require to be represented by means of a full-field approach.

4.3. The Necessity of Quantifying Both Fabric Tensors

Considering the ice matrix as (i) an isotropic polycrystal arranged in a geometrically anisotropic structure or as (ii) an anisotropic polycrystal arranged in a geometrically isotropic structure lead to the same result: the homogenized mechanical properties are anisotropic. Whereas the structural anisotropy naturally dominates at the surface, in deep ice cores only the crystallographic anisotropy remains. In the snow-firn column in between, both types of anisotropy occur and their relative strength must be quantified for a faithful mechanical modeling.

Deep in the firn, the dense and (structurally) isotropic structure is expected to weaken the effect of local stresses on the mechanical behavior. Grain boundary migration mechanisms associated with normal grain growth, which govern the microstructure evolution in firn (de la Chapelle et al., 1998), likely reduce the anisotropy inherited from metamorphism. Both mechanisms (densification and normal grain growth) favor evolution toward a weaker structural and a weaker crystallographic anisotropy with depth (Montagnat et al., 2011; Calonne et al., 2019).

Despite a reduced structural fabric anisotropy with depth (Calonne et al., 2019), the layered structure of the snowpack inherited from anisotropy variations may still survive and impact the lock-in zone characteristics (thickness and depth) down to the close off depth (Fujita et al., 2009, 2014; Gregory et al., 2014; Fourteau et al., 2019). In particular, the existence of a seasonal signal in the structural fabric strengthens the interpretation of Gregory et al. (2014) that hypothesizes an impact of the microstructure on the lock-in processes. Also, the interaction between a layered structure of the snow pack and the development of a cluster-type crystallographic fabric, as suggested here, tends to confirm the hypothesis of Fujita et al. (2014) about the role of the layering on the close-off mechanisms.

Among the many firn densification models (Lundin et al., 2017), the approach developed initially by Arnaud et al. (2000)

is based on a mechanical description that utilizes the idea of a densification mechanisms by grain boundary sliding in the upper snow cover (density lower than 550 kg m^{-3}), as first suggested by including the seasonal variations, however suggests that other geometrical-structural aspects may influence the effective (compactive) viscosity of snow, accompanied by the layering. Our result indicate that viscoplastic deformation occurs in low density snow and induces crystallographic fabric anisotropy, while firn models mentioned above integrate either grain boundary sliding (Arnaud et al., 2000) or diffusion creep (Arthern et al., 2010) that do not produce any crystallographic rotation. These later mechanisms are used for the purpose to introduce an artificial grain-size (microstructure) dependence in the densification law. Most firn models are following a single layer and the evolution of its properties with depth without considering the layering structure of the snow and firn column. Our results also highlight that the imposed surface conditions result into a strong structural layering of the snowpack (down to 3 m, $\rho \leq 450$ kg m^{-3}). This layering impacts snow metamorphism under varying temperature gradients, but also induces a heterogeneous response to the overburden load. The fact that these aspects are not taken into account in firn models are partly compensated by the use of many adjustable parameters. This strategy partly prevents firn models to converge toward an "universal" firn description able to represent various densification conditions (Lundin et al., 2017).

5. CONCLUSIONS

In this work, we analyzed the microstructural characteristic of snow along a three-meter deep pit from the EastGRIP site, Greenland. These characteristics were derived from two signals influencing the mechanical processes during snow and firn densification. The structural anisotropy was retrieved from continuous X-ray microCT evaluation of the ice and pore matrix. The crystallographic anisotropy was evaluated by optical measurement of ice crystal orientations on regularly-spaced thin sections. The key results obtained are the following:

- In contrast to parameters like density or specific surface area, the structural fabric profile unambiguously reveals the seasonal cycles at EastGRIP.
- The crystallographic fabric reveals some strong cluster-type textures at shallow depth, that were not observed in the Antarctic Point Barnola snowpack (Calonne et al., 2017).
- Model-based arguments suggest that the asymmetric saw-tooth pattern in the structural anisotropy is imprinted into the signal by the interplay of accumulation and near-surface metamorphism through diurnal and seasonal temperature gradients.
- The emergence of a cluster-type crystallographic fabric at shallow depth can be roughly reproduced by a simplified viscoplastic modeling approach (homogeneous stress approximation) which is supposed to apply preferentially in soft layers.
- Current firn modeling may benefit from an improved representation of the snowpack to predict the layering of the compaction viscosity from both structural and crystallographic anisotropy.

DATA AVAILABILITY STATEMENT

The datasets generated for this study are available on request to the corresponding author.

AUTHOR CONTRIBUTIONS

MMo, HL, and NC co-treated the results and wrote the paper together. MMo made the AITA measurements and analyses. MMo, NC, MJ, and MMa made the microCT measurements. HL made the analyses of microCT measurements. NC and MS did the field work, field measurements, and field preparation of the snow blocks.

FUNDING

The Swiss Federal Institute for Forest, Snow, and Landscape Research WSL provided a research fellowship to MMo during her 1 year stay in WSL-SLF, Davos (2016-2017). NC was supported by grant 152845 from the Swiss National Science Foundation and by the WSL-project 201612N1411. This work benefited from support from the INSIS and INSU institutes of CNRS and from a grant from Labex OSUG@2020 (ANR10LABEX56). Field work in EastGRIP benefited from the financial support of US-NSF, NASA, and WSL-SLF within the frame of a Greenland Climate Network (GC-Net) maintenance program.

ACKNOWLEDGMENTS

We thank H-C. Steen-Larsen from University of Bergen for providing EastGRIP temperature data. We thank Lino Schmidt for his contribution to the field work and snow block extraction at EastGRIP. We are very grateful to Hubert Gallée and Xavier Fettweis for providing access to MAR re-analyses data. Many thanks to the reviewers for their useful critical evaluation of our work.

SUPPLEMENTARY MATERIAL

The Supplementary Material for this article can be found online at: https://www.frontiersin.org/articles/10.3389/feart.2020.00365/full#supplementary-material

REFERENCES

Alley, R. B. (1988). Fabrics in polar ice sheets - Development and prediction. *Science* 240, 493–495.

Alley, R. B. (1992). Flow-law hypotheses for ice-sheet modeling. *J. Glaciol.* 38, 245–255.

Arnaud, L., Weiss, J., Gay, M., and Duval, P. (2000). Shallow-ice microstructure at Dome Concordia. *Ann. Glaciol.* 30, 8–12. doi: 10.3189/172756400781820813

Arthern, R. J., Vaughan, D. G., Rankin, A. M., Mulvaney, R., and Thomas, E. R. (2010). *In situ* measurements of antarctic snow compaction compared with predictions of models. *J. Geophys. Res. Earth Surface* 115:F03011. doi: 10.1029/2009JF001306

Bender, M. L. (2002). Orbital tuning chronology for the vostok climate record supported by trapped gas composition. *Earth Planet. Sci. Lett.* 204, 275–289. doi: 10.1016/S0012-821X(02)00980-9

Burr, A., Noël, W., Trecourt, P., Bourcier, M., Gillet-Chaulet, F., Philip, A., et al. (2017). The anisotropic contact response of viscoplastic monocrystalline ice particles. *Acta Mater.* 132, 576–585. doi: 10.1016/j.actamat.2017.04.069

Calonne, N., Flin, F., Lesaffre, B., Dufour, A., Roulle, J., Puglièse, P., et al. (2015). Celldym: a room temperature operating cryogenic cell for the dynamic monitoring of snow metamorphism by time-lapse x-ray microtomography. *Geophys. Res. Lett.* doi: 10.1002/2015GL063541

Calonne, N., Geindreau, C., Flin, F., Morin, S., Lesaffre, B., Rolland du Roscoat, S., et al. (2012). 3-d image-based numerical computations of snow permeability: links to specific surface area, density, and microstructural anisotropy. *Cryosphere* 6, 939–951. doi: 10.5194/tc-6-939-2012

Calonne, N., Milliancourt, L., Burr, A., Philip, A., Martin, C. L., Flin, F., et al. (2019). Thermal conductivity of snow, firn, and porous ice from 3-d image-based computations. *Geophys. Res. Lett.* 46, 13079–13089. doi: 10.1029/2019GL085228

Calonne, N., Montagnat, M., Matzl, M., and Schneebeli, M. (2017). The layered evolution of fabric and microstructure of snow at point barnola, central east Antarctica. *Earth Planet. Sci. Lett.* 460, 293–301. doi: 10.1016/j.epsl.2016.11.041

Castelnau, O., Duval, P., Lebensohn, R. A., and Canova, G. (1996). Viscoplastic modeling of texture development in polycrystalline ice with a self-consistent approach: comparison with bound estimates. *J. Geophys. Res.* 101, 13851–13868.

Coléou, C., Lesaffre, B., Brzoska, J-B., Ludwig, W., Boller, E. (2001). Three-dimensional snow images by x-ray microtomography. *Ann. Glaciol.* 32, 75–81. doi: 10.3189/172756401781819418

Dahl-Jensen, D., Gundestrup, N., Miller, H., Watanabe, O., Johnsen, S. J., Steffensen, J. P., et al. (2002). The northGRIP deep drilling programme. *Ann. Glaciol.* 35, 1–4. doi: 10.3189/172756402781817275

de la Chapelle, S., Castelnau, O., Lipenkov, V., and Duval, P. (1998). Dynamic recrystallization and texture development in ice as revealed by the study of deep ice cores in Antarctica and Greenland. *J. Geophys. Res.* 103, 5091–5105.

Duval, P., Ashby, M., and Anderman, I. (1983). Rate controlling processes in the creep of polycrystalline ice. *J. Phys. Chem.* 87, 4066–4074.

Fettweis, X., Hofer, S., Krebs-Kanzow, U., Amory, C., Aoki, T., Berends, C. J., et al. (2020). GrSMBMIP: intercomparison of the modelled 1980-2012 surface mass balance over the greenland ice sheet. *Cryosphere Discuss.* 2020, 1–35. doi: 10.5194/tc-2019-321

Fisher, N. I., Lewis, T., and Embleton, B. J. (1987). *Statistical Analysis of Spherical Data*. Cambridge: Cambridge University Press.

Fourteau, K., Faïn, X., Martinerie, P., Landais, A., Ekaykin, A. A., Lipenkov, V. Y., et al. (2017). Analytical constraints on layered gas trapping and smoothing of atmospheric variability in ice under low-accumulation conditions. *Clim. Past* 13, 1815–1830. doi: 10.5194/cp-13-1815-2017

Fourteau, K., Martinerie, P., Faïn, X., Ekaykin, A. A., Chappellaz, J., and Lipenkov, V. (2020) Estimation of gas record alteration in very low-accumulation ice cores. *Clim. Past* 16, 503–522. doi: 10.5194/cp-16-503-2020

Fourteau, K., Martinerie, P., Faïn, X., Schaller, C. F., Tuckwell, R. J., Löwe, H., et al. (2019). Multi-tracer study of gas trapping in an east antarctic ice core. *Cryosphere* 13, 3383–3403. doi: 10.5194/tc-13-3383-2019

Fujita, S., Hirabayashi, M., Goto-Azuma, K., Dallmayr, R., Satow, K., Zheng, J., et al. (2014.) Densification of layered firn of the ice sheet at neem, greenland. *J. Glaciol.* 60, 905–921. doi: 10.3189/2014JoG14J006

Fujita, S., Okuyama, J., Hori, A., and Hondoh, T. (2009). Metamorphism of stratified firn at dome fuji, antarctica: a mechanism for local insolation modulation of gas transport conditions during bubble close off. *J. Geophys. Res. Earth Surface*. 114. doi: 10.1029/2008JF001143

Gerling, B., Löwe, H., and van Herwijnen, A. (2017). Measuring the elastic modulus of snow. Geophys. Res. Lett. 44, 11088–11096. doi: 10.1002/2017GL075110

Gow, A. J., and Williamson, T. C. (1976) Rheological implications of the internal structure and crystal fabrics of the West Antarctic ice sheet as revealed by deep core drilling at Byrd station. *Geol. Soc. Am. Bull.* 87, 1665–1677.

Gregory, S. A., Albert, M. R., and Baker, I. (2014). Impact of physical properties and accumulation rate on pore close-off in layered firn. *Cryosphere* 8, 91–105. doi: 10.5194/tc-8-91-2014

Hagenmuller, P., Chambon, G., Lesaffre, B., Flin, F., and Naaim, M. (2013). Energy-based binary segmentation of snow microtomographic images. *J. Glaciol.* 59, 859–873. doi: 10.3189/2013JoG13J035

Hagenmuller, P., Chambon, G., and Naaim, M. (2015). Microstructure-based modeling of snow mechanics: a discrete element approach. *The Cryosphere* 9, 1969–1982. doi: 10.5194/tc-9-1969-2015

Hagenmuller, P., Theile, T. C., and Schneebeli, M. (2014). Numerical simulation of microstructural damage and tensile strength of snow. *Geophys. Res. Lett.* 41, 86–89. doi: 10.1002/2013GL058078

Heggli, M., Frei, E., and Schneebeli, M. (2009). Snow replica method for three-dimensional x-ray microtomographic imaging. *J. Glaciol.* 55, 631–639. doi: 10.3189/002214309789470932

Kuramoto, T., Goto-Azuma, K., Hirabayashi, M., Miyake, T., Motoyama, H., Dahl-Jensen, D., et al. (2011). Seasonal variations of snow chemistry at neem, greenland. *Ann. Glaciol.* 52, 193–200. doi: 10.3189/172756411797252365

Laepple, T., Hörhold, M., Münch, T., Freitag, J., Wegner. A., and Kipfstuhl, S. (2016) Layering of surface snow and firn at Kohnen station, Antarctica –noise or seasonal signal? *J. Geophys. Res. Earth Surface* 121, 1849–1860. doi: 10.1002/2016JF003919

Lamb, D., and Scott, W. D. (1972). Linear growth rates of ice crystals grown from the vapor phase. *J. Crystal Growth* 12, 21–31. doi: 10.1016/0022-0248(72)90333-8

Leinss, S., Löwe, H., Proksch, M., and Kontu, A. (2020). Modeling the evolution of the structural anisotropy of snow. *Cryosphere* 14, 51–75. doi: 10.5194/tc-14-51-2020

Leinss, S., Löwe, H., Proksch, M., Lemmetyinen, J., Wiesmann, A., and Hajnsek, I. (2016). Anisotropy of seasonal snow measured by polarimetric phase differences in radar time series. *Cryosphere* 10, 1771–1797. doi: 10.5194/tc-10-1771-2016

Lipenkov, V. Y., Raynaud, D., Loutre, M. F., and Duval, P. (2011). On the potential of coupling air content and o2/n2 from trapped air for establishing an ice core chronology tuned on local insolation. *Q. Sci. Rev.* 30, 3280–3289. doi: 10.1016/j.quascirev.2011.07.013

Löwe, H., Riche, F., and Schneebeli, M. (2013). A general treatment of snow microstructure exemplified by an improved relation for thermal conductivity. *Cryosphere* 7, 1473–1480. doi: 10.5194/tc-7-1473-2013

Lundin, J. M. D., Stevens, C. M., Arthern, R., Buizert, C., Orsi, A., Ligtenberg, S. R. M., et al. (2017). Firn model intercomparison experiment (firnmice). *J. Glaciol.* 63, 401–422. doi: 10.1017/jog.2016.114

Montagnat, M., Azuma, N., Dahl-Jensen, D., Eichler, J., Fujita, S., Gillet-Chaulet, F., et al. (2014). Fabric measurement along the NEEM ice core, greenland, and comparison with GRIP and NGRIP ice cores. *Cryosphere* 8, 1129–1138. doi: 10.5194/tc-8-1129-2014

Montagnat, M., Blackford, J. R., Piazolo, S., Arnaud, L., and Lebensohn, R. A. (2011). Measurements and full-field predictions of deformation heterogeneities in ice. *Earth Planet. Sci. Lett.* 305, 153–160. doi: 10.1016/j.epsl.2011.02.050

Moreno, R., Borga, M., and Smedby, Ö. (2014). "Techniques for computing fabric tensors: a review," in: *Visualization and Processing of Tensors and Higher Order Descriptors for Multi-Valued Data,* eds C. F. Westin, A. Vilanova, and B. Burgeth (Berlin, Heidelberg: Springer), 271–292.

Moser, D. E., Hörhold, M., Kipfstuhl, S., and Freitag, J. (2020). Microstructure of snow and its link to trace elements and isotopic composition at Kohnen station, dronning maud land, Antarctica. *Front. Earth Sci.* 8:23. doi: 10.3389/feart.2020.00023

Nakaya, U., and Marshall, J. (1954). Snow crystals. *Am. J. Phys.* 22, 573–573.

Perutz, M. F., Seligman, G., and Bragg, W. H. (1939). A crystallographic investigation of glacier structure and the mechanism of glacier flow. *Proc. R. Soc. Lond. Ser. A Math. Phys. Sci.* 172, 335–360. doi: 10.1098/rspa.1939.0108

Peternell, M., Russell-Head, D., and Wilson, C. (2011). A technique for recording polycrystalline structure and orientation during *In situ* deformation cycles of rock analogues using an automated fabric analyser. *J. Microsc.* 242, 181–188. doi: 10.1111/j.1365-2818.2010.03456.x

Pinzer, B. R., and Schneebeli, M. (2009). Snow metamorphism under alternating temperature gradients: Morphology and recrystallization in surface snow. *Geophys. Res. Lett.* 36. doi: 10.1029/2009GL039618

Proksch, M., Rutter, N., Fierz, C., and Schneebeli, M. (2016). Intercomparison of snow density measurements: bias, precision, and vertical resolution. *Cryosphere* 10, 371–384. doi: 10.5194/tc-10-371-2016

Riche, F., Montagnat, M., and Schneebeli, M. (2013). Evolution of crystal orientation in snow during temperature gradient metamorphism. *J. Glaciol.* 59, 1–9. doi: 10.3189/2013JoG12J116

Riche, F., Schneebeli, M., and Tschanz, S. (2012). Design-based stereology to quantify structural properties of artificial and natural snow using thin sections. *Cold Regions Sci. Technol.* 79–80, 67–74. doi: 10.1016/j.coldregions.2012.03.008

Rolland du Roscoat, S., King, A., Philip, A., Reischig, P., Ludwig, W., Flin, F., et al. (2011). Analysis of snow microstructure by means of x-ray diffraction contrast tomography. *Adv. Eng. Mater.* 13, 128–135. doi: 10.1002/adem.201000221

Sachs, G. (1928). Zur Ableitung einer Fliessbedingung. *Z. Verein Deutscher Ing.* 72, 734–736.

Schaller, C. F., Freitag, J., Kipfstuhl, S., Laepple, T., Steen-Larsen, H. C., and Eisen, O. (2016). A representative density profile of the north greenland snowpack. *Cryosphere* 10, 1991–2002. doi: 10.5194/tc-10-1991-2016

Schlegel, R., Diez, A., Löwe, H., Mayer, C., Lambrecht, A., Freitag, J., et al. (2019). Comparison of elastic moduli from seismic diving-wave and ice-core microstructure analysis in antarctic polar firn. *Ann. Glaciol.* 60, 220–230. doi: 10.1017/aog.2019.10

Schneebeli, M. (2004). Numerical simulation of elastic stress in the microstructure of snow. *Ann. Glaciol.* 38, 339–342. doi: 10.3189/172756404781815284

Schneebeli, M., and Sokratov, S. A. (2004). Tomography of temperature gradient metamorphism of snow and associated changes in heat conductivity. *Hydrol. Process.* 18, 3655–3665. doi: 10.1002/hyp.5800

Shearwood, C., and Whitworth, R. W. (1991). The velocity of dislocations in ice. *Philos. Mag.* A64, 289–302.

Srivastava, P. K., Chandel, C., Mahajan, P., and Pankaj, P. (2016). Prediction of anisotropic elastic properties of snow from its microstructure. *Cold Regions Sci. Technol.* 125, 85–100. doi: 10.1016/j.coldregions.2016.02.002

Steen-Larsen, H. C., Masson-Delmotte, V., Sjolte, J., Johnsen, S. J., Vinther, B. M., Bréon, F. M., et al. (2011). Understanding the climatic signal in the water stable isotope records from the neem shallow firn/ice cores in northwest greenland. *J. Geophys. Res. Atmos.* 116. doi: 10.1029/2010JD014311

Theile, T., Loewe, H., Theile, T., and Schneebeli, M. (2011). Simulating creep of snow based on microstructure and the anisotropic deformation of ice. *Acta Mater.* 59, 7104–7113. doi: 10.1016/j.actamat.2011.07.065

Thorsteinsson, T., Kipfstuhl, J., and Miller, H. (1997). Textures and fabrics in the GRIP ice core. *J. Geophys. Res.* 102, 26583–26600.

Torquato, S. (2005). *Random Heterogeneous Materials: Microstructure and Macroscopic Properties.* New York, NY: Springer.

Vallelonga, P., Christianson, K., Alley, R., Anandakrishnan, S., Christian, J., Dahl-Jensen, D., et al. (2014). Initial results from geophysical surveys and shallow coring of the northeast greenland ice stream (NEGIs). *Cryosphere* 8, 1275–1287. doi: 10.5194/tc-8-1275-2014

Wiese, M., and Schneebeli, M. (2017a). Snowbreeder 5: a micro-ct device for measuring the snow-microstructure evolution under the simultaneous influence of a temperature gradient and compaction. *J. Glaciol.* 63, 355–360. doi: 10.1017/jog.2016.143

Wiese, M., and Schneebeli, M. (2017b). Early-stage interaction between settlement and temperature-gradient metamorphism. *J. Glaciol.* 63, 652–662. doi: 10.1017/jog.2017.31

Wilson, C., Russell-Head, D., and Sim, H. (2003). The application of an automated fabric analyzer system to the textural evolution of folded ice layers in shear zones. *Ann. Glaciol.* 37, 7–17. doi: 10.3189/172756403781815401

Zuanon, N. (2013). "Icecube, a portable and reliable instruments for snow specific surface area measurement in the field," in *International Snow Science Workshop Grenoble-Chamonix Mont-Blanc 2013 Proceedings* (Chamonix-Mont Blanc), 1020–1023.

Conflict of Interest: The authors declare that the research was conducted in the absence of any commercial or financial relationships that could be construed as a potential conflict of interest.

The reviewer SL declared a past co-authorship with one of the authors HL to the handling editor.

Advantages of publishing in Frontiers

OPEN ACCESS
Articles are free to read for greatest visibility and readership

FAST PUBLICATION
Around 90 days from submission to decision

HIGH QUALITY PEER-REVIEW
Rigorous, collaborative, and constructive peer-review

TRANSPARENT PEER-REVIEW
Editors and reviewers acknowledged by name on published articles

Frontiers
Avenue du Tribunal-Fédéral 34
1005 Lausanne | Switzerland

Visit us: www.frontiersin.org
Contact us: info@frontiersin.org | +41 21 510 17 00

REPRODUCIBILITY OF RESEARCH
Support open data and methods to enhance research reproducibility

DIGITAL PUBLISHING
Articles designed for optimal readership across devices

FOLLOW US
@frontiersin

IMPACT METRICS
Advanced article metrics track visibility across digital media

EXTENSIVE PROMOTION
Marketing and promotion of impactful research

LOOP RESEARCH NETWORK
Our network increases your article's readership